UNIVERSITY OF OKLAHOMA

GRADUATE COLLEGE

APPLICATIONS OF GAUSSIAN MIXTURE MODEL TO WEATHER OBSERVATIONS

A DISSERTATION

SUBMITTED TO THE GRADUATE FACULTY

in partial fulfillment of the requirements for the

Degree of

DOCTOR OF PHILOSOPHY

By

ZHENGZHENG LI
Norman, Oklahoma
2011

Downloaded from SHAREOK. Persistent Handle URL: https://hdl.handle.net/11244/318575

APPLICATIONS OF GAUSSIAN MIXTURE MODEL TO WEATHER OBSERVATIONS

A DISSERTATION APPROVED FOR THE
SCHOOL OF ELECTRICAL AND COMPUTER ENGINEERING

BY

Dr. Yan Zhang, Chair

Dr. Robert Palmer

Dr. Tian-You Yu

Dr. Alexander Ryzhkov

Dr. Amy McGovern

© Copyright by ZHENGZHENG LI 2011
All Rights Reserved.

Acknowledgments

I would like to express my deepest appreciation to my advisor and chair, Dr. Yan Zhang, for his guidance throughout my Ph.D study. His enthusiasm and passion in research set up a role model for me. I have been very fortunate to have an advisor who always welcomes new ideas and offers me insightful advice. His support has helped me overcome many difficulties I have faced in the last four years.

My appreciation and gratitude go to my committee members, Dr. Robert Palmer, Dr. Tian-You Yu, Dr. Alexander Ryzhkov and Dr. Amy McGovern, for their generous supports and helps. I am also thankful for members in RIL and ARRC, who have worked with me, helped me and inspired me during my study at OU.

I am grateful of the grant supports from NASA Langley Research Center and NOAA-NSSL. This work would have been impossible without their supports. I am also grateful of all my friends. Life is more colorful with them.

Last but not least, I would like to thank my family, my wife and better half, Aimei, who opened my eyes to the beauty of the world with her endless love; my son, Edan, whose lovely smile always lights up my day; and my parents, who have always supported and encouraged me. It is a blessing to have them in my life.

Contents

Acknowledgments **iv**

List Of Tables **viii**

List Of Figures **x**

Abstract **xiv**

1 Introduction **1**
1.1 Introduction 1
1.2 Organization of the Dissertation 5

2 Weather Radar Systems and Measurements **7**
2.1 Introduction to Weather Radar Systems 7
2.1.1 Transmit and Receive Waveform 7
2.1.2 Weather Radar Measurements 9
2.1.3 Sampling and Aliasing Effects 10
2.1.4 Weather Radar Equation 11
2.2 Polarimetric Radar Measurements 12

3 Monte-Carlo Simulation and Physical Models **18**
3.1 Drop Size Distribution (DSD) 19
3.1.1 DSD Models 19
3.1.2 DSD Moments and Related Variables 23
3.2 General Hydrometeor Models 23
3.3 Melting Models and Effective Dielectric Constants of Mixtures 27
3.4 Scattering Theory 32
3.5 Single-Cell Monte Carlo Simulation and Simulated Radar Variables 36
3.5.1 Scattering Plots of Hydrometers at X-band 37
3.5.2 Dual-Pol Variables of Rain at S-, C- and X-band 41
3.6 Radar Simulations with ARPS Model Outputs 45
3.6.1 Scenario I 51
3.6.2 Scenario II 52

4 Gaussian Mixture Model (GMM) and Classifier 59
4.1 Definitions . . . 59
4.2 Training GMMs . . . 63
4.2.1 The Expectation-Maximization Algorithm . . . 63
4.2.2 The k-means Clustering Algorithm . . . 67
4.3 GMM-based Hydrometeor Classification . . . 69
4.3.1 Bayesian Classification Theory . . . 73
4.3.2 Hydrometeor Hazard Detection for Airborne Sense and Avoid Radar . . . 74
4.3.3 Hail Hazard Detection . . . 78

5 Gaussian Mixture Parameter Estimator (GMPE) 83
5.1 Theoretical fundamentals . . . 83
5.1.1 Derivation . . . 83
5.1.2 Proof of Eq. (5.10) . . . 86
5.1.3 Proof of Bayes' Least Square Estimate . . . 87
5.1.4 Definitions of Error Terms . . . 89
5.2 Performance Evaluation for GMPE . . . 89
5.2.1 Attenuation Estimation for Rain, Snow and Hail . . . 92
5.2.2 Rainfall Rate Estimation Through Dual-Frequency and Dual-Polarized Radar Measurements . . . 95
5.2.3 Conclusions on Performance of GMPE . . . 96
5.3 S-band DSD Retrieval Using GMPE . . . 98
5.4 Gaussian Mixture Rainfall Rate Estimator . . . 102
5.4.1 Training Dataset Construction . . . 103
5.4.2 Training of GMREs . . . 106
5.4.3 JPOLE Dataset Description . . . 113
5.4.4 Results and Comparisons . . . 115
5.4.5 Discussion and Conclusions for GMRE Study . . . 120
5.5 Correction of Rain Path Attenuation: A Constrained Iterative GMPE Approach . . . 122
5.5.1 Introduction . . . 123
5.5.2 Review of PIA Correction Techniques . . . 124
5.5.3 Constrained Iterative GMPE Approach . . . 128
5.5.4 Simulation Dataset Construction . . . 131
5.5.5 Numerical Results . . . 133

6 Sequential Gaussian Mixture Parameter Estimator with a Kalman Filter Structure 140
6.1 Sequential Gaussian Mixture Parameter Estimator (SGMPE) . . . 142
6.2 SGMPE Mixture Reduction . . . 153
6.3 Rainfall Rate Estimation at X-band Using SGMPE . . . 156
6.3.1 GMPE Construction . . . 157
6.3.2 Performance Evaluation for SGMPEs . . . 159

6.3.3 Conclusions 167

7 Conclusions **169**
7.1 Summary 169
7.2 Major Achievements 172
7.3 Future Work 174

Reference List **176**

Appendix A - List Of Symbols **186**

Appendix B - List Of Acronyms and Abbreviations **190**

List Of Tables

2.1 Radar Frequencies and Wavelengths 8

3.1 Dielectric constants of ice (ϵ_i) at different frequencies and temperatures 30
3.2 Dielectric constants of water (ϵ_w) at different frequencies and temperatures 30
3.3 Sizes of Particles Used in Simulations for Different Species (all in [mm]) 36
3.4 Mixing and Melting Ratio Ranges used in the Single-Cell Simulations. (M for Melting) 38
3.5 General Decision Regions for Hydrometeors at 10 GHz (M for Melting) 40
3.6 Key Parameters of the Single Cell Monte-Carlo Simulation for Rain. . 45
3.7 Key Parameters of the Simulated Airborne Radar Sensor 48
3.8 Parameters Used in Simulations for Different Species 49
3.9 Information for Scenario I 51
3.10 Information for Scenario II 56

4.1 Mixing and Melting Ratio Ranges used in the Single-Cell Simulations. (M for Melting) 75
4.2 Classification accuracy of GMM model for airborne radar system (X-band). (M for Melting) 77

5.1 Key Parameters of the Radar Simulator. 90
5.2 RMSEs in [db km^{-1}] for A_h Estimations Based on PLRs. 92
5.3 RMSEs in [mm hr^{-1}]for R estimation based on PLRs. 96
5.4 Performance of DSD Retrieval from the β Method. (All in [mm hr^{-1}]) 99
5.5 Performance of DSD Retrieval from GMPE with 20 mixtures. (All in [mm hr^{-1}]) 100
5.6 Key Parameters of the Single Cell Monte-Carlo Simulation used in the GMRE Study. 105
5.7 Rain parameters retrieved by GMREs with 5 mixtures for the simulation dataset. N_0 [mm^{-1}m^{-3}], Λ [mm^{-1}], all rainfall rate R [mm hr^{-1}] 108
5.8 Rain parameters retrieved by GMREs with 20 mixtures for the simulation dataset. N_0 [mm^{-1}m^{-3}], Λ [mm^{-1}], all rainfall rate R [mm hr^{-1}] 110
5.9 Performance comparison of rainfall retrieval algorithms for the ARS dataset. All in [mm hr^{-1}] 116

5.10 Performance comparison of rainfall retrieval algorithms for the MES dataset. All in [mm hr^{-1}] 117
5.11 Required constants for Eq. (5.32) and Eq. (5.31) 127
5.12 Key Parameters of the Single Cell Monte-Carlo Simulation 132
5.13 Performance of PLR algorighms and GMPE with 12 mixtures 134
5.14 Performance of different path-integrated attenuation techniques in low noise environment (1 [dB] for Z_H, 0.3 [dB] for Z_{DR} and 2^o for Φ_{dp}). Results are from averaging over 200 realizations and 20 random generated paths. 135
5.15 Performance of different path-integrated attenuation techniques in high noise environment (2 [dB] for Z_H, 0.6 [dB] for Z_{DR} and 4^o for Φ_{dp}). Results are from averaging over 200 realizations and 20 random generated paths. 136

6.1 Performance of GMPE with 6 mixtures for rainfall rate estimation (all in [mm hr^{-1}]) 158

List Of Figures

1.1 Structure of this study. 4

3.1 Example of different DSD models. DSD models are fitted from observations from a 2D disdrometer. 22
3.2 Particle scattering geometry. 24
3.3 Axis raio for an oblate spheroid. 25
3.4 Different raindrop axis ratio models. 26
3.5 Axis ratio r_a with randomness. 26
3.6 The instrumentation setup for hydrometeor scattering measurement. . 29
3.7 Comparison between measured and theoretically predicted scattering cross-section curves of melting ice spheres with ice as background and water as inclusion. 30
3.8 Relations between temperature and melting ratios for hail (top) and snow (bottom). 33
3.9 Relationships among melting ratio, fractional water content and particle diameter change, for snow and hail. From top to bottom, (a) Melting ratio changes versus fraction of water changes for snow and hail. (b) Melting ratio changes versus fraction of diameter changes for snow and hail. 34
3.10 Concepts of single-Cell Monte Carlo simulations. 37
3.11 Scatter plots of hydrometeor species at 10 GHz. From top to bottom, (a) Z_H and Z_{DR} plot, (b) Z_H and K_{DP} plot. 39
3.12 Simulated dual-pol variable scatter plots of rain for KOUN (S-band). From top to bottom, (a) Z_H and Z_{DR} plot, (b) Z_H and K_{dp} plot. . . 42
3.13 Simulated dual-pol variable scatter plots of rain for OU-PRIME (C-band). From top to bottom, (a) Z_H and Z_{DR} plot, (b) Z_H and K_{dp} plot. 43
3.14 Simulated dual-pol variable scatter plots of rain for RaxPol (X-band). From top to bottom, (a) Z_H and Z_{DR} plot, (b) Z_H and K_{dp} plot. . . 44
3.15 Basic concepts for airborne polarimetric radar sensing simulations. . . 47
3.16 The simulation data-flow diagram. 47
3.17 Geometries of airborne volume scanning observation of hazardous weather regions with PPI and RHI scanning schemes, PPI-I and RHI scans are performed at 12.2 km height, PPI-II scan is performed at 9 km height around melting layer. 50

3.18 Weather field for PPI scan at altitude 12.2 km. From left to right, (a) Mixing ratio of snow - q_s, (b) Mixing ratio of hail - q_h 52
3.19 Simulated radar returns for PPI scan at altitude 12.2 km. From left to right and top to bottom, (a) Reflectivity - Z_H, (b) Differential reflectivity - Z_{DR}, (c) Specific differential phase - K_{DP} 53
3.20 Weather field for RHI scan at altitude 12.2 km. From left to right and top to bottom, (a) Mixing ratio of rain - q_r, (b) Mixing ratio of snow - q_s, (c) Mixing ratio of hail - q_h. 54
3.21 Simulated radar returns for RHI scan at altitude 12.2 km. From left to right and top to bottom, (a) Reflectivity - Z_H, (b) Differential reflectivity - Z_{DR}, (c) Specific differential phase - K_{DP} 55
3.22 Weather field for PPI scan at altitude 9.2 km. From left to right and top to bottom, (a) Mixing ratio of rain - q_r, (b) Mixing ratio of snow - q_s, (c) Mixing ratio of hail - q_h. 57
3.23 Simulated radar returns for PPI scan at altitude 9.2 km. From left to right and top to bottom, (a) Reflectivity - Z_H, (b) Differential reflectivity - Z_{DR}, (c) Specific differential phase - K_{DP} 58

4.1 Example of GMM with different number of mixtures. Data set is generated from $0.6\mathcal{N}(5, 1.5) + 0.4\mathcal{N}(15, 3)$. From left to right and top to bottom, (a) GMM with 2 mixture; (b) GMM with 5 mixture; (c) GMM with 10 mixture; (d) GMM with 20 mixture; 62
4.2 Example of training GMMs with different thresholds. Data set is generated from $0.6\mathcal{N}(5, 1.5) + 0.4\mathcal{N}(15, 3)$. From left to right, (a) GMM with 6 mixture and threshold 10^{-4}; (b) GMM with 6 mixture and threshold 10^{-10}. 67
4.3 Example of clustering using k-means algorithm. Four clusters are generated from Gaussian distribution with variance 1 at both dimensions. The centers of the four clusters are $[2, 0]$, $[-2, 0]$, $[0, 2]$, $[0, -2]$, respectively. From top to bottom, (a) Original Clusters; (b) Clusters from k-means. 70
4.4 Scatter plots of hydrometeor species at 10 GHz. From top to bottom, (a) Z_H and Z_{DR} plot, (b) Z_H and ρ_{hv} plot. 76
4.5 Approximate distribution from GMM for rain (Z_H and Z_{DR}). 77
4.6 Weather field at about 11 km within the stratosphere for case one. From left to right, (a) Mixing ratio of snow; (b) Mixing ratio of hail. . 78
4.7 Simulated PPI scan for case one (with and without attenuation). From left to right, (a) Simulated reflectivity; (b) Simulated reflectivity with attenuation. 79
4.8 Hazards detection results for case one (with and without attenuation). From left to right, (a) Hazard detection results with no attenuation; (b) Hazard detection results with attenuation. 80
4.9 Weather field for case two. From left to right, (a) Mixing ratio of rain; (b) Mixing ratio of hail. 80

4.10 Simulated PPI scan for case two (with and without attenuation). From left to right, (a) Simulated reflectivity; (b) Simulated reflectivity with zttenuation. 81
4.11 Hazards detection results for case two (with and without attenuation). From left to right, (a) Hazard detection results with no attenuation; (b) Hazard detection results with attenuation. 82
4.12 Hail hazards detection ratio at different hail mixing ratio levels for case two with and without attenuation. 82

5.1 Scatter plots and Monte-Carlo simulated distributions of dual-polarized, dual-frequency radar signatures. From left to right and top to bottom, (a) Scatter plot of Z_H and Z_{DR} at C-Band, (b)Scatter plot of Z_H and Z_{DR} at X-Band, (c) Approximate distribution from G_3 at C-Band, (d) Approximate distribution from G_4 at X-Band. 91
5.2 Performance of G_1 and G_2 for estimating A_h of Rain. 93
5.3 Performance of G_3 for estimating A_h of Rain ($Z = [Z_h, Z_{dr}, K_{dp}]^T$). . 94
5.4 Performance of G_4 for rainfall rate estimation. 97
5.5 Results of rainfall rate retrieval by the C-G method. (All in [mm hr^{-1}]) 100
5.6 Results of rainfall rate retrieval by GMPE with 20 mixtures. (All in [mm hr^{-1}]) 101
5.7 Results of rainfall rate retrieval by the β method. (All in [mm hr^{-1}]) 101
5.8 Flowchart of Gaussian Mixture Rainfall-Rate Estimator. 102
5.9 Distribution of rainfall rate (R) in Monte Carlo Simulation. 104
5.10 Scatter plots of S-band dual-polarized radar signatures From Monte-Carlo simulation. From top to bottom, (a) Z_H and Z_{DR} plot, (b) Z_H and K_{dp} 107
5.11 Approximate distribution from GMM for simulated radar signatures. From top to bottom, (a) Approximate distribution from GMM with 5 mixtures, (b) Approximate distribution from GMM with 20 mixtures. In both plots, warmer color represents higher probability density. . . 109
5.12 RMSEs of GMRE with different inputs as number of mixtures Increases. 111
5.13 Plots of estimated rainfall rate and true rainfall rate for simulation dataset. From left to right and top to bottom, (a) R_G retrieved by GMRE with 5 mixtures, (b) R_{DSD} retrieved by GMRE with 5 mixtures, (c) R_G retrieved by GMRE with 20 mixtures, (d) R_{DSD} retrieved by GMRE with 20 mixtures. Bias and RMSE are in [mm hr^{-1}] for all plots. 112
5.14 Scatter plots of measurement dataset. From top to bottom, (a) Scatter plot of measured Z_H and Z_{DR} at ARS gauges. (b) Scatter plot of measured Z_H and Z_{DR} at MES gauges. 114
5.15 Comparison plots of radar-gauge hourly accumulated rainfall rate for ARS dataset. From top to bottom, (a) R_{SYN} retrieved from ARS dataset. (b) R_G retrieved by GMRE with 5 mixtures from ARS dataset. Bias, STD and RMSE are in [mm] for both plots. 118

5.16 Comparison plots of radar-gauge hourly accumulated rainfall rate for MES dataset. From top to bottom, (a) R_{SYN} retrieved from MES dataset. (b) R_G retrieved by GMRE with 5 mixtures from MES dataset. Bias, STD and RMSE are in [mm] for both plots. 119
5.17 Block diagram of the DP-GMPE Algorithm. 128
5.18 Block diagram of the CI-GMPE technique 130
5.19 Simulated scatter plot of X-band dual-polarized radar signature and approximate distribution from GMM. From left to right, (a) Scatter plot of Z_H and Z_{DR}; (b) Approximate distribution from GMM with 12 mixtures. 132
5.20 Simulated scatter plots of rain and fitted power law relations. From left to right, (a) A_h and K_{dp}; (b) A_h and Z_h 133
5.21 RMSEs of GMPE with different inputs as number of mixture increases. DP-GMPE ($\mathbf{z} = [K_{dp}]^T$) and GMPE ($\mathbf{z} = [Z_H, Z_{DR}, K_{dp}]^T$). 134
5.22 Average error over range from different path-integrated attenuation correction techniques in low noise environment (1 [dB] for Z_H, 0.3 [dB] for Z_{DR} and 2^o for Φ_{dp}). From top to bottom, (a) Error of corrected Z_H over range; (b) Error of corrected Z_{DR} over range. 138
5.23 Average error over range from different path-integrated attenuation correction techniques in high noise environment (2 [dB] for Z_H, 0.6 [dB] for Z_{DR} and 4^o for Φ_{dp}). From top to bottom, (a) Error of corrected Z_H over range; (b) Error of corrected Z_{DR} over range 139

6.1 Diagrammatic view of the role of observations and models in SGMPE. In the figure, MF refers to Model Forecast and DA refers to Data Assimilation. 152
6.2 RMSEs of rainfall estimation from GMPE with different inputs as number of mixtures increases. 158
6.3 RMSEs of SGMPEs after mixture reduction for the 'clean' rain path test. From top to bottom, (a) Comparision between 'Pruning' and 'Merging'; (b) Comparison between DP-GMPE and SGMPE with K_{dp} as input; (c) RMSEs of SGMPE with Z_H as input. 162
6.4 RMSEs of SGMPEs after mixture reduction for the 'noisy' rain path test. From top to bottom, (a) Comparision between 'Pruning' and 'Merging'; (b) Comparison between DP-GMPE and SGMPE with K_{dp} as input; (c) RMSEs of SGMPE with Z_H as input. 164
6.5 Error of estimated rainfall rate over range. Results are obtained by taking the average of 750 random paths. In the figure, 'SGMPE - Pruning' and 'SGMPE - Merging' both refer to SGMPE with $\mathbf{z}_k = [Z_H^m(r_k), Z_{DR}^m(r_k), \Delta\Phi_{DP}^f(r_0, r_k)]^T$ but different mixture reduction algorithm. 166

Abstract

The estimation of weather parameters such as attenuation and rainfall rates from weather radar data has been based mainly on deterministic regression models. The applications of a Bayesian approach to weather parameters classification and estimation have also been limited by a single Gaussian assumption. A computational intelligence model, i.e., Gaussian mixture model (GMM), is introduced in this work to characterize the prior distribution of weather parameters and the corresponding radar observation variables. Since a GMM would converge to any given distribution as the number of mixture increases, it provides an efficient way to accommodate extra information from antenna and frequency diversities and an 'omnipotent' solution to extract and model the 'knowledge' from training data. Hydrometeor classification and weather parameters estimation through a Bayesian approach are also made possible by the precisely represented prior distribution. A linear Bayesian estimator based on GMM, namely the Gaussian Mixture Parameter Estimator (GMPE), is then developed and tested in applications such as drop size distribution (DSD) retrieval, rainfall rate estimation and attenuation correction. The advantages of GMPE include 1) it is a 'best' estimator in terms of minimum-variance, unbiased performance; 2) it can easily include/exclude different radar observation variables and remains a 'best' estimator; 3) it provides a general framework that is applicable to different radar-meteorological applications. GMPE is further extended to explore the spatial relations with a Kalman Filter structure. Applications of the Kalman filter GMPE to rainfall rate estimation at X-band are analyzed and discussed.

Chapter 1

Introduction

1.1 Introduction

Radar, which is short for Radio Detection And Ranging, is a term for devices that detect, track and locate targets of interests by transmitting electromagnetic (EM) waves and analyzing the echo wavse scattered by different targets. Early radars were mainly used by military to monitor aircrafts and missiles. Usage of modern radars have been extended to civilian applications such as navigation and collision avoidance radars for airplanes, air traffic monitoring radars for airports and weather monitoring radars.

The first meteorological application of radar to observe the atmosphere was made by Ian C. Browne and Peter Barratt in England a half century ago where an incoherent pulsed-Doppler radar was used (Doviak and Zrnić 1993). After the pioneering attempt, various weather radars were built and employed in different meteorological applications (Atlas 1990).

Due to its ability to cover a large area, Doppler weather radars have been an important tool for severe weather monitoring and quantitative precipitation estimation (QPE). Many phenomenological models that link the weather radar observations and underlying weather parameters such as drop size distribution (DSD), rainfall rate and hydrometeor attenuations, have been developed and used extensively in practical

operations. Such models are mainly deterministic and derived from curve fitting or empirical interpretations. For example, a power law relation (PLR) between radar reflectivity factor Z and rainfall rate R, such as $Z = 300R^{1.4}$ (Doviak and Zrnić 1993) or $Z = 250R^{1.2}$ (Rosenfeld et al. 1993), has been implemented mainly in conventional QPE approaches. A similar situation can be found in rain attenuation correction, where a PLR between Z and specific power attenuation A is widely used. A common source of error for those methods is that PLR coefficients are often customized to particular longer-term climatology or seasonal/regional precipitation regimes and therefore are not universally applicable (e.g., Bringi et al. 2004; Cifelli et al. 2011; Fulton et al. 1998; Ryzhkov et al. 2005a; Wang and Chandrasekar 2010). Space-time variability in the DSD is believed to contribute the most to such apparent diversity in power law coefficients (Lee and Zawadzki 2005).

The advancement of weather radar sensors with polarization and frequency diversity has greatly increased the incorporations of *physical* models. Weather radars with dual polarization capability provide additional insights into the precipitation medium and can help resolve some uncertainties from DSD variability and additional sources (Seliga and Bringi 1976). For example, the dual-polarized radar measurements such as differential reflectivity (Z_{dr}) and specific differential phase (K_{dp}) are highly sensitive to microphysical parameters including the size, shape and orientation of hydrometeor (e.g., Hogan 2007; Cao et al. 2010; Marzano et al. 2010). Dual-frequency operation also provides additional insights into the evolution phases of hydrometeors. New algorithms based on advanced and diversified measurements have been proposed in many studies (e.g., Haddad et al. 2006; Rose and Chandrasekar 2006). Algorithms that utilize polarimetric radar measurements (PRM) show significant improvement over traditional $R(Z)$ relations and lessened sensitivity to DSD variability and partial attenuation in rain (e.g., Bringi et al. 2004; Ryzhkov et al. 2005a).

Most of the polarimetric weather parameter estimators are still deterministic PRLs, where Z_h, Z_{dr} and K_{dp} are used in different combinations or the most appropriate estimator is selected for a given set of PRM. Deterministic estimators usually fail to account for the fact that microphysics vary in space and time even within the same precipitation regime, leading to estimates that are less than optimal. For handling uncertainties in observation conditions and improving estimation accuracies, Bringi et al. (2004) derived a new $R(Z)$ where PLR coefficients can vary in space and time. Hogan (2007) presented a spatially variational method where coefficients in $R(Z)$ are iteratively refined. Vulpiani et al. (2005) developed a constrained iterative technique for dual-polarization radar correction of rain path attenuation based on a neural network. Some initial applications of Bayesian approach (e.g., Hogan 2007; Marzano et al. 2008; Cao et al. 2010) have started to appear, although they are still limited to simple Gaussian assumptions. For example, in Cao et al. (2010) only Z_h and Z_{dr} are used due to the assumption of single Gaussian distribution of the joint distribution of Z_h and Z_{dr} given DSD parameters.

In this dissertation study, a Gaussian mixture model (GMM) is introduced to characterize the prior distribution of weather parameters and the corresponding radar observation variables. Ensured by the convergence of the GMM to any specific distribution as the number of mixtures increase, microphysics variation in space and time can be learned and embedded in the model. The convergence capability of the GMM also provides a general framework to accommodate extra information not only from dual-polarization diversities, but also from other diversities such as multiple frequencies and multiple observation sources, for instance, measurements from different radars or measurements from radar and satellite-based microwave sensors. Statistically optimized hydrometeor classification and weather parameters estimation through a Bayesian approach are made possible by the precisely represented prior distribution.

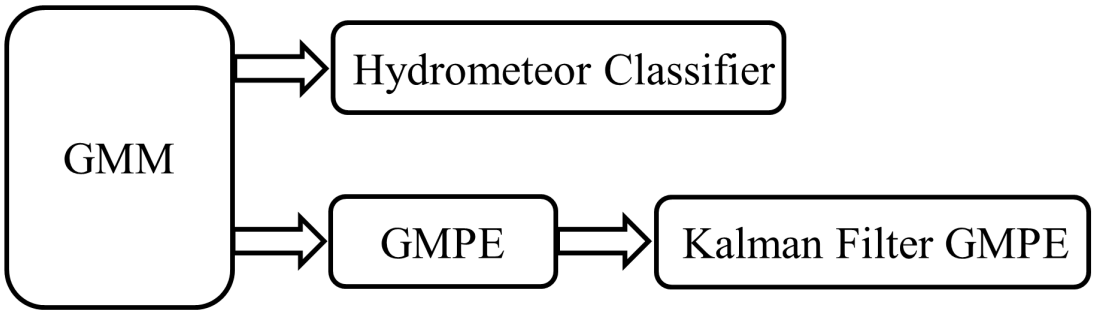


Figure 1.1: Structure of this study.

A Bayesian hydrometeor classifier is constructed based on GMM and tested using simulated PRM from numerical weather prediction (NWP) model in this study. Compared with the fuzzy logic approach (Marzano et al. 2007), where the critical step is to design membership function for each class, the crucial step for a Bayesian classifier is to model the *a-posteriori* probability density function (PDF) for each class, which can be computed from GMM-based *a-prior* PDF. The GMM-based Bayesian classifier has several advantages: 1) Cross correlations among different dimensions/variables can be properly modeled; 2) PDF of the occurrence of each hydrometeor class can also be precisely approximated by GMM; 3) The Classification result is statistically optimal.

Based on the GMM and Bayesian estimation method (Lewis et al. 2006, Chapter. 16), a linear Bayesian estimator for weather parameter estimation, namely the Gaussian Mixture Parameter Estimator (GMPE), is developed and applied to applications such as DSD retrieval, rainfall rate estimation and attenuation correction. As the detailed discussions in the following sections will point out, GMPE also has several advantages over conventional PLR approaches and other Bayesian approaches: GMPE is a best estimator in terms of minimum-variance and unbiased performance; GMPE is a flexible approach where different radar observation variables can be included/excluded from inputs and remains a best estimator; GMPE is applicable to

different radar-meteorological applications and estimation of different parameters can be done at the same time.

GMPE is further extended to explore spatial relations with a sequential Kalman Filter structure. The Kalman filter GMPE is configured to take into account the path-integrated attenuation effects. It is an iterative estimator that performs estimation from the first range bin until the last range bin of a radar range beam. While Kalman filter GMPE enjoys the benefits of optimized estimation, the number of mixtures needed in the GMM increases dramatically from one radar bin to the next. The major challenge in using Kalman filter GMPE efficiently is keeping the number of mixtures as small as possible without losing significant information. Two different types of mixture reduction algorithms are discussed. Applications of the Kalman filter GMPE to path-integrated attenuation correction and rainfall rate estimation at X-band are analyzed.

1.2 Organization of the Dissertation

This study is organized as follows:

- Chapter 2 describes basic concepts of weather radar systems and dual-polarization measurements. The emphasis is placed on definitions of dual-polarization variables and how to calculate them from dual-polarization measurements.

- Chapter 3 introduces single cell Monte-Carlo simulation and the physical models used in the simulation. Different DSD models and DSD-related hydrometeor variables are described, followed by drop shape models and melting models of different hydrometeors. Particle Scattering theories including Rayleigh, Mie and T-Matrix are then discussed, followed by simulations of radar variables in S-, C- and X-band. At the end of this chapter, the single cell simulation is

extended to work with NWP model outputs, where the simulated radar scans are presented.

- In Chapter 4, the Gaussian mixture model is introduced and training GMMs using *Expectation-Maximization* algorithm is emphasized. At the end of this chapter, a Bayesian hydrometeor classifier is constructed based on GMM and tested using simulated PRMs from numerical weather prediction (NWP) model outputs.

- In Chapter 5, a linear Bayesian estimator (GMPE) is formulated and derived from prior distribution characterized by the GMM. Applications of GMPE to DSD retrieval, rainfall rate estimation and attenuation correction are demonstrated. Validation of GMPE is achieved by comparing the performance of GMPE and other existing approaches from both simulations and the Joint Polarization Experiment (JPOLE) data sets.

- In Chapter 6, GMPE is further extended to a Kalman filter structure. Theoretical derivation of the algorithm is demonstrated. Methods for mixture number reduction are discussed. Applications of the Kalman filter GMPE to rainfall rate estimation at X-band are presented at an the end of this chapter.

- Chapter 7 summarizes works in this study and outlines future work.

Chapter 2

Weather Radar Systems and Measurements

2.1 Introduction to Weather Radar Systems

2.1.1 Transmit and Receive Waveform

Most weather radars are coherent and pulsed-modulated Doppler radars which transmit a series of short-duration pulses that are spaced at the pulse repetition time (PRT) T_s interval. Each pulse is identical and has an amplitude of A_t and duration τ as given in the following equation.

$$V_t(t) = A_t \exp[j2\pi ft + j\psi_t]U(t), \tag{2.1}$$

where f is the frequency of radar waveform, ψ_t is a constant phase shift from the waveform generator and $U(t)$ is defined as

$$U(t) = \begin{cases} 1 & 0 \leq t \leq \tau, \\ 0 & \text{otherwise.} \end{cases} \tag{2.2}$$

Note that, the pulsed radar waveform is usually generated at baseband then modulated to the radio frequency. A list of radio frequencies that are commonly used by weather radars is shown in Table 2.1. Additionally, the peak power of each pulse is proportional to A_t^2. Since a radar is actively transmitting a pulse over τ and remains

inactive to receive any echo signals over $T_s - \tau$, the duty cycle of a radar's transmitter is defined as τ/T_s and average power of each power is $A_t^2\tau/T_s$.

Table 2.1: Radar Frequencies and Wavelengths

Band	Frequencies	Wavelengths
L	1-2 GHz	30-15 cm
S	2-4 GHz	15-7.5 cm
C	4-8 GHz	7.5-3.75 cm
X	8-12 GHz	3.75-2.5 cm
Ku	12-18 GHz	2.5-1.67 cm
K	18-27 GHz	1.67-1.11 cm
Ka	27-40 GHz	1.11-0.75 cm

If there is a point scatterer at range r, the voltage of the echo signal $V_r(t)$ received by the radar is proportional to the transmitted waveform and can be written as

$$V_r(t,r) = A_r \exp[j2\pi f(t - \frac{2r}{c}) + j\psi_t + j\psi_s]U(t - \frac{2r}{c}), \tag{2.3}$$

where c is the speed of light, ψ_s is the phase shift produced by the scatterer and $2r$ is the total path traveled by the incident and scattered electromagnetic wave. If the received waveform is down converted to baseband, the phase term of the received waveform becomes

$$\psi_e = -\frac{4\pi r}{\lambda} + \psi_t + \psi_s. \tag{2.4}$$

As can be seen in Eq. (2.4), ψ_e is time independent if the scatterer is stationary. If the scatterer is moving, ψ_e is dependent on time. The time rate of phase change,

$$\frac{d\psi_e}{dt} = -\frac{4\pi}{\lambda}\frac{dr}{dt} = -\frac{4\pi}{\lambda}v_r = \omega_d, \tag{2.5}$$

is the Doppler shift in [rad s^{-1}]. From $\omega_d = 2\pi f_d$, Doppler frequency $f_d = -2v_r/\lambda$. If the scatterer is moving toward the radar (v_r is negative), frequency of the echo signal is higher than that of the transmitted signal (f_d is positive). If frequency of the echo

signal is lower than that of the transmitted signal, the scatterer is moving away from the radar.

2.1.2 Weather Radar Measurements

Doppler radars often output both the in-phase component $I(t)$ and the quadrature component $Q(t)$ of the echo signal $V_r(t)$ for better detection of Doppler frequency shift. From Eq. (2.3),

$$I(t) = \frac{|A_r|}{\sqrt{2}} U(t - \frac{2r}{c}) \cos[\frac{4\pi r}{\lambda} - j\psi_t - j\psi_s], \tag{2.6a}$$

$$Q(t) = \frac{-|A_r|}{\sqrt{2}} U(t - \frac{2r}{c}) \sin[\frac{4\pi r}{\lambda} - j\psi_t - j\psi_s]. \tag{2.6b}$$

$I(t)$ and $Q(t)$ are sampled first at sample time $t = (m-1)\tau_s$ and then at $t = (n-1)T_s$, where range time τ_s is the time delay between any transmitted pulse and its echo. The samples are labeled as $I(m\tau_s, nT_s)$ and $Q(m\tau_s, nT_s)$ and grouped into a two-dimensional matrix with two indexes: the range index m whose sample interval is $c\tau_s/2$ and the time index n whose sample interval is T_s. The range index is often dropped and the notation becomes $I(nT_s)$ and $Q(nT_s)$ assuming they are sampled at every range gate. Therefore, the echo voltage can be constructed from

$$V_r(nT_s) = I(nT_s) + jQ(nT_s). \tag{2.7}$$

If the unbiased estimate of the autocorrelation function (ACF) of $V_r(nT_s)$ is defined as

$$\hat{R}(kT_s) = \begin{cases} \dfrac{1}{N - |k|} \displaystyle\sum_{n=0}^{N-|k|-1} V_r^*(n) V_r(n+k) & |k| \leq N-1, \\ 0 & \text{otherwise} \end{cases} \tag{2.8}$$

the power estimate can be obtained from the ACF at lag 0 as

$$\hat{S} = \hat{R(0)} - \hat{N}. \tag{2.9}$$

Note that, in Eq. (2.9), the estimate of noise power is required. To avoid the zero lag ACF with noise contamination, the power estimate may be obtained from the ACF

at lag 1, i.e. $\hat{S} = \hat{R}(T_s)$, though the estimate would be lower than the actually value. The Mean velocity can be also calculated from ACF at lag 1,

$$\hat{v}_r = -\left(\frac{\lambda}{4\pi T_s}\right) \arg[\hat{R}(T_s)]. \tag{2.10}$$

Eq. (2.10) is also known as the pulse pair processor. Mean velocity may be obtained from other methods related to the power spectrum $S(f)$, which is defined as the Fourier transform of the ACF (Doviak and Zrnić 1993).

2.1.3 Sampling and Aliasing Effects

From the sampling strategy that was described in section 2.1.2, range resolution of the radar is given by

$$\Delta r = \frac{c\tau_s}{2} \tag{2.11}$$

and the maximum unambiguous range can be computed from

$$R_u = \frac{cT_s}{2}. \tag{2.12}$$

If the true range of a target is r and $r > R_u$, the estimated range of the target from the radar is $\mathrm{mod}_{R_u}(r)$, which means the range of targets located outside of R_u will be always estimated to fall within R_u. For example, if the unambiguous range for a radar is 150 km and a target located at 400 km, the estimated range for the target is 100 km (third trip echo).

Similarly, from the Shannon sampling theorem, the maximum unambiguous absolute Doppler frequency $|f_D| = \dfrac{1}{2T_s}$. According to Eq. (2.5),

$$|v_r| \leq v_a = \frac{\lambda}{4T_s}, \tag{2.13}$$

where v_a is called the aliasing velocity. When $|v_r| \geq v_a$, aliasing occurs and the estimated v_r will always fall within $[-v_a, v_a]$. Combine Eq. (2.12) and Eq. (2.13), the Doppler dilemma can be shown in Eq. (2.14), which implies that the maximum

unambiguous range and Doppler frequency cannot be improved at the same time. When the maximum Doppler frequency is increased, R_u will decrease. The opposite is also true when R_u is decreased.

$$R_u \times |f_D| \leq \frac{c}{4} \tag{2.14}$$

2.1.4 Weather Radar Equation

The radar range equation is a basic equation that describes the radar environment and connects the power transmitted by radar, power intercepted and scattered by scatterers and power received by radar. For a single point target at range r with radar cross section $\sigma_b(D)$ and a radar with transmit antenna gain G_t and effective aperture A_e, the range equation can be expressed as (Skolnik 2001)

$$P_r = \frac{P_t G_t}{4\pi r^2 l} \times \frac{\sigma_b(D)}{4\pi r^2 l} \times A_e, \tag{2.15}$$

where P_r is the received signal power, P_t is the transmitted power and l is the propagation loss. In the right hand side of Eq. (2.15), the first term describes the power density at the target and the second term describes the power density back at the radar which depends on the target characteristics. The third term describes how much power is captured by the radar antenna. For weather radar observations, there are usually large number of hydrometeors/scatterers in the radar resolution volume. Eq. (2.15) is further then written by Doviak and Zrnić (1993) as

$$\bar{P}_r \approx \frac{P_t G_t}{4\pi r^2 l} \times \frac{\eta \Delta V}{4\pi r^2 l} \times \frac{G_r \lambda}{4\pi}, \tag{2.16}$$

where $\bar{P}_r$ is the average received power, η is the average radar cross section per unit volume given in Eq. (2.17) and ΔV is the radar resolution volume. Note that, effective aperture A_e has been replaced with the general value $\frac{G_r \lambda}{4\pi}$, where G_r is the receive antenna gain and λ is the wavelength.

$$\eta = \int_0^\infty \sigma_b(D) N(D) dD \tag{2.17}$$

In Eq. (2.17), $N(D)$ is the drop size distribution of hydrometeors. Detailed description of different DSD models is given in section 3.1. If radar resolution volume is approximated by the volume of a cylinder, $\Delta V = \frac{c\tau\pi r^2\theta_1^2}{8}$ with the one-way half-power beamwidth θ_1, Eq. (2.16) can be further simplified to a standard form (Le 2009).

$$\bar{P}_r \approx \frac{P_t\lambda^2 G_t G_r}{(4\pi)^3 r^2 l^2}\eta\frac{c\tau\pi\theta_1^2}{8} \tag{2.18}$$

Eq. (2.18) can be considered as the weather radar equation for distributed targets (Doviak and Zrnić 1993). It is worth mentioning that η in Eq. (2.17) is called *reflectivity* and it is often related to a term that has more meteorological significance, which is *reflectivity factor* Z as given by

$$\eta = \frac{\pi^5}{\lambda^4}|K_w|^2 Z, \tag{2.19}$$

where K_w is the dielectric factor of water. $K_w = (\epsilon_w - 1)/(\epsilon_w + 2)$ and ϵ_w is the dielectric constant of water. The unit of Z is [$\text{mm}^6\ \text{m}^{-3}$] but it is usually transferred to dBZ [$10\log_{10}(\text{mm}^6\ \text{m}^{-3})$] for a smaller dynamic range. Eq. (2.19) is called the Rayleigh approximation which is valid when diameters of hydrometeors are small compared to radar wavelengths (Doviak and Zrnić 1993).

2.2 Polarimetric Radar Measurements

Natural hydrometeors have different shapes rather that simple spheres which lead to different wave scattering properties at orthogonal polarizations. Weather radars with dual-polarization capability not only provide power measurement at horizontal (H) and vertical (V) polarizations but also other measurements such as phase difference between two polarizations and correlations between two polarizations. With the additional insights into the precipitation medium, dual-polarization measurements can help resolve some uncertainties from DSD variability and additional sources (Seliga and Bringi 1976). Operational WSR-88D radars are being considered to be updated

to employ simultaneous transmission of H and V polarized waves (Doviak et al. 2000). This section addresses the commonly used polarimetric radar variables, including reflectivity factor ($Z_{h,v}$), differential reflectivity (Z_{dr}), specific differential phase (K_{dp}) and correlation coefficient (ρ_{hv}).

Assuming $X_h(nT_s)$ and $X_v(nT_s)$ are well-calibrated timeseries measurements from H polarization and V polarization, similar to Eq. (2.8), the estimates of autocorrelation function and cross correlation function of H and V channel are define as

$$\hat{C}_{h,v}(kT_s) = \frac{1}{N-|k|} \sum_{n=0}^{N-|k|-1} X^*_{h,v}(n) X_{h,v}(n+k), \tag{2.20a}$$

$$\hat{C}_{hv}(kT_s) = \frac{1}{N-|k|} \sum_{n=0}^{N-|k|-1} X^*_{h}(n) X_{v}(n+k). \tag{2.20b}$$

Dual polarization variables can be obtained using either or both Eq. (2.20a) and Eq. (2.20b). Definitions of the variables and how to calculate them from timeseries data are introduced as follows:

- Reflectivity factor

  As shown in Eq. (2.19), reflectivity factor is associated to reflectivity and radar wavelength. Reflectivity factor is often called reflectivity for convenience. Reflectivity factors for horizontal polarization, Z_h, and vertical polarization, Z_v, are defined as (Bringi and Chandrasekar 2001)

  $$Z_{h,v} = \frac{4\lambda^4}{\pi^4 |K_w|^2} \int |f_{hh,vv}(\pi, D)|^2 N(D) dD, \tag{2.21}$$

  where $f_{hh}(\pi, D)$ and $f_{vv}(\pi, D)$ are complex scattering amplitudes of a particle with equivolume diameter D at horizontal and vertical directions, respectively. π refers to the angle between incident wave and scattering wave. 0 means forward scattering and π means backscattering. In this study, reflectivity factor in [mm^6 m^{-3}] is denoted as $Z_{h,v}$ assuming unit of $Z_{H,V}$ is dBZ. As shown in Eq. (2.21), the integral over drop size distribution transfers point scattering properties of each particle ($f_{hh,vv}$) to the average scattering properties of all particles ($Z_{h,v}$),

given a distribution within the volume ($N(D)$). It also suggests that $Z_{h,v}$ are sensitive to the number and size of hydrometeors which are characterized by DSD. Under Rayleigh scattering assumption (Bringi and Chandrasekar 2001), reflectivity factor can be approximated by the 6^{th} DSD moment (Eq. (3.9)).

Estimates of $Z_{h,v}$ can be obtained from

$$\hat{Z}_{h,v} = \hat{C}_{h,v}(0) = \frac{1}{N}\sum_{n=0}^{N-1} |X_{h,v}(n)|^2. \tag{2.22}$$

The typical variance of the measurement error/noise of Z_H and Z_V may be around 1 dB but it is different for different radar systems (Bringi and Chandrasekar 2001).

- Differential reflectivity

  Differential reflectivity is defined as the ratio between Z_h and Z_v as shown in Eq. (2.23a).

$$Z_{dr} = \frac{Z_h}{Z_v}, \tag{2.23a}$$

$$Z_{DR} = Z_H - Z_V. \tag{2.23b}$$

  Differential reflectivity measures the backscattering difference between H and V directions, therefore, it is sensitive to the shape and canting angle (Bringi and Chandrasekar 2001) of hydrometeors within the radar resolution volume. Since different hydrometeors have different shapes and shows different canting angle behavior, differential reflectivity helps to distinguish them from each other as shown in some hydrometeors classification studies (e.g., Ryzhkov et al. 2005b; Marzano et al. 2008). Differential reflectivity can also help to distinguish intensity of rains due to the fact that heavy rains have more large raindrops than light rains where there are mainly small raindrops and large raindrops are more oblate than small raindrops which are close to a sphere. Differential reflectivity is also very sensitive to measurement noise since value of differential reflectivity

is mainly within 5 dB which is relatively small compared to the variance of the measurement error of Z_H and Z_V.

Estimate of Z_{dr} can be obtained using $\hat{Z}_h$ and $\hat{Z}_h$ from Eq. (2.22).

$$\hat{Z}_{dr} = \frac{\hat{Z}_h}{\hat{Z}_v}. \tag{2.24}$$

The typical variance of the measured Z_{DR} is around 0.3 dB (Bringi and Chandrasekar 2001) but it depends on different radar systems.

- Specific differential phase

  Specific differential phase is defined as the rate of change in one-way phase difference between H and V polarizations along a propagation path. It is given by

$$K_{dp} = 10^{-3}\frac{180\lambda}{\pi}\int \Re[f_{hh}(0,D) - f_{vv}(0,D)]N(D)dD, \tag{2.25}$$

  where $f_{hh}(0,D)$ and $f_{vv}(0,D)$ are the complex forward scattering amplitudes of a particle with equivolume diameter D at horizontal and vertical directions, respectively. The unit of K_{dp} is [deg km^{-1}] in Eq. (2.25). K_{dp} is also sensitive to shape and canting angle of hydrometeors within the radar resolution volume. Since propagation phase is independent of attenuation and calibration effects, K_{dp} plays an important role in correcting attenuation for power measurements and precipitation estimation.

  Estimation of K_{dp} cannot be obtained directly from time series data. However it can be calculated from the range derivative of differential phase (ϕ_{dp}) which is the accumulated phase difference between H and V polarizations along a propagation path. The estimate of ϕ_{dp} can be obtained by

$$\hat{\phi}_{dp} = \frac{1}{2}\arg[C_h^*(1)C_v(1)], \tag{2.26}$$

  and the estimate of K_{dp} can be computed from

$$\hat{K}_{dp}(r_m) = \frac{\hat{\phi}_{dp}(r_{m+1}) - \hat{\phi}_{dp}(r_m)}{r_{m+1} - r_m}, \tag{2.27}$$

where r_m and r_{m+1} are the mth and $(m+1)$th range bin. It is worth mentioning that effects of backscattering differential phase δ_{hv} (defined in Eq. (2.28b)) has to be eliminated by an effective iterative filter from $\hat{\phi}_{dp}$ before estimating K_{dp}. It is usually done by averaging phase measurements over multiple range gates as suggested by Ryzhkov et al. (2005a). Note that, in this dissertation study, specific differential phase is denoted as both K_{dp} and K_{DP}. They are all in [deg km^{-1}].

- Correlation coefficient

  Correlation coefficient is defined as the correlation between backscattering signals at H and V polarizations. It is computed from

$$\rho_{hv} = \frac{\int f_{hh}^{*}(\pi, D) f_{vv}(\pi, D) N(D) dD}{\sqrt{\int |f_{hh}(\pi, D)|^2 N(D) dD} \sqrt{\int |f_{vv}(\pi, D)|^2 N(D) dD}} \tag{2.28a}$$

$$= |\rho_{hv}| e^{j\delta_{hv}}. \tag{2.28b}$$

  Correlation coefficient is sensitive to objects that have irregular shapes. Raindrops have high ρ_{hv} values that are close to 1 since the shape of raindrops are close to spherical. Hail and snow normally have a lower ρ_{hv} than raindrops due to their irregular shapes. Mixed phase hydrometeors and melting ice particles also have relatively low ρ_{hv}. Value of ρ_{hv} is a common indicator to separate meteorological radar returns from non-meteorological ones, since ρ_{hv} of meteorological returns are usually above 0.75.

  The estimate of ρ_{hv} can be obtained from

$$\hat{\rho}_{hv} = \frac{|\hat{C}_{hv}(0)|}{\sqrt{|\hat{C}_h(0)|} \sqrt{|\hat{C}_v(0)|}} = \frac{|\hat{C}_{hv}(0)|}{\sqrt{\hat{Z}_h \hat{Z}_v}}. \tag{2.29}$$

The dual-pol variables previously introduced can be directly estimated from radar measurements. There are other important variables that cannot be obtained directly from measurements but are frequently applied to represent attenuation in the precipitation medium. Those variables are specific attenuation at H and V polarization

($A_{h,v}$) and specific differential attenuation A_{dp}. Definitions of those variables are shown in the followings:

- Specific attenuation

  Specific attenuation is defined as the rate of change in attenuation along a propagation path. It is associated with the imagine part of the forward scattering amplitudes.

$$A_{h,v} = 8.686 \times 10^{-3} \lambda \int \Im[f_{hh,vv}(0, D)] N(D) dD. \tag{2.30}$$

- Specific differential attenuation Specific differential attenuation is defined as the difference between specific attenuation at H and V polarizations.

$$A_{h,v} = 8.686 \times 10^{-3} \lambda \int \Im[f_{hh}(0, D) - f_{vv}(0, D)] N(D) dD \tag{2.31a}$$

$$= A_h - A_v. \tag{2.31b}$$

  The unit of A_h, A_v and A_{dp} are all [dB km^{-1}].

Chapter 3

Monte-Carlo Simulation and Physical Models

Algorithms that use polarimetric radar measurements can be developed either through simulations or real radar measurements.

Development of intelligent processing algorithms based on real radar measurements faces some issues. 1) Real measurements are not 'clean' data. Measurements contain noise and other radar calibration errors. Also, measurements are often contaminated by attenuation. And there are usually more than one hydrometeor species. 2)Real measurements are usually lack of ground truths. It is hard to relate real measurements to the underlying microphysics parameters of interests. Algorithms developed from measurements are usually optimized for specific radar and regions but less suitable for others since radars may have different calibration errors and noise levels, and different regions have different climatologies.

On the other hand, data from simulations are 'clean' data without noise or other contaminations. Scenarios with different numbers, sizes and types of hydrometeors can be simulated. More importantly, ground truths are precisely known. Algorithms developed from simulations are more general and less sensitive to measurement error, but they depend on different assumptions used in the simulation. Due to the natural variability of hydrometeor size, shape, canting angle and terminal velocity, there is no 'perfect' deterministic model to precisely describe all the polarimetric radar measurements.

To avoid unreliable assumptions or losing generality, many variables including hydrometeor shape, canting angle and drop size distribution are allowed to have uncertainties (randomness) in this study. Monte-Carlo simulation, which provides statistical samplings of a complex system, is an efficient approach to incorporate all the random variables and extract knowledge from those variables (e.g., Metropolis and Ulam 1949; MacKeown 1997; Robert and Casella 2004; Rubinstein and Kroese 2007). Different from other simulation techniques that usually output mean value or ensemble average value, each realization from Monte-Carlo simulation is a specific sample given certain input parameters. These outputs will better embody the variable distributions other than just a mean value, thus contain important statistical information, and are more suitable for GMM training.

In this chapter, different physical models that are employed in Monte-Carlo simulation are introduced, followed by simulations of radar variables in different frequencies and simulated radar scans from NWP model outputs.

3.1 Drop Size Distribution (DSD)

3.1.1 DSD Models

Similarly to probability density function (PDF), number and size of hydrometeors in a volume are characterized by DSD which are usually represented by distribution models that contain some free parameters. The following DSD models are widely used in meteorology community:

- Marshall-Palmer (M-P) DSD model (Marshall and Palmer 1948)

$$N(D) = 8000\exp(-\Lambda D) \tag{3.1}$$

  With only one free parameter (slope parameter Λ), the M-P DSD model is easy to implement and has been widely used in rainfall rate estimation from

single-polarization weather radar and bulk-scheme rain parametrization since it is proposed by Marshall and Palmer (1948).

- Exponential DSD model

$$N(D) = N_0 \exp(-\Lambda D) \tag{3.2}$$

Exponential DSD model depends on two parameters, intercept parameter N_0 [$\mathrm{mm}^{-1}\mathrm{m}^{-3}$] and slope parameter Λ [mm^{-1}], thus it is more flexible than M-P DSD model which can be considered as a exponential DSD model with a fixed $N_0 = 8000$. Besides raindrops, exponential DSD model are also applicable to model size distributions of snow particles and ice particles. Slope Λ is uniquely determined if N_0 and water content W is known as given in the following equation:

$$\Lambda = \frac{\pi N_0 \rho_x}{W}, \tag{3.3}$$

where ρ_x can be the density of water, snow or ice.

- Gamma DSD model (Ulbrich 1983)

$$N(D) = N_0 D^{\mu} \exp(-\Lambda D) \tag{3.4}$$

As can be seen in Eq. (3.4), a shape parameter μ is added to exponential DSD model. With three free parameters, the Gamma DSD model is widely accepted in meteorology community and considered to be able to account for most the variability of DSD in nature. Note that, unit of N_0 in Eq. (3.4) is μ-dependent, therefore, N_0 is not physically meaningful when $\mu \neq 0$. A normalized Gamma DSD model, given in Eq. (3.7), is introduced and applied in some recent studies (e.g., Testud et al. 2001; Vulpiani et al. 2005; Gorgucci et al. 2002; Park et al. 2005).

$$N(D) = N_w f(\mu) \left(\frac{D}{D_0}\right)^{\mu} \exp\left[-(3.67+\mu)\frac{D}{D_0}\right] \tag{3.5}$$

In Eq. (3.5), D_0 is the median volume drop diameter, N_w is the normalized drop concentration and the function $f(\mu)$ is defined by

$$f(\mu) = \frac{6}{(3.67)^4} \frac{(3.67+\mu)^{\mu+4}}{\Gamma(\mu+4)}. \tag{3.6}$$

It is worth mentioning that N_w and D_0 in Eq. (3.5) have specific physical meanings. N_w equals to the intercept parameter of an exponential DSD (N_0 in Eq. (3.2)) that has the same W and D_0 and can be calculated as a function of W and D_0 as given in the following equation:

$$N_w = \frac{(3.67)^4}{\pi \rho_w} \left(\frac{W}{D_0^4} \right), \tag{3.7}$$

where ρ_w is the density of water. Although Gamma distribution is flexible representing natural DSDs, its three parameters may not be mutually independent. Derived from disdrometer dataset, Zhang et al. (2001) introduced a constraint-gamma (C-G) DSD model, which had a constraint $\mu - \Lambda$ relation as given in Eq. (3.8).

$$\mu = -0.016\Lambda^2 + 1.213\Lambda - 1.957 \tag{3.8}$$

The C-G DSD model has also been used in some recent studies (e.g., Zhang et al. 2001; Brandes et al. 2004; Cao et al. 2010).

Fig. (3.1) shows an example of the DSD models mentioned above. Among those DSD models, Gamma DSD model generally has the best performance in modeling observed DSDs. This is because with more free parameters, the DSD model would have more freedom adapting to different DSD shapes. However, every DSD model has its own advantages and limitations. It is inevitable that model error will be introduced no matter which DSD model is used.

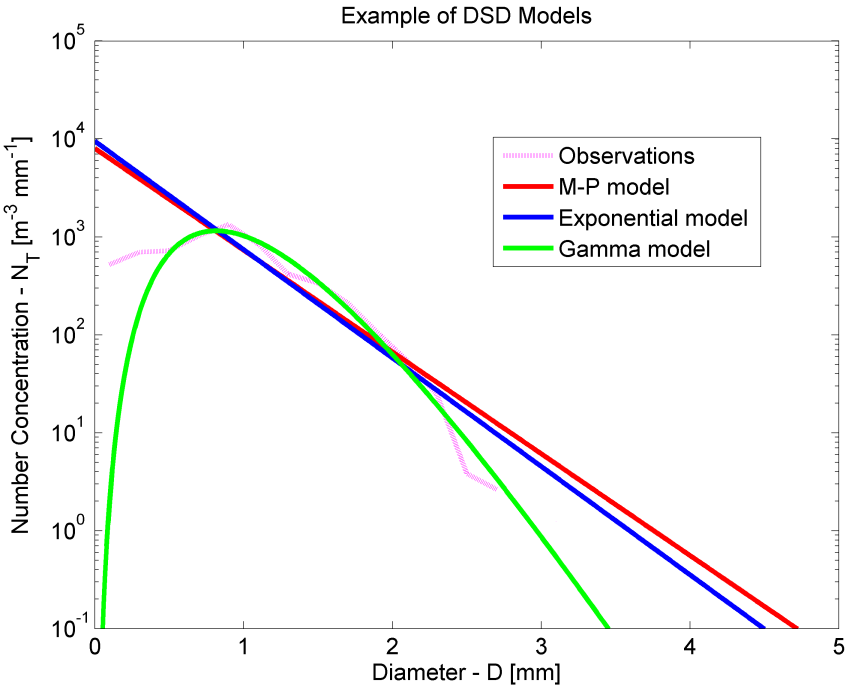


Figure 3.1: Example of different DSD models. DSD models are fitted from observations from a 2D disdrometer.

3.1.2 DSD Moments and Related Variables

Since DSD characterizes number and size of hydrometeors in a volume, microphysics properties of hydrometeors can be learnt from DSD. If the n^{th} DSD moment is defined as

$$M_n = \int_{D_{\min}}^{D_{\max}} D^n N(D) dD, \tag{3.9}$$

where M_n is in [mm^{n}m^{-3}], water content W [g m^{-3}] (shown in Eq. (3.10)), total number concentration $N_T = M_0$ [m^{-3}], reflectivity factor $Z \approx M_6$ [mm^6 m^{-3}] and effective diameter $D_e = M_3/M_2$ [mm] are all linked to different DSD moments.

$$W = \frac{\pi}{6} \times 10^{-3} M_3. \tag{3.10}$$

Other important hydrometeor variables that are associated with the DSD include rainfall rate R [mm hr^{-1}] as shown in Eq. (3.11) and median volume diameter D_0 [mm] as shown in Eq. (3.12).

$$R = 6 \times 10^{-3} \pi \int_{D_{\min}}^{D_{\max}} D^3 v(D) N(D) dD \tag{3.11}$$

$$\int_{D_{\min}}^{D_0} D^3 N(D) dD = \int_{D_0}^{D_{\max}} D^3 N(D) dD \tag{3.12}$$

In Eq. (3.11), $v(D)$ is the terminal velocity of raindrops.

3.2 General Hydrometeor Models

Natural hydrometeors have different shapes rather than simple spheres (Straka et al. 2000). The utility of dual polarizations in weather radar is based on the fact that an electromagnetic wave scatters and propagates differently for horizontal and vertical polarizations when it is incident on a hydrometeor (Zhang et al. 2001) (geometry of particle scattering is shown in Fig. (3.2)).

Observations show that the larger the raindrop, the more oblate the shape is (Brandes et al. 2002). The oblateness of a raindrop is determined by its axis ratio

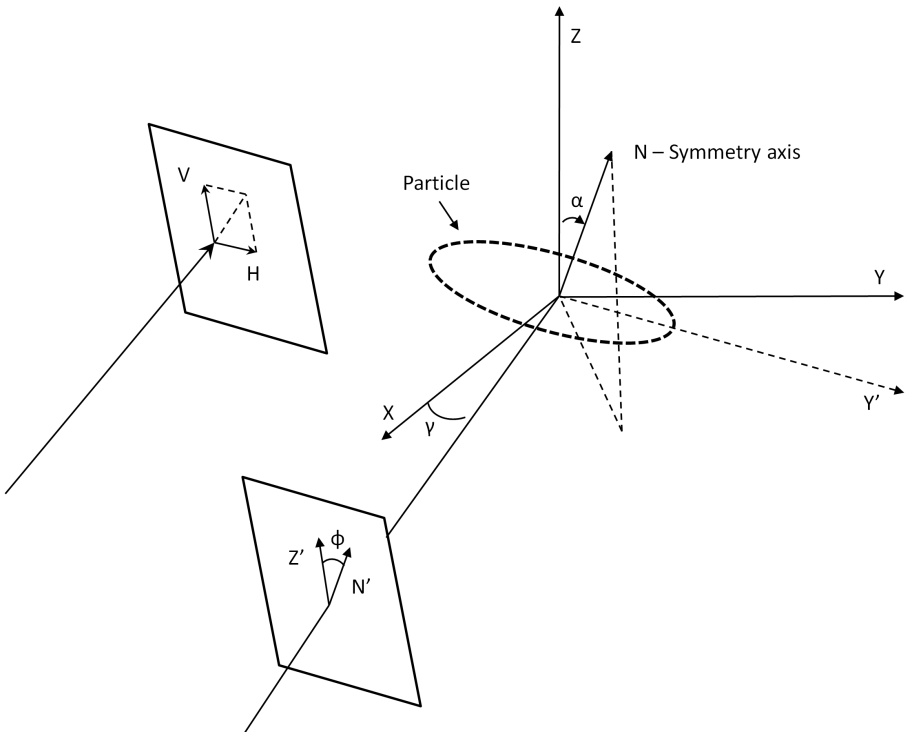


Figure 3.2: Particle scattering geometry.

which is defined as the ratio of the diameter of vertical axis to the diameter of horizontal axis (illustrated in Fig. (3.3)). The relation between equivalent diameter and axis ratio of a raindrop has drawn many attentions, such as the empirical relations proposed in Pruppacher and Beard (1970), Chuang and Beard (1990), Andsager et al. (1999), Keenan et al. (2001) and Brandes et al. (2002). A plot of the above empirical relations is shown in Fig. (3.4). Different raindrop shape models may lead to a distinct difference in dual-pol variables, especially for Z_{DR} (Brandes et al. 2002). Due to the large variance in raindrop shape observations, none of the empirical relations is universally applicable.

Raindrops in this study are modeled as oblate spheroids with the polynomial relation between the axis ratio r_a and the equivalent diameter D (detailed definition in Green (1975)) given in Brandes et al. (2002).

$$r_a = 0.9951 + 0.02510D - 0.03644D^2 + 0.005303D^3 - 0.0002492D^4. \qquad (3.13)$$

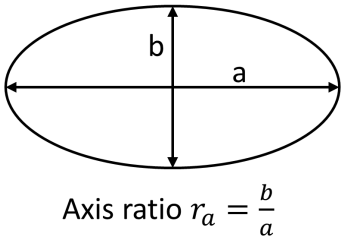


Figure 3.3: Axis raio for an oblate spheroid.

Supported by agreement between measurement from radar and gauges, this relation yields more spherical shapes for drops with $1 \leq D \leq 4$ mm than other previous studies. Randomness between $[-0.12(1 - r_a)\ 0.12(1 - r_a)]$ is added to r_a to make it more general for different kind of raindrops. Region of r_a with randomness is shown in Fig. (3.5). Some observational and theoretical studies suggest that the standard deviation of the canting angles (ϕ in Fig. (3.2)) of rain drops is likely not 0^o but between 7^o and 8^o (Huang et al. 2008) or 5^o and 15^o (Ryzhkov et al. 2002). Standard deviation (SD) of the canting angle in this study is assumed to be 10^o, which should cover most situations. The mean canting angle is assumed to be 0^o, as suggested by observations (Hendry and McCormick 1976). Terminal velocity of raindrops is assumed to follow the polynomial relation given in Brandes et al. (2002):

$$v(D) = -0.1021 + 4.932D - 0.9551D^2 + 0.07934D^3 - 0.002362D^4. \tag{3.14}$$

Snow has a large variety of shapes from approximately spherical to extremely oblate (aggregates), or from extreme prolate and oblate to essentially spherical (crystals). However, they tend to fall with the major axis horizontally oriented (Straka et al. 2000), and, can be modeled as spheroid with axes a and b where a is the axis of rotation. Axis ratio r_a is randomly selected from 0.5 to 2 so that both oblate and prolate spheroid are covered. The density of snow also varies from 50 to 900 [kg m^{-3}], depending on the mixing ratio of ice and air. Dry Snow density (ρ_s) is fixed at 100 [kg m^{-3}] in this study, consistent with the Advanced Regional Prediction System

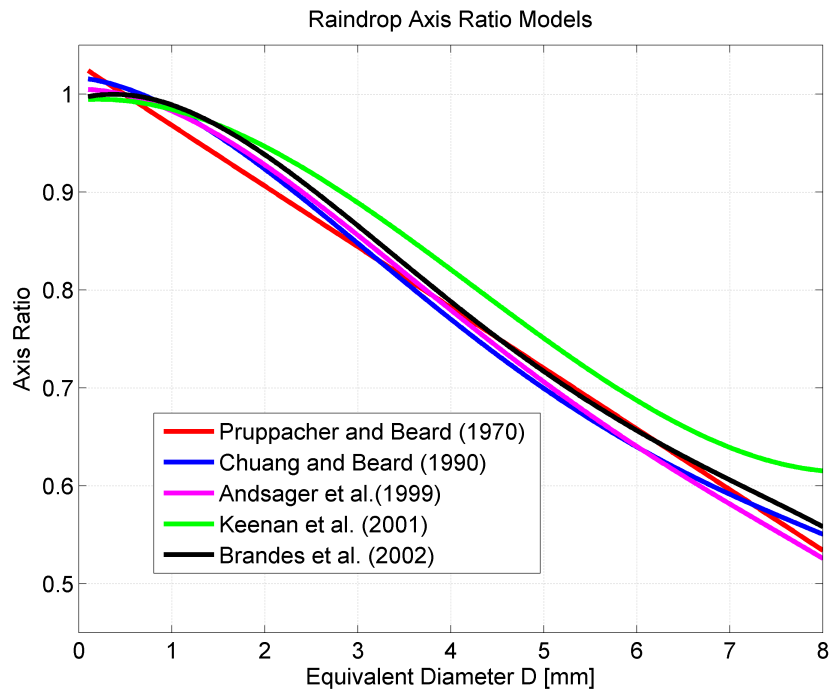


Figure 3.4: Different raindrop axis ratio models.

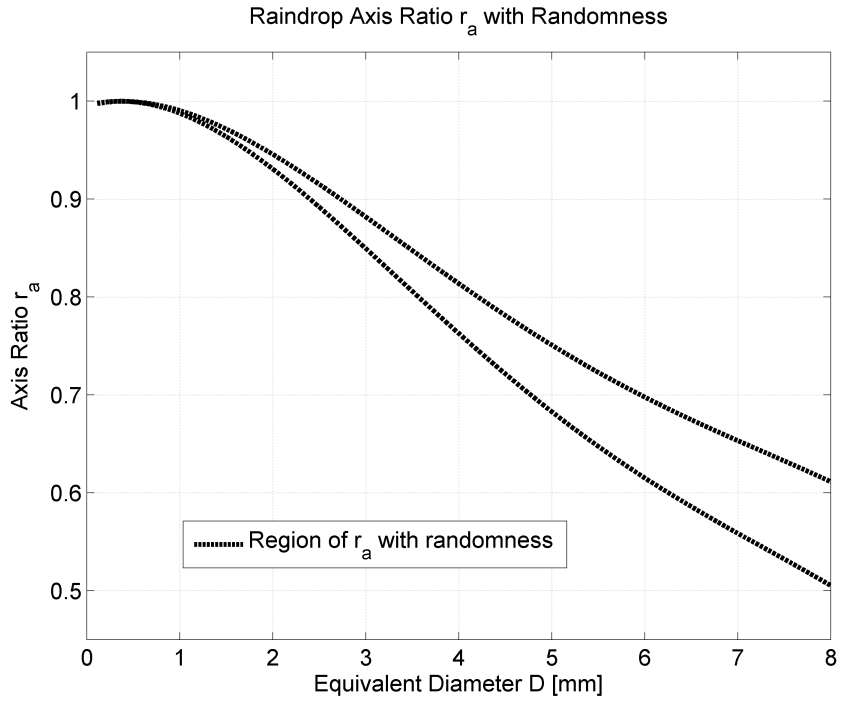


Figure 3.5: Axis ratio r_a with randomness.

(ARPS) model which will be introduced in section 3.6. When snow melts, its density increases as the melted portion grows, and eventually reaches 1000 [kg m^{-3}] (becomes water). The melting effect will be discussed in section 3.3. The mean canting angle of snow is assumed to be 0^o, and standard deviation is assumed to be 20^o (Jung et al. 2008).

Similar to snow, hail is observed as oblate to some degree or conical, with lobes and other protuberances on the surface. Straka et al. (2000) shows that larger hail, with $D \geq 10$ [mm], tends to be more irregular, whereas small hail is less oblate and closer to spherical. Therefore, we model hail as spheroid, with the axis ratio r_a (minor to major axis) randomly chosen from 0.8 to 1 for small hail ($D \leq 10$ [mm]) and 0.6 to 1 for large hail ($10 \leq D \leq 50$ [mm]) (Knight 1986). Falling hail may exhibit gyrating and tumbling motions (Knight and Knight 1970), which makes the orientation of falling hail somewhat questionable. Therefore, a large standard deviation of canting angles of hailstone should be expected. In this study, the mean canting angle of hail is assumed to be 0^o while SD is assumed to be 60^o. Also, a fixed density (ρ_h) of 913 [kg m^{-3}] is used, which is consistent with the ARPS model.

3.3 Melting Models and Effective Dielectric Constants of Mixtures

The study of the radar signature of melting hydrometeors is important because the melting layer radar scattering has significant differences from the general, "dry" hydrometeors (Liao and Meneghini 2005). Melting snow and hail are often modeled as two layered models, with dry snow or ice cores surrounded by water or a wet snow mixture, or modeled as uniform mixtures of air-ice-water or ice-water (e.g., Fabry and Szyrmer 1999; Bringi et al. 1986; Aydin and Zhao 1990). Both types of particle models can be characterized by an effective dielectric constant ϵ_e. There are

many formulas to calculate ϵ_e of the mixture, however, the various dielectric formulas yield very different results not only from different mathematical expressions, but also from different ways of forming a mixture (background and inclusion issue) (e.g., Meneghini and Liao 1996, 2000). One of the most commonly used formulas is the Maxwell-Garnett (MG) mixing formula (Maxwell Garnett 1904):

$$\epsilon_e = \frac{1 + 2f_v y_p}{1 - f_v y_p}\epsilon_b \tag{3.15a}$$

$$y_p = \frac{\epsilon_i - \epsilon_b}{\epsilon_i + 2\epsilon_b}, \tag{3.15b}$$

where ϵ_e, ϵ_b and ϵ_i are the dielectric constant of the mixture, the background species and the inclusion species, respectively. f_v is the fractional volume of the inclusion and y_p is the polarizability factor given in Eq. (3.15b).

To study the natural polarimetric hydrometeor scattering signatures, an experimental approach was designed with the assistance of a controlled laboratory environment. An advanced vector network analyzer-based scatterometer system has been developed together with an environmentally-monitored anechoic chamber configured for hydrometeor measurements. The polarimetric Radar Cross Section (RCS) of various natural and man-made icy hydrometeor samples are measured across wide X-band frequencies and compared with theoretical modeling results. The instrumentation setup is illustrated in Fig. (3.6). The dual-polarized radar variables and hydrometeor melting parameters are derived from the RCS measurements with interesting observations obtained (Zhang et al. 2010).

Recent theoretical studies (e.g., Meneghini and Liao 1996, 2000) indicate that the predictions from the MG formula for a water-ice mixture with ice as background and water as inclusion agree with realistic melting hails, especially when the fraction of water is low. A preliminary result for lab measurement of melting ice spheres compared with such theoretical predictions as shown in Fig. (3.7). Water at the surface of a melting hailstone tends to shed off due to different falling speeds and water portion of a melting snowflake tends to break up from ice portion, which both

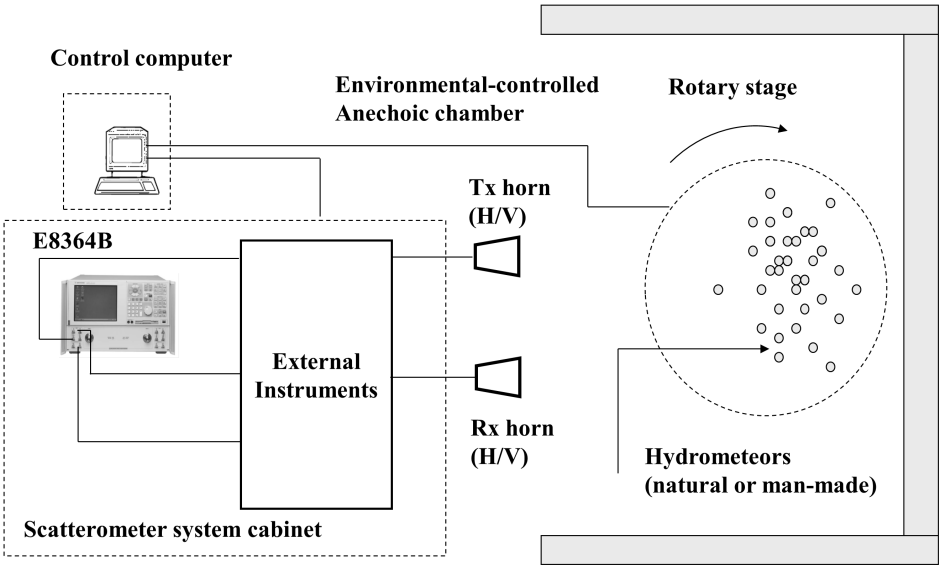


Figure 3.6: The instrumentation setup for hydrometeor scattering measurement.

result in smaller melting ratio of melting particles (Rasmussen and Heymsfield 1987). Thus, maximum melting ratios of snow and hail have been limited to 0.5 in this study (melting ratio is defined as the ratio of water weight to the hydrometeor weight in a melting process). Therefore, the effective dielectric constant ϵ_e for melting hail is calculated from mixing water and ice with ice as background. For melting snow, ϵ_e is calculated from mixing air and snow with snow as background and then mixing water with air-snow mixture as background.

Dielectric constants of water and ice vary with temperature. In this study, dielectric constants of water and ice at a particular temperature are obtained by applying the equations introduced by Ray (1972). In the melting process, both water and ice dielectric constants are calculated at 0^oC no matter what the environment temperature is. Table. 3.1 and Table. 3.2 give the dielectric constants of ice and water at different frequencies and temperatures.

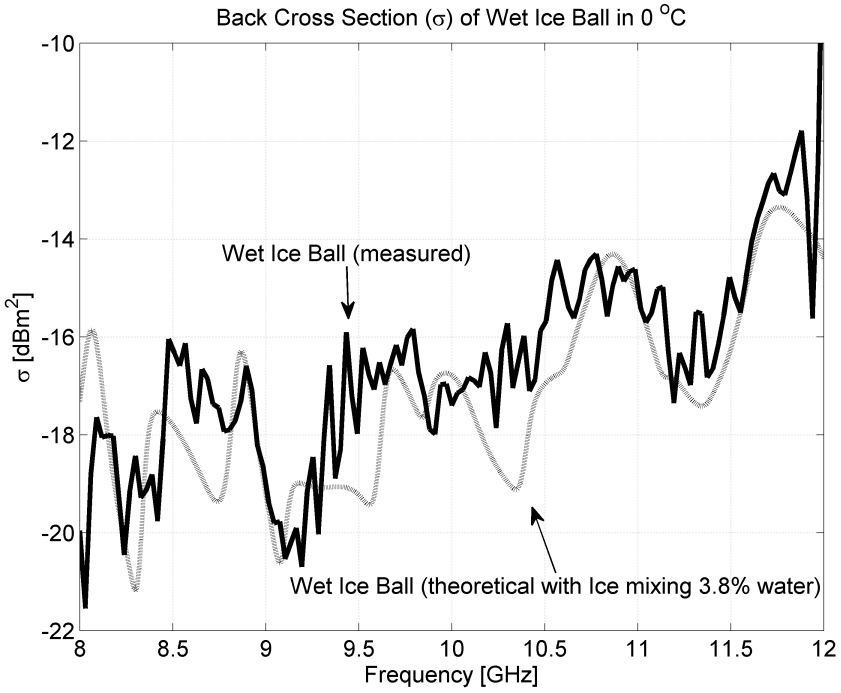


Figure 3.7: Comparison between measured and theoretically predicted scattering cross-section curves of melting ice spheres with ice as background and water as inclusion.

Table 3.1: Dielectric constants of ice (ϵ_i) at different frequencies and temperatures

	-20^oC	-10^oC	0^oC
2.705 GHz (KOUN)	3.1684 + j0.0009	3.1686 + j0.0013	3.1700 + j0.0041
5.510 GHz (OU-PRIME)	3.1682 + j0.0005	3.1683 + j0.0008	3.1692 + j0.0025
9.73 GHz (RaxPol)	3.1682 + j0.0004	3.1682 + j0.0005	3.1688 + j0.0016

Table 3.2: Dielectric constants of water (ϵ_w) at different frequencies and temperatures

	0^oC	10^oC	20^oC
2.705 GHz	81.1430 + j23.1731	80.4632 + j16.6259	78.3412 + j12.0251
5.510 GHz	65.1406 + j37.1941	70.9023 + j29.4124	72.7890 + j22.4553
9.73 GHz	42.9297 + j41.3297	53.7770 + j38.2775	61.0809 + j32.6422

Considering that the density of hail increases during melting, fractional volume for water (f_w) in melting hail given melting ratio γ_w is calculated from

$$f_w = \frac{\gamma_w \rho_i}{\gamma_w \rho_i + (1 - \gamma_w)\rho_w}, \tag{3.16}$$

where ρ_w and ρ_i are densities for water and ice(hail) in [kg m^{-3}]. As a special case of dry hail, $\gamma_w = 0$; therefore, $f_w = 0$, effective dielectric constant is the dielectric constant of pure ice.

Calculations of the fractional volumes of air (f_a), ice (f_i) and water (f_w) in melting snow are more complicated since snow itself is a mixture of ice and air. Assuming the density of the dry portion of snow in a melting snowflake is unchanged (100 [kg m^{-3}]), while the density of the whole melting snowflake increases when the melting ratio increases. Eq. (3.17) provides how f_a, f_i and f_w are obtained given the melting ratio γ_w, with ρ_s, ρ_w and ρ_i being densities for snow, water and ice (hail) in [kg m^{-3}], respectively.

$$f_w = \frac{\gamma_w \rho_s}{\gamma_w \rho_s + (1 - \gamma_w)\rho_w} \tag{3.17a}$$

$$f_i = \frac{(1 - f_w)\rho_s}{\rho_i} \tag{3.17b}$$

$$f_a = 1 - f_w - f_i. \tag{3.17c}$$

A new relation between temperature and melting ratio is developed in this work based on a model introduced by Yokoyama and Tanaka (1984), which is shown in Eq. (3.18) and depicted in Fig. 3.8. Random fluctuation of $[-0.2\gamma_x \; 0.2\gamma_x]$ is added to simulate various situations.

$$\gamma_x = \begin{cases} 0.5(t/t_x)^{1.8} & 0 \le t \le t_x \\ 0.5 & t_x < t. \end{cases} \tag{3.18}$$

In Eq. (3.18). $t_x(x = s, h)$ is the temperature that snow or hail reaches their maximum melting ratio. Because hailstones usually fall faster than snowflakes, t_s is set to 5^o for snow and t_h is 8^o for hail. As melting continues, part of the water from melted

snow/hail would shed from the original particle and become a rain drop. To include those effects, the maximum melting ratio of snow and hail are set to 0.5 in order to avoid too much water in a melting hydrometeor without shedding off or breaking up.

As the hydrometeors melt, the diameter of the particle would shrink due to the density difference between snow/hail and water. Fig. 3.9 shows how the melting ratio affects the diameter and the water fraction of snow and hail particles by assuming diameter of a particle is the cubic root of its volume (Eq. (3.19)). The size of a hailstone does not shrink significantly if it does not breakup. On the other hand, the snow particles diameter will reduce to 80% when the melting ratio reaches 0.5. The fraction of water for hail changes at the same pace as the melting ratio, but for snow, the fraction of water remains below 0.1 when the melting ratio reaches 0.5.

$$D_{mx} = D(\frac{\gamma_w \rho_x}{\rho_w} + (1 - \gamma_w))^{\frac{1}{3}} \tag{3.19}$$

In Eq. (3.19), ρ_x stands for density of snow or hail. Accordingly, D_{mx} stands for diameter for melting snow or hail.

3.4 Scattering Theory

When electromagnetic waves are incident on a particle, the particle may absorb a portion of the radiation energy and scatter the rest of the energy. The scattered energy can be described in terms of scattering amplitudes. Fig. 3.2 shows the scattering geometry of a single particle. Assuming the incident polarization of the wave aligned along the major and minor axis of the particle, the scattering amplitude of the major and minor axes, f_a and f_b, can be calculated from Rayleigh scattering approximation as given in Eq. (3.20) if the diameter of the particle is much less than radiation wavelength (e.g. $D/\lambda < 1/16$).

$$f_{a,b}(0, D) = f_{a,b}(\pi, D) = \frac{\pi^2 D^3}{6\lambda^2} \frac{\epsilon - 1}{1 + (\epsilon - 1)L_{a,b}}. \tag{3.20}$$

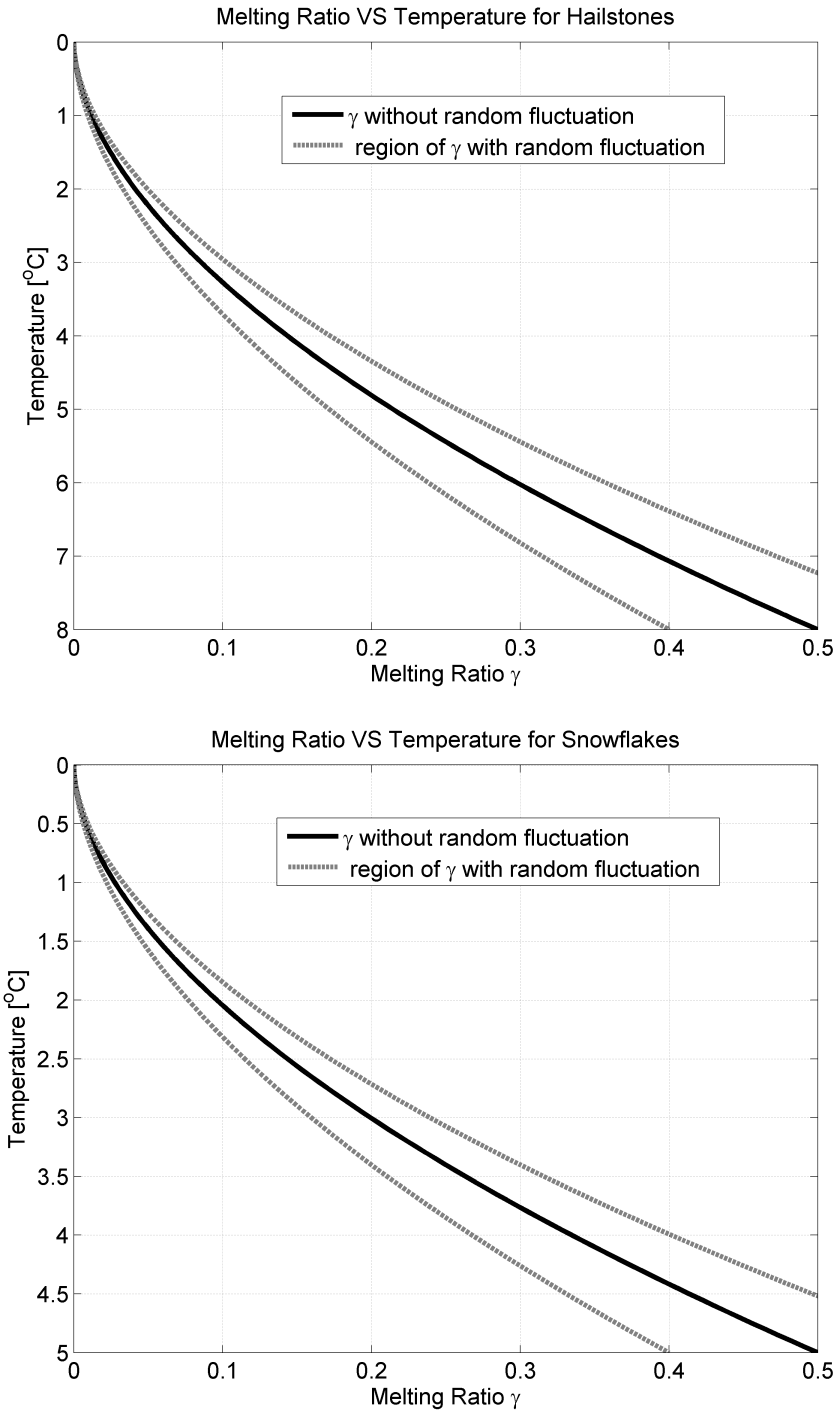


Figure 3.8: Relations between temperature and melting ratios for hail (top) and snow (bottom).

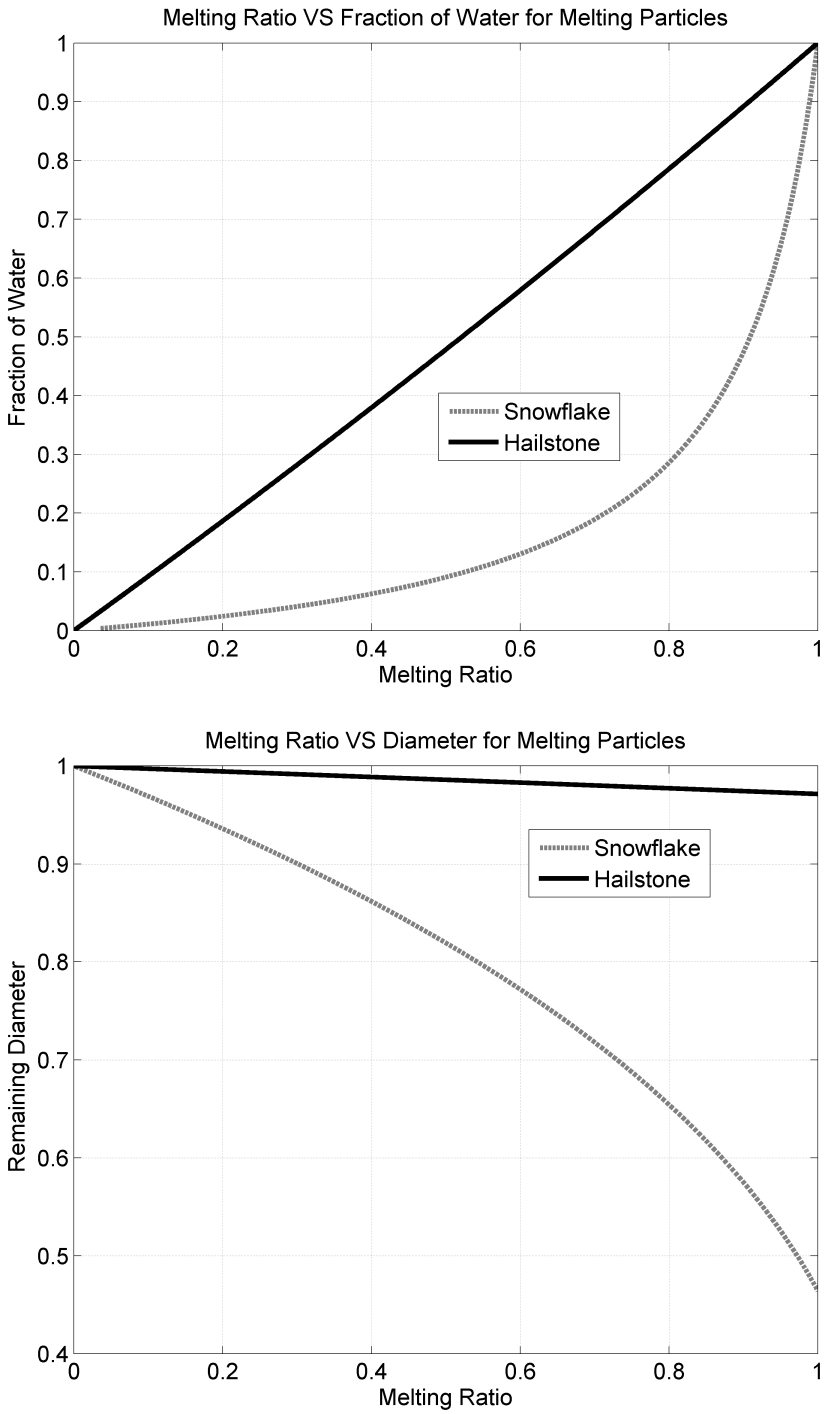


Figure 3.9: Relationships among melting ratio, fractional water content and particle diameter change, for snow and hail. From top to bottom, (a) Melting ratio changes versus fraction of water changes for snow and hail. (b) Melting ratio changes versus fraction of diameter changes for snow and hail.

In Eq. (3.20), ϵ is the dielectric constant of the particle and $L_{a,b}$ can be calculated from

$$g = \frac{1}{r_a^2} - 1 \tag{3.21a}$$

$$L_b = \frac{1+g^2}{g^2}\left(1 - \frac{1}{g}\arctan g\right) \tag{3.21b}$$

$$L_a = \frac{1}{2}(1 - L_b). \tag{3.21c}$$

Rayleigh scattering approximation may be applied in S-band. For higher frequency such as C-band and X-band, Rayleigh scattering approximation is no longer accurate for the hydrometeors models since the diameter-to-wavelength ratio is already in Mie scattering region, where fluctuation, instead of monotonic increasing, of the scattering amplitude of a single particle should be expected, as the diameter of a particle increases. The T-Matrix method, also called the extended boundary condition method, is an effective numerical solution for electromagnetic scattering by homogeneous, rotationally symmetric nonspherical particles. In this study, f_a and f_b, along with the cross-polarization terms, are computed from T-matrix calculations using the T-Matrix code for nonspherical particles in a fixed orientation introduced in Mishchenko (2000).

For hydrometeor scatterings, the incident polarization of the wave often does not align along the major and minor axis of a hydrometeor. Then the scattering amplitudes of those particles with a canting angle (ϕ) are calculated from:

$$\mathbf{f} = \begin{bmatrix} f_{hh} & f_{hv} \\ \\ f_{vh} & f_{vv} \end{bmatrix} = \begin{bmatrix} f_a\cos^2\phi + f_b\sin^2\phi & (f_a - f_b)\sin\phi\cos\phi \\ \\ (f_a - f_b)\sin\phi\cos\phi & f_a\sin^2\phi + f_b\cos^2\phi \end{bmatrix} \tag{3.22}$$

Note that, the dependency on scattering direction and particle size of scattering amplitude $\mathbf{f}$ is implicit in Eq. (3.22).

3.5 Single-Cell Monte Carlo Simulation and Simulated Radar Variables

A single-cell Monte Carlo simulation can be considered as a single radar resolution volume (cell) filled with uniformly distributed hydrometeors as illustrated in Fig. 3.10. The total number and size of hydrometeors in the volume are controlled by the DSD as given in Eq. (3.23). Melting behavior of ice species is controlled by temperature as given in Eq. (3.18).

$$N_t = \sum_{D_{\min}}^{D_{\max}} VN(D)\Delta D \tag{3.23}$$

In Eq. (3.23), ΔD is the diameter interval between two adjacent size bins. $D_{\min}$ and $D_{\max}$ specify the diameter ranges of hydrometeors. Table 3.3 shows the details of diameter sizes used in the simulations.

Table 3.3: Sizes of Particles Used in Simulations for Different Species (all in [mm])

	$D_{\min}$	$D_{\max}$	ΔD
Rain	0.5	8	0.1
Snow	1	20	0.2
Hail	1	50	0.5

Outputs from the simulation are the composite of echoes scattered by hydrometeors. If V is the size of the volume in [m^3], reflectivity factor defined in Eq. (2.21) and specific differential phase defined in Eq. (2.25) can be rewritten as

$$Z_{h,v} = \frac{4\lambda^4}{\pi^4 |K_w|^2 V} \sum |f_{hh,vv}(\pi)|^2, \tag{3.24}$$

$$K_{dp} = 10^{-3} \frac{180\lambda}{\pi V} \sum \Re[f_{hh}(0) - f_{vv}(0)], \tag{3.25}$$

where $\sum$ indicates summation over all hydrometeors in the volume. Similarly, specific attenuation defined in Eq. (2.30) can be computed from

$$A_{h,v} = 10^{-3} \frac{8.686\lambda}{V} \sum \Im[f_{hh,vv}(0)]. \tag{3.26}$$

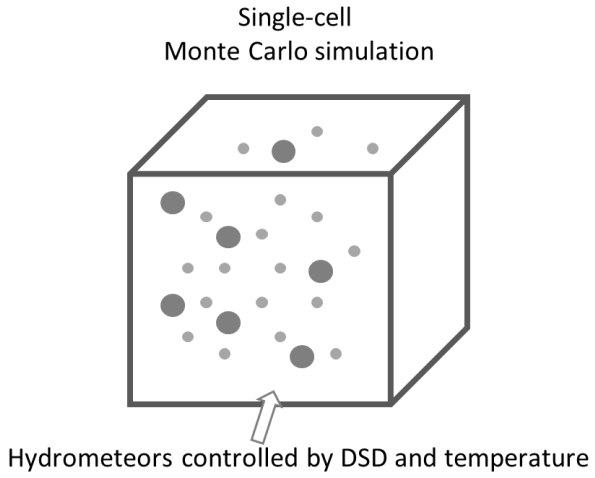


Figure 3.10: Concepts of single-Cell Monte Carlo simulations.

3.5.1 Scattering Plots of Hydrometers at X-band

One of the advantages of the Single-Cell Monte Carlo simulation is that the number, size, types and even the melting behavior of the hydrometeors in the volume can be controlled by artificially setting the model parameters. For example, a scenario where there is only a certain amount of hailstones with 10% melting and nothing else in the volume may be created. By creating many scenarios and calculating the returns, radar signatures for all the species and all kinds of melting levels can be obtained. Since the intercept parameter of DSDs and melting ratio are both random variables within a reasonable range, different types of precipitation can also be emulated.

DSDs of rain, snow and hail are assumed to have an exponential form to match the bulk microphysics scheme of ARPS model which is introduced in 3.6. Inputs to the simulation including mixing ratio of rain, snow and hail (q_r, q_s and q_h) also matches ARPS outputs. The slope parameter Λ is calculated from Eq. (3.28) while mixing ratio and intercept parameter of each species are randomly generated according to Table 3.4 and Table 3.8. The scattering map generated in Monte-Carlo simulation

can serve as the knowledge base for the advanced airborne development introduced in section 3.6. Details of the airborne radar parameters can be found in Table 3.7.

Table 3.4: Mixing and Melting Ratio Ranges used in the Single-Cell Simulations. (M for Melting)

	Rain	Snow	Hail	Msnow	Mhail	Rain and Hail
Mixing ratio [g kg^{-1}]	0 - 10	0 - 10	0 - 10	0 - 3	0 - 5	0 - 3/0 - 3
Melting ratio	0	0	0	0 - 0.3	0 - 0.5	0/0 - 0.5

Additional cautions should be taken for the following issues. 1) The created scenarios must be reasonable and realistic. In other words, the mixing ratio of each species must be within a certain range to ensure that there are not too many hailstones or snowflakes in a single volume. 2) The size of the volume used in simulation must be large enough, so that there are enough particles presenting. For the first issue, a statistical study has been performed on ARPS model outputs. The results show that the mixing ratios of rain, snow and hail can reach as high as 15 [g kg^{-1}]. Thus the mixing ratio of rain, snow or hail is generated as a random number uniformly distributed at range 0 to 10 [g kg^{-1}], which covers most situations. For melting hail and snow, a random melting ratio is also generated besides hail or snow mixing ratio, Table 3.4 lists the detailed mixing ratio and melting ratio ranges used in the simulations. For the second issue, a compromise needs to be made between the size of the volume and the required computational load in the simulation. The size of the volume is set at $100 \times 100 \times 100$ [m^3]. A set of 6000 scenarios for six species including rain, snow, hail, melting snow, melting hail and mixed rain and hail have been carried out in order to have a statistical significance. In each scenario, only one out of the six species is generated according to the mixing ratio and melting ratio randomly chosen within its range. The scattering plots of the result are shown in Fig. 3.11.

Compared with the results from other simulations and observations, the regions for these six species from scatter plots seem to be consistent with those in Straka et al.

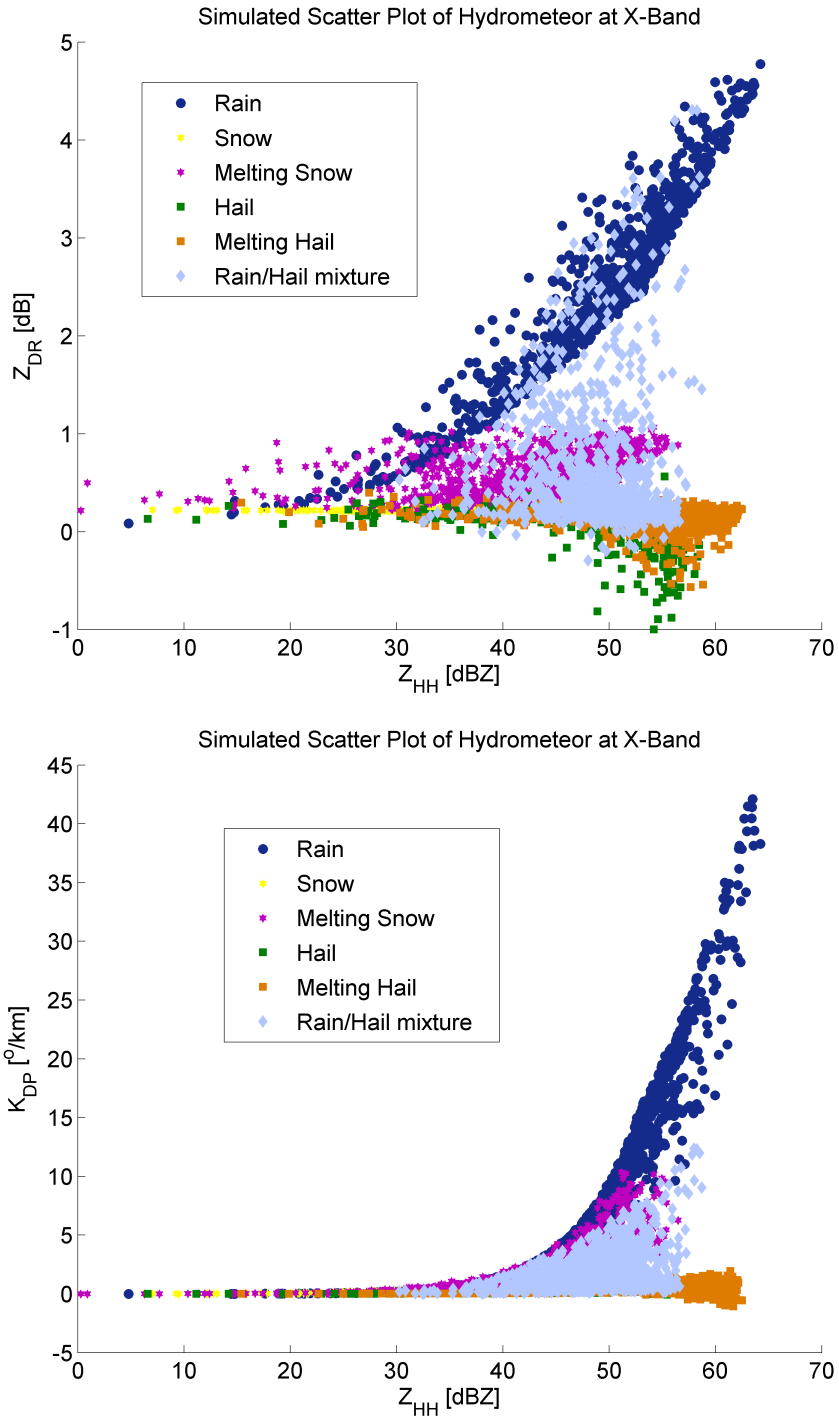


Figure 3.11: Scatter plots of hydrometeor species at 10 GHz. From top to bottom, (a) Z_H and Z_{DR} plot, (b) Z_H and K_{DP} plot.

(2000) and Marzano et al. (2007) except that the scale is different, which is due to different radar frequencies. Rain tends to have higher Z_{DR} than hail or snow. Water species including rain, melting snow and melting hail would have a significantly larger K_{dp} than dry species (snow and hail). As expected, the signatures of mixed rain and hail reside in between the signatures of hail and rain, and the higher the mixing ratio of hail in the rain/hail mixture, the closer the signature region to that of dry hail. Due to the random canting angles of the particles, the range of Z_{DR} in this X-band radar is smaller compared with the results in Straka et al. (2000) and Marzano et al. (2007) (C band). As shown in Fig. 3.11(b), the range of K_{dp} is much larger than that in Straka et al. (2000) and Marzano et al. (2007) especially for rain and melting snow. This is because wavelength in X-band is small compared to particle size, which leads to high K_{DP}. Another important reason is that these outputs are 'clean' data without noise. In a real radar system, phase measurements are contaminated by noise, which may lead to lower K_{dp}. Mixing ratios of all species are much higher than their normal values in the Monte Carlo simulations. However, a larger mixing ratio range is valuable to cover some extreme scenarios. Knowledge gained from the radar signature scatter plots will assist in the development of the hazard detection system designed to distinguish rain, snow, hail and mixtures. To keep the processing efficient, correlation coefficient (ρ_{hv}) and linear depolarization ratio (LDR) are not included at the current stage, while similar plots of these variables can be generated in the same way. Table 3.5 shows the general decision regions derived from scatter plots for the six species.

Table 3.5: General Decision Regions for Hydrometeors at 10 GHz (M for Melting)

	Rain	Snow	Hail	Msnow	Mhail	Rain and Hail
Z_H [dBZ]	20 - 65	15 - 60	20 - 65	15 - 65	20 - 65	15 - 60
Z_{DR} [dB]	0 - 5	0 - 0.5	-1 - 0.5	0 - 1	-0.5 - 0.5	0 - 4
K_{DP} [deg km^{-1}]	0 - 45	0 - 4	0 - 3	0 - 10	0 - 4	0 - 15

3.5.2 Dual-Pol Variables of Rain at S-, C- and X-band

Quantitative precipitation estimation (QPE) and quantitative precipitation forecasts (QPF) demand better knowledge of dual polarization signature of rain at different radar frequencies. To better support and serve the development of polarimetric rain attenuation correction algorithms and rainfall rate estimation algorithms, dual-pol variables of rain at S-, C- and X-band are obtained using single-cell Monte Carlo simulations.

DSD of rain is assumed to be normalized gamma distribution as defined in Eq. (3.5). Parameters of the normalized gamma distribution are randomly generated within the ranges specified by Ulbrich (1983) and Bringi and Chandrasekar (2001) as shown in Eq. (3.27). Those ranges are widely used and belived to cover most natural rain DSDs. Note that while the range in Eq. (3.27) may match local precipitation climatology, the frequency of individual data points probably does not. Details are list in Table 3.6.

$$0.5 \leq D_0 \leq 3.5 \text{ [mm]} \tag{3.27a}$$

$$10^2 \leq N_w \leq 10^5 \text{ [mm}^{-1}\text{m}^{-3}\text{]} \tag{3.27b}$$

$$-1.0 \leq \mu \leq 5.0. \tag{3.27c}$$

It is worth mentioning that all three parameters have a uniform distribution within the given range, which leads to equal probability for different rain types. This assumption may not hold in reality since smaller rainfall ($R < 40$ [mm hr^{-1}]) is more frequent than heavier rainfall intervals/cases. All datasets are limited to rainfall values up to 300 [mm hr^{-1}] and Z_H up to 55 [dBZ]. A total of 6000 scenarios has been carried out. Note that, simulations at different frequencies are performed at the same time using the same scenario/DSD, which means those dual-pol variables can be combined and assist the development of dual-frequency and/or dual-polarization rainfall rate estimation algorithms.

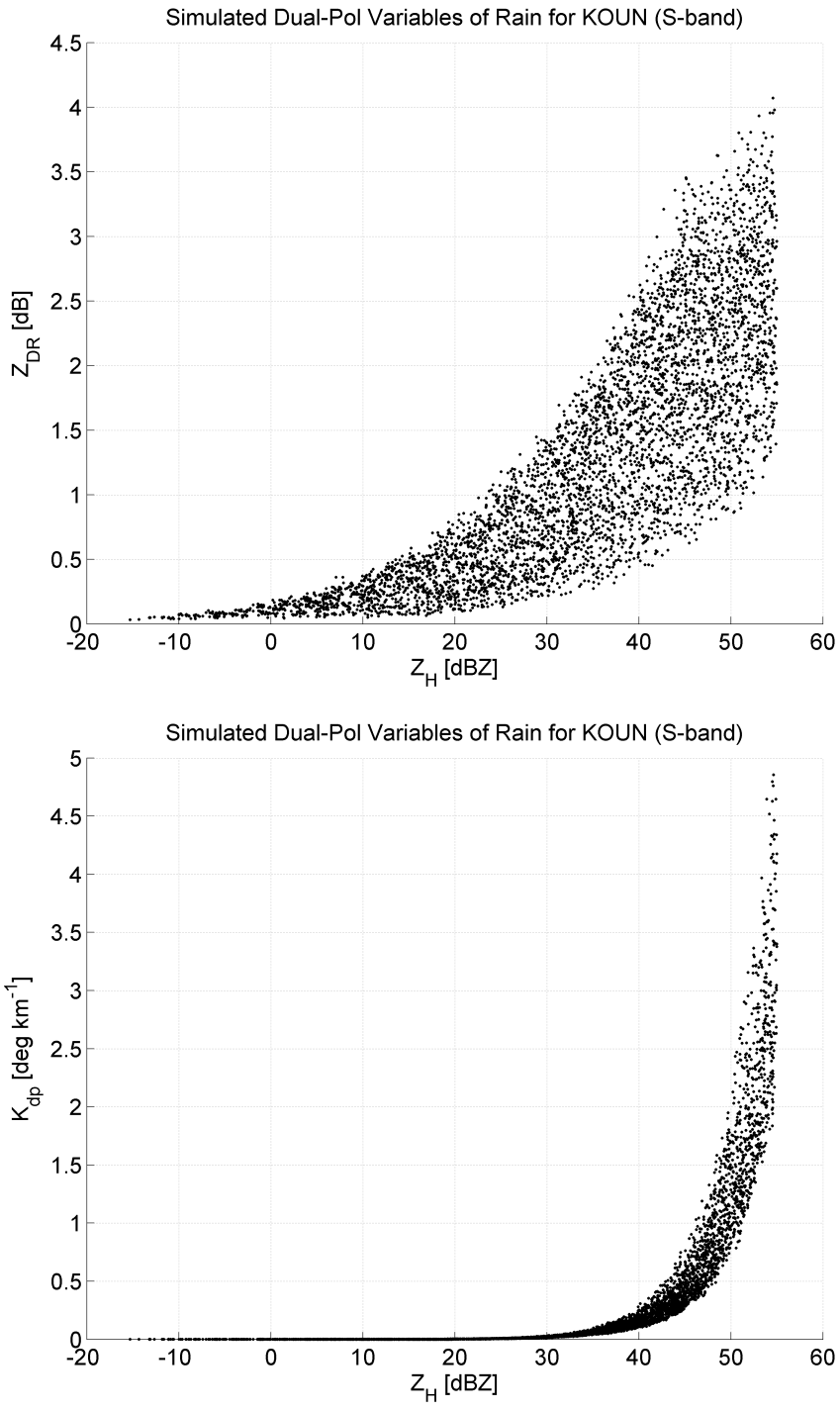


Figure 3.12: Simulated dual-pol variable scatter plots of rain for KOUN (S-band). From top to bottom, (a) Z_H and Z_{DR} plot, (b) Z_H and K_{dp} plot.

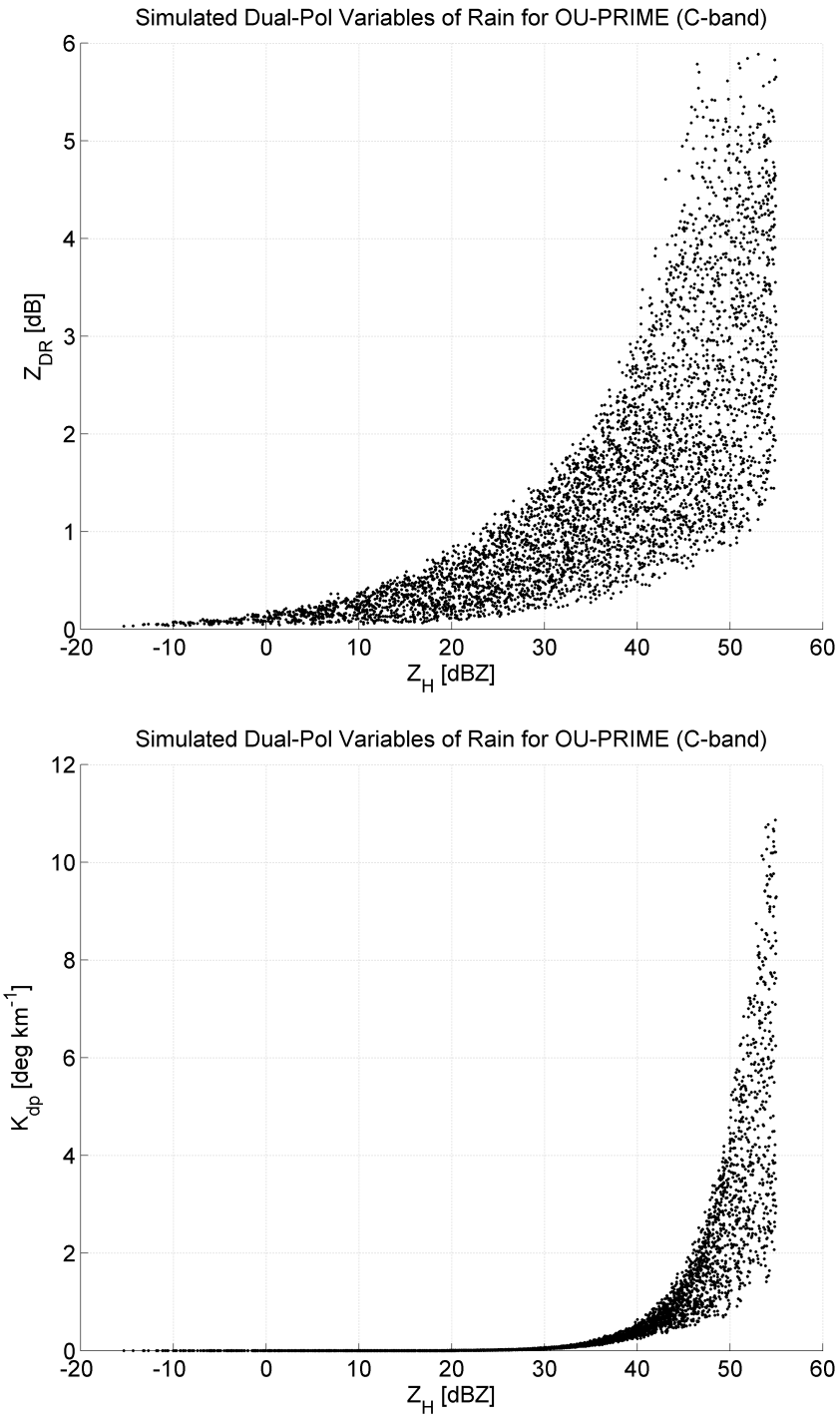


Figure 3.13: Simulated dual-pol variable scatter plots of rain for OU-PRIME (C-band). From top to bottom, (a) Z_H and Z_{DR} plot, (b) Z_H and K_{dp} plot.

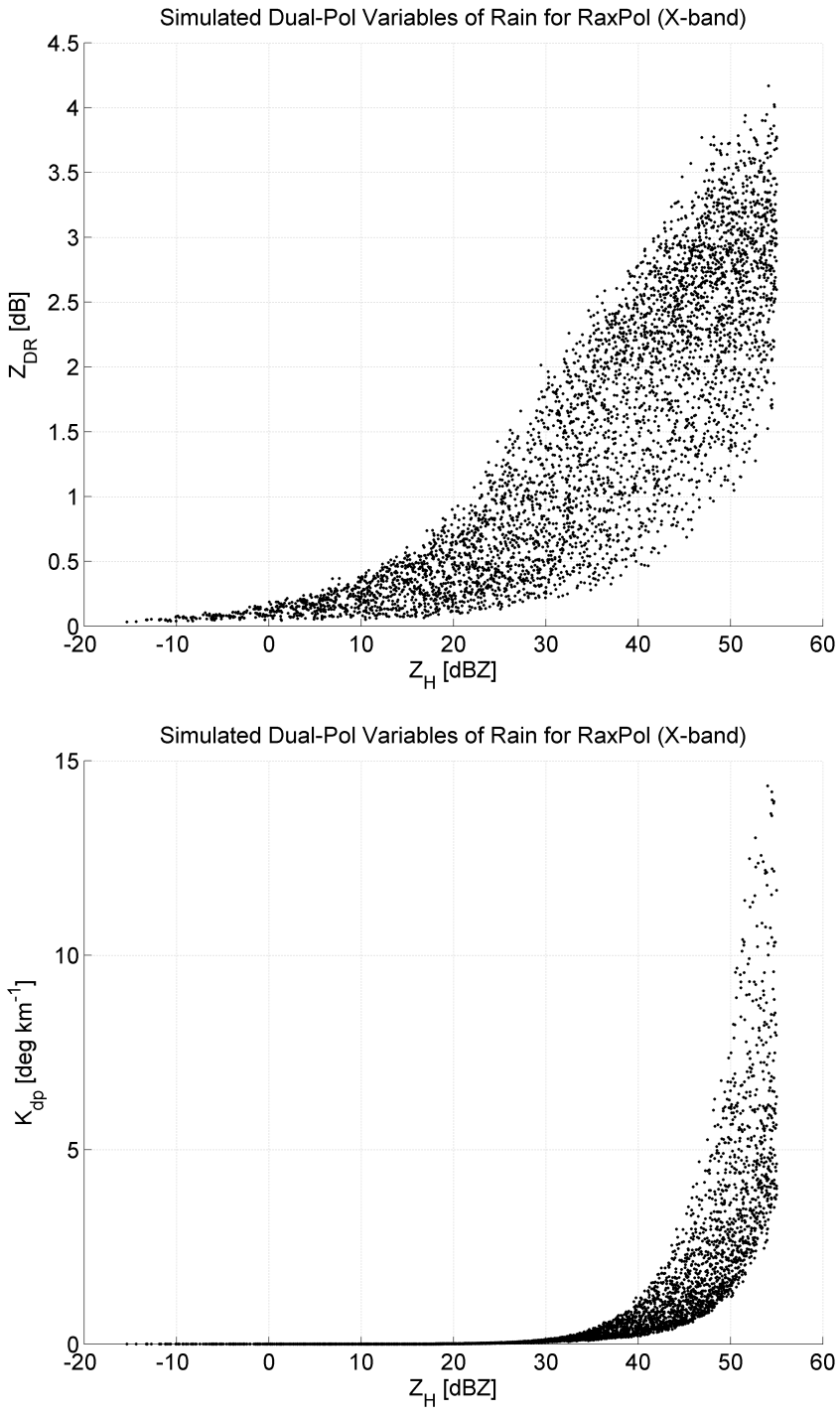


Figure 3.14: Simulated dual-pol variable scatter plots of rain for RaxPol (X-band). From top to bottom, (a) Z_H and Z_{DR} plot, (b) Z_H and K_{dp} plot.

Table 3.6: Key Parameters of the Single Cell Monte-Carlo Simulation for Rain.

Radar frequency (S-band)	2.705 GHz (KOUN)
Radar frequency (C-band)	5.510 GHz (OU-PRIME)
Radar frequency (X-band)	9.730 GHz (RaxPol)
Radar elevation angle	0^o
Volume of the single cell	1000 m^3
Temperature	Uniformly between 5^oC to 20^oC
Raindrop size [mm]	0.5 to 8 (step size 0.1)
Canting angle distribution	Gaussian with mean 0 and SD 10^o
Scattering model	T-Matrix
Axis ratio of raindrops	Brandes et al. (2002) with randomness
Terminal velocity of raindrops	Brandes et al. (2002)

Scatter plots are shown in Fig. 3.12, Fig. 3.13 and Fig. 3.14. While regions of Z_H and Z_{DR} plots are similar among the three frequency bands, value of K_{dp} significantly increases as frequency increases.

3.6 Radar Simulations with ARPS Model Outputs

Recent advances in numerical weather models have made it possible to simulate a weather field at fine scales over a broad range of environmental scenarios. Thus, developing a software radar simulator based on high-resolution weather simulation is feasible.

The Advanced Regional Prediction System (ARPS) used by Jung et al. (2008), Cheong et al. (2008) and May et al. (2007) in weather radar simulations, is a multi-scale nonhydrostatic atmospheric simulation and prediction model whose prognostic state variables include potential temperature, pressure, mixing ratios for rainwater,

snow and hail (q_r, q_s and q_h), plus 3D wind components and the turbulent kinetic energy used by the 1.5-order subgrid-scale turbulent closure scheme (e.g., Xue et al. 2000, 2001, 2003). A simulated-high-resolution atmospheric field produced by the ARPS model has a horizontal grid spacing of 100 [m] and vertical spacing of 400 [m] over a $64 \times 64 \times 12$ [km^3] volume. This simulated field was for a supercell thunderstorm which was initiated by a thermal bubble in a horizontally homogeneous environment defined by the 20 May 1977 Del City, Oklahoma sounding reported in Ray et al. (1981).

Advanced aviation hazard detection and monitoring require the capabilities to discriminate different types of hazards including hydrometeors. To assist modern airborne radar development and evaluate radar performance in extreme scenarios like flying close by a storm or other severe weather conditions, the single-cell simulation is then applied to the entire radar scanning volume supported by ARPS outputs. The basic concepts and data-flow of this approach are summarized in Fig. 3.15 and Fig. 3.16. This study emphasizes on 'snap-shot' type hazard imaging, which are enabled by a fast-scanning array antenna system design. In other words, airborne platform can be considered at fixed position within one scan. Dual-polarization airborne radar signatures corresponding to a mixed-phase storm case from both plan position indicator (PPI) and range height indicator (RHI) scan schemes are generated, and the results are compared with the simulated weather field truth data. For computation efficiency, the simulated aircraft flies at different altitudes near the most intense portion of the severe weather, which is a small part of the simulated atmospheric field.

Key parameters of the airborne radar used in the simulation are lists in Table 3.7. DSDs of rain, snow and hail are assumed to have an exponential form as given in Eq. (3.2), which matches the bulk microphysics scheme of LFO83 used in ARPS

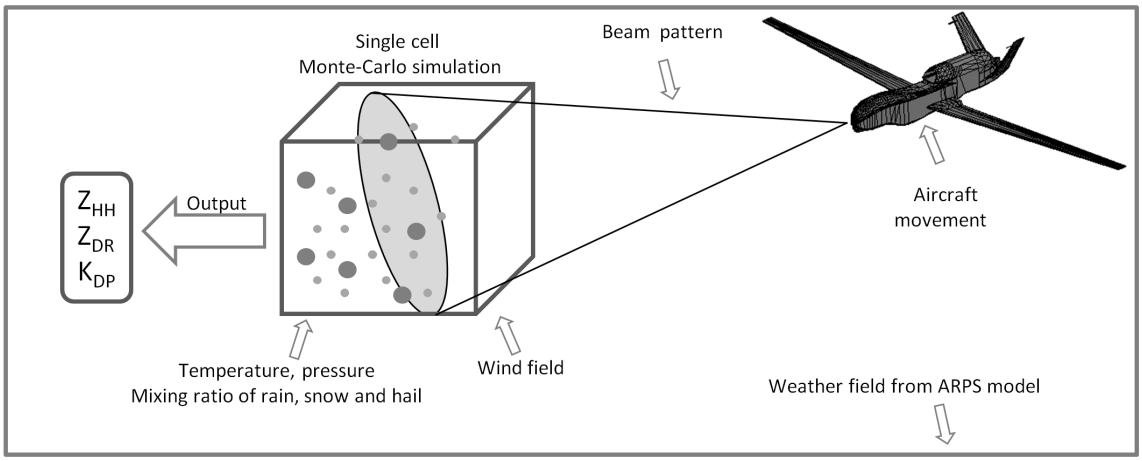


Figure 3.15: Basic concepts for airborne polarimetric radar sensing simulations.

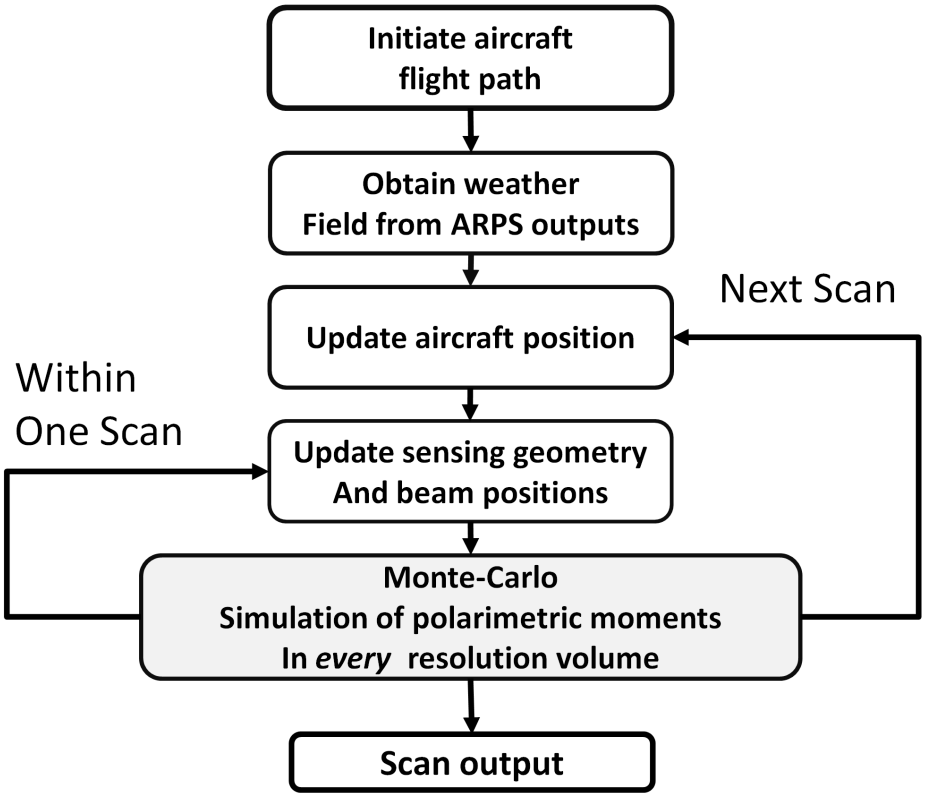


Figure 3.16: The simulation data-flow diagram.

model. Given ARPS model output q_r, q_s and q_h, the slope parameter Λ can be diagnosed by following Smith's work (Green 1975)

$$\Lambda_x = \frac{\pi N_x \rho_x}{\rho_a q_x}, \tag{3.28}$$

where ρ_a is the air density in [kg m^{-3}], ρ_x is the density of rain, snow or hail in [kg m^{-3}], q_x is the mixing ratio of each species from ARPS outputs in [kg kg^{-1}]. Typical intercept parameter for an exponential DSD is $N_r = 8.0 \times 10^6$ [m^{-4}] for rain, $N_s = 3.0 \times 10^6$ [m^{-4}] for snow, and $N_h = 4.0 \times 10^4$ [m^{-4}] for hail. A fixed intercept parameter is widely used for representing warm rain (Kessler 1969) and ice (e.g., Lin et al. 1983; Hong et al. 2004) microphysics. A number of observational studies (e.g., Waldvogel 1974; Zhang et al. 2008) indicate that, for different rain types and intensity, the intercept parameter is far from constant. Even within the same precipitation, the intercept parameters can vary spatially. The empirical range of the intercept parameter is 10^6 to 10^8 [m^{-4}] for rain (Joss and Waldvogel 1969), 10^5 to 10^8 [m^{-4}] for snow (Tong and Xue 2008) and 10^2 to 10^8 [m^{-4}] for hail (Gilmore et al. 2004). In this work, the intercept parameter is randomly chosen from 1/10 to 10 times its typical value, as shown in Table 3.8.

Table 3.7: Key Parameters of the Simulated Airborne Radar Sensor

Radar frequency (wavelength)	10 GHz (3 cm)
Pulse width	0.5 μs
Pulse repetition frequency (PRF)	4000 Hz
Range resolution	75m
Antenna beamwidth	5^o
Unambiguous range (PPI)	37,500m
Unambiguous range (RHI)	22,500m

Simulated radar signatures from scenarios where an Unmanned Aerial Vehicle (UAV) flies through different layers of the atmosphere and performs PPI and RHI

Table 3.8: Parameters Used in Simulations for Different Species

	Typical N_0 [m^{-4}]	N_0 used in this study
Rain	8.0×10^6	8.0×10^5 to 8.0×10^7
Snow	3.0×10^6	3.0×10^5 to 3.0×10^7
Hail	4.0×10^4	4.0×10^3 to 4.0×10^5

scans are used to evaluate weather-sensing capabilities. The detailed geometries of airborne sensing are shown in Fig. 3.17. As discussed previously, the input weather field produced by the ARPS system includes mixing ratio of rain, snow and hail q_r, q_s, q_h plus the potential temperature pt and pressure pr. The ground speed of the aircraft is set to a constant of 100 [m s^{-1}], while its position in the atmosphere is updated every second. The key parameters of the radar are listed in Table 3.7. For computational efficiency, only one scan is taken in each position/second and there is no overlap between adjacent beams. Since the platform moves less than 1 m during the time of one scan, the aircraft is treated as in fixed position during one scan. Once the aircraft arrives at a position, it points its beam to one direction, transmits two pulses, and scans its beam to the next direction, until the entire scan is finished. Radar return at one beam direction is simply the average of two pulses. The range of intercept parameters for DSDs of rain, snow and hail are given in Table 3.8, and are randomized from scan to scan. In other words, the intercept parameters for all species are fixed during one scan and randomly generated again in next scan. The size of the single cell for the Monte Carlo simulation is $100 \times 100 \times 400$ m^3, which matches the grid sizes from the input weather field. If the radar resolution volume contains more than one single cell, the parameter inputs to Monte Carlo simulation are the averaged values across the entire radar resolution volume.

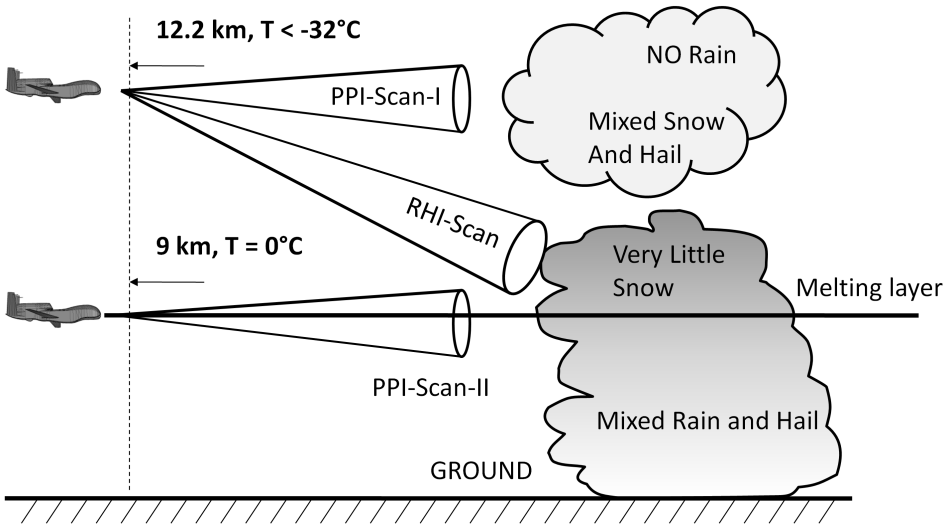


Figure 3.17: Geometries of airborne volume scanning observation of hazardous weather regions with PPI and RHI scanning schemes, PPI-I and RHI scans are performed at 12.2 km height, PPI-II scan is performed at 9 km height around melting layer.

3.6.1 Scenario I

An aircraft is enroute at an altitude around 10-13 km within the stratosphere where the atmospheric conditions are relatively stable. As the temperature can be far below 0^oC at this layer, there exists supercold liquid and ice mixtures (snow and hail), resulting in potential hazards. A simulated aircraft flying at about 12 km altitude with both electronic PPI and RHI scans is assumed. Table 3.9 lists the detailed information for this scenario. Fig. 3.18 and Fig. 3.20 show the weather fields for the PPI scan and RHI scan, respectively.

As shown in Fig. 3.18(a), although snow mixing ratio is not high, there is plenty of snow ahead of the aircraft. Meanwhile, Fig. 3.18(b) shows that the mixing ratio of hail is very high within the region to the right to the aircraft.

Fig. 3.19 shows the simulated radar signatures for the PPI scan. The reflectivity plot (Fig. 3.19(a)) doesnt show much information about what is ahead of the aircraft except for the moderate level of ice mixture. However, in the Z_{DR} plot, there is a region where Z_{DR} value is very small (even lower than 0), while the other regions around have much higher values. This is an indication of a high density of hail. Though the K_{dp} plot (Fig. 3.19(c)) also shows the relatively high value in the same region, its not a typical sign of hail content, since a large mixing ratio of snow can also cause similar K_{dp} features. Combining these observations, the aircraft/pilot will be able to adjust the flight path for weather hazard avoidance.

Table 3.9: Information for Scenario I

Ground speed	100 [m s^{-1}]
Altitude	12.2 [km]
Temperature	-32^oC
Wind speed	Less than 35 [m s^{-1}]
PPI scan range	-30^o to 30^o azimuth
RHI scan range	0^o to -30^o elevation

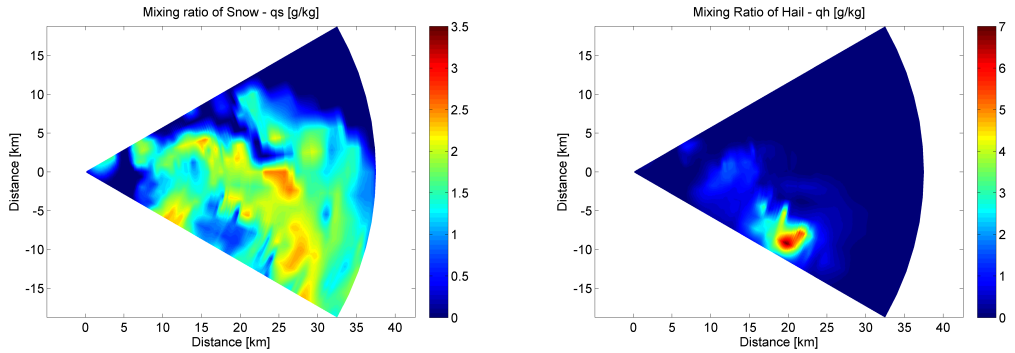


Figure 3.18: Weather field for PPI scan at altitude 12.2 km. From left to right, (a) Mixing ratio of snow - q_s, (b) Mixing ratio of hail - q_h

An RHI scan simulation is also performed at the same altitude, but at different horizontal locations, in order to observe the melting effects. As shown in Fig. 3.20, the melting layer is located at a height of 9 km. Snow mainly appears above the melting layer and almost completely disappears at the boundary of the melting layer. The distribution of hail is similar to snow, except that there is plenty of hail at the melting layer, as hail melts slower than snow. On the other hand, besides this very small amount of hail, only rain exists below the melting layer. Fig. 3.21 shows the simulated radar signatures for this RHI scan. The melting effects can be observed, as both reflectivity and differential reflectivity show a bright-band at the melting layer, and decrease gradually outside the melting layer (shown in Fig. 3.21(a) and Fig. 3.21(b)). Another observation is that high K_{dp} values occur at the regions containing high mixing ratio of liquid water.

3.6.2 Scenario II

Weather conditions are much more complicated within a melting layer than in the stratosphere. As both icy mixtures and liquid water exist in this layer, it is even more dangerous to aviation. A simulated aircraft flying within a melting layer with

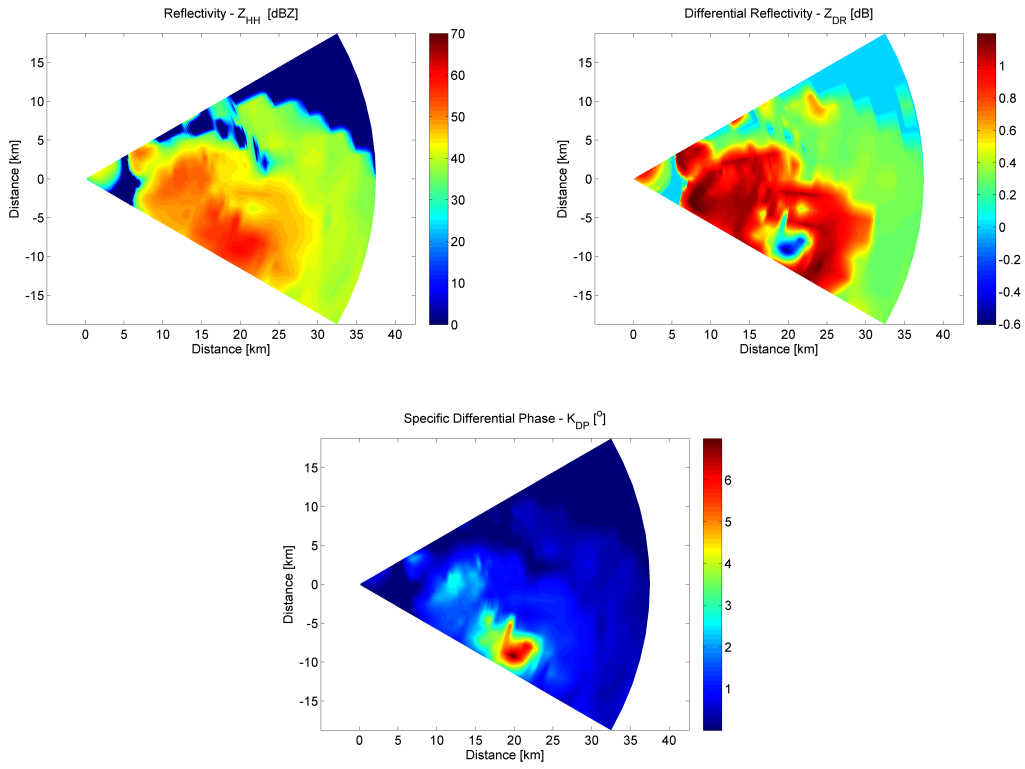


Figure 3.19: Simulated radar returns for PPI scan at altitude 12.2 km. From left to right and top to bottom, (a) Reflectivity - Z_H, (b) Differential reflectivity - Z_{DR}, (c) Specific differential phase - K_{DP}

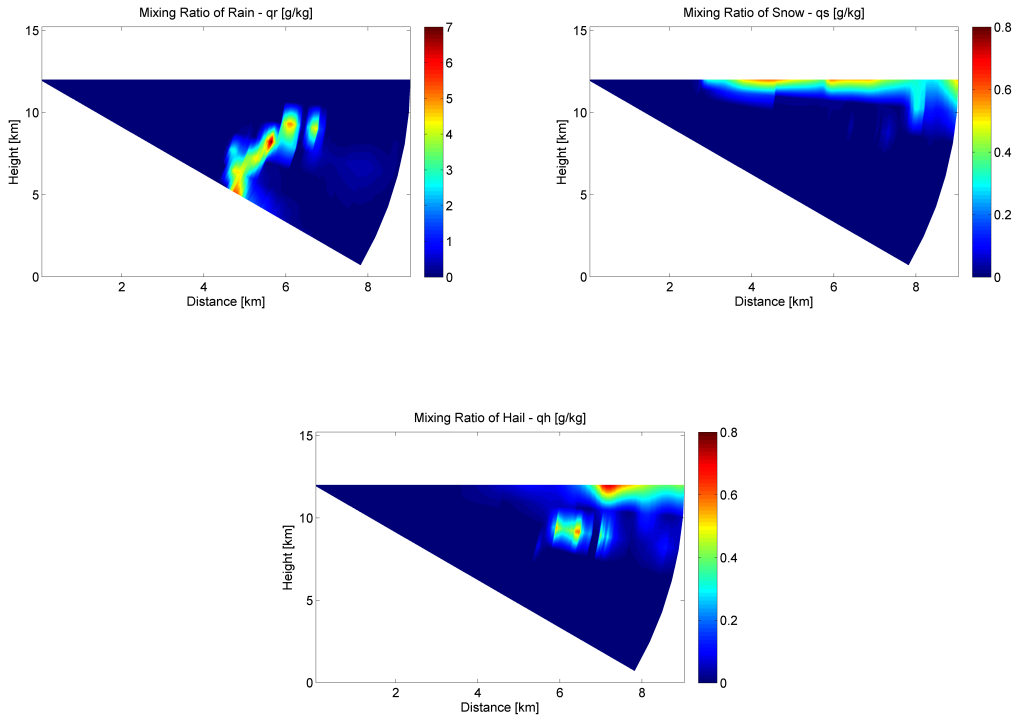


Figure 3.20: Weather field for RHI scan at altitude 12.2 km. From left to right and top to bottom, (a) Mixing ratio of rain - q_r, (b) Mixing ratio of snow - q_s, (c) Mixing ratio of hail - q_h.

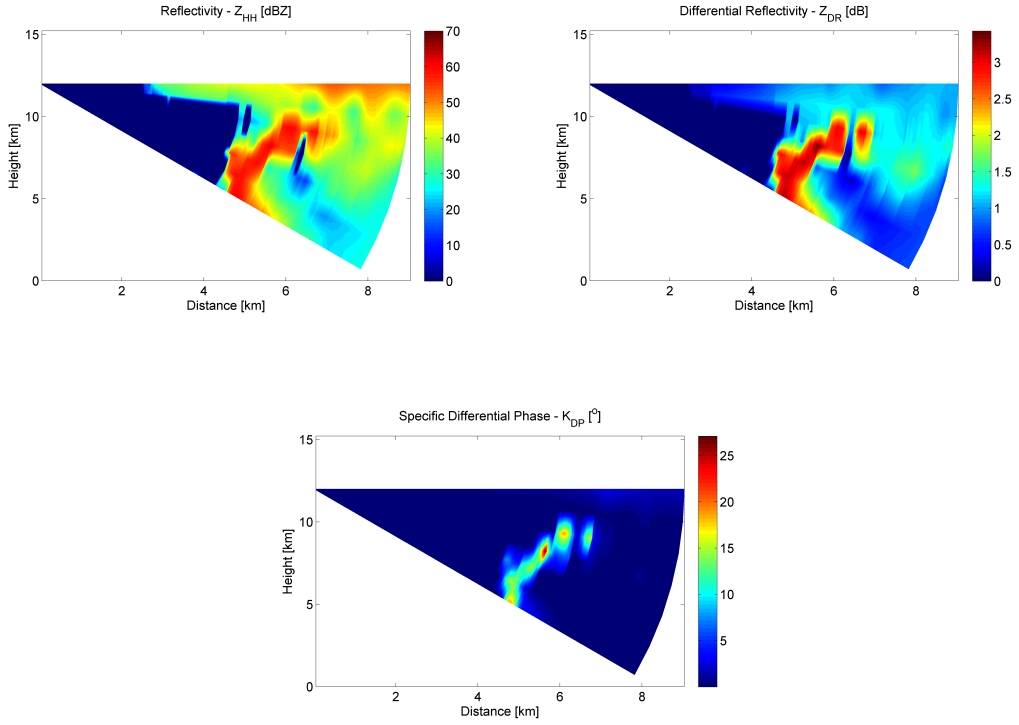


Figure 3.21: Simulated radar returns for RHI scan at altitude 12.2 km. From left to right and top to bottom, (a) Reflectivity - Z_H, (b) Differential reflectivity - Z_{DR}, (c) Specific differential phase - K_{DP}

PPI scan is assumed to validate the potential hazard detection ability of the radar system. Table 3.10 lists detailed information for this scenario. The truth weather field for this scenario is depicted in Fig. 3.22.

Table 3.10: Information for Scenario II

Ground speed	100 [m s^{-1}]
Altitude	9.2 [km]
Temperature	Around 0^oC
Wind speed	Less than 25 [m s^{-1}]
PPI scan range	-30^o to 30^o azimuth

The mixing ratio of snow is low at this altitude while the mixing ratio of rain is very high. Simulated radar signatures for this PPI scan are shown in Fig. 3.23. Attention has been focused on the hazardous region where melting hail and rain co-exist (the highlighted region with a black circle in Fig. 3.23(a), Fig. 3.23(b) and Fig. 3.23(c)). In this region, reflectivity is high while Z_{DR} is low, indicating a large mixing of hail. Also, the high values imply a large content of liquid water, which in turn means a high melting ratio of hail. At the same time, a low K_{DP} indicates the region where the melting ratio of hail is low. Again, the above observations can potentially lead to an automatic monitoring algorithm which both detects the presence of mixed-phase hazards, and performs an analysis about the content and levels of the threats.

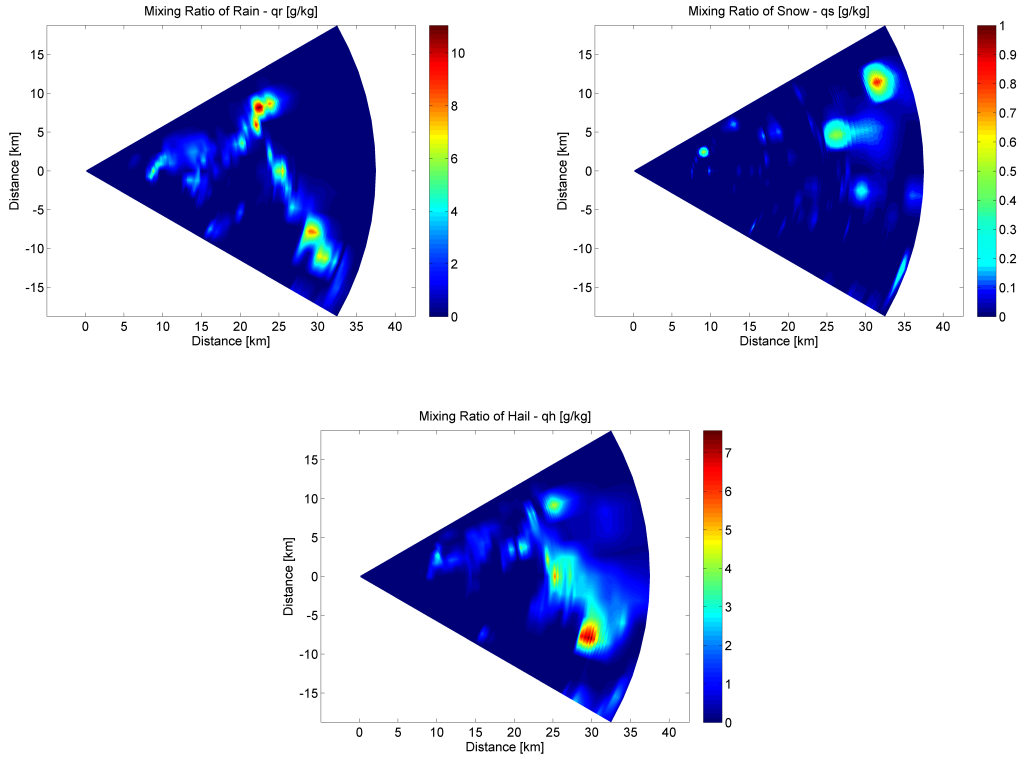


Figure 3.22: Weather field for PPI scan at altitude 9.2 km. From left to right and top to bottom, (a) Mixing ratio of rain - q_r, (b) Mixing ratio of snow - q_s, (c) Mixing ratio of hail - q_h.

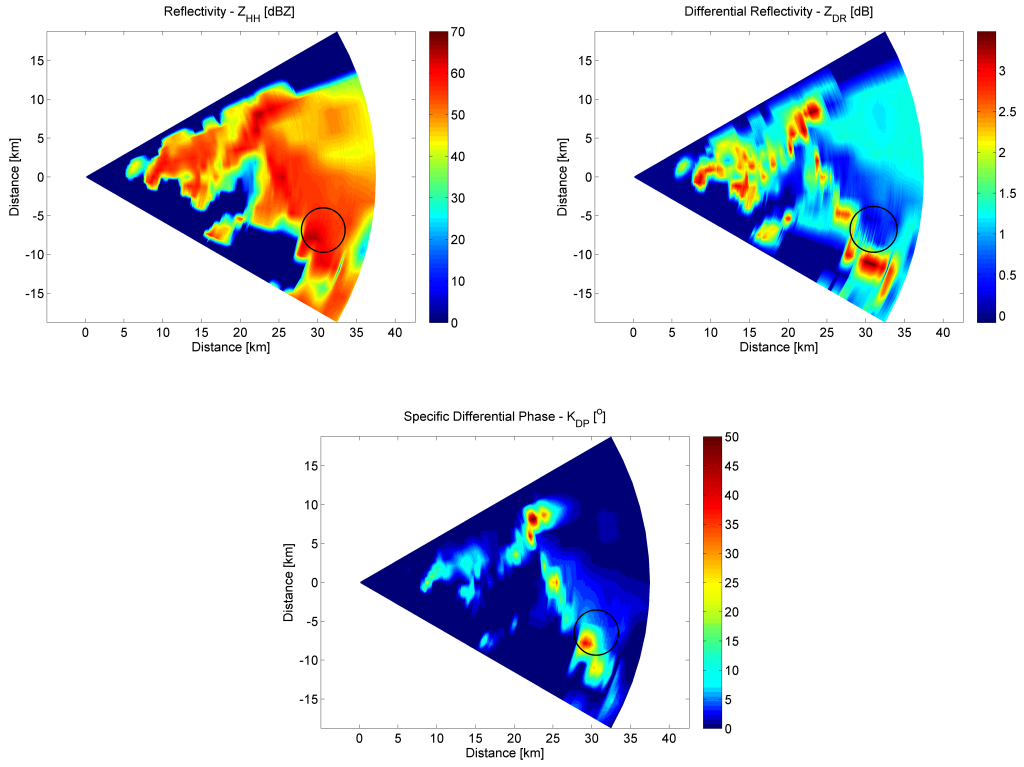


Figure 3.23: Simulated radar returns for PPI scan at altitude 9.2 km. From left to right and top to bottom, (a) Reflectivity - Z_H, (b) Differential reflectivity - Z_{DR}, (c) Specific differential phase - K_{DP}

Chapter 4

Gaussian Mixture Model (GMM) and Classifier

Radar observation variables such as Z_h, Z_{dr} and K_{dp} as well as the underneath microphysics parameters such as R, W, N_0 and Λ of a radar resolution volume (bin) can be combined and considered as an unknown and random vector $\mathbf{x}$, such as $\mathbf{x} = [Z_h, Z_{dr}, K_{dp}, \rho_{hv}]$ or $\mathbf{x} = [N_0, \Lambda, Z_h, Z_{dr}, K_{dp}, A_h, A_{dp}]$. Hydrometeor classification and weather parameters estimation through a Bayesian approach are possible if the distribution of $\mathbf{x}$ is precisely modeled. A Gaussian mixture model (GMM), is introduced in this Chapter to characterize such distribution.

4.1 Definitions

A Gaussian Mixture Model (GMM) is a weighted sum of Gaussian densities that represents a probability density function as given by

$$f(\mathbf{x}) = \sum_{i=1}^{M} \alpha_i \mathcal{N}(\mathbf{x}; \mu_i, \mathbf{\Sigma}_i), \tag{4.1}$$

where $\mathcal{N}(\mu, \mathbf{\Sigma})$ is Gaussian distribution with mean μ and covariance matrix $\mathbf{\Sigma}$ as defined in Eq. (4.2), where d is the dimension of variable $\mathbf{y}$, M is the number of Gaussian mixtures used and α_i, μ_i and $\mathbf{\Sigma}_i$ are the weighting, mean and covariance matrix for the ith Gaussian mixture.

$$\mathcal{N}(\mathbf{y}; \mu, \mathbf{\Sigma}) = \frac{1}{\sqrt{(2\pi)^d |\mathbf{\Sigma}|}} e^{-\frac{1}{2}(\mathbf{y}-\mu)^T \mathbf{\Sigma}^{-1} (\mathbf{y}-\mu)}. \tag{4.2}$$

Note that, $\mu_i \in \mathbb{R}^n$, $\mathbf{\Sigma}_i \in \mathbb{R}^{n \times n}$ is symmetric positive definite ($\mathbf{\Sigma}_i > 0$), $\alpha_i > 0$ and $\sum_{i=1}^{M} \alpha_i = 1$. The mean of a Gaussian mixture is

$$\mu = E[\mathbf{x}] = \sum_{i=1}^{M} = \alpha_i \mu_i \tag{4.3}$$

and the covariance is

$$\mathbf{\Sigma} = VAR[\mathbf{x}] = \sum_{i=1}^{M} \alpha_i (\mathbf{\Sigma}_i + \mu_i \mu_i^T) - \mu \mu^T \tag{4.4a}$$

$$= \sum_{i=1}^{M} \alpha_i (\mathbf{\Sigma}_i + (\mu_i - \mu)(\mu_i - \mu)^T), \tag{4.4b}$$

where $E[.]$ and $VAR[.]$ are the expectation operator and variance operator, respectively. A complete GMM is parameterized by mixture weights α_i, means μ_i and covariance matrices $\mathbf{\Sigma}_i$. These parameters are collectively noted as

$$\theta = \{\alpha_i, \mu_i, \mathbf{\Sigma}_i\} \qquad i = 1, ..., M. \tag{4.5}$$

There are several forms of GMM depending on the choice of parameters shown in Eq. (4.5). Parameters can be tied or shared among the Gaussian mixtures/components, such as having a common weight or common covariance matrix for all components. Parameters may also be constrained, such as having all covariance matrices to be diagonal (Celeux and Govaert 1995). Number of mixtures is also flexible depending on different applications. The choice of GMM configuration is often determined by how GMM parameters are estimated and how GMM is used in particular applications. It is worth mentioning that the overall density function represented by a GMM are modeled by all components in the GMM acting together. Even with the diagonal covariance matrices, the correlations between different dimensions can still be modeled by GMM. In other words, the effect of having a GMM with full covariance matrices can be equally obtained by having a GMM with diagonal covariance matrices. The difference is that having a GMM with diagonal covariance matrices may need a larger number of mixtures. In this study, the general form of GMM is used.

The GMM would converge to any specific distribution as number of mixtures increases. An intuitive proof is given as follows: a Gaussian component with zero covariance matrix is like a spike from the delta function. Having a GMM with an infinite number of such components equals to having infinite delta functions. Since any specific distribution can be represented by infinite delta functions, it can also be represented by a GMM with infinite mixtures. The convergence of the GMM ensures that a large and complex multidimensional distribution can be precisely characterized by a GMM with a large number of mixtures, such as the Universal Background Model (UBM) in speaker recognition systems (Hasan and Hansen 2011).

Another important attributes of the GMM is its ability to form smooth approximations to arbitrarily shaped densities. With the smoothing capability, the GMM is capable of discovering general distribution from an incomplete data set with a finite number of samples.

The convergence and smoothing capabilities of the GMM are illustrated in Fig. 4.1 where a total of 500 samples are generated from $0.6\mathcal{N}(5, 1.5) + 0.4\mathcal{N}(15, 3)$. Shown in Fig. 4.1(a), GMM with 2 mixtures is able to smooth all the fluctuations and discover two main peaks. In this case, the GMM keeps the main shape but ignore local details of the probability density. As number of mixture increases in Fig. 4.1(b)-(d), GMM converges closer to the details. In these cases, while the convergence capability of GMM can be seen, effects of over-fitting are also shown. So, smoothing and convergence of the GMM depend on number of mixtures used in the model. Insufficient number of mixtures may lead to bad approximation while too many mixtures may risk over-fitting to the particular training data set.

GMMs are commonly used to model the probability distribution of continuous features or measurements where there are multiple peaks. For example, vocal spectral features in a speaker/speech recognition system and is often modeled by GMM (e.g.,

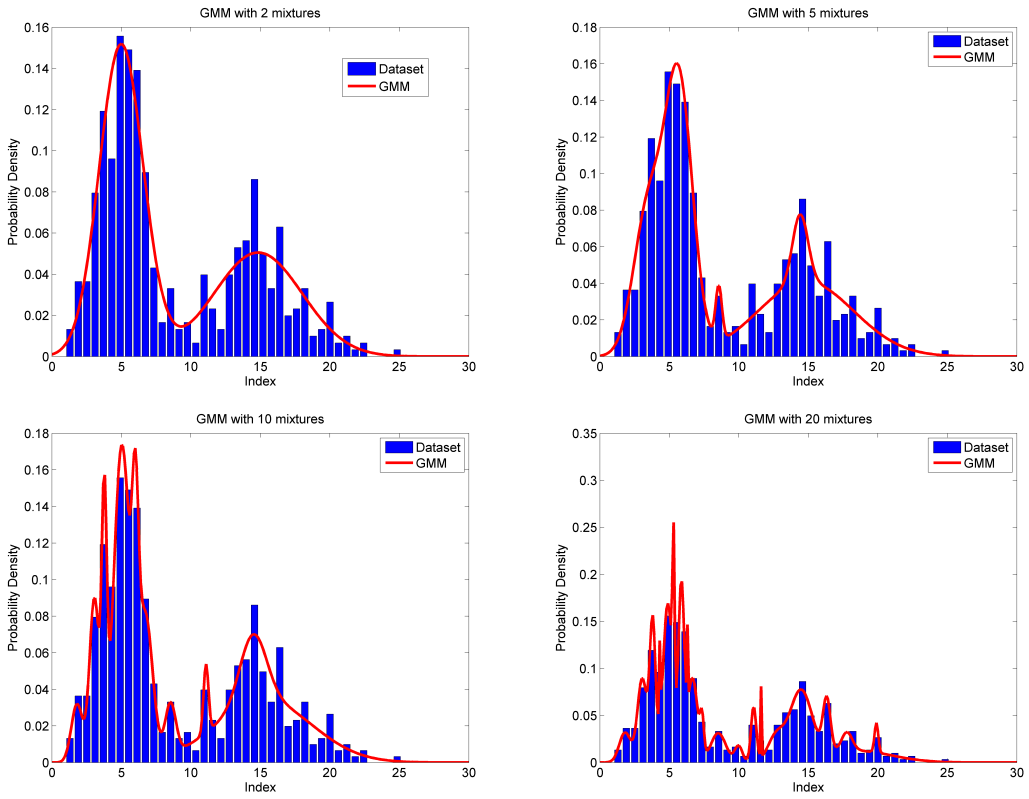


Figure 4.1: Example of GMM with different number of mixtures. Data set is generated from $0.6\mathcal{N}(5, 1.5) + 0.4\mathcal{N}(15, 3)$. From left to right and top to bottom, (a) GMM with 2 mixture; (b) GMM with 5 mixture; (c) GMM with 10 mixture; (d) GMM with 20 mixture;

Gomez and Kawahara 2010; Du et al. 2011). GMMs are also widely used in tracking and navigation systems (e.g., Alspach and Sorenson 1972; Ali-Loytty 2008).

4.2 Training GMMs

4.2.1 The Expectation-Maximization Algorithm

GMM may be trained from any data set. Given a training data set and a GMM configuration which refers to number of mixtures, M, in this study, training GMM is a learning process during which GMM parameters $\theta = \{\alpha_i, \mu_i, \mathbf{\Sigma}_i\}$ are estimated from the training data set. The goal is to find θ which in some sense best matches the distribution embodied in the training data set. In other words, finding θ that specifies the GMM from which the data points in the training dataset are most likely to be drawn. Among the techniques available for estimating the parameters of a GMM (McLachlan and Basford 1988), the most popular and well-established one is the maximum likelihood (ML) method.

The ML method measures the global likelihood of a particular model given the set of data points and maximize it, through a likelihood function $\Lambda(\mathbf{X};\theta)$ where $\mathbf{X} = \{\mathbf{x}_1, \mathbf{x}_2, ..., \mathbf{x}_N\}$ is the set of data points. Λ is maximized for θ such that the GMM $f(\mathbf{x};\theta)$ is mostly to generate the set of data points, $\mathbf{X}$. Assuming that each data point in the set is independent from others, the likelihood function can be defined as follows:

$$\Lambda(\mathbf{X};\theta) = \prod_{n=1}^{N} f(\mathbf{x}_n;\theta) \tag{4.6a}$$

$$= \prod_{n=1}^{N} \sum_{i=1}^{M} \alpha_i \mathcal{N}(\mathbf{x}_n;\mu_i,\mathbf{\Sigma}_i). \tag{4.6b}$$

Then, the estimation problem can be written as

$$\hat{\theta} = \arg\max_{\theta} \Lambda(\mathbf{X};\theta). \tag{4.7}$$

To better present the ML method, $q(i,n)$ is defined as

$$q(i,n) = \alpha_i \mathcal{N}(\mathbf{x}_n; \mu_i, \mathbf{\Sigma}_i), \tag{4.8}$$

which is the probability of data point $\mathbf{x}_n$ from the ith mixture. The conditional probability that point $\mathbf{x}_n$ was generated by the ith mixture component can be calculated from

$$p(i|n) = \frac{q(i,n)}{\sum_{i=1}^{M} q(i,n)}. \tag{4.9}$$

It can be easily shown that $\sum_{i=1}^{M} p(i|n) = 1$, therefore, $p(i|n)$ is also considered as the estimated weighting of the ith mixture component given data point $\mathbf{x}_n$. To characterize the maximum of $\Lambda(\mathbf{X};\theta)$, derivatives of the logarithm of Λ with respect to θ are taken and set to zero as shown in Eq. (4.10).

$$\frac{\partial log[\Lambda]}{\partial \alpha_i} = 0 \tag{4.10a}$$

$$\frac{\partial log[\Lambda]}{\partial \mu_i} = 0 \tag{4.10b}$$

$$\frac{\partial log[\Lambda]}{\partial \mathbf{\Sigma}_i} = 0 \tag{4.10c}$$

Note that, the derivative of $log[\Lambda]$ with respect to weightings α_i of each component (Eq. (4.10a)) cannot be performed directly, since the weightings are constrained to being positive and adding up to one. So, instead of taking derivative with respect to constrained α_i, α_i is written in turn as a function of an unconstrained variable b_i and the derivative of $log[\Lambda]$ is taken with respect to b_i as shown in Eq. (4.11) and Eq. (4.12).

$$\alpha_i = \frac{e^{b_i}}{\sum_{i=1}^{M} e^{b_i}} \tag{4.11}$$

$$\frac{\partial log[\Lambda]}{\partial \alpha_i} = \frac{\partial log[\Lambda]}{\partial b_i} \cdot \frac{\partial b_i}{\partial \alpha_i} = 0 \tag{4.12}$$

Solving Eq. (4.10b), Eq. (4.10c) and Eq. (4.12), the estimations of the weightings, the means, and the covariance matrices of the GMM are obtained as

$$\hat{\alpha}_i = \frac{1}{N}\sum_{n=1}^{N} p(i|n) \tag{4.13a}$$

$$\hat{\mu}_i = \frac{\sum_{n=1}^{N} p(i|n)\mathbf{x}_n}{\sum_{n=1}^{N} p(i|n)} \tag{4.13b}$$

$$\hat{\mathbf{\Sigma}}_i = \frac{\sum_{n=1}^{N} p(i|n)(\mathbf{x}_n - \hat{\mu}_i)(\mathbf{x}_n - \hat{\mu}_i)^T}{d\sum_{n=1}^{N} p(i|n)}, \tag{4.13c}$$

where d is the dimension of variable $\mathbf{x}$.

All three expressions in Eq. (4.13) can be easily understood. Estimated weighting for the ith component $\hat{\alpha}_i$ is the mean/expectation of the conditional probabilities that the set of data points $\mathbf{X}$ were generated by the ith mixture. $\hat{\mu}_i$ and $\hat{\mathbf{\Sigma}}_i$ for the ith component are the mean and covariance of the data set, weighted by the conditional probability that point $\mathbf{x}_n$ was generated by the ith mixture component. However, these three equations are not mutually independent, because GMM parameters $\hat{\alpha}_i$, $\hat{\mu}_i$ and $\hat{\mathbf{\Sigma}}_i$ are estimated based on the values of $p(i|n)$ which depends on those parameters.

Since Eq. (4.13) cannot be solved directly, the Expectation-Maximization (E-M) Algorithm, an iterative optimization method, provides a solution. The basic idea is to start with a first guess of θ, calculate $p(i|n)$, refine $\hat{\theta}$, calculate new $p(i|n)$ and so forth. The algorithm will stop until the global likelihood Λ cannot be increased. Proof of the convergence of the E-M algorithm can be found in Dempster et al. (1977) and McLachlan and Krishnan (2008). Detailed procedures of the E-M algorithm are summarized as follows:

Assume that the kth estimates of parameters θ are available and noted as $\alpha_i^{(k)}$, $\mu_i^{(k)}$ and $\mathbf{\Sigma}_i^{(k)}$, conditional probabilities $p^{(k)}(i|n)$ are obtained in the E step and new estimates of $\alpha_i^{(k+1)}$, $\mu_i^{(k+1)}$ and $\mathbf{\Sigma}_i^{(k+1)}$ are obtained in the M step.

- E Step:

$$p^{(k)}(i|n) = \frac{\alpha_i^{(k)} \mathcal{N}(\mathbf{x}_n; \mu_i^{(k)}, \mathbf{\Sigma}_i^{(k)})}{\sum_{i=1}^{M} \alpha_i^{(k)} \mathcal{N}(\mathbf{x}_n; \mu_i^{(k)}, \mathbf{\Sigma}_i^{(k)})}. \tag{4.14}$$

- M Step:

$$\alpha_i^{(k+1)} = \frac{1}{N} \sum_{n=1}^{N} p^{(k)}(i|n), \tag{4.15a}$$

$$\mu_i^{(k+1)} = \frac{\sum_{n=1}^{N} p^{(k)}(i|n) \mathbf{x}_n}{\sum_{n=1}^{N} p^{(k)}(i|n)}, \tag{4.15b}$$

$$\mathbf{\Sigma}_i^{(k+1)} = \frac{\sum_{n=1}^{N} p^{(k)}(i|n)(\mathbf{x}_n - \hat{\mu}_i)(\mathbf{x}_n - \hat{\mu}_i)^T}{d \sum_{n=1}^{N} p^{(k)}(i|n)}. \tag{4.15c}$$

Given an initial estimate $\alpha_i^{(0)}$, $\mu_i^{(0)}$ and $\mathbf{\Sigma}_i^{(0)}$, E-M iterates the E step and M step until it reaches the situation where the logarithm of the new global likelihood $\Lambda(\mathbf{X}; \theta^{(k+1)})$ equals to the logarithm of the previous global likelihood $\Lambda(\mathbf{X}; \theta^{(k)})$. In this study, E-M is considered converged if Eq. (4.16) is satisfied.

$$\frac{log[\Lambda(\mathbf{X}; \theta^{(k+1)})]}{log[\Lambda(\mathbf{X}; \theta^{(k)})]} < 1 - 10^{-10} \tag{4.16}$$

Note that, smooth approximations to arbitrarily shaped densities from GMM may be achieved by choosing a larger threshold than the one (10^{-10}) used in Eq. (4.16). Example of training GMMs using E-M with different thresholds is illustrated in Fig. 4.2. With the same configuration (6 mixtures), the GMM with larger threshold 10^{-4} in Fig. 4.2(a) managed to preserve the general shape of the probability density while the GMM with smaller threshold 10^{-10} converged much closer to the details. Depends on training data sets and applications, different thresholds may be used in E-M for different purposes. In this study, threshold is fixed at 10^{-10} but number of mixtures varies while training GMMs.

It can be proven that E-M would reach a local maximum in likelihood. In same rare cases, it could reach a local minimum (Russell and Norvig 2009). Since how

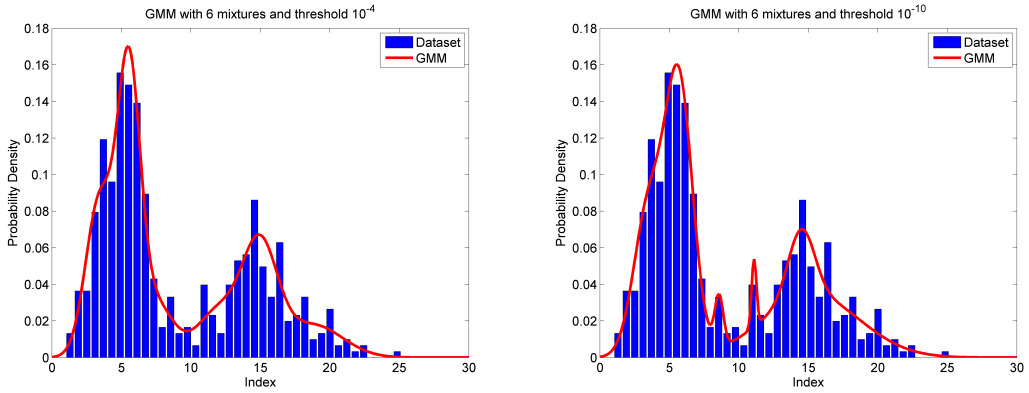


Figure 4.2: Example of training GMMs with different thresholds. Data set is generated from $0.6\mathcal{N}(5, 1.5) + 0.4\mathcal{N}(15, 3)$. From left to right, (a) GMM with 6 mixture and threshold 10^{-4}; (b) GMM with 6 mixture and threshold 10^{-10}.

E-M converges depends on the initial values $\alpha_i^{(0)}$, $\mu_i^{(0)}$ and $\mathbf{\Sigma}_i^{(0)}$, initial clustering of the data set is essential in training GMMs. Better initial clustering would lead to better initial guess of θ which leads to faster convergence to better local maximum or even global maximum point. In this study, the k-means clustering algorithm is used in initial clustering of the training data sets. Details of the k-means algorithm are given in section 4.2.2. There is another point to notice. The log likelihood for the final trained GMM may exceed that of the original model, from which the data were generated. It simply reflects the fact that incomplete data set with a finite number of data points might not provide an exact reflection of the underlying model (Russell and Norvig 2009).

4.2.2 The k-means Clustering Algorithm

Data clustering is to group objects in such a way that objects in one group are more similar than objects in other groups. Data clustering is different from classification. In data clustering, there is no predefined class though classes may be defined after

clustering. Clustering algorithms vary for different data types and different measurement of similarity between objects. The k-means clustering algorithm, which is one of the most famous clustering algorithms, falls in to the center-based clustering algorithm category.

The k-means algorithm is an iterative approach, where two phases are involved: the initialization phase and the iteration phase. In the initialization phase, data points are randomly assigned into k groups/clusters. In the iteration phase, distance between each data point and the mean of each group is computed and each data point is then assigned to the nearest group. Mean of a group is updated after all data points have been assigned. The algorithm will stop until no further changes of group membership after one iteration. Details of the k-means algorithm go as follows:

Same as section 4.2.1, let $\mathbf{X} = \{\mathbf{x}_1, \mathbf{x}_2, ..., \mathbf{x}_N\}$ be a data set with n data points. Let g_1, g_2,..., g_k be the k disjoint group/cluster of $\mathbf{X}$ and $\mu(g_i)$ is the center/mean of cluster g_i. $d_{n,i}$ is denoted as the distance between data point $\mathbf{x}_n$ and center $\mu(g_i)$. The choice of distance measures is flexible, depending on different data sets. In this study, the Euclidean distance is used.

- Initialization
  1. Randomly assign data point x_n into group g_i.
  2. Compute $\mu(g_i)$.
- Iteration
  3. Compute $d_{n,i}$ for all data points and groups.
  4. Find $c_n = \arg\min_{1 \le i \le k} d_{n,i}$.
  5. Assign data point x_n to a group according to c_n
  6. Recompute $\mu(g_i)$.
  7. Repeat 3-6 until no further changes of group membership after one iteration.

The k-means algorithm has some important properties (Gan et al. 2007): (1) it is efficient and fast; (2) it often terminates at a local maximum and its performance

depends on the initial groups; (3) the clusters have convex shapes, such as a ball in three-dimensional space. As a result of the dependence on the initialization, selecting good initial centers/groups are crucial for the k-means algorithm. Pena et al. (1999) compares four initialization methods and shows that the random and the Kaufman initial values (Kaufman and Rousseeuw 1990) outperform the rest of the compared methods as they make the k-means more effective and more independent on initial clustering and on instance order. In this study, the random initialization method is used. Since the k-means algorithm is fast, it is possible to perform k-mean clustering several times, compare the outputs, such as the total distance or total variance, and choose the best result. In this study, the best result which is the one with least total distance is chosen from 5 k-means clustering replicates.

Fig. 4.3 shows an example of clustering using k-means algorithm. Four clusters are generated from Gaussian distribution with variance 1 at both dimensions. The centers of the four clusters are $[2, 0]$, $[-2, 0]$, $[0, 2]$, $[0, -2]$, respectively. As shown in Fig. 4.3(b), the k-means algorithm does a good job as the centroid of each cluster is close to the original one despite there are some points that are grouped into a wrong cluster.

It is easy to see that the k-means algorithm and the E-M algorithm share a lot in common, such as their dependency on initial values and the way they update the clusters/Gaussian mixtures in one iteration. Actually, the E-M algorithm can be considered as one of the variation forms of the k-means algorithm (Gan et al. 2007).

4.3 GMM-based Hydrometeor Classification

Dual-polarized weather radar systems can offer the capability to detect and identify different classes of hydrometeors (e.g., Vivekanandan et al. 1999; Zrnić et al. 2001; Lim et al. 2005; Ryzhkov et al. 2005b; Marzano et al. 2007). Most hydrometeor classification techniques are developed based on fuzzy logic approach which is flexible and

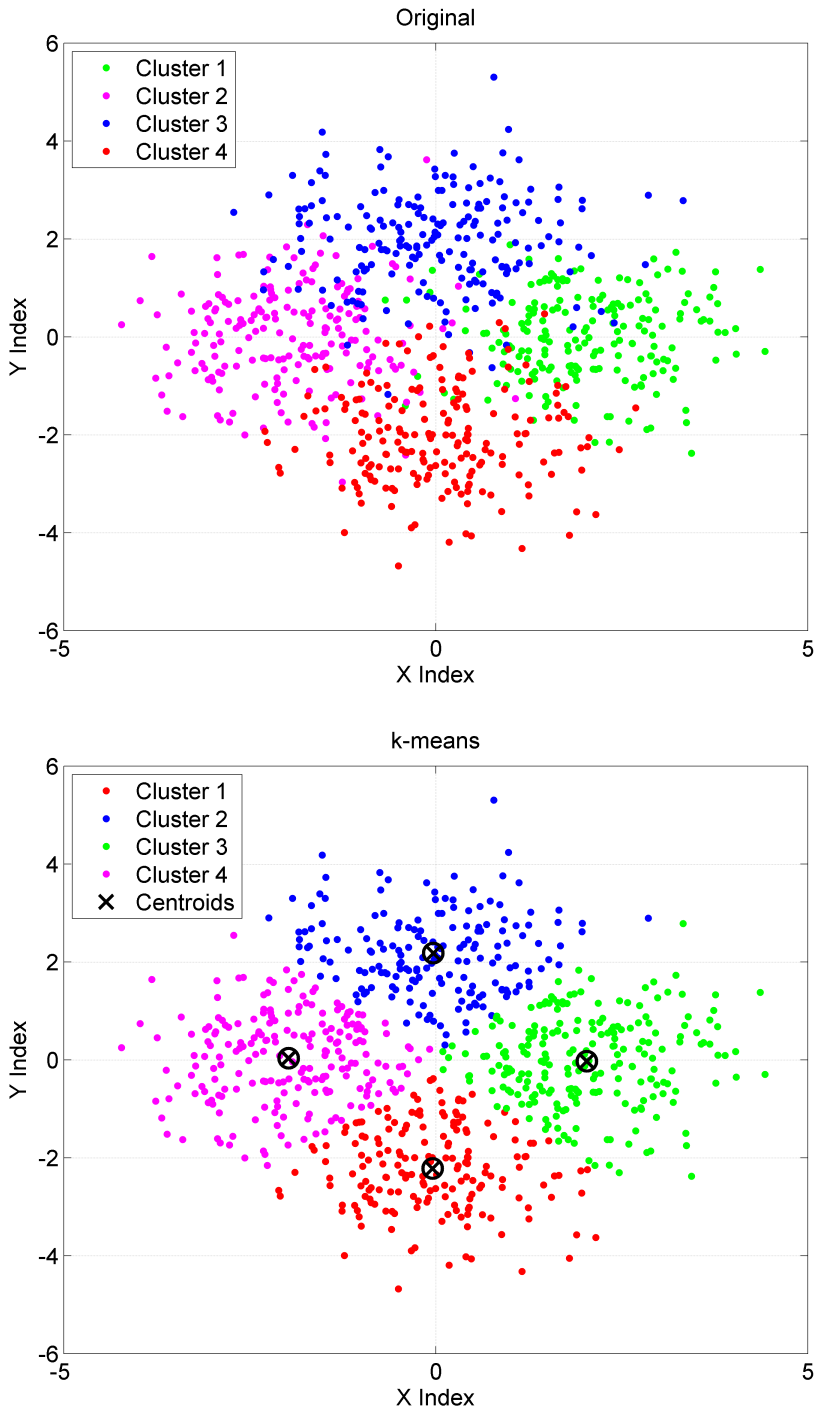


Figure 4.3: Example of clustering using k-means algorithm. Four clusters are generated from Gaussian distribution with variance 1 at both dimensions. The centers of the four clusters are $[2, 0]$, $[-2, 0]$, $[0, 2]$, $[0, -2]$, respectively. From top to bottom, (a) Original Clusters; (b) Clusters from k-means.

able to adapt to different membership functions (MBF), either developed from experimental evidences or simulations. The GMM may be considered as a superset of the fuzzy logic approach, since MBFs in a fuzzy logic approach can be approximated and modeled by a GMM. Thus, the performance of a GMM-based hydrometeor classifier would at least match the performance of any fuzzy logic approach.

The classification problem can also be approached by different techniques, such as the Bayesian approach and the Neural Network (NN) approach. The Bayesian approach is based on the *maximum a posteriori* (MAP) probability decision rule. Compared with the fuzzy logic approach, the Bayesian approach is capable of modelling the joint distribution of different variables while fuzzy logic approach cannot properly model the cross correlations among different variables/dimensions. Being able to model the cross correlations among different variables, the Bayesian approach processes the polarimetric radar measurements more efficient than the fuzzy logic approach, which would lead to better performance. Shown in Marzano et al. (2008), the Bayesian approach has better accuracy than their previously developed fuzzy logic approach (Marzano et al. (2007)) for C-band. Note that, both the Bayesian approach in Marzano et al. (2008) and Marzano et al. (2007) are developed from the same data set generated from simulations.

Same as the MBF for each hydrometeor class, the crucial step is to model the prior probability density function (PDF) for each class. A multidimensional Gaussian PDF is usually used, as it may simplify the mathematical treatment of the Bayesian problem (e.g., Richards and Jia 1999; Lillesand 2006). The Gaussian assumption does not have a theoretical foundation nor observational foundation. The choice of the Gaussian PDF is based on the assumptions that the polarimetric signatures of hydrometeor classes are hyperellipsoids in the multidimensional observation space. Shown in Fig. 3.11, the polarimetric signatures of hydrometeor classes tend to have arbitrary shapes other than hyperellipsoids and may vary if different physical models

are used. Thus, the Gaussian assumption may not hold especially when more dual-pol variables are included. GMM-based Bayesian classifiers are not limited by the Gaussian assumption. While enjoying the mathematical benefits from Gaussian density function, the prior PDFs of each hydrometeor class can also be precisely modeled by the GMM.

Most hydrometeor classification algorithms are developed from simulations (e.g., Straka et al. 2000; Zrnić et al. 2001; Lim et al. 2005). A polarimetric radar simulator can provide physically representative training data sets for different hydrometeor classes if proper models are used. Compared with measurement data sets, simulation data sets are often clean data with ground truth, without noise and contaminations from other species. Though simulation data sets may suffer from the physical models/assumptions that has been used, they have the freedom to choose specific models that are suitable for special applications. While there is no explicit boundary in nature, four rain classes may be defined, such as large drops, light rain, medium rain and heavy rain, for rainfall rate estimation applications. Different physical models, such as different DSD models, raindrop shape models and terminal velocity models, may be adopted to generate polarimetric signatures for those four rain classes. Similarly, two classes may be defined for hail, such as large hail and small hail/graupel. According to different melting levels and shapes, snow may be group into dry snow, wet snow or ice crystals. Moreover, mixing species may be defined, such as rain/hail mixture. Different classes and physical models may be adopted to serve different interests. In this study, five classes of hydrometeors are considered to assist the development of the All-Weather Sense-and-Avoid radar for unmanned aero-vehicles (UAV). They are rain, snow, melting snow, hail and melting hail.

4.3.1 Bayesian Classification Theory

A Bayesian classifier assigns a hydrometeor class according to its conditional posterior probabilities $p(c_i|\mathbf{x})$ where c_i refers to hydrometeor classes and $\mathbf{x}$ is a radar observation vector that consists of dual-pol variables. The classification rule, which is also known as maximum-likelihood rule, is quite intuitive, as the hydrometeor class is obtained by the index c_i that maximizes the conditional posterior probability

$$\mathbf{x} \in c_i <=> p(c_i|\mathbf{x}) > p(c_j|\mathbf{x}) \quad \forall j \neq i. \tag{4.17}$$

However, conditional posterior probabilities are usually unknown. From Bayes theorem, posterior probabilities can be calculated from prior probabilities and conditional likelihood PDF, which is

$$p(c_i|\mathbf{x}) = \frac{p(c_i)p(\mathbf{x}|c_i)}{p(\mathbf{x})}. \tag{4.18}$$

Prior probability of hydrometeor class c_i, $p(c_i)$, is set equal here for all classes, even though they are likely different from each other in different temperatures and environment. Also, $p(\mathbf{x})$ is assumed constant with respect to c_i. $p(\mathbf{x}|c_i)$, which is the priori PDF of hydrometeor class c_i, is approximated here using multidimensional GMM as given by

$$p(\mathbf{x}|c_i) = \sum_{m=1}^{M} \alpha_m^{(i)} \mathcal{N}(\mathbf{x}; \mu_m^{(i)}, \mathbf{\Sigma}_m^{(i)}), \tag{4.19}$$

where $\mathcal{N}(\mu, \mathbf{\Sigma})$ is Gaussian distribution defined in Eq. (4.2), M is total number of Gaussian mixtures and $\alpha_m^{(i)}$, $\mu_m^{(i)}$ and $\mathbf{\Sigma}_m^{(i)}$ are the weighting, mean and covariance matrix for the mth Gaussian mixture of hydrometeor class c_i. Therefore, the classifier assigns each observation a class by maximizing the conditional prior probability, as given in Eq. (4.20).

$$\mathbf{x} \in c_i <=> p(\mathbf{x}|c_i) > p(\mathbf{x}|c_j) \quad \forall j \neq i. \tag{4.20}$$

4.3.2 Hydrometeor Hazard Detection for Airborne Sense and Avoid Radar

Sense-and-Avoid is becoming a key capability for the future operations of unmanned aero-vehicles (UAV). Although the GPS and satellite links can provide relayed ground radar data, the space and time resolutions are not sufficient for critical safety applications. Also, the pilots (human or automatic) need a comprehensive picture of hazard, including both weather and collision objects, in order to make timely and efficient decisions. Using multiple frequency bands, different antenna polarizations and other diversities is the solution to achieve fast-scanning, multiple functions, and deeper insight into hazard physics (Zhang et al. 2008). On the other hand, the diversities of antenna system raise a true challenge on how to calibrate, interpret, and understand these data intelligently. This study assumes airborne radar with multiple receiving channels and dual-polarization is used as the key sensor for hazard detection. The proposed airborne radar system also has to perform in various situations where types, shapes and sizes of hydrometeors may vary significantly, like in summer rain environment or winter storm environment, or in low altitude as well as high altitude, bringing more challenges to the hazard detection system.

One well-known difficulty for aerospace hydrometeor hazards detection is the lack of knowledge of radar signatures for different kind of hydrometeor hazards at X-band, which is widely used by airborne weather radar. The single-cell Monte Carlo simulation introduced in Chapter 3 is used to generate realistic radar signatures for five hydrometeor classes including rain, snow, melting snow, hail and melting hail. Table 4.1 lists the detailed mixing ratio and melting ratio ranges used in the simulations and Table 3.8 lists the details of DSD parameter for different hydrometeor species. Frequency of the simulation is set at 9.41 GHz to match the hardware system under development, and it can be easily changed or extended to dual-frequency applications. Outputs of the simulation are equivalent reflectivity factor at both horizontal

and vertical polarization ($Z_{H,V}$), differential reflectivity (Z_{DR}), specific differential phase (K_{dp}), correlation coefficients (ρ_{hv}) and specific attenuation ($A_{h,v}$). In order to have a statistical significance, a set of 10,000 scenarios for each species have been carried out. Only one species out of the five species is generated in each scenario. In other words, simulation outputs of each case are clear data for that particular hydrometeor species. Scatter plots of Z_H and Z_{DR} as well as Z_H and ρ_{hv} are shown in Fig. 4.4.

Table 4.1: Mixing and Melting Ratio Ranges used in the Single-Cell Simulations. (M for Melting)

	Rain	Snow	Hail	MSnow	MHail
Mixing ratio [g kg^{-1}]	0 - 12	0 - 12	0 - 12	0 - 3	0 - 5
Melting ratio	0	0	0	0 - 0.3	0 - 0.5

The GMM-based detection and classification scheme introduced in 4.3.1 has been applied here for hydrometeor hazard detection. Radar observation vector is set as $\mathbf{x} = [Z_H, Z_{DR}, K_{dp}, \rho_{hv}]^T$, class index c_i where $i = 1, ..., 5$ refers to the five hydrometeor classes. Five GMMs, one for each hydrometeor class, are used. Number of mixtures in each GMM is $M = 4$. $\alpha_m^{(i)}$, $\mu_m^{(i)}$ and $\mathbf{\Sigma}_m^{(i)}$ for each hydrometeor class are trained by using the E-M algorithm introduced in section 4.2.1. Fig. 4.5 shows the GMM model for rain in Z_H and Z_{DR} dimensions. By comparing it with the scatter plot (Fig. 4.4(a)), it can be seen that GMM model well presents the original distribution. Data from simulation has been randomly divided into two parts. 80% data for training and 20% data for testing. Table 4.2 lists the accuracy of this classifier. As is shown, the classifier does a good job in distinguishing rain, snow and hail but makes some mistakes when telling if snow/hail is melting. This situation may be improved by including temperature information as input to the GMM-based classifier.

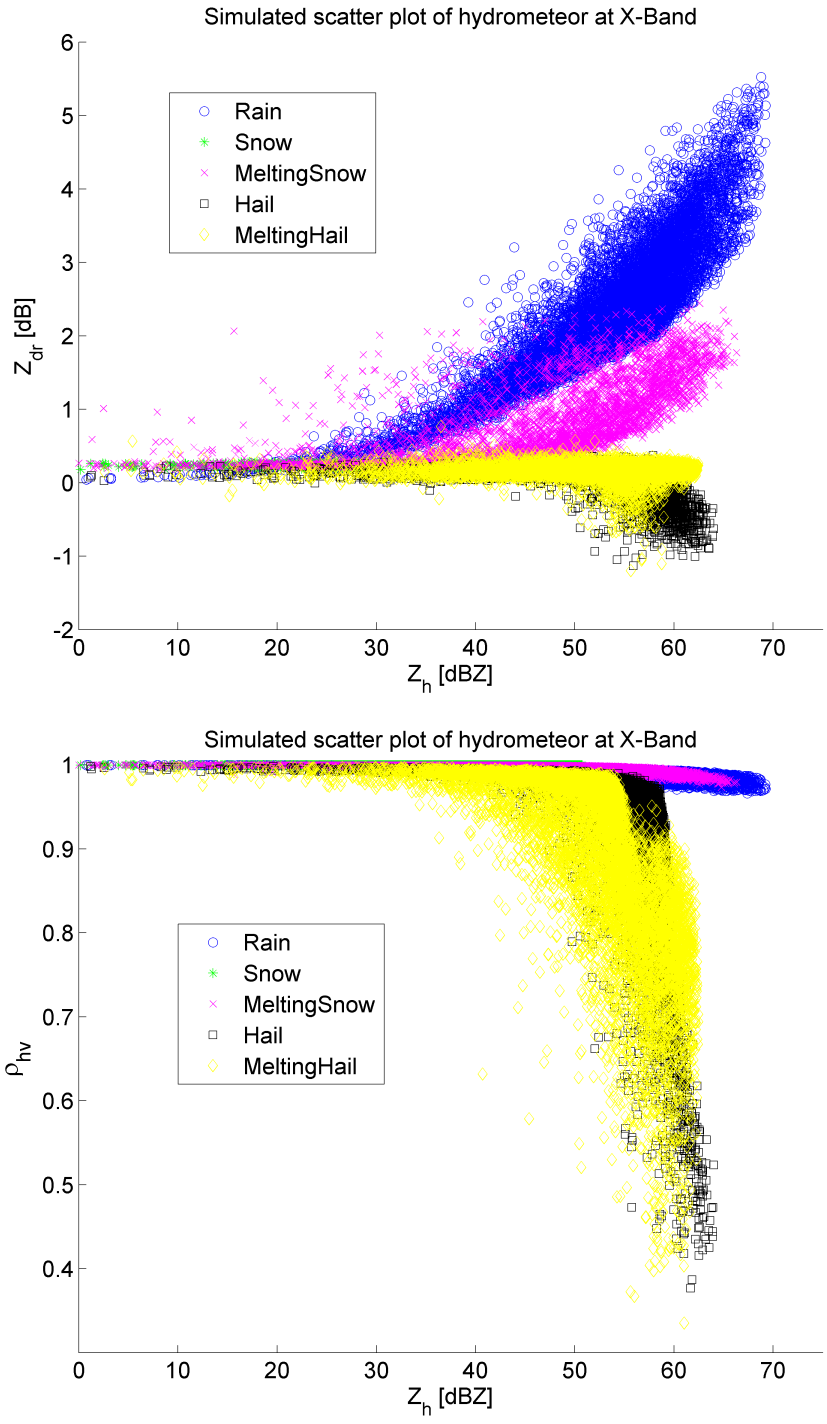


Figure 4.4: Scatter plots of hydrometeor species at 10 GHz. From top to bottom, (a) Z_H and Z_{DR} plot, (b) Z_H and ρ_{hv} plot.

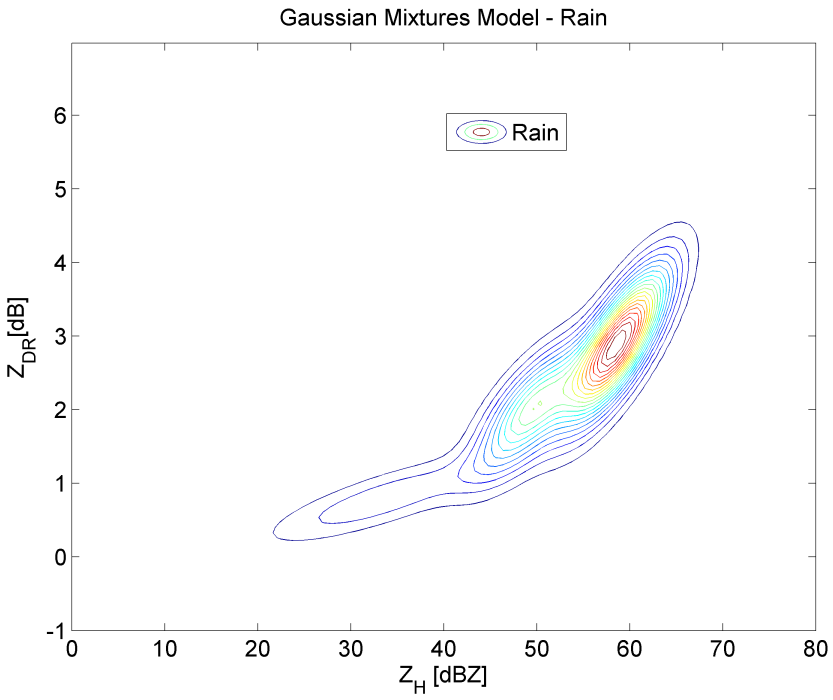


Figure 4.5: Approximate distribution from GMM for rain (Z_H and Z_{DR}).

Table 4.2: Classification accuracy of GMM model for airborne radar system (X-band). (M for Melting)

	Rain	Snow	MSnow	Hail	MHail
Rain	**0.9855**	0.0075	0.005	0	0.002
Snow	0	**0.798**	0.202	0	0
MSnow	0.044	0.3515	**0.6045**	0	0
Hail	0	0	0.002	**0.6695**	0.3285
MHail	0.0005	0	0.001	0.161	**0.8375**

4.3.3 Hail Hazard Detection

Detection accuracy shown in Table 4.2 is results for 'clear' data, which means only one species existing in a radar resolution volume. However, in a real weather field, there are usually more than one species considering the huge size of one radar resolution volume. Therefore, performance of the system needs to be inspected in simulated weather field where different species mixes with each other. As attenuation in X-band cannot be ignored, how attenuation affects the system also need to be examined. Since the hazards detection system is expected to detect dominant hail species from rain or snow background, only three species including rain, snow and hail are considered (melting hail or melting snow are considered as hail or snow, respectively).

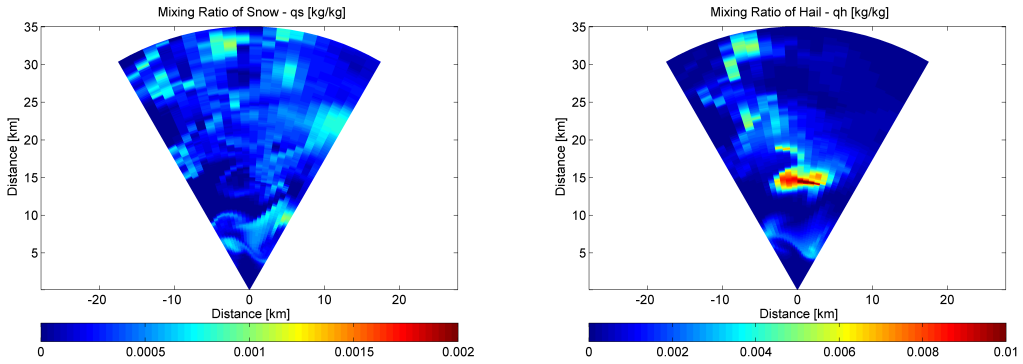


Figure 4.6: Weather field at about 11 km within the stratosphere for case one. From left to right, (a) Mixing ratio of snow; (b) Mixing ratio of hail.

As airplane would fly in different layers in the atmosphere, two cases generated from ARPS model (section 3.6) are studied. Simulated radar returns includes Z_H, Z_{DR}, K_{dp} and ρ_{hv} are used as input to hazards detection system. Plots of Z_H with and without attenuation are shown in Fig. 4.7 and Fig. 4.10. In case one, A PPI scan is generated at about 11 km within the stratosphere where only snow and hail exist. Fig. 4.6 shows the weather field for this case. In case two, simulated PPI scan is generated within a melting layer where weather conditions are more complicated.

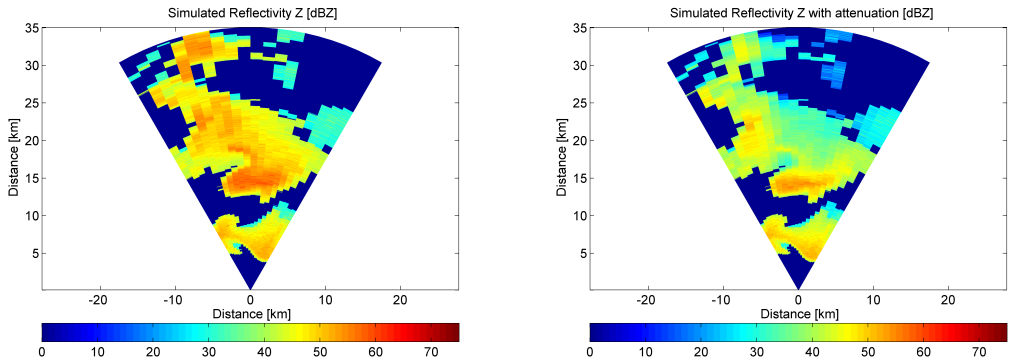


Figure 4.7: Simulated PPI scan for case one (with and without attenuation). From left to right, (a) Simulated reflectivity; (b) Simulated reflectivity with attenuation.

Not only rain but also hail and wet melting hail exist in this layer. Fig. 4.9 show the weather field for case two.

In case one, in front of the radar there is a large snow mixing hail area. Although the snow-mixing ratio is not high, at about 15 km ahead of the airplane, there is a region with very high hail density as shown in Fig. 4.6(b). In simulated PPI scans with and without attenuation (Fig. 4.7), attenuation effects that lead to 3 to 5 dB difference in reflectivity are shown. As shown in the hazard detection results (Fig. 4.8), the classifier performs very well in this case. When no attenuation in radar returns, the classifier picks up almost all the region where hailstone exists and labels out other snow area. Results completely match the underneath weather field. Even when radar returns are affected by attenuation, though it makes some mistakes (labels some area as rain), the classifier is still able to identify most of the hail regions.

In case 2, in front of the radar there is a large rain mixing hail area. Rain mainly locates at the left side while hail is everywhere. Both mixing ratios of rain and hail are very high at about 15 km ahead of the airplane as shown in Fig. 4.9. Shown in simulated PPI scans with and without attenuation (Fig. 4.10), reflectivity attenuates greatly after the high rain-hail density area. There is about 20 dB difference. As

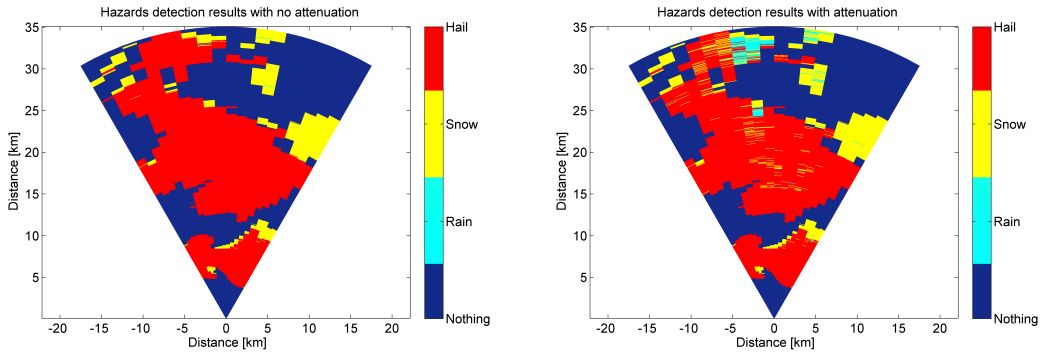


Figure 4.8: Hazards detection results for case one (with and without attenuation). From left to right, (a) Hazard detection results with no attenuation; (b) Hazard detection results with attenuation.

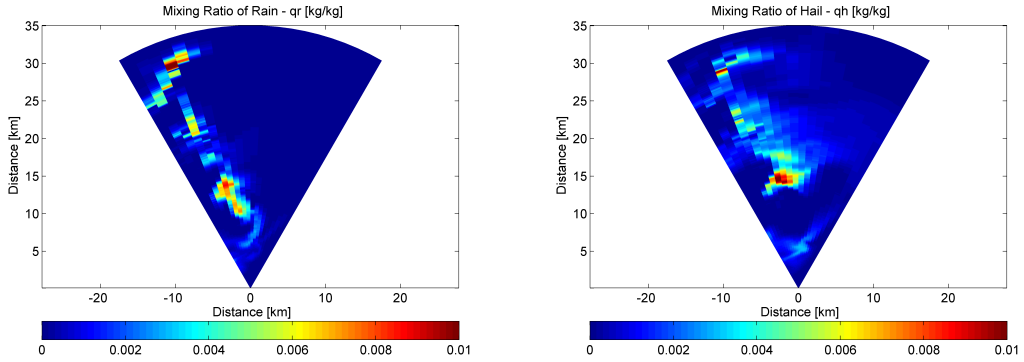


Figure 4.9: Weather field for case two. From left to right, (a) Mixing ratio of rain; (b) Mixing ratio of hail.

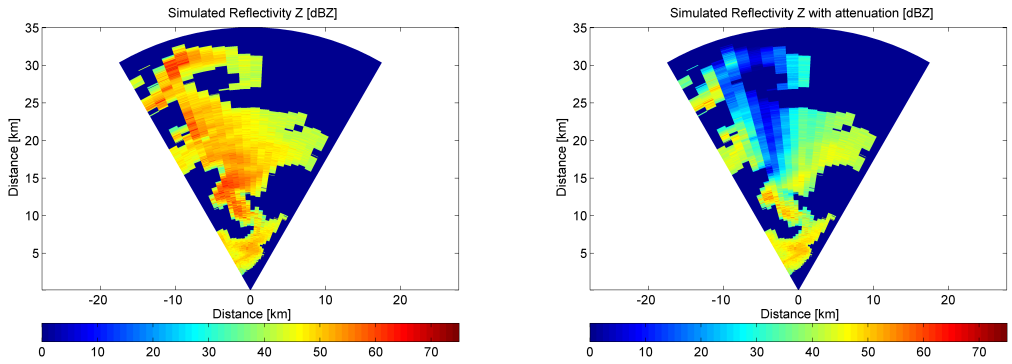


Figure 4.10: Simulated PPI scan for case two (with and without attenuation). From left to right, (a) Simulated reflectivity; (b) Simulated reflectivity with zttenuation.

shown in Hazards detection results (Fig. 4.11), the classifier also performs well for this case. When no attenuation in radar returns, the classifier identifies most regions where hail is the dominant species except the high rain-hail density area. This is acceptable since the model is trained from 'clear' data. It works well in areas where one species is dominant but it is hard to predict when no dominant species exists. Similar conclusion may be drawn from Fig. 4.12 where hail hazard detection ratio at different hail mixing ratio levels is shown. It can be seen that, the GMM classifier is able to detect hail hazard even at very low hail mixing ratio level. Since in this case, there is a large high rain-hail density area where mixing ratios of rain and hail are both high, hail detection ratio decreases as hail mixing ratio increases. This problem may be solved by defined a rain-hail mixture class where both hail and rain are mixed at different mixing levels. Performance of the GMM classifier is degraded when radar measurements are contaminated by high attenuation. Attenuation correction using the Gaussian mixture parameter estimator (GMPE) is discussed in Chapter 5.

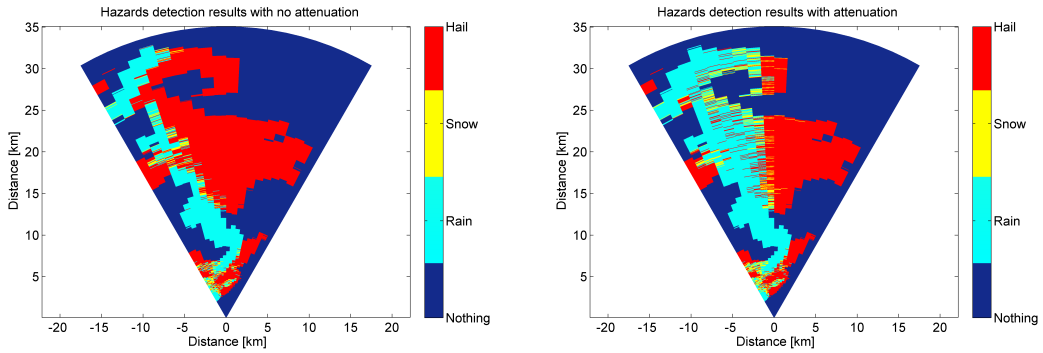


Figure 4.11: Hazards detection results for case two (with and without attenuation). From left to right, (a) Hazard detection results with no attenuation; (b) Hazard detection results with attenuation.

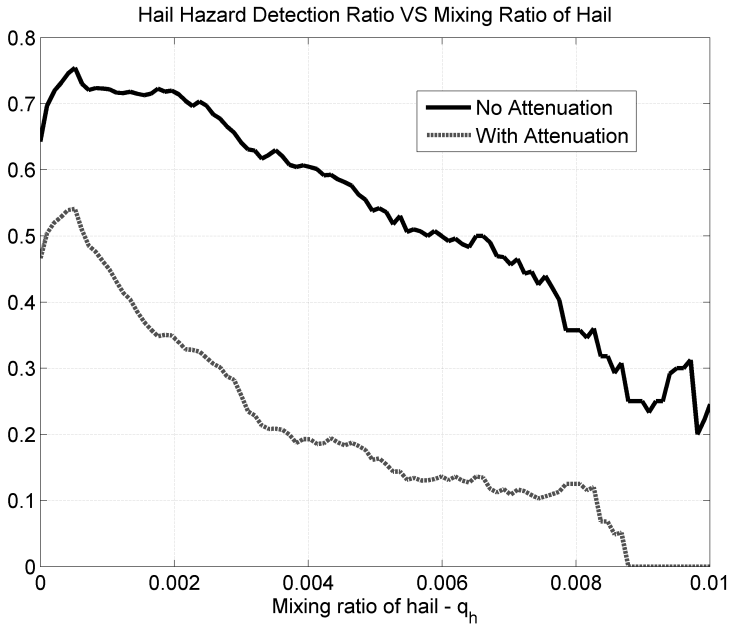


Figure 4.12: Hail hazards detection ratio at different hail mixing ratio levels for case two with and without attenuation.

Chapter 5

Gaussian Mixture Parameter Estimator (GMPE)

If polarimetric radar measurements are denoted as vector $\mathbf{z}$, the weather parameter estimation problem can be simplified as finding the connections between observation $\mathbf{z}$ and parameters of interests $\mathbf{x}$. There are mainly three kinds of estimation approaches. Many conventional polarimetric approaches assume PLRs between $\mathbf{z}$ and $\mathbf{x}$ and use linear regression models (e.g., Gorgucci et al. 2002; Bringi et al. 2004; Cifelli et al. 2011; Ryzhkov et al. 2005a). Neural network approaches consider a black box that has $\mathbf{z}$ as input and $\mathbf{x}$ as output (e.g., Vulpiani et al. 2006, 2009). Bayesian probability approaches try to estimate $\mathbf{x}$ from maximizing the posterior probability $p(\mathbf{x}|\mathbf{z})$ (e.g., Evans et al. 1995; Di Michele et al. 2005; Chiu and Petty 2006; Cao et al. 2010). Gaussian mixture parameter estimator falls into the third category. Different from other Bayesian approaches, the prior distribution of $\mathbf{x}$ can be precisely modeled by a GMM in the GMPE approach. Thus, the GMPE approach is a "best" estimator in terms of minimum-variance and unbiased performance.

5.1 Theoretical fundamentals

5.1.1 Derivation

Microphysics parameters such as R, W, N_0 and Λ and the corresponding radar variables such as Z_h, Z_{dr} and K_{dp} of a radar resolution volume (bin) can be combined

and considered as an unknown and random vector (called state vector) $\mathbf{x}$, such as $\mathbf{x} = [R, Z_h, Z_{dr}]$ or $\mathbf{x} = [N_0, \Lambda, Z_h, Z_{dr}, K_{dp}, A_h, A_{dp}]$. The prior knowledge of $\mathbf{x}$ (or prior distribution) is denoted as $p(\mathbf{x})$. As shown in Chapter 4, $p(\mathbf{x})$, can be learned and represented by the Gaussian mixture model as follows:

$$p(\mathbf{x}) = \sum_{i=1}^{M} \alpha_i \mathcal{N}(\mathbf{x}; \mu_i, \mathbf{\Sigma}_i), \tag{5.1}$$

where $\mathcal{N}(\mu, \mathbf{\Sigma})$ is Gaussian distribution with mean μ and covariance matrix $\mathbf{\Sigma}$ as defined in Eq. (4.2), M is the number of Gaussian components and α_i, μ_i and $\mathbf{\Sigma}_i$ are the weighting, mean and covariance matrix for the ith Gaussian component. If $\mathbf{x} \in \mathbb{R}^n$, then $\mu_i \in \mathbb{R}^n$ and $\mathbf{\Sigma}_i \in \mathbb{R}^{n \times n}$.

If radar measurements are denoted as observation vector $\mathbf{z}$, such as $\mathbf{z} = [Z_h, Z_{dr}, K_{dp}]$ or $\mathbf{z} = [Z_{dr}, \rho_{hv}]$, the estimation problem can be formulated based on a linear relationship:

$$\mathbf{z} = \mathbf{H}\mathbf{x} + \mathbf{v}, \tag{5.2}$$

where $\mathbf{v}$ is sensor noise vector. If $\mathbf{z} \in \mathbb{R}^m$, then $\mathbf{v} \in \mathbb{R}^m$ and $\mathbf{H} \in \mathbb{R}^{m \times n}$. Normally, $m < n$. Matrix $\mathbf{H}$ links state vector to observation and can be easily modified to accommodate different observation variables.

According to Bayesian theorem, conditional distribution $p(\mathbf{x}|\mathbf{z})$, also known as the posterior distribution, yields

$$p(\mathbf{x}|\mathbf{z}) = \frac{p(\mathbf{z}|\mathbf{x})p(\mathbf{x})}{p(\mathbf{z})}. \tag{5.3}$$

Since $p(\mathbf{x})$ is known, $p(\mathbf{x}|\mathbf{z})$ can be obtained if $p(\mathbf{z})$ and $p(\mathbf{z}|\mathbf{x})$ are acquired. Assume state vector $\mathbf{x}$ and noise vector $\mathbf{v}$ are uncorrelated, which is usually true, $p(\mathbf{z}|\mathbf{x})$ equals

$$\begin{aligned} p(\mathbf{z}|\mathbf{x}) &= p(\mathbf{H}\mathbf{x} + \mathbf{v}|\mathbf{x}) \\ &= p(\mathbf{v}) = p(\mathbf{z} - \mathbf{H}\mathbf{x}|\mathbf{v}). \end{aligned} \tag{5.4a}$$

If measurement noise $\mathbf{v}$ is modeled as white Gaussian noise from $\mathcal{N}(0, \mathbf{R})$ then $p(\mathbf{z}|\mathbf{x})$ yields

$$p(\mathbf{z}|\mathbf{x}) = \mathcal{N}(\mathbf{z} - \mathbf{H}\mathbf{x}; 0, \mathbf{R}) = \mathcal{N}(\mathbf{z}; \mathbf{H}\mathbf{x}, \mathbf{R}). \tag{5.5}$$

According to linear transformation property of Gaussian distribution, $p(\mathbf{Hx})$ follows

$$p(\mathbf{Hx}) = \sum_{i=1}^{M} \alpha_i \mathcal{N}(\mathbf{Hx}; \mathbf{H}\mu_i, \mathbf{H}\mathbf{\Sigma}_i\mathbf{H}^T). \tag{5.6}$$

Since $\sum_{i=1}^{M} \alpha_i = 1$ (section 4.1), $p(\mathbf{v})$ can be written as

$$p(\mathbf{v}) = \mathcal{N}(\mathbf{v}; 0, \mathbf{R}) = \sum_{i=1}^{M} \alpha_i \mathcal{N}(\mathbf{v}; 0, \mathbf{R}). \tag{5.7}$$

Therefore, according to linear addition property of Gaussian distribution, $p(\mathbf{z})$ yields

$$p(\mathbf{z}) = p(\mathbf{Hx} + \mathbf{v}) = \sum_{i=1}^{M} \alpha_i \mathcal{N}(\mathbf{z}; \mathbf{H}\mu_i, \mathbf{P}_i), \tag{5.8}$$

where $\mathbf{P}_i = \mathbf{H}\mathbf{\Sigma}_i\mathbf{H}^T + \mathbf{R}$ is the covariance matrix for ith Gaussian component in $p(\mathbf{z})$. As it can be seen from Eq. (5.8), $p(\mathbf{z})$ is also a Gaussian mixture with the same number of mixtures as $p(\mathbf{x})$.

Plugging $p(\mathbf{z}|\mathbf{x})$, $p(\mathbf{x})$ and $p(\mathbf{z})$ into Eq. (5.3) yields

$$p(\mathbf{x}|\mathbf{z}) = \frac{\mathcal{N}(\mathbf{z}; \mathbf{Hx}, \mathbf{R}) \sum_{i=1}^{M} \alpha_i \mathcal{N}(\mathbf{x}; \mu_i, \mathbf{\Sigma}_i)}{\sum_{i=1}^{M} \alpha_i \mathcal{N}(\mathbf{z}; \mathbf{H}\mu_i, \mathbf{P}_i)}. \tag{5.9}$$

Since the product of two Gaussian distributions is still Gaussian (proof is given in section 5.1.2),

$$\mathcal{N}(\mathbf{z}; \mathbf{Hx}, \mathbf{R})\mathcal{N}(\mathbf{x}; \mu_i, \mathbf{\Sigma}_i) = \mathcal{N}(\mathbf{z}; \mathbf{H}\mu_i, \mathbf{P}_i)\mathcal{N}(\mathbf{x}; \hat{\mu}_i, \hat{\mathbf{P}}_i), \tag{5.10}$$

where $\hat{\mu}_i = \mu_i + \mathbf{K}_i(\mathbf{z} - \mathbf{H}\mu_i)$, $\hat{\mathbf{P}}_i = (\mathbf{I} - \mathbf{K}_i\mathbf{H})\mathbf{\Sigma}_i$ and $\mathbf{K}_i = \mathbf{\Sigma}_i\mathbf{H}^T\mathbf{P}_i^{-1}$. Eq. (5.9) becomes

$$p(\mathbf{x}|\mathbf{z}) = \frac{\sum_{i=1}^{M} \alpha_i \mathcal{N}(\mathbf{z}; \mathbf{H}\mu_i, \mathbf{P}_i)\mathcal{N}(\mathbf{x}; \hat{\mu}_i, \hat{\mathbf{P}}_i)}{\sum_{i=1}^{M} \alpha_i \mathcal{N}(\mathbf{z}; \mathbf{H}\mu_i, \mathbf{P}_i)}. \tag{5.11}$$

If β_i is set to be

$$\beta_i = \frac{\alpha_i \mathcal{N}(\mathbf{z}; \mathbf{H}\mu_i, \mathbf{P}_i)}{\sum_{i=1}^{M} \alpha_i \mathcal{N}(\mathbf{z}; \mathbf{H}\mu_i, \mathbf{P}_i)}, \tag{5.12}$$

Eq. (5.11) can be further written as

$$p(\mathbf{x}|\mathbf{z}) = \sum_{i=1}^{M} \beta_i \mathcal{N}(\mathbf{x}; \hat{\mu}_i, \hat{\mathbf{P}}_i). \tag{5.13}$$

As shown in Eq. (5.13), posterior $p(\mathbf{x}|\mathbf{z})$ is also a Gaussian mixture with the same number of mixtures as $p(\mathbf{x})$ and β_i is the weighing of the ith Gaussian mixture in $p(\mathbf{x}|\mathbf{z})$.

Bayes' *least square estimate* of $\mathbf{x}$ is given as the conditional mean (proof is given in section 5.1.3):

$$\hat{\mathbf{x}} = E[\mathbf{x}|\mathbf{z}] = \sum_{i=1}^{M} \beta_i \hat{\mu}_i, \tag{5.14}$$

where $E[.]$ is the expectation operator. $\hat{\mathbf{x}}$ is considered the "best" estimate of $\mathbf{x}$ in terms of minimum-variance and unbiased performance.

5.1.2 Proof of Eq. (5.10)

Assume:

$$\begin{aligned}
\mathcal{N}(\mathbf{z}; \mathbf{H}\mathbf{x}, \mathbf{R})\mathcal{N}(\mathbf{x}; \mu_i, \mathbf{\Sigma}_i) &= \frac{1}{\sqrt{(2\pi)^{(m+n)}}\sqrt{|\mathbf{R}| \cdot |\mathbf{\Sigma}_i|}} e^{-\frac{1}{2}||\mathbf{z}-\mathbf{H}\mathbf{x}||^2_{\mathbf{R}^{-1}} - \frac{1}{2}||\mathbf{x}-\mu_i||^2_{\mathbf{\Sigma}_i^{-1}}} \\
&= \frac{1}{\sqrt{(2\pi)^{(m+n)}}\sqrt{C_2}} e^{-\frac{1}{2}C_1} \\
&= \mathcal{N}(\mathbf{z}; \mathbf{H}\mu_i, \mathbf{P}_i)\mathcal{N}(\mathbf{x}; \hat{\mu}_i, \hat{\mathbf{P}}_i)
\end{aligned}$$

According to Sherman-Morrison-Woodbury formula (Lewis et al. 2006):

$$\begin{aligned}
\mathbf{P}_i^{-1} &= (\mathbf{H}\mathbf{\Sigma}_i\mathbf{H}^T + \mathbf{R})^{-1} \\
&= \mathbf{R}^{-1} - \mathbf{R}^{-1}\mathbf{H}(\mathbf{H}^T\mathbf{R}^{-1}\mathbf{H} + \mathbf{\Sigma}_i^{-1})^{-1}\mathbf{H}^T\mathbf{R}^{-1} \\
&= \mathbf{R}^{-1} - \mathbf{R}^{-1}\mathbf{H}\hat{\mathbf{P}}_i\mathbf{H}^T\mathbf{R}^{-1}
\end{aligned}$$

Then

$$
\begin{aligned}
C_1 &= ||\mathbf{x}-\hat{\mu}_i||^2_{\hat{\mathbf{P}}_i^{-1}} + ||\mathbf{z}||^2_{\mathbf{P}_i^{-1}} - 2\mu_i^T\mathbf{H}^T\mathbf{P}_i^{-1}\mathbf{z} + ||\mu_i||^2_{\mathbf{H}^T\mathbf{P}_i^{-1}\mathbf{H}} \\
&= ||\mathbf{x}-\hat{\mu}_i||^2_{\hat{\mathbf{P}}_i^{-1}} - 2\mu_i^T\mathbf{\Sigma}_i^T\hat{\mathbf{P}}_i\mathbf{H}^T\mathbf{R}^{-1}\mathbf{z} - ||\mathbf{H}^T\mathbf{R}^{-1}\mathbf{z}||^2_{\hat{\mathbf{P}}_i} - ||\mathbf{\Sigma}_i^{-1}\mu_i||^2_{\hat{\mathbf{P}}_i} + ||\mathbf{z}||^2_{\mathbf{R}^{-1}} + ||\mu_i||^2_{\mathbf{\Sigma}_i^{-1}} \\
&= ||\mathbf{x}-\hat{\mu}_i||^2_{\hat{\mathbf{P}}_i^{-1}} - ||\mathbf{H}^T\mathbf{R}^{-1}\mathbf{z}+\mathbf{\Sigma}_i^{-1}\mu_i||^2_{\hat{\mathbf{P}}_i} + ||\mathbf{z}||^2_{\mathbf{R}^{-1}} + ||\mu_i||^2_{\mathbf{\Sigma}_i^{-1}} \\
&= ||\mathbf{x}-\hat{\mathbf{P}}_i\mathbf{\Sigma}_i^{-1}\mu_i-\hat{\mathbf{P}}_i\mathbf{H}^T\mathbf{R}^{-1}\mathbf{z}||^2_{\hat{\mathbf{P}}_i^{-1}} - ||\mathbf{H}^T\mathbf{R}^{-1}\mathbf{z}+\mathbf{\Sigma}_i^{-1}\mu_i||^2_{\hat{\mathbf{P}}_i} + ||\mathbf{z}||^2_{\mathbf{R}^{-1}} + ||\mu_i||^2_{\mathbf{\Sigma}_i^{-1}} \\
&= ||\mathbf{x}||^2_{\mathbf{\Sigma}_i^{-1}+\mathbf{H}^T\mathbf{R}^{-1}\mathbf{H}} + ||\mathbf{z}||^2_{\mathbf{R}^{-1}} + ||\mu_i||^2_{\mathbf{\Sigma}_i^{-1}} - 2\mathbf{z}^T\mathbf{R}^{-1}\mathbf{H}\mathbf{x} - 2\mu_i^T\mathbf{\Sigma}_i^{-1}\mathbf{x} \\
&= ||\mathbf{z}-\mathbf{H}\mathbf{x}||^2_{\mathbf{R}^{-1}} + ||\mathbf{x}-\mu_i||^2_{\mathbf{\Sigma}_i^{-1}}
\end{aligned}
$$

and

$$
\begin{aligned}
C_2 &= |\mathbf{R}|\cdot|\mathbf{\Sigma}_i| \\
&= \det\left(\begin{bmatrix}\mathbf{R} & 0\\ 0 & \mathbf{\Sigma}_i\end{bmatrix}\right) \\
&= \det\left(\begin{bmatrix}\mathbf{I} & 0\\ \mathbf{H} & \mathbf{I}\end{bmatrix}\begin{bmatrix}\mathbf{R} & 0\\ 0 & \mathbf{\Sigma}_i\end{bmatrix}\begin{bmatrix}\mathbf{I} & \mathbf{H}^T\\ 0 & \mathbf{I}\end{bmatrix}\right) \\
&= \det\left(\begin{bmatrix}\mathbf{\Sigma}_i & \mathbf{\Sigma}_i\mathbf{H}^T\\ \mathbf{H}\mathbf{\Sigma}_i & \mathbf{H}\mathbf{\Sigma}_i\mathbf{H}^T+\mathbf{R}\end{bmatrix}\right) \\
&= \det\left(\begin{bmatrix}\mathbf{I} & \mathbf{K}_i\\ 0 & \mathbf{I}\end{bmatrix}\begin{bmatrix}\hat{\mathbf{P}}_i & 0\\ \mathbf{H}\mathbf{\Sigma}_i & \mathbf{P}_i\end{bmatrix}\right) \\
&= \det\left(\begin{bmatrix}\hat{\mathbf{P}}_i & 0\\ 0 & \mathbf{P}_i\end{bmatrix}\right) \\
&= |\mathbf{P}_i|\cdot|\hat{\mathbf{P}}_i|
\end{aligned}
$$

5.1.3 Proof of Bayes' Least Square Estimate

Bayes' least square estimate, which is the conditional mean of the posterior distribution, is a minimum-variance and unbiased estimate.

- **Unbiasedness:** Let

$$\hat{\mathbf{x}} = E[\mathbf{x}|\mathbf{z}].$$

Using the iterated law of conditional expectation ($E\{E[x|z]\} = E[x]$), $E[\mathbf{x}-\hat{\mathbf{x}}]$ can be written as

$$\begin{aligned} E[\mathbf{x}-\hat{\mathbf{x}}] &= E\{E[\mathbf{x}-\hat{\mathbf{x}}|\mathbf{z}]\} \\ &= E\{E[\mathbf{x}|\mathbf{z}] - E[\hat{\mathbf{x}}|\mathbf{z}]\} \\ &= E[\hat{\mathbf{x}}-\hat{\mathbf{x}}] \\ &= 0. \end{aligned}$$

- **Minimum-Variance:** Let

$$\mu = E[\mathbf{x}|\mathbf{z}].$$

$VAR[\hat{\mathbf{x}}]$ can be formulated as

$$\begin{aligned} VAR[\hat{\mathbf{x}}] &= E[(\mathbf{x}-\hat{\mathbf{x}})^T(\mathbf{x}-\hat{\mathbf{x}})] \\ &= E[(\mathbf{x}-\mu+\mu-\hat{\mathbf{x}})^T(\mathbf{x}-\mu+\mu-\hat{\mathbf{x}})] \\ &= E[(\mathbf{x}-\mu)^T(\mathbf{x}-\mu)] + E[(\mu-\hat{\mathbf{x}})^T(\mu-\hat{\mathbf{x}})] + 2E[(\mathbf{x}-\mu)^T(\mu-\hat{\mathbf{x}})] \end{aligned}$$

Using the iterated law of conditional expectation, the third term in last equation can be written as

$$\begin{aligned} 2E[(\mathbf{x}-\mu)^T(\mu-\hat{\mathbf{x}})] &= 2E\left\{E[(\mathbf{x}-\mu)^T(\mu-\hat{\mathbf{x}})|\mathbf{z}]\right\} \\ &= 2E\left\{E[(\mathbf{x}-\mu)|\mathbf{z}]^T(\mu-\hat{\mathbf{x}})\right\} \\ &= 2E\left\{(E[\mathbf{x}|\mathbf{z}]-\mu)^T(\mu-\hat{\mathbf{x}})\right\} \\ &= 0. \end{aligned}$$

Therefore, $VAR[\hat{\mathbf{x}}]$ becomes

$$VAR[\hat{\mathbf{x}}] = E[(\mathbf{x}-\mu)^T(\mathbf{x}-\mu)] + E[(\mu-\hat{\mathbf{x}})^T(\mu-\hat{\mathbf{x}})].$$

Since both two terms in $VAR[\hat{\mathbf{x}}]$ are non-negative, its minimum point is reached when the second third is zero leading to

$$\hat{\mathbf{x}} = \mu = E[\mathbf{x}|\mathbf{z}].$$

5.1.4 Definitions of Error Terms

To better analyze the performance of GMPE and compare with other approaches, four error terms including bias, root mean-square error (RMSE), fractional standard error (FSE) and correlation coefficient are considered. If X is the parameter (such as R, N_0 or A_h) being estimated, $\hat{X}$ is the estimated value of the parameter and estimation error is defined as

$$\epsilon_X = \hat{X} - X. \tag{5.15}$$

Thus the bias is the mean of estimation error, $\bar{\epsilon}_X$, RMSE can be calculated from

$$RMSE = \sqrt{\bar{\epsilon}_X^2 + \sigma_X^2}, \tag{5.16}$$

and FSE (expressed as percentage) yields

$$FSE = 100\frac{RMSE}{\bar{X}}, \tag{5.17}$$

where σ_X is the standard deviation (SD) of the estimation and $\bar{X}$ is mean of the parameter. Moreover, the correlation coefficient is defined as

$$r(\hat{X}, X) = \frac{Cov(\hat{X}, X)}{\sqrt{Cov(\hat{X}, \hat{X})Cov(X, X)}}, \tag{5.18}$$

where Cov is the covariance operator.

5.2 Performance Evaluation for GMPE

In this section, performance of GMPE is evaluated through two applications: attenuation estimation for different hydrometeors (section 5.2.1) and rainfall rate estimation using dual-frequency polarimetric radar measurements (section 5.2.2). A training dataset has been constructed using the single-cell Monte Carlo simulation described in section 3.5 for the performance evaluation.

Three hydrometeor species including rain, snow and hail are considered. Inputs into the simulator are mixing ratios of rain (q_r), snow (q_s) and hail (q_h). Outputs

Table 5.1: Key Parameters of the Radar Simulator.

Radar frequency (wavelength)	5 GHz (6 cm) and 10 GHz (3 cm)
Volume of single cell	1000 m^3
Mixing ratio of rain (q_r)	0-10 [g kg^{-1}]
Mixing ratio of snow (q_s)	0-10 [g kg^{-1}]
Mixing ratio of hail (q_h)	0-10 [g kg^{-1}]
Drop size distribution (DSD)	$N(D) = N_0 exp(-\Lambda D)$

include exponential drop size distribution (DSD) parameters N_0 and Λ, water content W(for all species), rainfall rate R (only for rain) and dual-polarized variables Z_h, Z_{dr}, K_{dp}, as well as attenuation factors A_h and A_v in both C-band and X-band. Parameters to be estimated, such as R or A_h for each resolution cell, are related to corresponding radar signatures of this volume. The GMM approximates the joint-distribution of all the variables and extracts the relationships underlying them. As a visual example and comparison, Fig. 5.1(a) and 5.1(b) show the scatter plots for radar observation variables (Z_H and Z_{DR}) for the three hydrometeor species at different frequencies, and Fig. 5.1(c) and 5.1(d) show the approximate distribution from trained GMMs. A set of 6000 simulations with all the output parameters are carried out for each hydrometeor type in order to be statistically significant (Total=18000). Noisy measurements are obtained from adding random noise to clean observations. Noise is assumed to be zero mean, uncorrelated Gaussian noise with standard deviation 1 [dB], 0.5 [dB] and 0.5 [deg km^{-1}] forZ_H, Z_{DR} and K_{dp}, respectively. Selections of these noise levels are mainly for demonstration purposes and to set up a performance boundary of estimators, and they should be adjusted based on the signal-to-noise ratio (SNR) and radar parameters in practical applications.

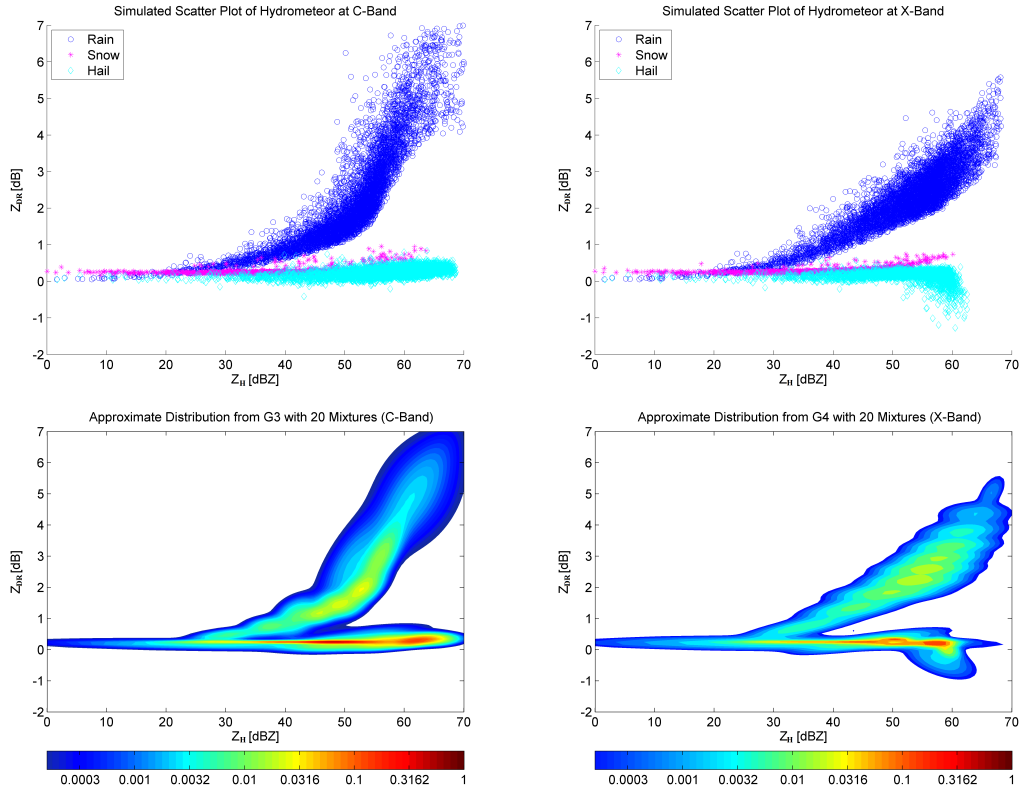


Figure 5.1: Scatter plots and Monte-Carlo simulated distributions of dual-polarized, dual-frequency radar signatures. From left to right and top to bottom, (a) Scatter plot of Z_H and Z_{DR} at C-Band, (b)Scatter plot of Z_H and Z_{DR} at X-Band, (c) Approximate distribution from G_3 at C-Band, (d) Approximate distribution from G_4 at X-Band.

5.2.1 Attenuation Estimation for Rain, Snow and Hail

Hydrometeors cause significant attenuation at C-band and X-band (e.g., Vulpiani et al. 2008; Anagnostou et al. 2006). As a consequence, radar measured reflectivity (Z_h and Z_{dr}) must be corrected before they can be used quantitatively. Researchers have been using PLRs (e.g., Anagnostou et al. 2006; Bringi and Chandrasekar 2001; Gorgucci et al. 2006; Gorgucci and Baldini 2007), such as $A_{h/v} = aK_{dp}$, $A_{h/v} = aZ_{h/v}^b$, $A_{h/v} = aZ_{h/v}^b Z_{dr}^c$ and $A_{h/v} = aZ_{h/v}^b Z_{dr}^c K_{dp}^d$ (Z_h in [mm^6 m^{-3}], Z_{dr} being dimensionless and K_{dp} in [deg km^{-1}]), to estimate and correct attenuations. Such relations, mainly used for rain, have been extended to other hydrometeor species (Marzano et al. 2010). As an example of C-band observations, regression coefficients (a, b, c, d) are derived from the simulated dataset and the root mean square errors (RMSE) of each PLR for A_h estimation based on clean and noisy measurements are given in Table 5.2. RMSEs of each PLR for A_v are similar

Table 5.2: RMSEs in [db km^{-1}] for A_h Estimations Based on PLRs.

	$A(K_{dp})$		$A(Z_h)$		$A(Z_h, Z_{dr})$		$A(Z_h, Z_{dr}, K_{dp})$	
	Clean	Noisy	Clean	Noisy	Clean	Noisy	Clean	Noisy
Rain	0.459	0.461	0.229	0.294	0.171	0.235	0.125	0.205
Snow	0.522	0.523	0.53	0.532	> 1	> 1	> 1	> 1
Hail	0.219	0.497	0.137	0.152	0.136	0.155	0.127	0.139
All Three	0.470	0.472	0.476	0.477	> 1	> 1	> 1	> 1

As more variables are used in power law relations, better results are obtained, except that Z_{dr} measurements of snow have a negative impact.

To evaluate and compare performance of GMPE, three different estimators are trained, namely G_1, G_2 and G_3. For G_1, state vector $\mathbf{x} = [A_h, A_v, K_{dp}]^T$ and only the rain data are used in training. For G_2, state vector $\mathbf{x} = [A_h, A_v, Z_h, Z_{dr}, K_{dp}]^T$ and

only the rain data are used in training. For G_3, state vector $\mathbf{x} = [A_h, A_v, Z_h, Z_{dr}, K_{dp}]^T$ and all the data (rain, snow and hail) are used in training.

The approximate distribution of Z_H and Z_{DR} form G_3 is shown in Fig. 5.1(c), while the RMSEs of G_1, G_2 and G_3 for A_h estimation are shown in Fig. 5.2 and Fig. 5.3. The RMSEs for A_v, which are not shown here, are slightly better than that of A_h. Compared to PLRs, GMPEs have significantly better accuracies in all scenarios.

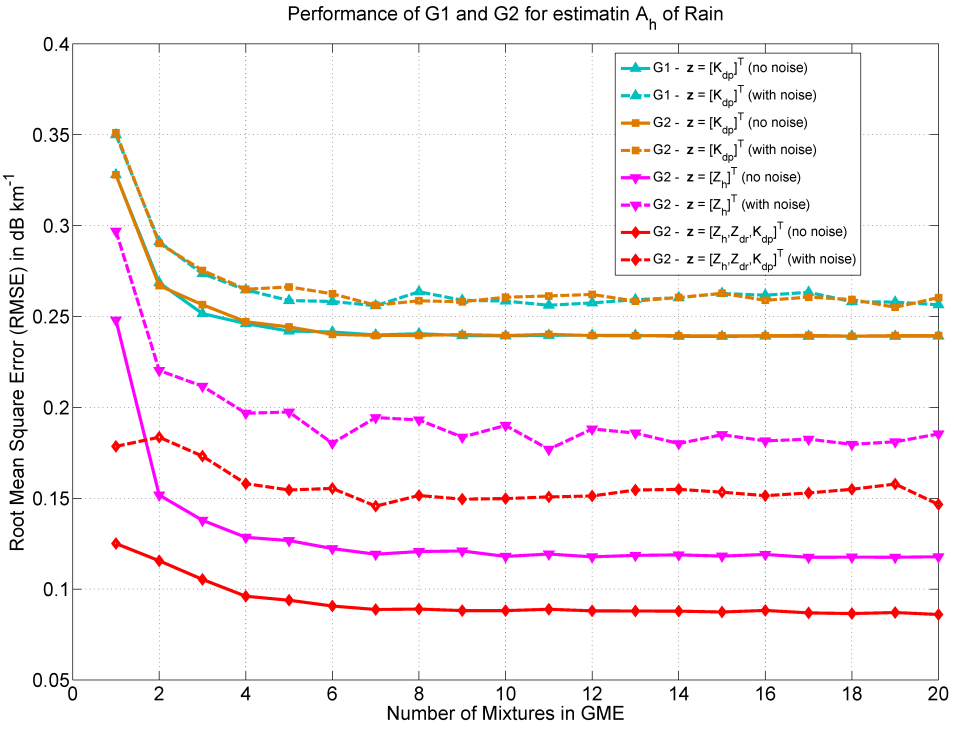


Figure 5.2: Performance of G_1 and G_2 for estimating A_h of Rain.

Given the same weather radar observations such as $Z = [K_{dp}]^T$, both G_1 (smaller model) and G_2 (larger model) can be used for rain attenuation correction, whereas $\mathbf{H} = [0, 0, 1]$ for G_1 and $\mathbf{H} = [0, 0, 0, 0, 1]$ for G_2. The two GMPEs perform almost the same for clean and noisy observation, assuming six mixtures are used, as shown in Fig. 5.2. If the radar observation is given as $Z = [Z_h, Z_{dr}, K_{dp}]^T$ instead, either G_2 or

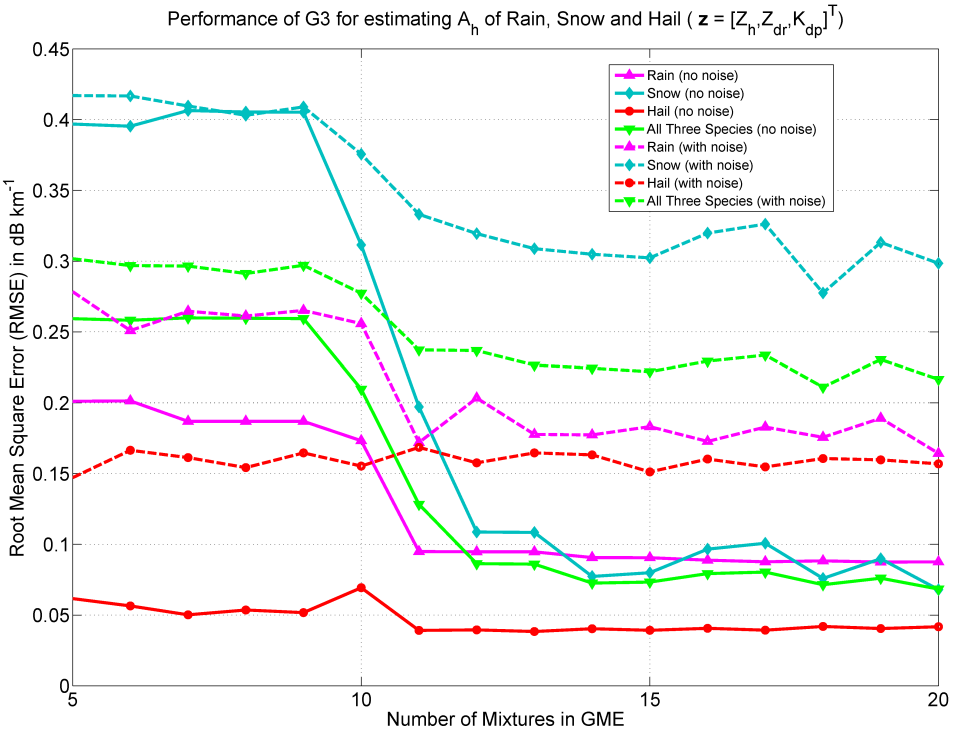


Figure 5.3: Performance of G_3 for estimating A_h of Rain ($Z = [Z_h, Z_{dr}, K_{dp}]^T$).

G_3 can be used for rain attenuation correction. However, G_3 needs more (11) mixtures to reach the same performance as G_3 (which uses 7 mixtures). This is because G_3 is used to model a much more complex distribution that includes rain, snow and hail, while G_2 only converges to the distribution of rain. In real-world applications, a small model can be trained and used in platforms such as mobile radars, and a large model can be trained and used in ground-based radars with more computing resources. Due to the convergence of GMM, there is no negative impact if more observation variables are incorporated into GMM. Furthermore, a 'super-model' for all seasons, areas and hydrometeor species may be trained and readily tuned for specific applications with different observations by selecting different **H**.

In addition, GMPE is able to include path attenuation correction techniques, such as the constrained parameter technique (e.g., Bringi and Chandrasekar 2001; Gorgucci et al. 2006), to optimize the attenuation correction along a radar bin. The detailed discussion is given in section 5.5.

5.2.2 Rainfall Rate Estimation Through Dual-Frequency and Dual-Polarized Radar Measurements

DSD variability is well recognized as the major source of the diversity of conventional $R(Z)$ relations. Dual-frequency and dual-polarized measurements provide more information on DSD, and as a result, approaches that use such radar data have improved rainfall rate estimation (e.g., Ryzhkov et al. 2005a; Cao et al. 2010; Rose and Chandrasekar 2006; Vulpiani et al. 2006). Those existing approaches are still mostly PLRs, such as $R(Z_h, Z_{dr}) = aZ^bZ_{dr}^c$ and $R(Z_h, Z_{dr}, K_{dp}) = aZ_h^bZ_{dr}^cK_{dp}^d$. According to Ryzhkov et al. (2005a), $R(Z_h, Z_{dr}, K_{dp})$ outperforms other relations in most categories. Although there are some studies that compare rainfall rate estimation in different frequencies (Testud et al. 1992) and retrieve DSD (e.g., Haddad et al. 2006; Rose and Chandrasekar 2006), none of the existing work has used both dual-polarization

and dual-frequency radar observations. In this sudsy, regression coefficients (a, b, c, d) are derived from the simulation dataset, and RMSE of $R(Z_h, Z_{dr}, K_{dp})$ based on clean and noisy measurements are given in Table 5.3 for both X and C-bands. A combined state vector $\mathbf{x} = [R, Z_h^X Z_{dr}^X, K_{dp}^X, Z_h^C, Z_{dr}^C, K_{dp}^C]^T$ (superscript $(.)^X$ and $(.)^C$ denote measurement from X-band and C-band, respectively) is used for GMM. A GMPE, G_4, is trained from simulated rain data with the combined state vector $\mathbf{x}$. The approximate distribution of Z_H and Z_{DR} form G_4 is shown in Fig. 5.1(d), and the performance of G_4 with respect to different numbers of mixtures is presented in Fig. 5.4. Again, GMPE outperforms $R(Z_h, Z_{dr}, K_{dp})$ in both X-band and C-band for all the scenarios. For combined 'clean' X-band and C-band observations, RMSE of the R estimation is only 2.7 [mm hr^{-1}] for G_4 estimator (72% improvement from the PLR estimator).

Table 5.3: RMSEs in [mm hr^{-1}]for R estimation based on PLRs.

	$R(Z_h^X, Z_{dr}^X, K_{dp}^X)$	$R(Z_h^C, Z_{dr}^C, K_{dp}^C)$
clean	9.82	15.35
Noisy	31.58	26.44

5.2.3 Conclusions on Performance of GMPE

GMM provides an efficient way to accommodate extra information from antenna and frequency diversities and an 'omnipotent' solution to model the 'knowledge' in training data. The GMPE also provides minimum variance estimations for weather parameters, without the limitation of deterministic models or simple Gaussian models. By utilizing both measurement data and Monte-Carlo simulation data in training, the GMM approach establishes a framework to merge the advantages of phenomenological models and physical models and therefore achieves better accuracies and flexibilities than existing methods. GMM/GMPE can be applied to other radar-meteorological

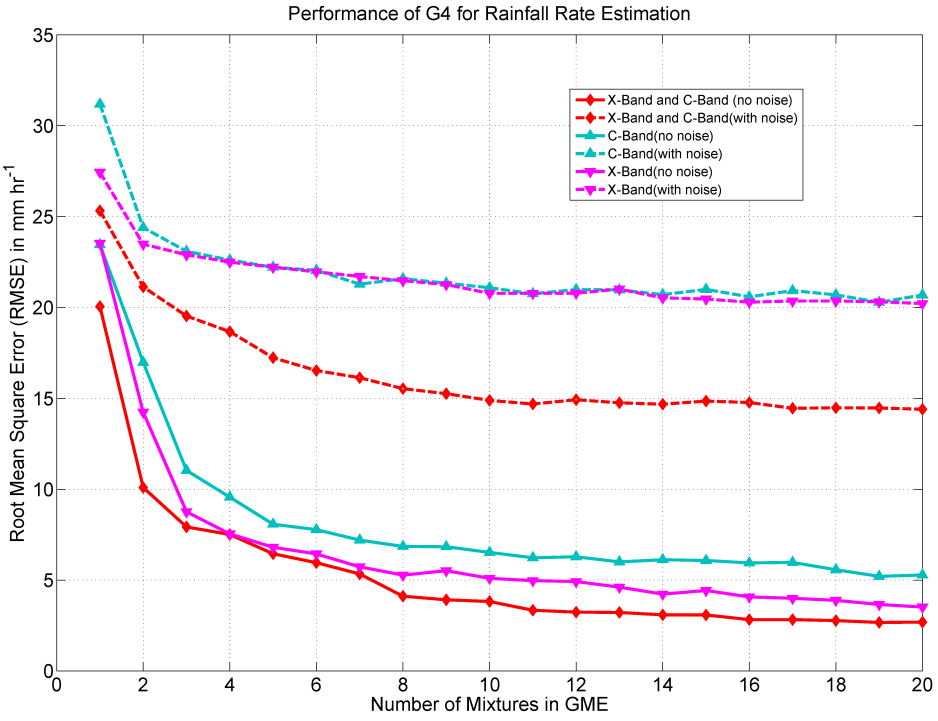


Figure 5.4: Performance of G_4 for rainfall rate estimation.

applications such as DSD retrieval, water content estimation or other parameters (wind, temperature, etc.) associated with radar observations. Also it can incorporate more observation variables such as linear depolarization ratio (LDR) and correlation coefficients (ρ_{hv}) and improve estimation accuracy, and can be extended to using more complex measurement noise models. Furthermore, a 'super model', or a global GMPE for parameter estimations based from multiple-sensor observations, is possible. The structure of the GMPE also makes it easy to extend to explore the spatial or temporal relations (Hogan 2007) in a Kalman Filter structure (Lewis et al. 2006). GMPE with a Kalman Filter structure is discussed in Chapter 6.

5.3 S-band DSD Retrieval Using GMPE

The GMPE is applied to retrieve DSD parameters using S-band polarimetric radar measurements in this section. Retrieval results are compared with those from two physically based polarimetric algorithms, which have been recently proposed. The first one is known as the β method which is introduced by Gorgucci et al. (2002) and later improved in Bringi et al. (2004). The β method is based on the normalized Gamma DSD (defined in Eq. (3.5)). The basic idea assumes raindrop axis ratio to be of the form $r_a = 1 - \beta D$, treats raindrop shape as a variable and tries to retrieve β from Z_H, Z_{DR} and K_{DP}. After β is estimated, the intercept parameter N_w and median diameter D_0 are estimated by means of the retrieved β, Z_H and Z_{DR}. The shape parameter μ is computed as a function of the retrieved D_0 and β as well as Z_{DR}. The details of the β method are present as follows:

$$\beta = 2.08 Z_h^{-0.365} K_{DP}^{0.380} Z_{dr}^{0.965} \tag{5.19a}$$

$$log_{10} N_w = 3.29 Z_h^{0.058} Z_{dr}^{-0.023\beta^{-1.389}} \tag{5.19b}$$

$$D_0 = 0.56 Z_h^{0.064} Z_{dr}^{0.024\beta^{-1.42}} \tag{5.19c}$$

$$\mu = \frac{200\beta^{1.89} D_0^{2.23\beta^{0.039}}}{Z_{dr} - 1} - 3.16\beta^{-0.046} Z_{dr}^{0.374\beta^{-0.355}} \tag{5.19d}$$

where Z_h in [mm^6 m^{-3}], Z_{dr} being dimensionless and K_{dp} in [deg km^{-1}]. Rainfall rate R is given by (Bringi et al. 2004)

$$R = 0.105\beta^{0.865} Z_h^{0.93} Z_{dr}^{-0.585\beta^{-0.703}}. \tag{5.20}$$

The second one is known as the C-G method which is introduced by Zhang et al. (2001) and improved in Brandes et al. (2004). The C-G method is based on the constrained-Gamma DSD (given in Eq. (3.8)), where a constraint $\mu - \Lambda$ relation is added to a Gamma DSD (defined in Eq. (3.4)). The constraint $\mu - \Lambda$ relation from Brandes et al. (2004) yields

$$\Lambda = 0.0365\mu^2 + 0.735\mu + 1.935. \tag{5.21}$$

This constraint reduces the three-parameter Gamma DSD to a two-parameter model. By assuming the raindrop axis ratio follows the one proposed in Brandes et al. (2002), the shape parameter μ is estimated from Z_{dr}. After μ is retrieved, D_0 is calculated from Eq. (5.21) and Λ is computed by making use of the constrained relationship and Z_h. Rainfall rate R from the C-G method is given by:

$$R = 0.00760 Z_h \times 10^{0.165 Z_{DR}^2 - 0.897 Z_{DR}}, \tag{5.22}$$

where Z_h in [mm^6 m^{-3}] and Z_{DR} is in [dB].

Table 5.4: Performance of DSD Retrieval from the β Method. (All in [mm hr^{-1}])

Parameters	Bias	STD	RMSE	FSE
$log_{10}N_w$	0.20	0.48	0.52	15.88%
μ	-0.41	2.21	2.25	110.89%
D_0	-0.12	0.27	0.29	16.63%

The S-band simulation dataset generated in section 3.5.2 is used in this study. Scatter plots of this dataset is shown in Fig. 3.12. The dataset has been divided into two portions: 4000 cases are used to train GMM and the other 2000 cases are used to

Table 5.5: Performance of DSD Retrieval from GMPE with 20 mixtures. (All in [mm hr^{-1}])

Parameters	Bias	STD	RMSE	FSE
$log_{10}N_w$	-0.01	0.24	0.24	7.52%
μ	0.01	1.6 6	1.66	82.12%
D_0	0	0.18	0.18	10.02%

test all three algorithms. A zero mean random fluctuation of the polarimetric variables has been introduced to realistically reproduce the testing dataset, resulting in a noise standard deviation of 1 [dB] for Z_H, 0.2 [dB] for Z_{DR}, and 0.32 [deg km^{-1}] for K_{dp}. The state vector for GMPE is constructed as $\mathbf{x} = [R, log_{10}N_w, \mu, D_0, Z_H, Z_{DR}, K_{dp}]^T$, therefore, DSD parameters and rainfall rate can be retrieved at the same time from GMPE. Number of mixture in the GMM is 20. Results of DSD retrieval by the β method and GMPE are shown in Table 5.4 and Table 5.5. GMPE outperforms the β method in every error category. Results of rainfall rate retrieval by the C-G method, GMPE and the β method are shown in Fig. 5.5, Fig. 5.6 and Fig. 5.7, respectively. Again, GMPE has the best performance in every error category.

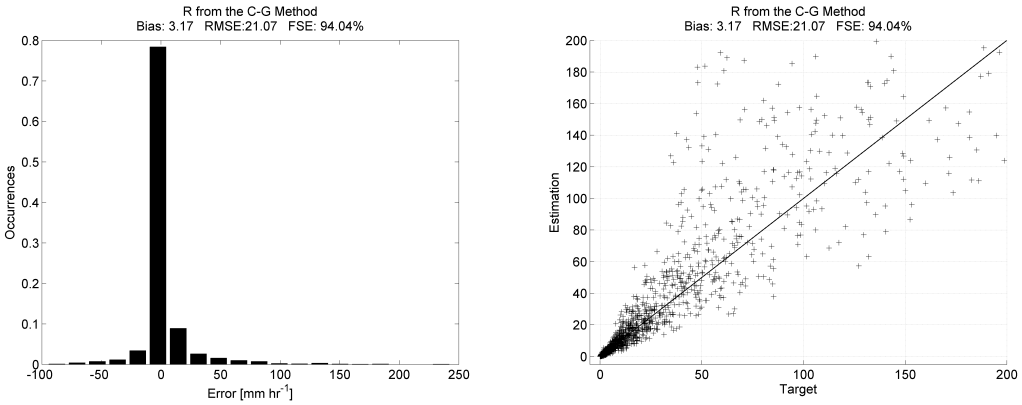


Figure 5.5: Results of rainfall rate retrieval by the C-G method. (All in [mm hr^{-1}])

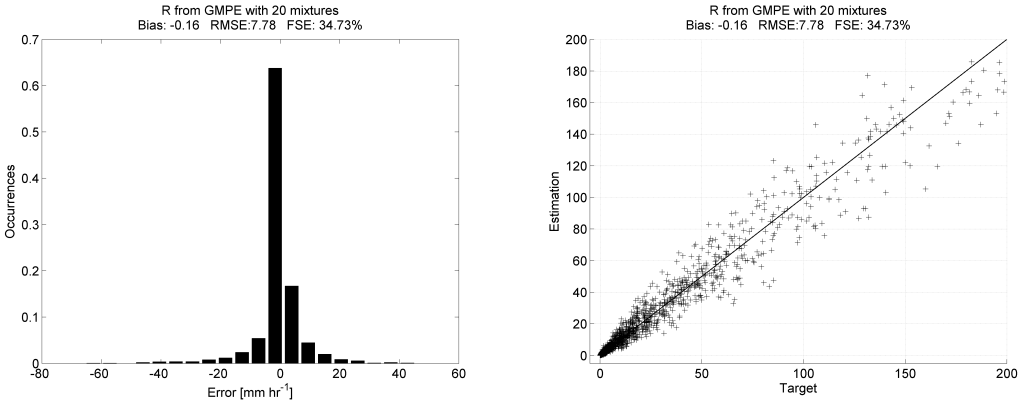


Figure 5.6: Results of rainfall rate retrieval by GMPE with 20 mixtures. (All in [mm hr^{-1}])

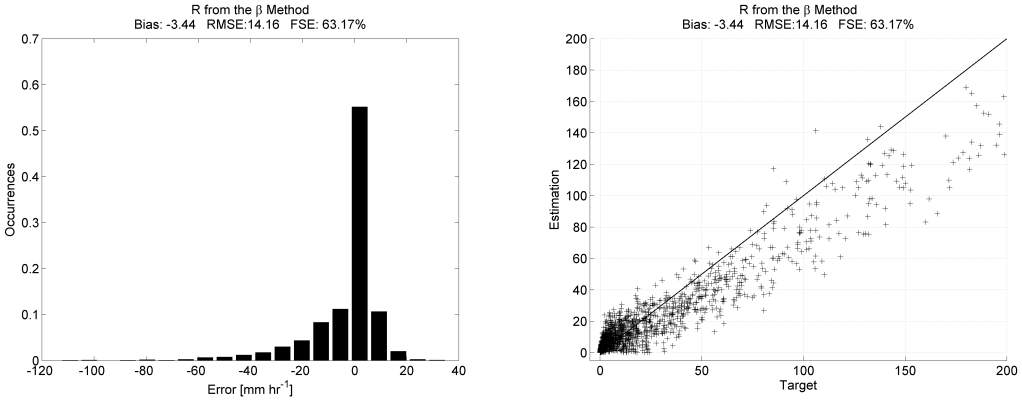


Figure 5.7: Results of rainfall rate retrieval by the β method. (All in [mm hr^{-1}])

5.4 Gaussian Mixture Rainfall Rate Estimator

In this section, the GMPE approach is applied to polarimetric radar-based rainfall rate estimation. To distinguish from general GMPE, it is renamed the Gaussian Mixture Rainfall-rate Estimator (GMRE). The flowchart of the GMRE approach is shown in Fig. 5.8. The GMRE approach was validated by using data collected during the Joint Polarization Experiment (JPOLE) from the well-gauged central Oklahoma region and S-band radar data from the KOUN radar (Doviak et al. (2002), polarimetric prototype of the WSR88D) over a multi-year period (Ryzhkov et al. 2005b). Performance of GMRE will be compared to other rainfall rate estimators that were developed and tested on the JPOLE dataset.

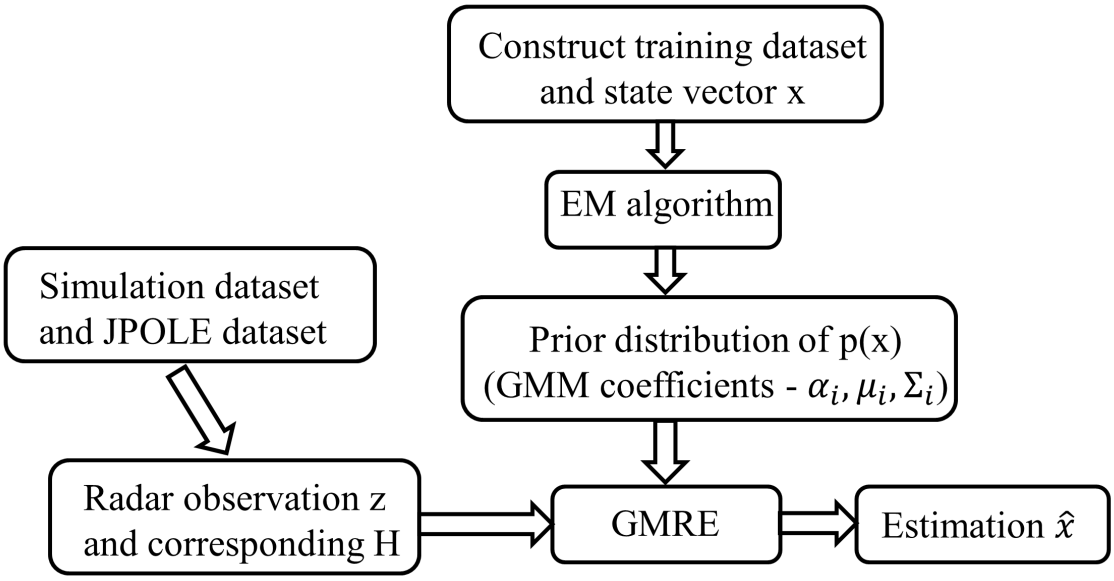


Figure 5.8: Flowchart of Gaussian Mixture Rainfall-Rate Estimator.

5.4.1 Training Dataset Construction

This study adopted the sing-cell Monte Carlo simulation technique introduced in section 3.5 to construct a training dataset for GMRE. An exponential distribution (defined in Eq. (3.2)) is used to represent raindrop size distribution:

$$N(D) = N_0 exp(-\Lambda D).$$

This distribution depends on two parameters: the intercept parameter N_0 [$\mathrm{m^{-3}mm^{-1}}$] and slope parameter Λ [$\mathrm{mm^{-1}}$]. Slope is uniquely determined if N_0 and water content W are known when given by

$$\Lambda = (\frac{\pi N_0 \rho_w}{W}),$$

where ρ_w is the density of water. Since N_0 and W have physical meaning, the dynamic range of both are well-studied and only a weak correlation is found between those parameters (Zhang et al. 2008). Even though the exponential distribution may not represent very small or large raindrops as well as the Gamma distribution (three free parameters), selecting this distribution helps reduce the number of unrealistic parameter cases.

Shown by many observation studies, intercept parameter and water content vary for different rain regimes (e.g., Waldvogel 1974; Zhang et al. 2008). Reciprocally, different types of rain may be emulated from randomly generating N_0 and W. The empirical range of N_0 is from $10^{1.5}$ to 10^6 [$\mathrm{m^{-3}mm^{-1}}$], while W can reach 10 [g $\mathrm{m^{-3}}$] (Zhang et al. 2008). While the ranges of N_0 and W are well studied, the distribution of N_0 and W remains less certain. In some studies (e.g., Li et al. 2011; Vulpiani et al. 2006), a uniform distribution of DSD parameters is assumed, which leads to equal probability for different rain types. This assumption may not hold in general since smaller rainfall ($R < 30 - 40$ [mm $\mathrm{hr^{-1}}$]) is more frequent than heavier rainfall intervals/cases.

In this study, prior distributions of N_0 and W are designed to favor rainfall lower than 40 [mm $\mathrm{hr^{-1}}$] and marginalize the probability of extreme rain cases by setting

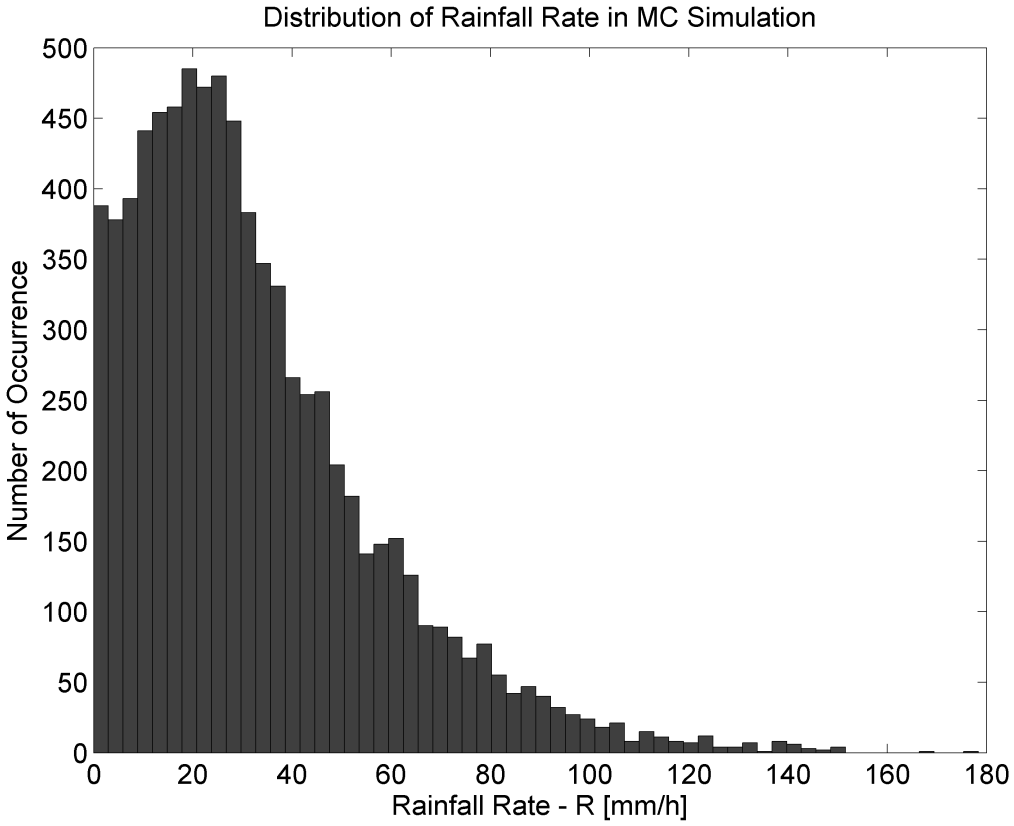


Figure 5.9: Distribution of rainfall rate (R) in Monte Carlo Simulation.

Table 5.6: Key Parameters of the Single Cell Monte-Carlo Simulation used in the GMRE Study.

Radar frequency	2.705 GHz (matching KOUN frequency)
Radar elevation angle	0^o
Volume of a single cell	1000 m^3
Temperature	Uniformly distributed between 5^oC to 20^oC
Raindrop size	0.5 mm to 8 mm with step size 0.1 mm
Canting angle distribution	$\mathcal{N}(0, 10)$
Scattering model	T-Matrix
Axis ratio of raindrops	Brandes et al. (2002) as shown in Eq. (3.13)
Terminal velocity of rain drops	Brandes et al. (2002) as shown in Eq. (3.14)
Intercept parameter N_0 [$m^{-3}mm^{-1}$]	Uniformly between $10^{1.5}$ to 10^4
Water Content W [g mm^{-3}]	One-sided $\mathcal{N}(0, 2)$

W from a one-sided Gaussian distribution and N_0 from a uniform distribution with a smaller upper bound. Table 5.6 gives details of the simulation. Outputs of the simulation includes rain microphysics parameters N_0, Λ, R and the corresponding dual-polarization variables Z_h, Z_{dr}, and K_{dp}. It is worth mentioning that 8,000 cases have been generated to help provide statistical significance. As illustrated in Fig. 5.9, in the majority of the cases R is lower than 40 [mm hr^{-1}] and the number of occurrences decreases significantly as R increases. Even though the prior distribution input into the Monte-Carlo simulation emphasizes smaller rainfall, a broad range of rainfall is still covered as R reaches as high as 180 [mm hr^{-1}]. Fig. 5.10(a) and 5.10(b) show the scatterplots of Z_H and Z_{DR} as well as Z_H and K_{dp} from the MC simulation. According to the NEXRAD $R(Z_h)$ relationship (Eq. (5.23)), $R = 20$ [mm hr^{-1}] corresponds to approximately 43 [dBZ] for observed reflectivity. Combined with R distribution in Fig. 5.9, where 70 percent of the occurrences are $R > 20$[mm hr^{-1}],

the majority of cases concentrated between 43 [dBZ] to 60 [dBZ] can be explained. Due to a large amount of big and oblate raindrops caused by a combination of large R and N_0 as well as randomness added to the axis ratio relation, there are some extreme cases where $Z_H > 55$ [dBZ], $Z_{DR} > 5$ [dB] and $K_{DP} > 2.5$ [deg km^{-1}] in the simulation dataset. An advantage of the Monte-Carlo simulation is that it can provide the relative possibility of occurrence for extreme cases. The incorporation of extreme cases are necessary for training the GMM and it will not influence the performance of GMRE, since the GMM always converges to the true distribution as the number of mixtures increases (GMM and number of mixtures is defined in Eq. (4.1)). Fig. 5.11(a) and 5.11(b) present the approximate distribution of Z_H and Z_{DR} from one trained GMM with five mixtures and another one with 20 mixtures. The approximate distribution from the GMM with 20 mixtures clearly shows more details and is much closer to the original distribution in the simulation dataset (Fig. 5.10(a)). In contrast, the approximate distribution from the GMM with five mixtures ignores some details while preserving the 'key portions' of the original distribution.

5.4.2 Training of GMREs

Since rainfall rate R can be estimated directly from radar observations or recovered from DSD parameters N_0 and Λ, the state vector is set as $\mathbf{x} = [R, N_0, \Lambda, Z_H, Z_{DR}, K_{dp}]^T$ to compare the performance of both approaches. Even though other dual-polarization variables such as the linear depolarization ratio (LDR) and correlation coefficients (ρ_{hv}) are not included in the state vector in this study, GMRE can discover and use "hidden" relationships among different variables, and additional variables would generally lead to a better performance.

Simulation datasets are divided into 2 portions. 7000 cases are used for training and the remaining 1000 cases are used for testing GMRE. Once the GMRE has been constructed, it is ready to be tuned and perform in different scenarios. For example,

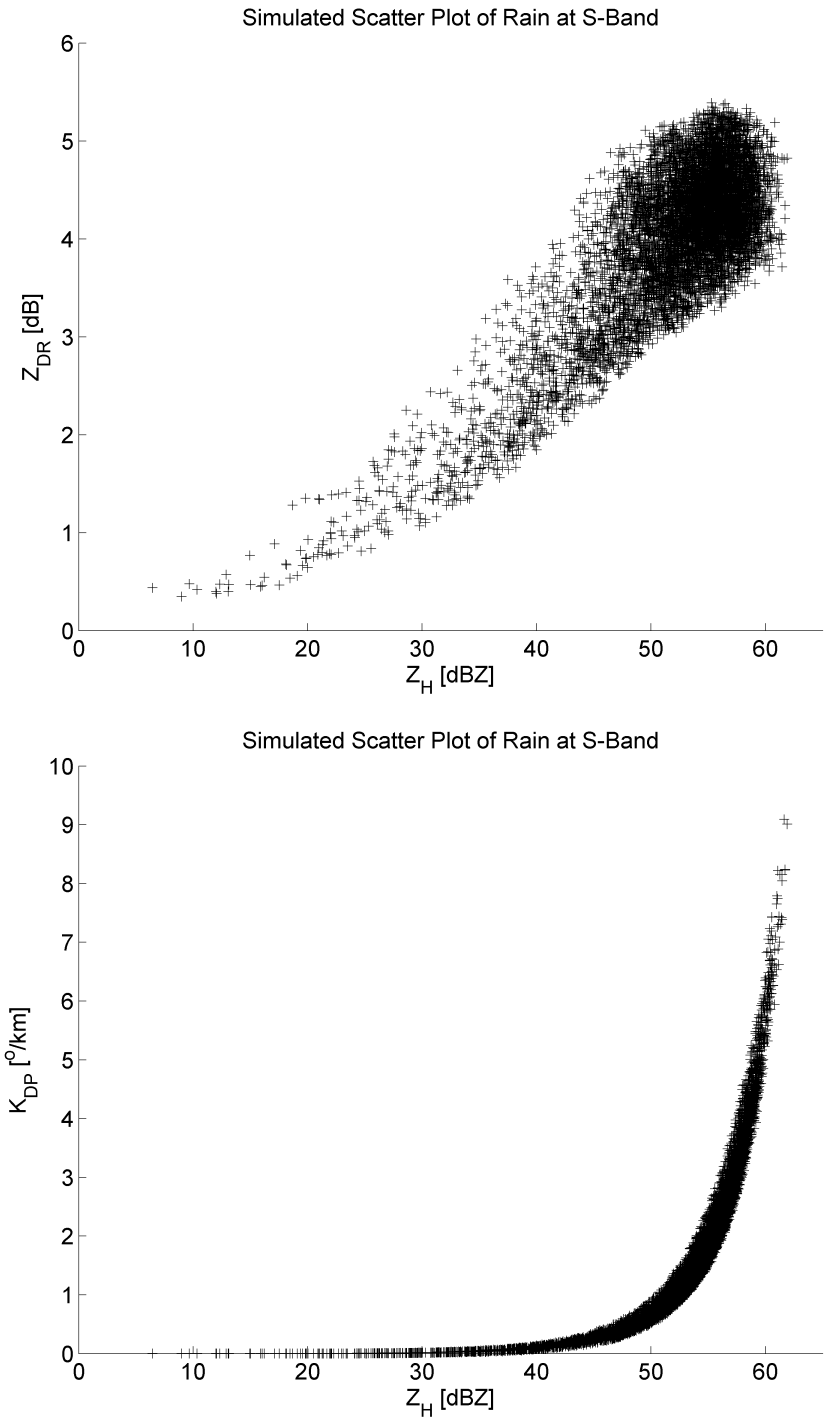


Figure 5.10: Scatter plots of S-band dual-polarized radar signatures From Monte-Carlo simulation. From top to bottom, (a) Z_H and Z_{DR} plot, (b) Z_H and K_{dp}

if only reflectivity factor Z_H is available, such as with the legacy WSR-88D, GMRE can be used with $\mathbf{H} = [0, 0, 0, 1, 0, 0]$. The rainfall rate retrieved by GMRE with Z_H will be denoted as $R_G(Z_H)$. For dual-polarized radar without (or with low quality) differential phase measurements, input to GMRE becomes $\mathbf{z} = [Z_H, Z_{DR}]^T$ and $\mathbf{H}$ yields

$$\mathbf{H} = \begin{bmatrix} 0 & 0 & 0 & 1 & 0 & 0 \\ 0 & 0 & 0 & 0 & 1 & 0 \end{bmatrix}.$$

The rainfall rate retrieved with $\mathbf{z} = [Z_H, Z_{DR}]^T$ will be denoted as $R_G(Z_H, Z_{DR})$. For radars with full dual-polarization capabilities ($\mathbf{z} = [Z_H, Z_{DR}, K_{dp}]^T$), the same GMRE also can be applied. With $\mathbf{z} = [Z_H, Z_{DR}, K_{dp}]^T$, R can be directly estimated from GMRE (denoted as R_G) or calculated from retrieved DSD parameters (N_0 and Λ) using Eq. (3.11) (denoted as R_{DSD}) as follows:

$$R_{DSD} = 6 \times 10^{-3} \pi \int_{D_{\min}}^{D_{\max}} D^3 v(D) N(D) dD.$$

Table 5.7: Rain parameters retrieved by GMREs with 5 mixtures for the simulation dataset. N_0 [mm^{-1}m^{-3}], Λ [mm^{-1}], all rainfall rate R [mm hr^{-1}]

	$log_{10}(N_0)$	Λ	$R_G(Z_H)$	$R_G(Z_H, Z_{DR})$	R_{DSD}	R_G
Bias	0.17	0.01	-0.16	-0.27	0.2	0.07
STD	1.47	0.11	10.07	6.66	4.31	1.65
RMSE	1.48	0.11	10.07	6.66	4.32	1.65
FSE	2.96%	12.96%	30.93%	20.47%	13.26%	5.08%

Fig. 5.12 illustrates the RMSEs of GMRE with different inputs and number of mixtures. In general, more observation variables input into GMRE would lead to better performance. As the number of mixtures increases, the RMSEs of $R_G(Z_H)$, $R_G(Z_H, Z_{DR})$ and R_G improve slowly while the RMSE of R_{DSD} significantly lowers from more than 4 [mm hr^{-1}] to less than 2 [mm hr^{-1}]. Table 5.7 and Table 5.8

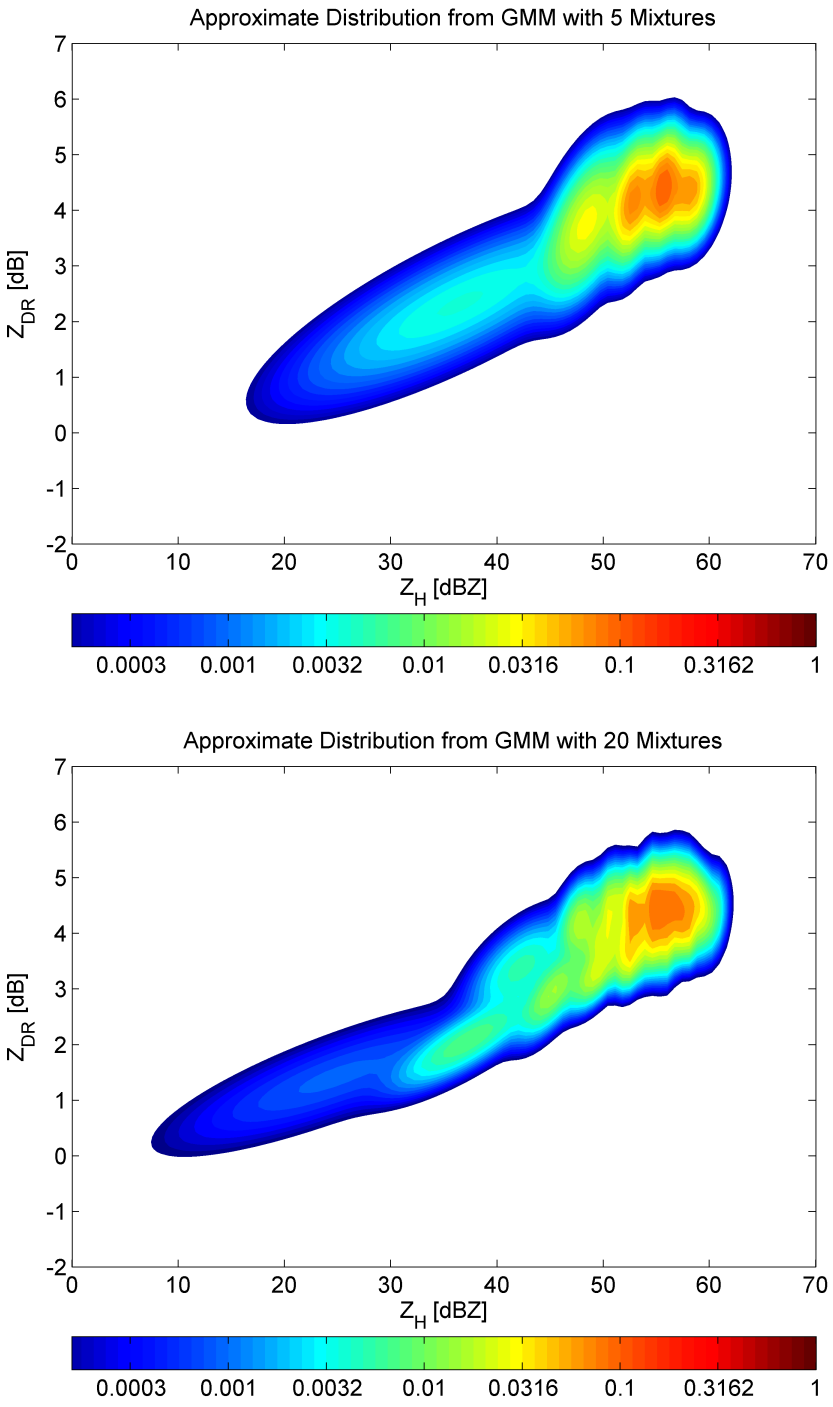


Figure 5.11: Approximate distribution from GMM for simulated radar signatures. From top to bottom, (a) Approximate distribution from GMM with 5 mixtures, (b) Approximate distribution from GMM with 20 mixtures. In both plots, warmer color represents higher probability density.

Table 5.8: Rain parameters retrieved by GMREs with 20 mixtures for the simulation dataset. N_0 [$\text{mm}^{-1}\text{m}^{-3}$], Λ [mm^{-1}], all rainfall rate R [mm hr^{-1}]

	$log_{10}(N_0)$	Λ	$R_G(Z_H)$	$R_G(Z_H, Z_{DR})$	R_{DSD}	R_G
Bias	0.08	0	-0.05	-0.01	0.12	0.03
STD	0.68	0.07	9.74	6.1	0.98	0.65
RMSE	0.69	0.07	9.74	6.1	0.98	0.65
FSE	1.37%	8.31%	29.9%	18.75%	3.02%	2.01%

compare the performance of GMRE with five and 20 mixtures. The GMRE with 20 mixtures is better than the GMRE with five mixtures in basically every category. As mentioned in last section, GMRE is a minimum-variance, unbiased estimator as long as GMM converged to prior distribution $p(\mathbf{x})$. More mixtures in GMM lead to a closer approximate distribution to $p(\mathbf{x})$ (as can be seen in Fig. 5.11(a) and 5.11(b)) and better estimation performance, which would eventually reach minimum-variance and unbiased estimations. Therefore, the question becomes how many mixtures are appropriate for GMRE, and the answer varies for different applications. For $R_G(Z_H)$ and $R_G(Z_H, Z_{DR})$, GMRE with five mixtures would be sufficient to perform near its optimal point (minimum-variance and unbiased estimation), while R_G needs 15 mixtures and R_{DSD} may need more than 20 to reach their optimal performance on the simulation dataset. Fig. 6 illustrates the plots of the rainfall rate estimation from R_G and R_{DSD} with five and 20 mixtures versus the simulated truth data. Given the same weather radar observations $\mathbf{z} = [Z_H, Z_{DR}, K_{dp}]^T$, R_G performs significantly better than R_{DSD} when GMRE has five mixtures because R_{DSD} is calculated from the retrieved N_0 and Λ, where the estimation error of N_0 and Λ accumulates and magnifies, therefore leading to larger RMSE for R_{DSD}. For GMRE with 20 mixtures, the better performance of R_{DSD} is obtained due to more accurate estimates of N_0 and Λ. As the number of mixtures increases, the performance of R_{DSD} improves, but it will not surpass R_G. Therefore, R_{DSD} will not be considered in later discussion.

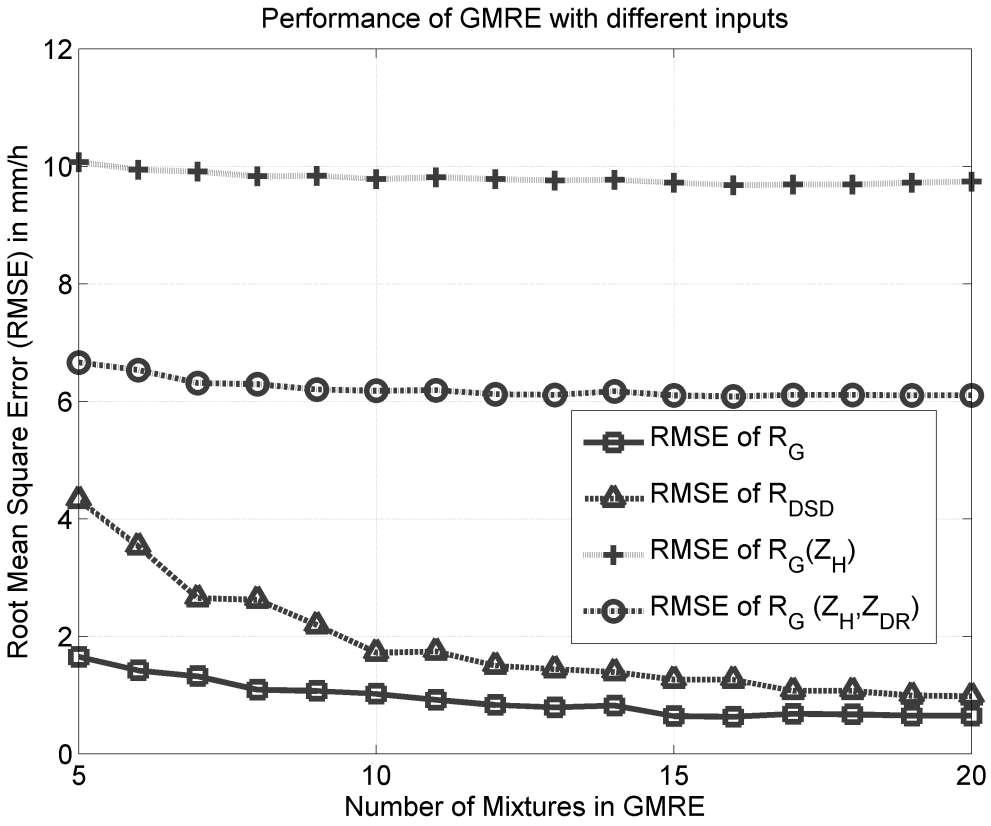


Figure 5.12: RMSEs of GMRE with different inputs as number of mixtures Increases.

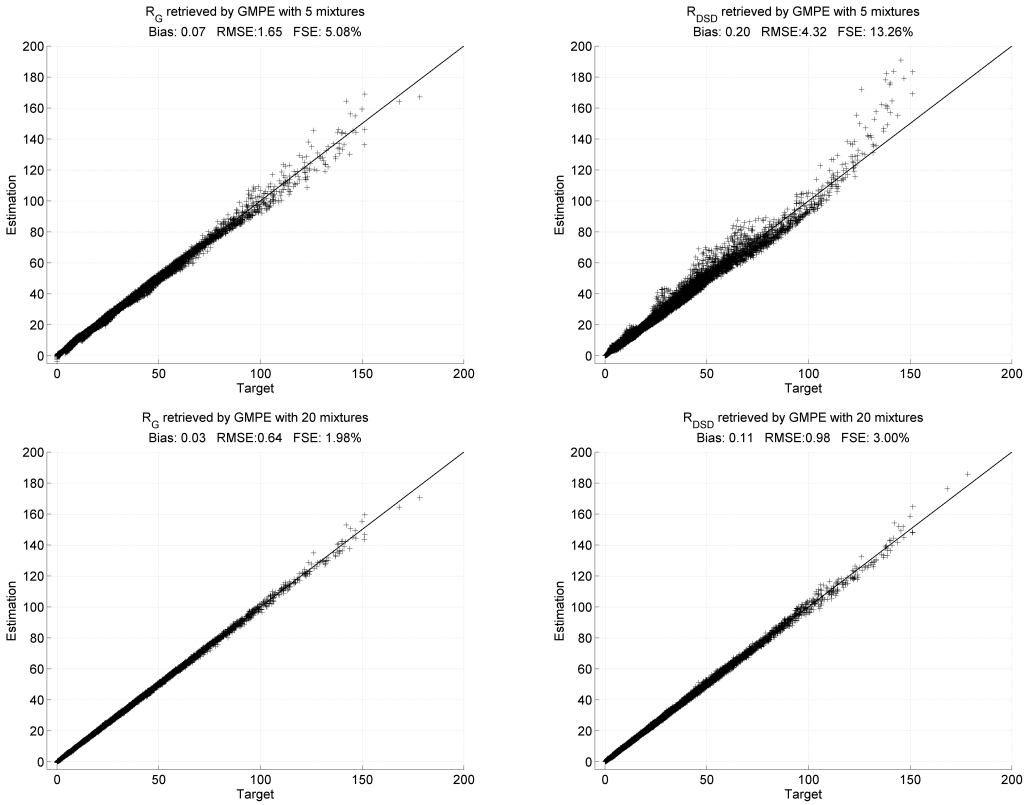


Figure 5.13: Plots of estimated rainfall rate and true rainfall rate for simulation dataset. From left to right and top to bottom, (a) R_G retrieved by GMRE with 5 mixtures, (b) R_{DSD} retrieved by GMRE with 5 mixtures, (c) R_G retrieved by GMRE with 20 mixtures, (d) R_{DSD} retrieved by GMRE with 20 mixtures. Bias and RMSE are in [mm hr^{-1}] for all plots.

The above simulation results indicate that if GMRE is trained from a dataset whose distribution matches that of the testing dataset, the GMRE with more mixtures has better performance since GMM converges closer to the "true" distribution as the number of mixtures increases. Also, these simulation results assume a noise-free environment which means noise covariance matrix $\mathbf{R} = 0$. In terms of the performance of the GMRE in a noisy environment, it has been shown that estimation from GMRE is robust when the observations contain Gaussian noise (Li and Zhang 2011). As long as the Gaussian noise assumption holds, GMRE would remain a minimum-variance and unbiased estimator.

5.4.3 JPOLE Dataset Description

The JPOLE dataset is a polarimetric radar dataset collected between 2002 and 2005 in central Oklahoma using the KOUN WSR-88D-quality radar. A total of 43 events of various precipitation types, including warm-season convective storms containing hail, mesoscale convective systems (MCS) with intense squall lines and trailing stratiform precipitation, widespread cold-season stratiform rain, and select tropical storm remnants, are observed and selected for analysis (Giangrande and Ryzhkov 2008). Concurrent gauge observations from the densely spaced Agricultural Research Service (ARS) and Oklahoma Mesonet (MES) network stations located at 50-150 km (e.g., Fiebrich et al. 2006; McPherson et al. 2007; Shafer et al. 2000) from the KOUN radar are also included with this dataset.

Dual-polarized measurements (Z_H and Z_{DR}) from KOUN have been compared and calibrated using cross-comparison with disdrometer, the nearby KTLX radar (Oklahoma City WSR-88D) and polarimetric signatures of dry aggregated snow above the melting level. Attenuation correction in rain has been performed on Z_H and Z_{DR} using differential phase Φ_{dp}. Non-meteorological echoes are filtered by a $\rho_{hv} > 0.85$ threshold. To mitigate hail contamination, the $Z_H < 53$ [dBZ] and $0 < Z_{DR} < 5$

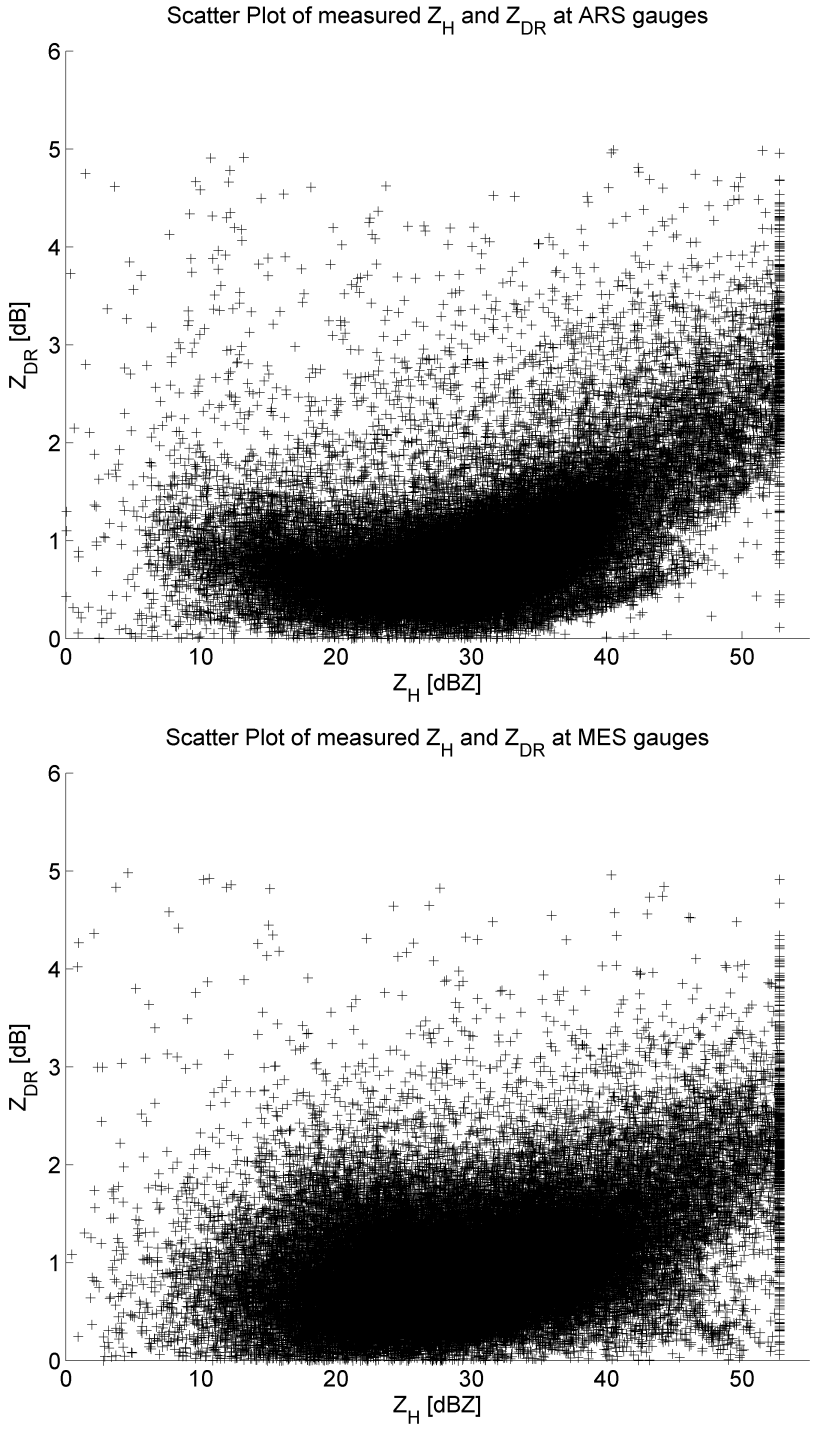


Figure 5.14: Scatter plots of measurement dataset. From top to bottom, (a) Scatter plot of measured Z_H and Z_{DR} at ARS gauges. (b) Scatter plot of measured Z_H and Z_{DR} at MES gauges.

[dB] threshold were applied. Gauges further than 150 km from the radar have been removed to avoid/reduce partial beam filling and melting layer effects. Figs. 5.14(a) and 5.14(b) show scatter plots of the Z_H and Z_{DR} measured at ARS and MES gauges. Compared to the scatter plots from the simulation, clear differences in distributions can be observed. There are extensive observations between 10 to 40 [dBZ] in the JPOLE dataset and the majority of the KOUN pairings have $Z_{DR} < 3$ [dB].

If *hourly radar accumulations* are defined as an hourly rainfall estimate centered on a gauge, validation of GMRE can be performed by comparing hourly gauge and radar rainfall accumulations over gauge locations. Since usually only 8-9 radar scans are available over the same gauge location within one hour, the nearest neighbor interpolation method is used to calculate hourly radar accumulations.

5.4.4 Results and Comparisons

For a performance comparison of the GMRE approach, three rainfall rate retrieval algorithms are selected. These relations are PLR-form, based on an empirical regression of the measured gauge (or, video disdrometer) and radar data. The first one, with Z_h as the only input, is the inversion of the standard NEXRAD rainfall formula for continental (nontropical) application (Fulton et al. 1998).

$$R(Z_h) = 1.7 \times 10^{-2} Z_h^{0.714} \tag{5.23}$$

The second one, with Z_h and Z_{dr} as inputs, had optimized performance for rain in central Oklahoma during the JPOLE field campaign (Ryzhkov et al. 2005a).

$$R(Z_h, Z_{dr}) = 1.42 \times 10^{-2} Z_h^{0.77} Z_{dr}^{-1.67} \tag{5.24}$$

The third, proposed in Ryzhkov et al. (2005b), combines the merits of different algorithms for various rain intensities and uses different combinations of radar variables Z_h, Z_{dr} and K_{dp} based on rainfall rate estimated from equation (18):

$$R_{SYN} = \begin{cases} R(Z_h)/(0.4 + 5.0|Z_{dr} - 1|^{1.3}) & R(Z_h) < 6 \\ 44.0|K_{dp}|^{0.822} sign(K_{dp})/(0.4 + 3.5|Z_{dr} - 1|^{1.7}) & 6 < R(Z_h) < 50 \\ 44.0|K_{dp}|^{0.822} sign(K_{dp}) & R(Z_h) > 50 \end{cases} \quad (5.25)$$

Note that the polarimetric algorithms Eq. (5.24) and Eq. (5.25) have been optimized to perform well over the entire JPOLE dataset and were proven in later studies to be solid references for Oklahoma precipitation climatology. In comparison, since the GMRE is constructed from a simulation dataset generated from general microphysical parameterization, it can be applied to other precipitation regimes.

Two GMREs, one with 5 mixtures ($G5$) and the other with 20 mixtures ($G20$), are tested using this JPOLE dataset. Since noise properties of different dual-polarization variables in the JPOLE dataset are unknown, $\mathbf{R}$ is set to be zero in the current implementation. As FSE statistics are heavily weighted toward small hourly precipitation accumulations, they are not examined during this test. Table 5.9 and Table 5.10 summarize the results and comparisons of all retrieval algorithms over the ARS and MES gauges.

Table 5.9: Performance comparison of rainfall retrieval algorithms for the ARS dataset. All in [mm hr^{-1}]

	$R(Z_h)$	$R(Z_h, Z_{dr})$	R_{SYN}	$R_{G5}(Z_H)$	$R_{G5}(Z_H, Z_{DR})$	R_{G5}	R_{G20}
Bias	1.68	-0.01	-0.24	-2.12	-0.80	-0.04	-0.49
STD	5.36	3.03	2.90	4.26	3.52	2.76	2.87
RMSE	5.62	3.03	2.91	4.76	3.61	2.76	2.91

With reflectivity Z_H as input, $R_{G5}(Z_H)$ outperforms conventional NEXRAD $R(Z_h)$ in terms of RMSE for both datasets. With Z_H and Z_{DR} as inputs, $R_{G5}(Z_H, Z_{DR})$

Table 5.10: Performance comparison of rainfall retrieval algorithms for the MES dataset. All in [mm hr^{-1}]

	$R(Z_h)$	$R(Z_h, Z_{dr})$	R_{SYN}	$R_{G5}(Z_H)$	$R_{G5}(Z_H, Z_{DR})$	R_{G5}	R_{G20}
Bias	1.58	0.31	-0.3	-1.76	-0.57	0.19	-0.27
STD	5.24	4.44	3.12	4.56	4.05	2.98	3.30
RMSE	5.47	4.45	3.13	4.88	4.09	2.99	3.31

performs slightly worse than the JPOLE $R(Z_h, Z_{dr})$ relation for the ARS dataset, but better for the MES dataset in terms of RMSE. With full polarimetric inputs Z_H, Z_{DR} and K_{dp}, R_{G5} has the best performance in every category for both datasets. R_{G20} is comparable to R_{SYN} for the closer ARS dataset, but slightly worse than R_{SYN} for the MES dataset. All estimates but one from the GMREs show a negative bias, probably due to the fact that they are trained from a dataset that favors smaller rainfall. From the previous section, the GMRE with 20 mixtures converges closer to the distribution of the simulation dataset (denoted as $p_s(\mathbf{x})$), while the GMRE with five mixtures is only able to represent a general outline of $p_s(\mathbf{x})$ without many details. However, since $p_s(\mathbf{x})$ does not precisely match the distribution of the KOUN-based measurement dataset (denoted as $p_m(\mathbf{x})$), the GMRE with 20 mixtures is apparently over-fitted to $p_s(\mathbf{x})$ and prohibits optimal performance in $p_m(\mathbf{x})$. However, the GMRE with five mixtures can outperform the JPOLE-tuned synthetic R_{SYN} relation in terms of bias and RMSE, even though it represents a less detailed $p_s(\mathbf{x})$ as highlighted in Fig. 5.15 and Fig. 5.16.

It is interesting to compare the performance of the simulation dataset-trained GMRE in this study with the neural network approach introduced in Vulpiani et al. (2009) for the same ARS dataset. For these particular events (table 2 in Vulpiani et al. (2009) and Table 5.9 in this study), both the neural network and GMRE approach outperformed the synthetic relation, with the five-mixture GMRE showing a slightly better performance overall in terms of bias, STD and RMSE.

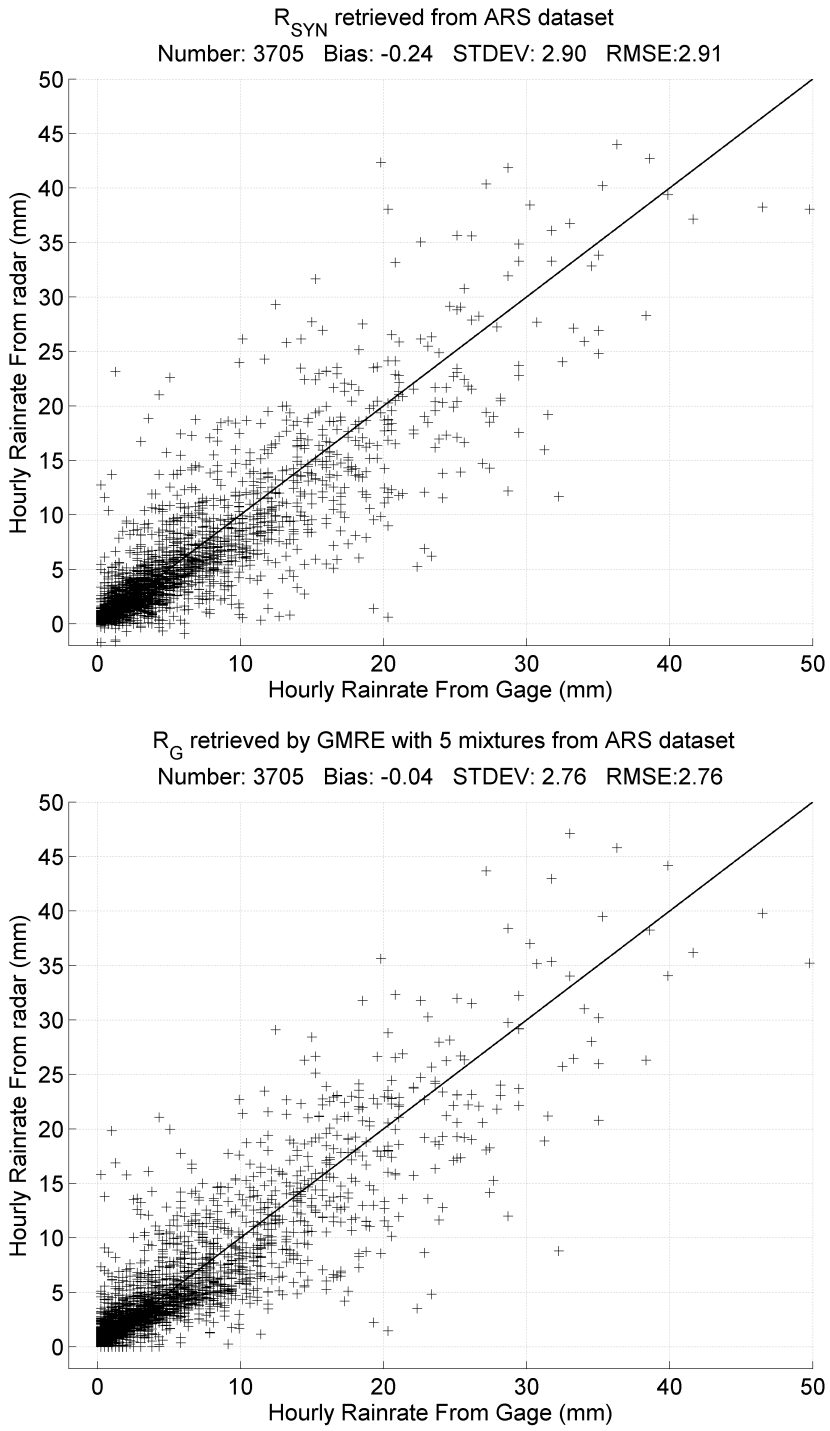


Figure 5.15: Comparison plots of radar-gauge hourly accumulated rainfall rate for ARS dataset. From top to bottom, (a) R_{SYN} retrieved from ARS dataset. (b) R_G retrieved by GMRE with 5 mixtures from ARS dataset. Bias, STD and RMSE are in [mm] for both plots.

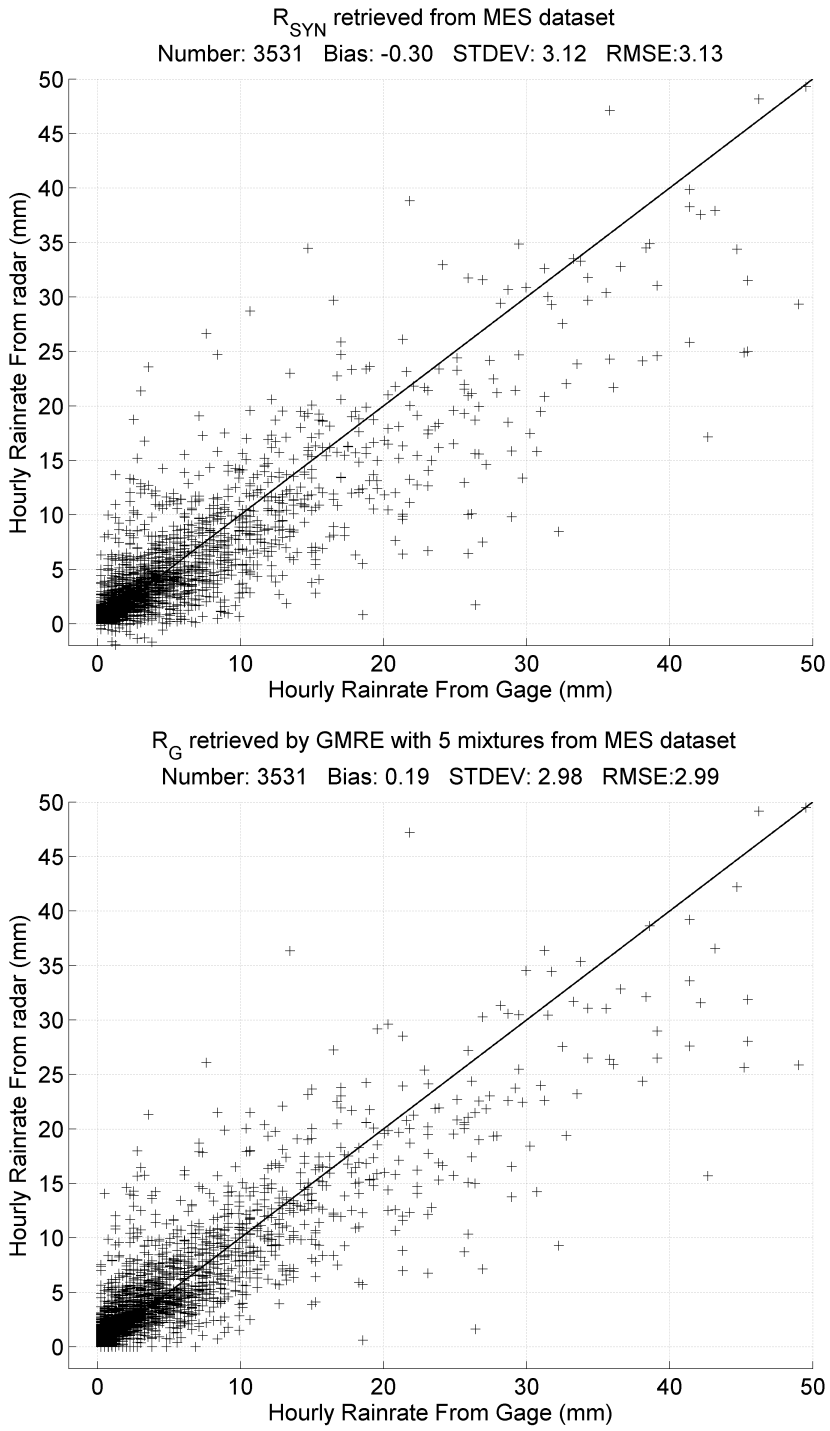


Figure 5.16: Comparison plots of radar-gauge hourly accumulated rainfall rate for MES dataset. From top to bottom, (a) R_{SYN} retrieved from MES dataset. (b) R_G retrieved by GMRE with 5 mixtures from MES dataset. Bias, STD and RMSE are in [mm] for both plots.

These results confirmed that if GMRE is trained from a dataset whose distribution does not precisely match (but approximates) the distribution of the testing dataset, GMRE is still able to perform very well. When $p_s(\mathbf{x}) \neq p_m(\mathbf{x})$, the GMRE with less mixtures may perform even better than the GMRE with more mixtures, which could be over-fitted to $p_s(\mathbf{x})$. However, depending on how $p_s(\mathbf{x})$ approximates $p_m(\mathbf{x})$ and how much $p_s(\mathbf{x})$ and $p_m(\mathbf{x})$ resemble, the optimal number of mixtures may vary. For example, comparing the dark blue area and light blue area where Z_H is between 15 [dBZ] and 50 [dBZ] in both Fig. 5.11(a) and 5.11(b) with the same areas in Fig. 5.14(a) and 5.14(b), the distribution of $G5$ (Fig. 5.11(a)) at this area is clearly much closer to the same area of Fig. 5.14(a) and 5.14(b) than $G20$ (Fig. 5.11(b)). This explains why R_{G5} outperforms R_{G20} in both ARS and MES datasets. It also explains why extreme cases in the training dataset will not affect the performance of GMRE since only the relative probabilities of cases at areas of interest matter. As a consequence, GMRE should be trained from a "large" $p_s(\mathbf{x})$ that covers a broader range of occurrences than $p_m(\mathbf{x})$ (such as the extreme cases covered in the simulation of this study), to ensure that it is capable of handling not only a particular dataset, but also the radar observations from different seasons/regions.

5.4.5 Discussion and Conclusions for GMRE Study

This study develops a Gaussian Mixture Rainfall-rate Estimator for polarimetric radar-based rainfall rate estimation. Theoretically, GMRE is the optimal estimator in terms of minimum-variance and unbiased performance. It is also a general and flexible approach that can be adapted easily to different observation variables and rain types without compromising its performance. The training dataset for GMRE is constructed from a single cell Monte-Carlo simulation where the parameters of exponential DSD, N_0 and W, are randomly generated from designed distributions that favor light and moderate rain.

GMREs with a different number of mixtures are trained and tested using the general simulation dataset. With more mixtures, the GMM converges more readily to the simulation distribution, leading to better estimation. For the same radar observations, the rainfall rate directly estimated from the radar moments (R_G) is more precise than the rainfall rate retrieved from taking an indirect path through the estimated DSD parameters (R_{DSD}) wherein estimation error accumulates and magnifies.

Two GMREs, one with 5 mixtures and the other with 20 mixtures, in company with three PLR algorithms, are tested using the JPOLE dataset. As expected, better results are achieved when more radar observation variables are available for both GMRE and PLR algorithms. While $R_{G5}(Z_H, Z_{DR})$ has a performance comparable to $R(Z_h, Z_{dr})$, $R_{G5}(Z_H)$ performs better than single-parameter $R(Z_h)$ and R_{G5} outperforms the synthetic R_{SYN} JPOLE relation, which is the standard benchmark for this JPOLE dataset. R_{G20} does not perform as well as R_{G5}, which can be attributed to over-fitting the GMRE to the specific simulation distribution that is dissimilar to the KOUN radar measurement distribution. Estimates from GMREs generally have a negative bias that may reflect that these methods were trained from datasets that favor smaller rainfall over heavier rainfall, and also the fact that KOUN polarimetric radar inputs such as specific differential phase that are smoothed somewhat in space-time.

In conclusion, GMRE shows great promise over conventional PLR techniques and provides a statistically optimized solution for rainfall rate estimation.The convergence capability of GMM provides a general framework to accommodate extra information not only from dual-polarization diversities, but also from other diversities such as multiple frequencies. A subject of ongoing research is to combine ground-based radar measurement with Ku-Ka band satellite radar measurements into the GMRE for

better quantitative precipitation estimation (QPE). Since GMRE is a "best" estimator in terms of variance and bias performance, as long as the prior distribution is accurate, the focuses of rainfall rate retrievals may be shifted from developing new algorithms/coefficients to constructing a better training dataset for GMRE. For example, better performance of GMRE may be achieved by tuning the distribution of N_0 and W in Monte-Carlo simulations. If GMRE is trained from a dataset, either from simulation or measurement, without any climatologically driven optimization, a global GMRE is possible for all rain types and regions. It is worth mentioning that applications of GMRE are not limited to S-band. Similarly, a GMRE can also be built for C-band or X-band radars. Like other rainfall rate estimation techniques, inputs to GMPE have to be corrected from attenuation before they could be used especially in C-band and X-band. Attenuation correlations using GMPE are studied in section 5.5.

5.5 Correction of Rain Path Attenuation: A Constrained Iterative GMPE Approach

This section extends the GMPE approach in an iterative form for path-integrated attenuation (PIA) correction of rain to retrieve both horizontal reflectivity and differential reflectivity using polarimetric radar measurements. Similar to algorithms that employ differential phase constraint, PIA of previous range bins is estimated from GMPE using only differential phase (K_{dp}) as input. Corrected power measurements as well as different phase of the current range bin are then input to GMPE again to acquire more accurate estimations. Performance of the proposed method is evaluated using X-band radar measurements from simulated radar range profiles generated under different microphysical scenarios.

5.5.1 Introduction

Polarization diversity of weather radar systems is known to provide valuable information for meteorological applications, such as rainfall rate estimation, DSD retrieval and hydrometeor classification. Affected by path-integrated attenuation (PIA) similar to single-polarized radar, successful applications of polarimetric radar measurement have been demonstrated mostly at S-band where rainfall rate estimation algorithms are well developed (e.g., Gorgucci et al. 2002; Brandes et al. 2002; Vulpiani et al. 2009; Cao et al. 2010). For frequencies higher than S-band, path attenuation effects caused by rainfall become significant and need to be corrected before power measurement can be used quantitatively.

For single-polarized radar, attenuation correction is limited by a power law relation between reflectivity and specific attenuation where the solution of a Riccati differential equation is obtained and applied to the first range bin that intercepts the rain cell and iteratively proceeded forward till the last bin. This approach is often unstable especially in strong precipitation events where PIA is high. Phase measurement, on the other hand, is immune to attenuation effects, which makes it a good candidate for correcting attenuation. Algorithms based on polarimetric radar measurement are greatly improved as total differential propagation phase between horizontal and vertical polarization is available, which can be linked to total PIA through a linear relation as a constraint. One of the algorithms that adopt differential phase constraint, the ZPHI algorithm, is described and evaluated in Testud et al. (2000). Bringi et al. (2001) further improved this algorithm by introducing a self-consistent scheme, where Z_{dr} correction is also included. Vulpiani et al. (2005) replaced the power law relation with a Neural Network approach but still employed the differential phase constraint. A fully self-consistent approach is introduced in Gorgucci et al. (2006) where a fixed power low relation between A_h and Z_h, Z_{dr}, K_{dp} is employed. Though coefficients of the power law relations are adjusted to obtain the

best performance, a fixed model is often applied to a whole range profile. Problems with differential phase constraint methods or the fully self-consistent approach come from the deterministic power law or linear models that have been used as deterministic models fail to account for the fact that microphysics such as drop size distribution (DSD), drop shape model as well as temperature varies in space and time even within the same precipitation.

5.5.2 Review of PIA Correction Techniques

Consider a range profile with rain in presence. Let r_0 is the beginning of the first range bin that contains rain and r_k represent the end point of the kth range bin. The two-way copular and differential path-integrated attenuation PIA_H and PIA_{DP} (both with unit [dB]) at r_k can be calculated from integrating A_h and A_{dp} [dB km^{-1}], which are the one-way specific power attenuation and differential power attenuation, over the path (from r_0 to r_k) as shown in Eq. (5.26).

$$PIA_H(r_0, r_k) = 2\int_{r_0}^{r_k} A_h(s)ds \tag{5.26a}$$

$$PIA_{DP}(r_0, r_k) = 2\int_{r_0}^{r_k} A_{dp}(s)ds. \tag{5.26b}$$

Similarly, the incremental two-way differential phase shift between r_0 and r_k can be defined as

$$\Delta\Phi_{DP}(r_0, r_k) = 2\int_{r_0}^{r_k} K_{dp}(s)ds = \Phi_{DP}(r_k) - \Phi_{DP}(r_0). \tag{5.27}$$

Note that, the effects of backscattering differential phase δ_{hv} (defined in Eq. (2.28b)) are neglected assuming an effective iterative filer is applied on $\Delta\Phi^m_{DP}$ (Vulpiani et al. 2008) (superscript m stands for measured). Eq. (5.26) and Eq. (5.27) can further written in a discrete form as K_{dp}, A_h and A_{dp} are assumed to be constant within one

range bin. Under this assumption, K_{dp}, A_h and A_{dp} may be viewed as the average quantity over one range bin.

$$PIA_H(r_k) = 2\sum_{i=1}^{k} A_h(r_i)\Delta r \tag{5.28a}$$

$$PIA_{DP}(r_k) = 2\sum_{i=1}^{k} A_{dp}(r_i)\Delta r. \tag{5.28b}$$

$$K_{dp}(r_k) = \frac{\Delta\Phi_{DP}(r_{k-1}, r_k)}{2\Delta r}. \tag{5.29}$$

Contaminated by path attenuation, the measured copular reflectivity factor $Z_H^m(r_k)$ [dBZ] and differential reflectivity factor $Z_{DR}^m(r_k)$ [dB] at r_k can be formulated as (measurement noise term is dropped for convenience)

$$Z_H^m(r_k) = Z_H(r_k) - PIA_H(r_k), \tag{5.30a}$$

$$Z_{DR}^m(r_k) = Z_{DR}(r_k) - PIA_{DP}(r_k). \tag{5.30b}$$

From Eq. (5.30), it is clear that path attenuation has to be accurately estimated and compensated before power measurements can be used quantitatively.

Early attempts to compensate for attenuation assume A_x is related to Z_x as

$$A_x = a_x Z_x^{b_x}, \tag{5.31}$$

where x can be h or v polarization. Assuming b_x is constant in range, Eq. (5.31) can be written as a differential equation and solved if proper boundary condition is taken. This relation is often unstable and easily affected by noise and radar calibration error. Since phase measurements are not affected by attenuation, parameterizations of A_h, A_v using K_{dp} are essential in many attenuation correction algorithms as shown in the following equation (x can be h or v).

$$A_x = \alpha_x K_{dp}^{\beta_x}. \tag{5.32}$$

It is worth mentioning that exponents β_h and β_v are close to unity between 2.8 to 10 GHz (Park et al. 2005). Therefore, Eq. (5.32) is often approximated by a

linear form (shown in Eq. (5.33)) and called specific attenuation-differential phase parameterization (DP) method.

$$A_x = \alpha_x K_{dp}. \tag{5.33}$$

Combined Eq. (5.26), Eq. (5.27) and Eq. (5.33), cumulative attenuation to the ending point of the path can be estimated from the total change of differential propagation phase as shown in the following equation

$$PIA_H(r_0, r_N) = \alpha_h \Delta\Phi_{DP}(r_0, r_N), \tag{5.34}$$

where r_N is the ending point of the path. A more stable approach (shown in Eq. (5.35)), which is termed ZPHI, is developed under the constraint that $PIA_H(r_0, r_N)$ must be consistent with $\Delta\Phi_{DP}(r_0, r_N)$ (Testud et al. 2000).

$$A_h(r) = \frac{[Z_h^m(r)]^{b_h}[10^{0.1 b_h \alpha_h \Delta\Phi_{DP}(r_0, r_N)} - 1]}{I(r_0, r_N) + [10^{0.1 b_h \alpha_h \Delta\Phi_{DP}(r_0, r_N)} - 1] I(r, r_N)}. \tag{5.35}$$

Function $I(r_1, r_2)$ in Eq. (5.35) is defined as

$$I(r_1, r_2) = 0.46 b_h \int_{r_1}^{r_2} [Z_h^m(s)]^{b_h} ds, \tag{5.36}$$

where coefficient b_h is from the parameterization of A_h using Z_h (Eq. (5.31)). In ZPHI algorithm, coefficient α_h is fixed. However, it is shown in many studies that α_h is not constant but varies widely with temperature and drop shape. To overcome the impact of such variability, Bringi et al. (2001) extended the ZPHI algorithm and introduced a self-consistent with constraints (SCWC) method, where minimum difference between the filtered $\Phi_{DP}^f(r)$ and the calculated (or estimated) $\Phi_{DP}^c(r; \alpha_h)$ over the entire path is obtained while searching an optimal α_h value within a predetermined range as given in Eq. (5.37) and Eq. (5.38). In simulations at X-band performed by Park et al. (2005), the range for α_h is between 0.173 and 0.315. In this study, a larger range for α_h is adopted which is from 0.150 to 0.350.

$$\Phi_{DP}^c(r) = 2 \int_{r_0}^{r} \frac{A_h(s :, \alpha_h)}{\alpha_h} ds. \tag{5.37}$$

$$\alpha_{opt} = \underset{0.15 \le \alpha_h \le 0.35}{\arg\min} \sum_{i=1}^{N} |\Phi_{DP}^{c}(r_0, r_i; \alpha_h) - \Phi_{DP}^{f}(r_0, r_i)| \tag{5.38}$$

In the self-consistent method, A_{DP} is obtained from $A_{DP}(r) = \gamma A_H(r)$ where optimal γ value is determined as

$$\gamma_{opt} = \frac{1}{\alpha_{opt}} \frac{|Z_{DR}^{m}(r_N) - Z_{DR}(r_N)|}{\Delta\Phi_{DP}(r_0, r_N)}, \tag{5.39}$$

where $Z_{DR}(r_N)$ can be estimated from the corrected $Z_H(r_N)$ using relation (Park et al. 2005)

$$Z_{DR}(r_N) = \begin{cases} 0 & \text{when } Z_H(r_N) \le 10 \text{ [dBZ]} \\ 0.0528 Z_H(r_N) - 0.511 & \text{when } 10 \le Z_H(r_N) \le 55 \text{[dBZ]} \\ 2.39 & \text{when } Z_H(r_N) \ge 55 \text{[dBZ]} \end{cases} \tag{5.40}$$

Another PIA correction algorithm, the final value (FV) algorithm, is also implemented in this study as it is claimed to be more accurate than the ZPHI approach when the radar is well calibrated (Marzano et al. 2010). In FV algorithm, Z_h and Z_v are recovered from

$$Z_x(r) = \frac{Z_x^{m}(r)}{[10^{0.1 b_x \alpha_x \Delta\Phi_{DP}(r_0, r_N)} + \alpha_x [I(r_0, r_N) - I(r_0, r)]]^{\frac{1}{b_x}}}, \tag{5.41}$$

where function $I(r_1, r_2)$ is defined in Eq. (5.36). Required constants for the four attenuation correction schemes can be found in Table 5.11. Note that, for DP and FV methods, corrected Z_{DR} is computed from corrected Z_H and Z_V.

Table 5.11: Required constants for Eq. (5.32) and Eq. (5.31)

$A_x = \alpha_x K_{dp}$		$A_x = a_x Z_x^{b_x}$			
α_h	α_v	a_h	b_h	a_v	b_v
0.3292	0.2827	1.5142×10^{-4}	0.7840	1.3375×10^{-4}	0.8169

5.5.3 Constrained Iterative GMPE Approach

GMPE is set up without considerations of radar beam path. For correction of path attenuation, Eq. (5.2) is further written in a iterative form as

$$\mathbf{z}_k = \mathbf{H}\mathbf{x}_k + \mathbf{v}_k \tag{5.42}$$

to outline the range dependency of observation, state vector and noise vector, where subscript k stands for the kth range bin. For PIA correction, the state vector is set at $\mathbf{x} = [A_h, A_{dp}, Z_H, Z_{DR}, K_{dp}]^T$. Similar to DP approach, a direct way of applying GMRE is to use phase measurement only and set $\mathbf{z}_k = [K^m_{dp}(r_k)]$. Accordingly, $\mathbf{H} = [0, 0, 0, 0, 1]$. This method will be referred as DP-GMPE and estimations from DP-GMPE are denoted as $\hat{\mathbf{x}}^p_k$. Block diagram of the DP-GMPE technique is illustrated in Fig. 5.17. According to derivations of GMPE, $\hat{\mathbf{x}}^p_k$ is an unbiased estimate of $\mathbf{x}_k$.

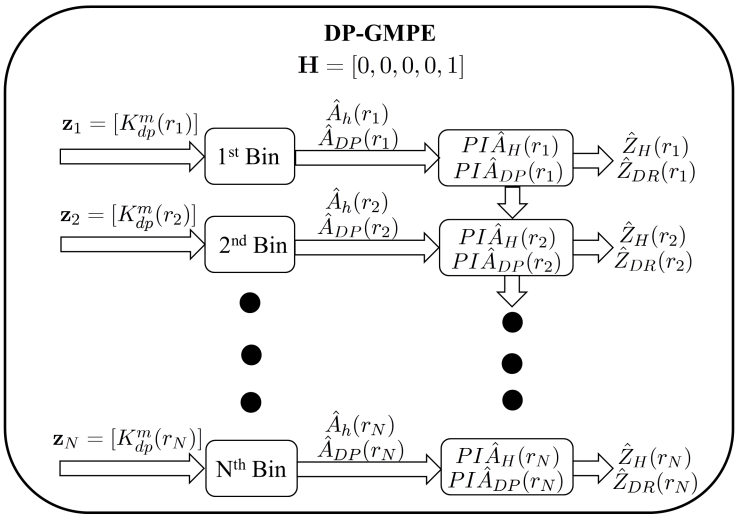


Figure 5.17: Block diagram of the DP-GMPE Algorithm.

While phase measurement $K_{dp}^m(r_k)$ does not depend on estimations from previous range bins, power measurements $Z_H^m(r_k)$ and $Z_{DR}^m(r_k)$ depend not only on path-integrated attenuation from previous bins but also attenuation of the current bin. Therefore, Eq. (5.30) can be written as

$$Z_H^m(r_k) + PIA_H(r_{k-1}) = Z_H(r_k) - 2A_h(r_k)\Delta r \tag{5.43a}$$

$$Z_{DR}^m(r_k) + PIA_{DP}(r_{k-1}) = Z_{DR}(r_k) - 2A_{dp}(r_k)\Delta r \tag{5.43b}$$

In practical applications, $PIA_H(r_{k-1})$ and $PIA_{DP}(r_{k-1})$ are unknown and have to be calculated from estimated $\hat{A}_h(r_i)$ and $\hat{A}_{dp}(r_i)$ $(i = 1, ..., k-1)$ using Eq. (5.28). If power measurement are included as input to GMRE, another way of applying GMRE is to set $\hat{\mathbf{z}}_k = [\hat{Z}_H^m(r_k), \hat{Z}_{DR}^m(r_k), K_{dp}^m(r_k)]$, where

$$\hat{Z}_H^m(r_k) = Z_H^m(r_k) + PI\hat{A}_H(r_{k-1}) \tag{5.44a}$$

$$\hat{Z}_{DR}^m(r_k) = Z_{DR}^m(r_k) + PI\hat{A}_{DP}(r_{k-1}) \tag{5.44b}$$

According to Eq. (5.43), matrix $\mathbf{H}$ becomes

$$\mathbf{H} = \begin{bmatrix} -2\Delta r & 0 & 1 & 0 & 0 \\ 0 & -2\Delta r & 0 & 1 & 0 \\ 0 & 0 & 0 & 0 & 1 \end{bmatrix} \tag{5.45}$$

This method will be referred as Simple-GMRE approach and estimations from Simple-GMRE are denoted as $\hat{\mathbf{x}}_k^s$. It is worth mentioning that distribution of $\hat{\mathbf{z}}_k$ in this case does not match the one shown in Eq. (5.8), therefore, $\hat{\mathbf{x}}_k^s$ is no longer an unbiased estimate of $\mathbf{x}_k$ when $k \geq 2$. Since PIAs are estimated from previous $\hat{\mathbf{x}}_k^s$ and new $\hat{\mathbf{x}}_k^s$ is based on estimated PIAs, the cumulative error would become larger and larger. As a result, this Simple-GMRE approach is extremely unstable even in noise-free environment.

To overcome the instability of Simple-GMPE approach and incorporate both power and phase measurements, a Constrained iterative GMPE (CI-GMRE) approach is developed. The methodology of CI-GMPE is described in Fig. 5.18. In

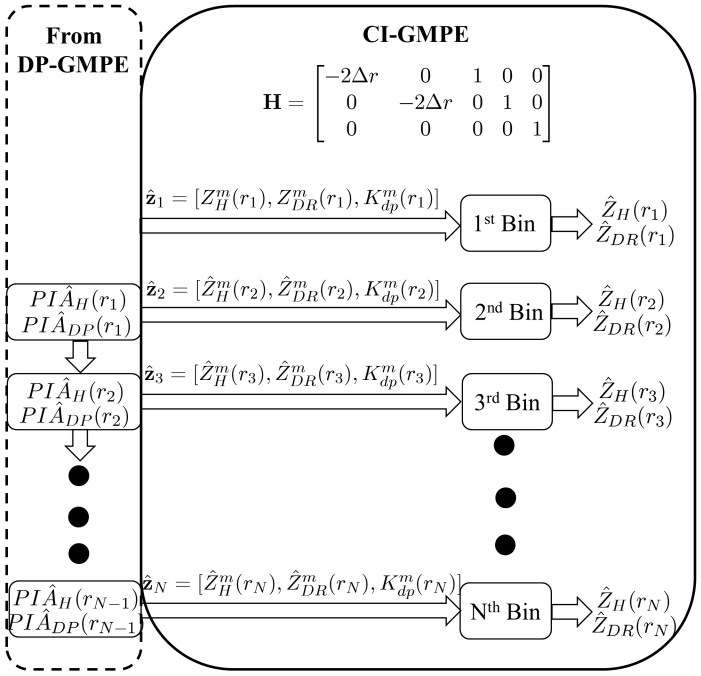


Figure 5.18: Block diagram of the CI-GMPE technique

CI-GMPE approach, at range bin r_k, path-integrated attenuation from previous bins $PI\hat{A}_H(r_{k-1})$ and $PI\hat{A}_{DP}(r_{k-1})$ are calculated using estimates from DP-GMRE method and yields

$$PI\hat{A}_H(r_{k-1}) = 2\sum_{i=1}^{k-1} \hat{\mathbf{x}}_i^p(1)\Delta r \tag{5.46a}$$

$$PI\hat{A}_{DP}(r_{k-1}) = 2\sum_{i=1}^{k-1} \hat{\mathbf{x}}_i^p(2)\Delta r. \tag{5.46b}$$

Similar to Simple-GMPE approach, construct $\hat{\mathbf{z}}_k = [\hat{Z}_H^m(r_k), \hat{Z}_{DR}^m(r_k), K_{dp}^m(r_k)]^T$ ($\hat{Z}_H^m(r_k)$ and $\hat{Z}_{DR}^m(r_k)$ are from Eq. (5.46 and Eq. (5.44)). In this case, distribution of $\hat{\mathbf{z}}_k$ still does not match distribution of $\mathbf{z}_k$ but it is much closer as $E[\hat{\mathbf{z}}_k] = \mathbf{z}_k$, since the estimated PIAs from Eq. (5.46) are unbiased. Therefore, estimations from CI-GMPE, $\hat{\mathbf{x}}_k^c$, is close to $\mathbf{x}_k$ but it is an biased estimate of $\mathbf{x}_k$. However, unlike $\hat{\mathbf{x}}_k^s$, there is no cumulative error in $\hat{\mathbf{x}}_k^c$ as estimation error of path-integrated attenuation is constrained by phase measurement. As a result, CI-GMPE approach is more accurate

than DP-GMPE approach since both power and phase measurement are incorporated and is more stable than the Simple-GMPE approach since there is no accumulated error in estimation.

5.5.4 Simulation Dataset Construction

The singe-cell Monte Carlo simulation (section 3.5) is adopted to generate polarimetric radar measurements at X-band. Raindrop size distribution is represented by a normalized Gamma DSD (Eq. (3.5)) which is widely used in attenuation correction studies (e.g., Bringi et al. 2001; Park et al. 2005; Vulpiani et al. 2005; Gorgucci et al. 2006). Observation studies show that DSD parameters for a normalized Gamma DSD N_w, μ and D_0 varies for different rain type and intensity. Reciprocally, different types of rain may be emulated from randomly generating N_w, μ and D_0 in a reasonable range. In this study, N_w, μ and D_0 are assumed to be uniformly distributed, which leads to equal prior probability for different rain types as in Gorgucci et al. (2006). Table 5.12 lists details of the simulation. It is worth mentioning that 15,000 cases have been carried out to have statistical significance in simulated dataset. To eliminate unrealistic cases and cover most DSD variability, the dataset is limited to Z_H up to 55 [dBZ] and rainfall rates up to 300 [mm hr^{-1}].

The simulation dataset is divided into 2 portions. 12000 cases are used for training and the remaining 3000 cases are used for testing GMPE and other polarimetric attenuation correction algorithms. Scatter plot of Z_H and Z_{DR} from training dataset is shown in Fig. 5.19(a) and the approximate distribution from GMPE with 12 mixtures is shown in Fig. 5.19(b).

Scatter plots of simulated A_h versus Z_h and K_{dp} as well as the fitted power law curves are illustrated in Fig. 5.20. As it can be seen in Fig. 5.20, relation $A_h(K_{dp})$ (defined in Eq. 5.32) has much smaller variance than $A_h(Z_h)$ (defined in Eq. 5.31) in estimated A_h.

Table 5.12: Key Parameters of the Single Cell Monte-Carlo Simulation

Radar frequency	9.41 GHz
Volume of the single cell	125 [m^3]
Temperature	Uniformly between 5^oC to 20^oC
Raindrop size [mm]	0.5 to 8 (step size 0.1)
Canting angle distribution	$\mathcal{N}(0, 10°)$
Scattering model	T-Matrix
Axis ratio of raindrops	Brandes et al. (2002) with randomness
$log_{10}N_w$	Uniformly between 3 to 5
μ	Uniformly between -1 to 4
D_0 [mm]	Uniformly between 0.5 to 3.5

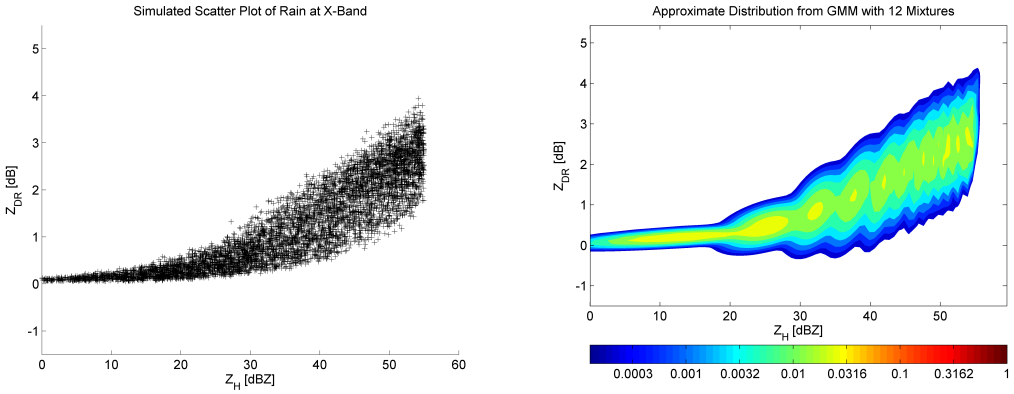


Figure 5.19: Simulated scatter plot of X-band dual-polarized radar signature and approximate distribution from GMM. From left to right, (a) Scatter plot of Z_H and Z_{DR}; (b) Approximate distribution from GMM with 12 mixtures.

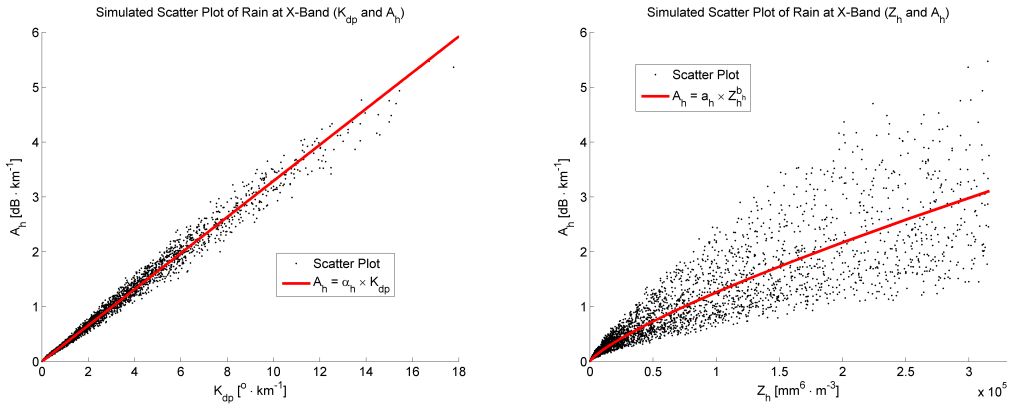


Figure 5.20: Simulated scatter plots of rain and fitted power law relations. From left to right, (a) A_h and K_{dp}; (b) A_h and Z_h

5.5.5 Numerical Results

Power law relations $A_h(K_{dp})$ from Eq. 5.32 and $A_h(Z_h)$ Eq. 5.31 as well as GMPE with different mixtures and inputs are tested using the test dataset. Since the test dataset is noise-free, the attenuation estimation results can be considered as the upper bound of performance for all the PLR-based PIA correction algorithms as well as the two GMPE-based algorithms. Results of GMPE with different inputs and different number of mixtures are illustrated in Fig. 5.21. As it is shown in Fig. 5.21, a GMPE with more than 12 mixtures would converge to its best performance. So a 12-mixture GMPE is constructed for this study. Performance of $A_h(K_{dp})$, $A_h(Z_h)$ and GMPE with 12 mixtures are given in Table 5.13.

As shown in Table 5.13, $A_h(Z_h)$ has the worse performance among the four techniques. With differential phase K_{dp} as input, $A_h(K_{dp})$ and GMPE perform good, while GMPE shows a slightly better performance in terms of RMSE. With input $\mathbf{z} = [Z_H, Z_{DR}, K_{dp}]^T$, GMPE has the best performance due to more variables are included.

To evaluate the performance of proposed approach in presence of PIA, a total of 20 rain paths are constructed from the test dataset. Each rain path consists of 150 range

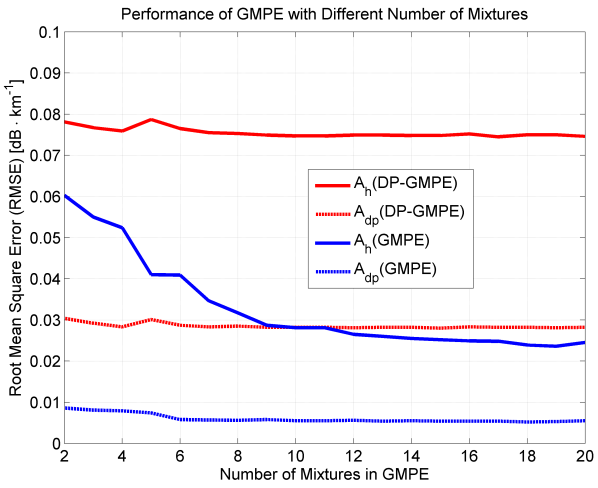


Figure 5.21: RMSEs of GMPE with different inputs as number of mixture increases. DP-GMPE ($\mathbf{z} = [K_{dp}]^T$) and GMPE ($\mathbf{z} = [Z_H, Z_{DR}, K_{dp}]^T$).

Table 5.13: Performance of PLR algorighms and GMPE with 12 mixtures

	A_h [dB km^{-1}]			A_{dp} [dB km^{-1}		
	Bias	SD	RMSE	Bias	SD	RMSE
$A_x = \alpha_x K_{dp}$	-0.0058	0.0783	0.0785	0	0.0304	0.0304
$A_x = a_x Z_x^{b_x}$	-0.0080	0.3574	0.3575	0.0116	0.1114	0.1120
GMPE($\mathbf{z} = [K_{dp}]^T$)	-0.0017	0.0752	0.0752	-0.0006	0.0283	0.0283
GMPE($\mathbf{z} = [Z_H, Z_{DR}, K_{dp}]^T$)	-0.0006	0.0308	0.0308	-0.0001	0.0072	0.0072

bins with the range spacing of 150 [m] and each range bin is a simulated case randomly taken from the test dataset. It can be seem that, such rain paths are not realistic in nature. However, having a rain path with randomly varying DSD parameters is the most challenging scenario for every PIA correction approach and effects from widely varying DSD parameters can be learnt from studying those scenarios. With different levels of noise added to the test dataset, the lower bound of performance for each algorithm can be obtained. Since all cases are from the same test dataset, it is possible to compare the PIA correction performance with single-volume performance in previous performance evaluation of GMPE. 200 realizations, in which there are 20 random paths in each realization, are generated and tested. Table 5.14 and Table 5.15 show the overall bias, SD and RMSE of all PIA correction algorithms for the 20 paths in low noise and high noise environments, respectively. Low noise environment refers to a noise standard deviation of 1 [dB] for Z_H, 0.3 [dB] for Z_{DR} and 2^o for Φ_{dp}. High noise environment refers to a noise standard deviation of 2 [dB] for Z_H, 0.6 [dB] for Z_{DR} and 4^o for Φ_{dp}.

Table 5.14: Performance of different path-integrated attenuation techniques in low noise environment (1 [dB] for Z_H, 0.3 [dB] for Z_{DR} and 2^o for Φ_{dp}). Results are from averaging over 200 realizations and 20 random generated paths.

	Z_H [dBZ]			Z_{DR} [dB]		
	Bias	SD	RMSE	Bias	SD	RMSE
DP	-0.1285	1.2200	1.2269	-0.0085	0.3228	0.3230
ZPHI	0.0033	1.1698	1.1711	0.0430	0.4274	0.4311
SCWC	-0.0630	1.2975	1.3016	0.0260	0.4301	0.4323
FV	0.0584	1.1303	1.1326	-0.0608	0.3312	0.3368
DP-GMPE	0.1099	1.1099	1.1155	-0.0138	0.3162	0.3165
CI-GMPE	0.1403	1.1155	1.1245	0.0412	0.2704	0.2735

Table 5.15: Performance of different path-integrated attenuation techniques in high noise environment (2 [dB] for Z_H, 0.6 [dB] for Z_{DR} and 4^o for Φ_{dp}). Results are from averaging over 200 realizations and 20 random generated paths.

	Z_H [dBZ]			Z_{DR} [dB]		
	Bias	SD	RMSE	Bias	SD	RMSE
DP	-0.1303	2.4043	2.4083	-0.0090	0.6316	0.6317
ZPHI	-0.0070	2.1687	2.1710	0.0338	0.7414	0.7451
SCWC	-0.1072	2.2732	2.2808	0.0186	0.7421	0.7453
FV	-0.1511	2.1077	2.1147	-0.0398	0.6208	0.6222
DP-GMPE	0.3923	2.1076	2.1443	0.0156	0.6113	0.6116
CI-GMPE	0.3568	2.0609	2.0920	0.0624	0.3526	0.3581

As shown in Table 5.14 and Table 5.14, CI-GMPE generally has the best overall performance for recovering attenuated Z_H and Z_{DR} in both low noise and high noise environments. That's because CI-GMPE is able to take advantage of all the phase measurements up to the current radar bin and power measurements of the current bin. Moreover, CI-GMPE performs especially good when correcting attenuation of Z_{DR} in the high noise environment. DP-GMPE claims the second best overall performance among the 6 algorithms. DP-GMPE even outperforms CI-GMPE when correcting attenuation of Z_H in low noise environment, which may be the fact that CI-GMPE includes both power measurements as input bringing in more noise and uncertainties into the system. With the same differential phase K_{dp} as input, the DP technique performs slightly worse than DP-GMPE. The FV algorithm also has very solid performs. It outperforms ZPHI and SCWS algorithms in both low noise and high noise environments. The ZPHI and SCWC algorithms has the worst overall performance due to the fact that they are developed under the assumption that a_h, which relates to N_w, is constant along the path. Since N_w is far from constant in the simulated paths. Large error should expect from these two algorithms. It is worth mentioning that all

PIA correction algorithms in this study depend on phase measurements. While DP, SCWC, DP-GMPE and CI-GMPE require differential phase measurement at every range bin, FV and ZPHI only requires the total differential phase measurement of the path, which make these two more immune to phase measurement noise.

Average error over range from different PIA correction techniques in low noise and high noise environments are illustrated in Fig. 5.22 and Fig. 5.23. Since the results are obtained by taking a average over 20 paths and 200 realizations, it can be seen from those two figures that, CI-GMPE, DP-GMPE and the DP technique are very stable and persistant over the range. The RMSEs of these three algorithms stays around the same level for the whole range. The FV approach and the ZPHI approach is able to stay at a low RMSE level at the beginning but fail at the end of the path where RMSEs of those two approaches increase significantly. The SCWC algorithm is shown very unstable as its RMSE increases as the range increases.

In conclusion, GMPE is successfully extended to correcting path-integrated attenuation. Both proposed GMPE-related approaches, DP-GMPE and CI-GMPE, are capable in PIA correction application. Shown by simulation results, with the same input, DP-GMPE outperforms the conventional DP approach. CI-GMPE also has the best performance in nearly every error category over the ZPHI, SCWC and FV algorithms. However, both DP-GMPE and CI-GMPE are heavily dependent on K_{dp} measurements which are sometimes unreliable. In Chapter 6, GMPE will be further extended to a Kalman filter structure where not only PIA correction but also estimating rainfall rate in high attenuation environment can be achieved with or without phase measurement.

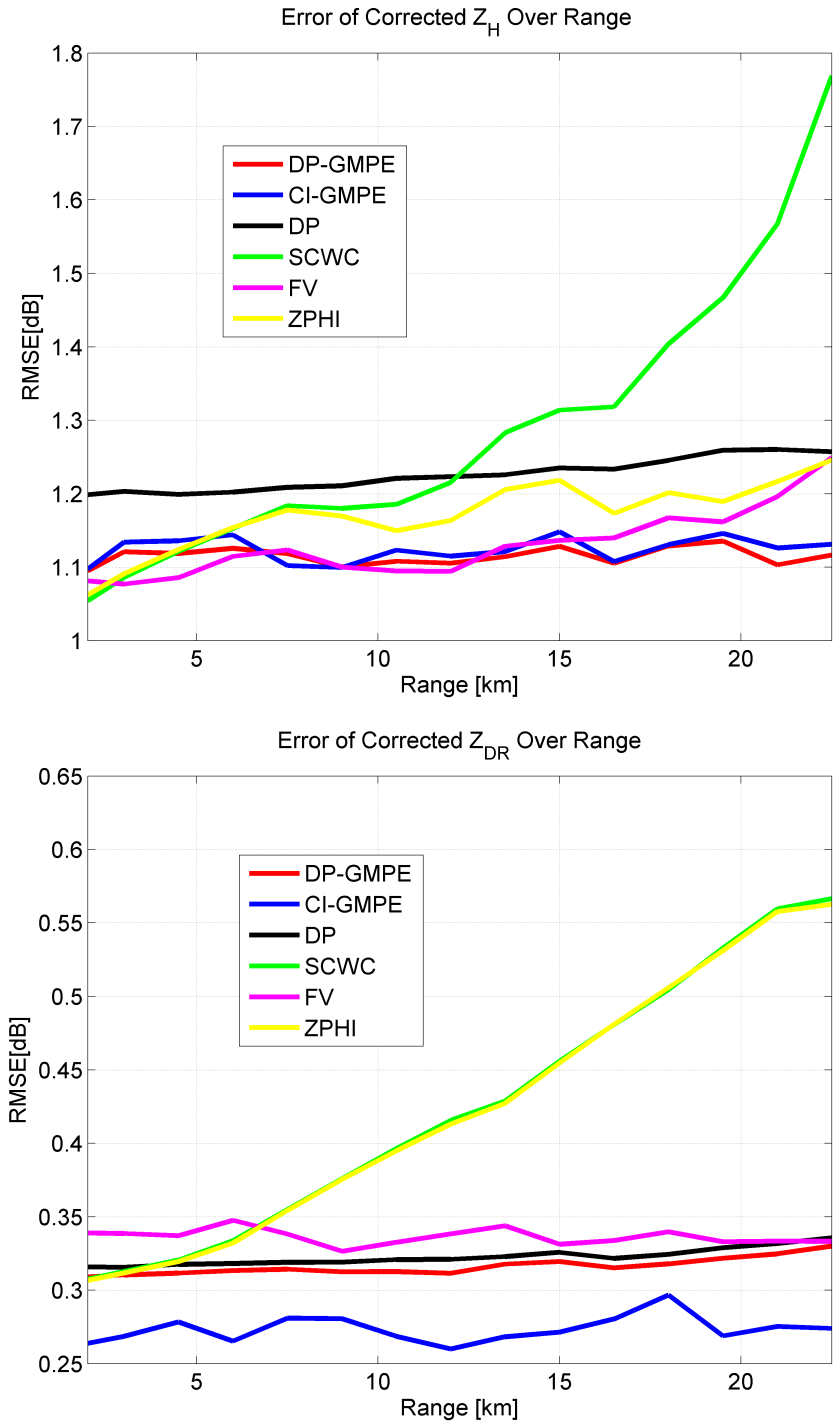


Figure 5.22: Average error over range from different path-integrated attenuation correction techniques in low noise environment (1 [dB] for Z_H, 0.3 [dB] for Z_{DR} and 2^o for Φ_{dp}). From top to bottom, (a) Error of corrected Z_H over range; (b) Error of corrected Z_{DR} over range.

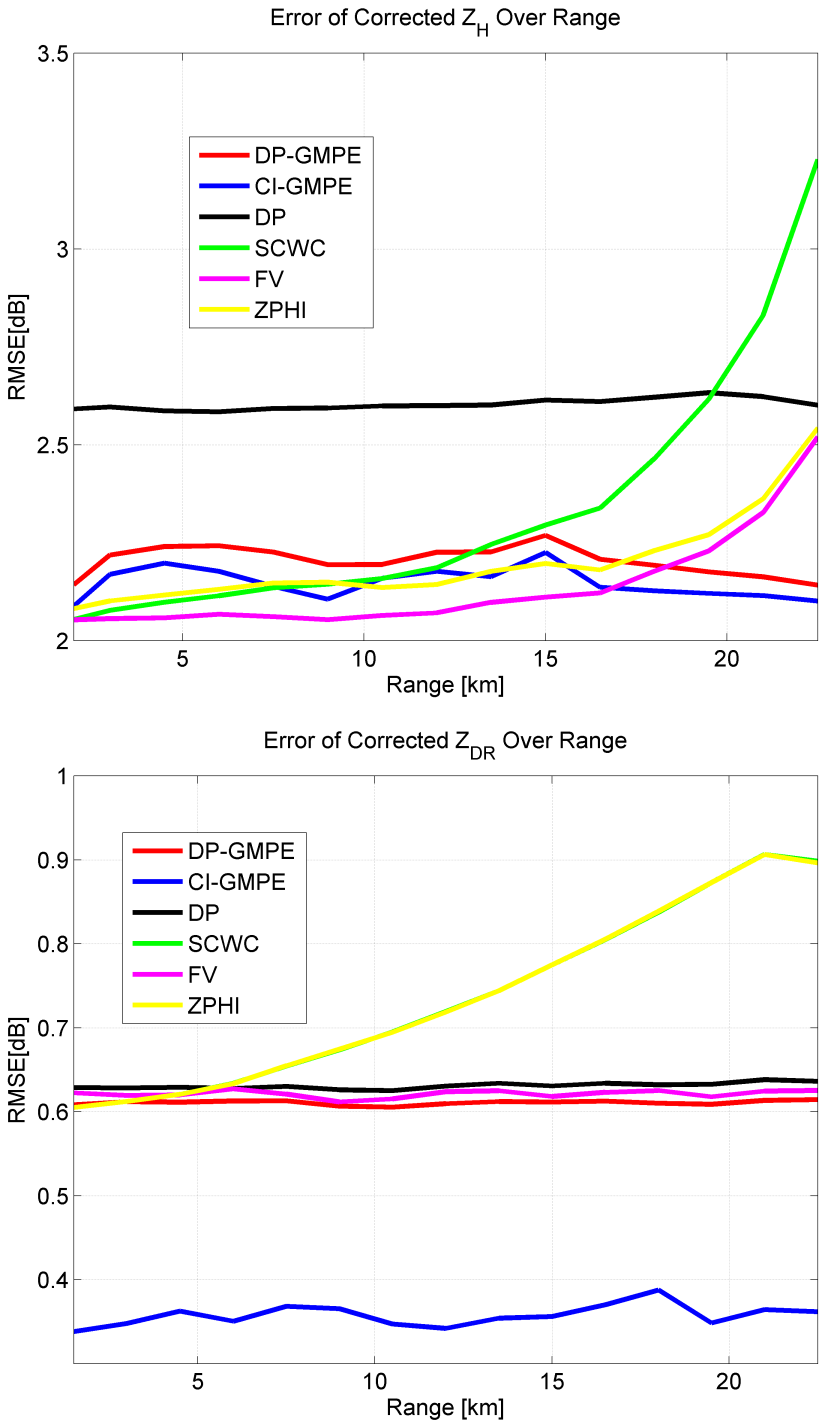


Figure 5.23: Average error over range from different path-integrated attenuation correction techniques in high noise environment (2 [dB] for Z_H, 0.6 [dB] for Z_{DR} and 4^o for Φ_{dp}). From top to bottom, (a) Error of corrected Z_H over range; (b) Error of corrected Z_{DR} over range

Chapter 6

Sequential Gaussian Mixture Parameter Estimator with a Kalman Filter Structure

GMPE developed in Chapter 5 considers only one radar resolution volume/bin. Microphysics parameters and the corresponding radar variables of a radar resolution volume are combined and constructed as state vector $\mathbf{x}$. Radar measurements of a volume are combined and constructed as observation vector $\mathbf{z}$. The estimation problem of a volume is formulated as a linear relation between observation $\mathbf{z}$ and state vector $\mathbf{x}$ with observation noise $\mathbf{v}$. In other word, GMPE is developed under the assumption that observation of a volume $\mathbf{z}$ is affected by only measurement noise $\mathbf{v}$. This assumption holds when attenuation effects are small and can be ignored, such as for S-band radars. This assumption may not hold for radars that have higher frequency than S-band, such as C-band and X-band, where power measurements are contaminated not only by noise but also attenuation.

However, attenuation effects do not prevent the uses of GMPE in higher frequency radars, such as C-hand and X-band. Example of applications of GMPE in X-band is given in section 5.5 where two GMPE-based path-integrated attenuation correction approaches are introduced. Those two approaches, namely DP-GMPE and CI-GMPE, are developed based on the fact that phase measurement is immune from

attenuation effects. The GMPE assumption holds for the DP-GMPE approach as DP-GMPE utilizes only differential phase measurements (K_{dp}) as inputs, which makes the outputs of DP-GMPE minimum-variance and unbiased estimates given the input K_{dp}. No power measurements are involved in DP-GMPE. To take advantage of power measurements, attenuation effects have to be corrected before Z_H and/or Z_{DR} can be used quantitatively. CI-GMPE is developed upon outputs from DP-GMPE. The basic idea is to recover power measurements from PIA effects using attenuation estmated by DP-GMPE. The recovered power measurements with differential phase measurement are then combined as inputs. CI-GMPE approach may be more accurate than DP-GMPE approach since power and phase measurements are incorporated, but the GMPE assumption does not hold for CI-GMPE, therefore, outputs of CI-GMPE are no longer minimum-variance, unbiased estimates.

Weather radars sample the atmosphere in a series of resolution volumes/bins within the radar beam width. Due to attenuation effects, measurements of one volume are dependent on properties of previous volumes. Even though GMPE is developed without the considerations of dependency of radar resolution volumes, its linear structure make it possible to be extended to adopting the Kalman filtering technique which is the basis for the *sequential linear minimum variance estimation*. Due to the unique feature of weather radar observations, GMPE adapts a similar but different sequential filtering structure. Also due to the introduction of Gaussian mixture model, new problems may also arise.

This chapter is organized as follows: derivation of the GMPE with sequential filtering structure, namely the sequential Gaussian mixture parameter estimator (SGMPE), is present in section 6.1, followed by the discussion of Gaussian mixture reductionin section 6.2. Application of SGMPE to rainfall rate estimation in X-band is given in section 6.3 as performance evaluation of SGMPE.

6.1 Sequential Gaussian Mixture Parameter Estimator (SGMPE)

Weather radar measurements, both phase and power, usually consist of contributions from three sources: measurements of current bin, cumulative effects from previous bins and measurement noise. Therefore, the estimation problem can be formulated as

$$\mathbf{z}_k = \mathbf{H}\mathbf{x}_k + \mathbf{y}_k + \mathbf{v}_k, \tag{6.1}$$

where observation vector for the kth range bin $\mathbf{z}_k \in \mathbb{R}^m$, state vector for the kth range bin $\mathbf{x}_k \in \mathbb{R}^n$, accumulation vector for the kth range bin $\mathbf{y}_k \in \mathbb{R}^m$ and noise vector for the kth range bin $\mathbf{v}_k \in \mathbb{R}^m$. Compared with definition of GMPE (Eq. 5.2), range bin denpendency and accumulation vector are added in the definition of the sequential GMPE. Observation matrix $\mathbf{H} \in \mathbb{R}^{m\times n}$ links state vector to observations.

Similar to GMPE, prior distribution of state vector for the kth range bin can be approximated by GMM and is expressed as

$$p(\mathbf{x}_k) \sim \sum_{i=1}^{N} \alpha_i \mathcal{N}(\mu_i, \mathbf{\Sigma}_i) \quad \text{for } k > 0, \tag{6.2}$$

where N is the number of Gaussian components and and α_i, μ_i and $\mathbf{\Sigma}_i$ are the weighting, mean and covariance matrix for the ith Gaussian component in $p(\mathbf{x}_k)$. As it can be seen, same prior distribution has been assumed for all state vectors as no k dependency exists in the right side of Eq. (6.2). This assumption is usually true since weather field within a range bin does not depend on the index of the range bin. Noise $\mathbf{v}_k$ is modelled as zero mean white Gaussian noise from $\mathcal{N}(0, \mathbf{R})$. Distribution of measurement noise also does not have range bin dependency.

According to Eq. (5.28), the two-way copular and differential path-integrated attenuation at r_k can be written as

$$PIA_H(r_k) = PIA_H(r_{k-1}) + 2A_h(r_k)\Delta r \tag{6.3a}$$

$$PIA_{DP}(r_k) = PIA_{DP}(r_{k-1}) + 2A_{dp}(r_k)\Delta r. \tag{6.3b}$$

Similarly, the incremental two-way differential phase shift between r_0 and r_k can be expressed as

$$\Delta\Phi_{DP}(r_0, r_k) = \Delta\Phi_{DP}(r_0, r_{k-1}) + 2K_{dp}(r_k)\Delta r, \tag{6.4}$$

where r_0 is defined as the beginning of the first range bin and r_k represents the end point of the kth range bin. Based on Eq. (6.3) and Eq. (6.4), accumulation vector can be formulated as

$$\mathbf{y}_k = \mathbf{M}\mathbf{x}_{k-1} + \mathbf{y}_{k-1}, \tag{6.5}$$

where accumulation matrix $\mathbf{M} \in \mathbb{R}^{m\times n}$, transfering state vector to accumulation vector. Therefore, a complete expression of the sequential Gaussian mixture estimator is the union of Eq. (6.1) and Eq. (6.5), which can be re-written as

$$\mathbf{y}_{k+1} = \mathbf{y}_k + \mathbf{M}\mathbf{x}_k \tag{6.6a}$$

$$\mathbf{z}_k = \mathbf{y}_k + \mathbf{H}\mathbf{x}_k + \mathbf{v}_k. \tag{6.6b}$$

Note that, subscript in Eq. (6.6a) is modified to match the expression of the model forecast equation in a Kalman filter (Lewis et al. 2006). The expression of the SGMPE is very similar to the expression of a Kalman filter. If $\mathbf{x}_k$ is considered as some kind of noise other than measurement noise, $\mathbf{x}_k$ and $\mathbf{v}_k$ can be combined as the total system noise since they are independent. It can be seen that SGMPE is actually a Kalman filter with state vector $\mathbf{y}_k$. Eq. (6.6a) can be considered as the Model Forecast (MF) step and Eq. (6.6b) can be considered as Data Assimilation (DA) step. It is also worth mentioning that $\mathbf{y}_k$, $\mathbf{x}_k$ and $\mathbf{v}_k$ are assumed to be uncorrelated, which is usually true because white Gaussian noise $\mathbf{v}_k$ is uncorrelated with $\mathbf{y}_k$ or $\mathbf{x}_k$ and $\mathbf{x}_k$, which is the

state vector for the kth bin, is uncorrelated with $\mathbf{y}_k$, which is the accumulated effects from previous bins before the kth bin.

To better derive the SGMPE, let state vector $\mathbf{x}_k = [R, A_h, A_{dp}, Z_H, Z_{DR}, K_{dp}]^T$ for a radar-based rainfall rate estimation application. If observation vector is given as $\mathbf{z}_k = [Z_H^m(r_k), Z_{DR}^m(r_k), \Delta\Phi_{DP}^f(r_0, r_k)]^T$, where superscript m refers to measured and f refers to filtered, observation matrix $\mathbf{H}$ can be constructed as

$$\mathbf{H} = \begin{bmatrix} 0 & -2\Delta r & 0 & 1 & 0 & 0 \\ 0 & 0 & -2\Delta r & 0 & 1 & 0 \\ 0 & 0 & 0 & 0 & 0 & 2\Delta r \end{bmatrix}. \tag{6.7}$$

Therefore, accumulation vector $\mathbf{y}_k = [-PIA_H(r_{k-1}), -PIA_{DP}(r_{k-1}), \Delta\Phi_{DP}(r_0, r_{k-1})]^T$ and accumulation matrix can be constructed as

$$\mathbf{M} = \begin{bmatrix} 0 & -2\Delta r & 0 & 0 & 0 & 0 \\ 0 & 0 & -2\Delta r & 0 & 0 & 0 \\ 0 & 0 & 0 & 0 & 0 & 2\Delta r \end{bmatrix}, \tag{6.8}$$

where Δr is the range resolution of the radar in [km]. Plugging $\mathbf{z}_k$, $\mathbf{y}_k$, $\mathbf{x}_k$ and $\mathbf{H}$ into Eq. (6.6b) and assume $\mathbf{v}_k = [v_H(r_k), v_D(r_k), v_K(r_k)]^T$, Eq. (6.6b) becomes

$$Z_H^m(r_k) = Z_H(r_k) - 2A_h(r_k)\Delta r - PIA_H(r_{k-1}) + v_H(r_k) \tag{6.9a}$$

$$Z_{DR}^m(r_k) = Z_{DR}(r_k) - 2A_{dp}(r_k)\Delta r - PIA_{DR}(r_{k-1}) + v_D(r_k) \tag{6.9b}$$

$$\Delta\Phi_{DP}^f(r_0, r_k) = 2K_{dp}(r_k)\Delta r + \Delta\Phi_{DP}(r_0, r_{k-1}) + v_K(r_k), \tag{6.9c}$$

which are the same as Eq. (5.29) and Eq. (5.30). Plugging $\mathbf{y}_{k+1}$, $\mathbf{y}_k$, $\mathbf{x}_k$ and $\mathbf{M}$ into Eq. (6.6a), Eq. (6.6a) becomes

$$-PIA_H(r_k) = -2A_h(r_k)\Delta r - PIA_H(r_{k-1}) \tag{6.10a}$$

$$-PIA_{DR}(r_k) = -2A_{dp}(r_k)\Delta r - PIA_{DR}(r_{k-1}) \tag{6.10b}$$

$$\Delta\Phi_{DP}(r_0, r_k) = 2K_{dp}(r_k)\Delta r + \Delta\Phi_{DP}(r_0, r_{k-1}), \tag{6.10c}$$

which also matches Eq. (6.3) and Eq. (6.4). So, a series of weather radar observations along the radar beam can be presicely modeled by the proposed SGMPE approach.

To begin the derivation of the SGMPE, initial values of the model need to be set up. Based on the definitions of $\mathbf{x}_k$ and $\mathbf{y}_k$, at the beginning of the first radar resolution bin, $\mathbf{x}_0 = 0$ and $\mathbf{y}_0 = 0$.

When $k = 1$, plugging $\mathbf{y}_0$, $\mathbf{x}_0$ into Eq. (6.6a), $\mathbf{y}_1 = 0$ can be obtained. Since $\mathbf{y}_1 = 0$, Eq. (6.6b) has the same form as GMPE (defined in Eq. (5.2)). Following GMPE approach (Eq. (5.13)), $p(\mathbf{x}_1|\mathbf{z}_1)$ is a Gaussian mixture with the same number of mixtures as $p(\mathbf{x}_1)$ and can be formulated as (Let $\hat{\mathbf{x}}_k$ be the estimation of $\mathbf{x}_k$ when given observation $\mathbf{z}_k$)

$$p(\hat{\mathbf{x}}_1) = p(\mathbf{x}_1|\mathbf{z}_1) \sim \sum_{i=1}^{N} \beta_i^{(1)} \mathcal{N}(\hat{\mu}_i^{(1)}, \hat{\mathbf{\Sigma}}_i^{(1)}), \tag{6.11}$$

where $\hat{\mu}_i^{(1)} = \mu_i + \mathbf{K}_i^{(1)}(\mathbf{z}_1 - \mathbf{u}_i^{(1)})$, $\hat{\mathbf{\Sigma}}_i^{(1)} = (\mathbf{I} - \mathbf{K}_i^{(1)}\mathbf{H})\mathbf{\Sigma}_i$ and Kalman gain $\mathbf{K}_i^{(1)} = \mathbf{\Sigma}_i\mathbf{H}^T(\mathbf{P}_i^{(1)})^{-1}$. According to Eq. (5.8), $\mathbf{P}_i^{(1)} = \mathbf{H}\mathbf{\Sigma}_i\mathbf{H}^T + \mathbf{R}$ and $\mathbf{u}_i^{(1)} = \mathbf{H}\mu_i$. $\beta_i^{(1)}$, which is the weighing of the ith Gaussian mixture in $p(\mathbf{x}_1|\mathbf{z}_1)$, yields

$$\beta_i^{(1)} = \frac{\alpha_i \mathcal{N}(\mathbf{z}_1; \mathbf{u}_i^{(1)}, \mathbf{P}_i^{(1)})}{\sum_{i=1}^{N} \alpha_i \mathcal{N}(\mathbf{z}_1; \mathbf{u}_i^{(1)}, \mathbf{P}_i^{(1)})}. \tag{6.12}$$

The estimate of $\mathbf{x}_1$ from GMPE is

$$\hat{\mathbf{x}}_1 = \sum_{i=1}^{N} \beta_i^{(1)} \hat{\mu}_i^{(1)}. \tag{6.13}$$

When $k = 2$, with $\mathbf{y}_1 = 0$ and $p(\hat{\mathbf{x}}_1) \sim \sum_{i=1}^{N} \beta_i^{(1)} \mathcal{N}(\mu_i^{(1)}, \mathbf{\Sigma}_i^{(1)})$, $p(\mathbf{y}_2)$ can be computed from Eq. (6.6a) and expressed as

$$p(\mathbf{y}_2) \sim \sum_{i=1}^{N} \gamma_i^{(2)} \mathcal{N}(\mathbf{m}_i^{(2)}, \mathbf{Q}_i^{(2)}), \tag{6.14}$$

where $\gamma_i^{(2)} = \beta_i^{(1)}$, $\mathbf{m}_i^{(2)} = \mathbf{M}\mu_i^{(1)}$ and $\mathbf{Q}_i^{(2)} = \mathbf{M}\mathbf{\Sigma}_i^{(1)}\mathbf{M}^T$. Since $\mathbf{y}_k$, $\mathbf{x}_k$ and $\mathbf{v}_k$ are uncorrelated, the conditional probability of $\mathbf{z}_2$ given $\mathbf{x}_2$ yeilds

$$\begin{aligned} p(\mathbf{z}_2|\mathbf{x}_2) &= p(\mathbf{z}_2 - \mathbf{H}\mathbf{x}_2|\mathbf{y}_2 + \mathbf{v}_2) \\ &= \sum_{i=1}^{N} \gamma_i^{(2)} \mathcal{N}(\mathbf{z}_2 - \mathbf{H}\mathbf{x}_2; \mathbf{m}_i^{(2)}, \mathbf{Q}_i^{(2)} + \mathbf{R}). \end{aligned} \tag{6.15}$$

According to Bayesian theorem,

$$p(\hat{\mathbf{x}}_2) = p(\mathbf{x}_2|\mathbf{z}_2) = \frac{p(\mathbf{z}_2|\mathbf{x}_2)p(\mathbf{x}_2)}{\int p(\mathbf{z}_2|\mathbf{x}_2)p(\mathbf{x}_2)d\mathbf{x}_2}, \tag{6.16}$$

where $p(\mathbf{z}_2|\mathbf{x}_2)p(\mathbf{x}_2)$ yields

$$\begin{aligned} p(\mathbf{z}_2|\mathbf{x}_2)p(\mathbf{x}_2) &= \sum_{i=1}^{N} \gamma_i^{(2)} \mathcal{N}(\mathbf{z}_2 - \mathbf{H}\mathbf{x}_2; \mathbf{m}_i^{(2)}, \mathbf{Q}_i^{(2)} + \mathbf{R}) \sum_{i=1}^{N} \alpha_i \mathcal{N}(\mathbf{x}_2; \mu_i, \mathbf{\Sigma}_i) \\ &= \sum_{j=1}^{N}\sum_{i=1}^{N} \gamma_j^{(2)} \alpha_i \mathcal{N}(\mathbf{z}_2 - \mathbf{H}\mathbf{x}_2; \mathbf{m}_j^{(2)}, \mathbf{Q}_j^{(2)} + \mathbf{R}) \mathcal{N}(\mathbf{x}_2; \mu_i, \mathbf{\Sigma}_i) \end{aligned} \tag{6.17}$$

Since the product of two Gaussian distributions is still Gaussian (proof is similar to the one given in section 5.1.2),

$$\mathcal{N}(\mathbf{z}_2 - \mathbf{H}\mathbf{x}_2; \mathbf{m}_j^{(2)}, \mathbf{Q}_j^{(2)} + \mathbf{R}) \mathcal{N}(\mathbf{x}_2; \mu_i, \mathbf{\Sigma}_i) = \mathcal{N}(\mathbf{z}_2; \mathbf{u}_{i,j}^{(2)}, \mathbf{P}_{i,j}^{(2)}) \mathcal{N}(\mathbf{x}_2; \hat{\mu}_{i,j}^{(2)}, \hat{\mathbf{\Sigma}}_{i,j}^{(2)}), \tag{6.18}$$

where $\mathbf{u}_{i,j}^{(2)} = \mathbf{H}\mu_i + \mathbf{m}_j^{(2)}$, $\mathbf{P}_{i,j}^{(2)} = \mathbf{H}\mathbf{\Sigma}_i\mathbf{H}^T + \mathbf{Q}_j^{(2)} + \mathbf{R}$, $\hat{\mu}_{i,j}^{(2)} = \mu_i + \mathbf{K}_{i,j}^{(2)}(\mathbf{z}_2 - \mathbf{u}_{i,j}^{(2)})$, $\hat{\mathbf{\Sigma}}_{i,j}^{(2)} = (\mathbf{I} - \mathbf{K}_{i,j}^{(2)}\mathbf{H})\mathbf{\Sigma}_i$ and $\mathbf{K}_{i,j}^{(2)} = \mathbf{\Sigma}_i\mathbf{H}^T(\mathbf{P}_{i,j}^{(2)})^{-1}$. Therefore,

$$p(\mathbf{z}_2|\mathbf{x}_2)p(\mathbf{x}_2) = \sum_{i=1}^{N}\sum_{j=1}^{N} \alpha_i \gamma_j^{(2)} \mathcal{N}(\mathbf{z}_2; \mathbf{u}_{i,j}^{(2)}, \mathbf{P}_{i,j}^{(2)}) \mathcal{N}(\mathbf{x}_2; \hat{\mu}_{i,j}^{(2)}, \hat{\mathbf{\Sigma}}_{i,j}^{(2)}), \tag{6.19}$$

and

$$\begin{aligned} \int p(\mathbf{z}_2|\mathbf{x}_2)p(\mathbf{x}_2)d\mathbf{x}_2 &= \int \sum_{j=1}^{N}\sum_{i=1}^{N} \gamma_j^{(2)} \alpha_i \mathcal{N}(\mathbf{z}_2; \mathbf{u}_{i,j}^{(2)}, \mathbf{P}_{i,j}^{(2)}) \mathcal{N}(\mathbf{x}_2; \hat{\mu}_{i,j}^{(2)}, \hat{\mathbf{\Sigma}}_{i,j}^{(2)}) d\mathbf{x}_2 \\ &= \sum_{i=1}^{N}\sum_{j=1}^{N} \alpha_i \gamma_j^{(2)} \mathcal{N}(\mathbf{z}_2; \mathbf{u}_{i,j}^{(2)}, \mathbf{P}_{i,j}^{(2)}) \int \mathcal{N}(\mathbf{x}_2; \hat{\mu}_{i,j}^{(2)}, \hat{\mathbf{\Sigma}}_{i,j}^{(2)}) d\mathbf{x}_2 \\ &= \sum_{i=1}^{N}\sum_{j=1}^{N} \alpha_i \gamma_j^{(2)} \mathcal{N}(\mathbf{z}_2; \mathbf{u}_{i,j}^{(2)}, \mathbf{P}_{i,j}^{(2)}). \end{aligned} \tag{6.20}$$

Plugging Eq. (6.19) and Eq. (6.20) into Eq. (6.16) yeilds

$$p(\hat{\mathbf{x}}_2) \sim \sum_{j=1}^{N}\sum_{i=1}^{N} \hat{\beta}_{i,j}^{(2)} \mathcal{N}(\hat{\mu}_{i,j}^{(2)}, \hat{\mathbf{\Sigma}}_{i,j}^{(2)}), \tag{6.21}$$

where

$$\hat{\beta}_{i,j}^{(2)} = \frac{\alpha_i \gamma_j^{(2)} \mathcal{N}(\mathbf{z}_2; \mathbf{u}_{i,j}^{(2)}, \mathbf{P}_{i,j}^{(2)})}{\sum_{j=1}^{N}\sum_{i=1}^{N} \alpha_i \gamma_j^{(2)} \mathcal{N}(\mathbf{z}_2; \mathbf{u}_{i,j}^{(2)}, \mathbf{P}_{i,j}^{(2)})}. \tag{6.22}$$

As it is shown in Eq. (6.21), $p(\hat{\mathbf{x}}_2)$ is still a Gaussian mixture with N^2 mixtures. Eq. (6.21) can be further processed to reduce the number of mixtures in the model. Details discussion are presented in section 6.2. Assuming the number of mixtures after mixture reduction is W, $p(\hat{\mathbf{x}}_2)$ can be simplified as

$$p(\hat{\mathbf{x}}_2) \sim \sum_{i=1}^{W} \beta_i^{(2)} \mathcal{N}(\hat{\mu}_i^{(2)}, \hat{\mathbf{\Sigma}}_i^{(2)}). \tag{6.23}$$

Since Bayes' *least square estimate* of $\mathbf{x}_2$ is given as the conditional mean of $p(\mathbf{x}_2|\mathbf{z}_2)$,

$$\hat{\mathbf{x}}_2 = \sum_{i=1}^{W} \beta_i^{(2)} \hat{\mu}_i^{(2)}. \tag{6.24}$$

Similarly to $p(\hat{\mathbf{x}}_2)$, if $\hat{\mathbf{y}}_k$ is the estimation of $\mathbf{y}_k$ when given observation $\mathbf{z}_k$, $p(\hat{\mathbf{x}}_2)$ can be formulated as

$$p(\hat{\mathbf{y}}_2) = p(\mathbf{y}_2|\mathbf{z}_2) = \frac{p(\mathbf{z}_2|\mathbf{y}_2)p(\mathbf{y}_2)}{\int p(\mathbf{z}_2|\mathbf{y}_2)p(\mathbf{y}_2)d\mathbf{y}_2}. \tag{6.25}$$

Since $\mathbf{y}_k$, $\mathbf{x}_k$ and $\mathbf{v}_k$ are uncorrelated, the conditional probability of $\mathbf{z}_2$ given $\mathbf{y}_2$ yields

$$\begin{aligned} p(\mathbf{z}_2|\mathbf{y}_2) &= p(\mathbf{z}_2 - \mathbf{y}_2|\mathbf{H}\mathbf{x}_2 + \mathbf{v}_2) \\ &= \sum_{i=1}^{N} \alpha_i \mathcal{N}(\mathbf{z}_2 - \mathbf{y}_2; \mathbf{H}\mu_i, \mathbf{H}\mathbf{\Sigma}_i\mathbf{H}^T + \mathbf{R}). \end{aligned} \tag{6.26}$$

Therefore,

$$\begin{aligned} p(\mathbf{z}_2|\mathbf{y}_2)p(\mathbf{y}_2) &= \sum_{j=1}^{N}\sum_{i=1}^{N} \gamma_j^{(2)} \alpha_i \mathcal{N}(\mathbf{z}_2 - \mathbf{y}_2; \mathbf{H}\mu_i, \mathbf{H}\mathbf{\Sigma}_i\mathbf{H}^T + \mathbf{R}) \mathcal{N}(\mathbf{y}_2; \mathbf{m}_j^{(2)}, \mathbf{Q}_j^{(2)}) \\ &= \sum_{j=1}^{N}\sum_{i=1}^{N} \gamma_j^{(2)} \alpha_i \mathcal{N}(\mathbf{z}_2; \mathbf{u}_{i,j}^{(2)}, \mathbf{P}_{i,j}^{(2)}) \mathcal{N}(\mathbf{y}_2; \hat{\mathbf{m}}_{i,j}^{(2)}, \hat{\mathbf{Q}}_{i,j}^{(2)}), \end{aligned} \tag{6.27}$$

where $\hat{\mathbf{m}}_{i,j}^{(2)} = \mathbf{m}_j^{(2)} + \tilde{\mathbf{K}}_{i,j}^{(2)}(\mathbf{z}_2 - \mathbf{u}_{i,j}^{(2)})$, $\hat{\mathbf{Q}}_{i,j}^{(2)} = (\mathbf{I} - \tilde{\mathbf{K}}_{i,j}^{(2)})\mathbf{Q}_j^{(2)}$ and $\tilde{\mathbf{K}}_{i,j}^{(2)} = \mathbf{Q}_j^{(2)}(\mathbf{P}_{i,j}^{(2)})^{-1}$. Since

$$p(\mathbf{z}_2) = \int p(\mathbf{z}_2|\mathbf{x}_2)p(\mathbf{x}_2)d\mathbf{x}_2 = \int p(\mathbf{z}_2|\mathbf{y}_2)p(\mathbf{y}_2)d\mathbf{y}_2,$$

according to Eq. (6.20),

$$\int p(\mathbf{z}_2|\mathbf{y}_2)p(\mathbf{y}_2)d\mathbf{y}_2 = \sum_{i=1}^{N}\sum_{j=1}^{N} \alpha_i \gamma_j^{(2)} \mathcal{N}(\mathbf{z}_2; \mathbf{u}_{i,j}^{(2)}, \mathbf{P}_{i,j}^{(2)}). \tag{6.28}$$

Plugging Eq. (6.27) and Eq. (6.28) into Eq. (6.25) yeilds

$$p(\hat{\mathbf{y}}_2) \sim \sum_{j=1}^{N}\sum_{i=1}^{N} \hat{\beta}_{i,j}^{(2)} \mathcal{N}(\hat{\mathbf{m}}_{i,j}^{(2)}, \hat{\mathbf{Q}}_{i,j}^{(2)}). \tag{6.29}$$

As it is shown in Eq. (6.29), $p(\hat{\mathbf{y}}_2)$ is still a Gaussian mixture with N^2 mixtures. Eq. (6.29) can be also further processed to reduce the number of mixtures in the model. Assuming the number of mixtures after mixture reduction is L, $p(\hat{\mathbf{y}}_2)$ can be simplified and written as

$$p(\hat{\mathbf{y}}_2) \sim \sum_{i=1}^{L} \hat{\gamma}_{i}^{(2)} \mathcal{N}(\hat{\mathbf{m}}_{i}^{(2)}, \hat{\mathbf{Q}}_{i}^{(2)}) \tag{6.30}$$

When $k = 3$, with $p(\hat{\mathbf{y}}_2)$ (given in Eq. (6.30)) and $p(\hat{\mathbf{x}}_2)$ (given in Eq. (6.23)), $p(\mathbf{y}_3)$ can be computed from

$$p(\mathbf{y}_3) = \int p(\mathbf{y}_3|\hat{\mathbf{y}}_2) p(\hat{\mathbf{y}}_2) d\hat{\mathbf{y}}_2. \tag{6.31}$$

Since $\hat{\mathbf{y}}_2$ and $\hat{\mathbf{x}}_2$ are indenpendent, $p(\mathbf{y}_3|\hat{\mathbf{y}}_2)$ can be formulated as

$$\begin{aligned} p(\mathbf{y}_3|\hat{\mathbf{y}}_2) &= p(\mathbf{y}_3 - \hat{\mathbf{y}}_2|\mathbf{M}\hat{\mathbf{x}}_2) \\ &= \sum_{j=1}^{W} \beta_j^{(2)} \mathcal{N}(\mathbf{y}_3 - \hat{\mathbf{y}}_2; \mathbf{M}\hat{\mu}_j^{(2)}, \mathbf{M}\hat{\mathbf{\Sigma}}_j^{(2)}\mathbf{M}^T). \end{aligned} \tag{6.32}$$

Therefore,

$$\begin{aligned} p(\mathbf{y}_3) &= \int \sum_{j=1}^{W} \beta_j^{(2)} \mathcal{N}(\mathbf{y}_3 - \hat{\mathbf{y}}_2; \mathbf{M}\hat{\mu}_j^{(2)}, \mathbf{M}\hat{\mathbf{\Sigma}}_j^{(2)}\mathbf{M}^T) \sum_{i=1}^{L} \hat{\gamma}_i^{(2)} \mathcal{N}(\hat{\mathbf{y}}_2; \hat{\mathbf{m}}_i^{(2)}, \hat{\mathbf{Q}}_i^{(2)}) d\hat{\mathbf{y}}_2 \\ &= \sum_{j=1}^{W}\sum_{i=1}^{L} \beta_j^{(2)} \hat{\gamma}_i^{(2)} \mathcal{N}(\mathbf{y}_3; \mathbf{m}_{i,j}^{(3)}, \mathbf{Q}_{i,j}^{(3)}), \end{aligned} \tag{6.33}$$

where $\mathbf{m}_{i,j}^{(3)} = \hat{\mathbf{m}}_i^{(2)} + \mathbf{M}\hat{\mu}_j^{(2)}$ and $\mathbf{Q}_{i,j}^{(3)} = \hat{\mathbf{Q}}_i^{(2)} + \mathbf{M}\hat{\mathbf{\Sigma}}_j^{(2)}\mathbf{M}^T$. As it is shown in Eq. (6.33), $p(\hat{\mathbf{y}}_3)$ is still a Gaussian mixture with $W \times L$ mixtures. Eq. (6.33) are further processed to reduce the number of mixtures in the model. Assuming the number of mixtures after mixture reduction is G, $p(\hat{\mathbf{y}}_3)$ can be simplified and written as

$$p(\mathbf{y}_3) = \sum_{i=1}^{G} \gamma_i^{(3)} \mathcal{N}(\mathbf{y}_3; \mathbf{m}_i^{(3)}, \mathbf{Q}_i^{(3)}) \tag{6.34}$$

Following the same procedures, $\hat{\mathbf{x}}_k$ ($k = 1, ..., N_g$, N_g is the number of radar range bins) can be obtained. A summary of the sequential Gaussian mixture parameter estimator approach is given as follows:

- Models:

$$p(\mathbf{v}_k) \sim \mathcal{N}(0, \mathbf{R}) \quad \text{for } k > 0 \tag{6.35a}$$

$$p(\mathbf{x}_k) \sim \sum_{i=1}^{N} \alpha_i \mathcal{N}(\mu_i, \mathbf{\Sigma}_i) \quad \text{for } k > 0 \tag{6.35b}$$

$$p(\hat{\mathbf{x}}_k) = p(\mathbf{x}_k|\mathbf{z}_k) \sim \sum_{i=1}^{W} \beta_i^{(k)} \mathcal{N}(\mu_i^{(k)}, \mathbf{\Sigma}_i^{(k)}) \quad \text{for } k > 0 \tag{6.35c}$$

$$p(\mathbf{y}_k) \sim \sum_{i=1}^{G} \gamma_i^{(k)} \mathcal{N}(\mathbf{m}_i^{(k)}, \mathbf{Q}_i^{(k)}) \quad \text{for } k > 1 \tag{6.35d}$$

$$p(\hat{\mathbf{y}}_k) = p(\mathbf{y}_k|\mathbf{z}_k) \sim \sum_{i=1}^{L} \hat{\gamma}_i^{(k)} \mathcal{N}(\hat{\mathbf{m}}_i^{(k)}, \hat{\mathbf{Q}}_i^{(k)}) \quad \text{for } k > 1 \tag{6.35e}$$

- For $k = 0$: $\mathbf{y}_0 = 0$ and $\mathbf{x}_0 = 0$.

- For $k = 1$: Given observation $\mathbf{z}_1$, $\mathbf{y}_1 = 0$ and

$$p(\hat{\mathbf{x}}_1) \sim \sum_{i=1}^{N} \beta_i^{(1)} \mathcal{N}(\mu_i^{(1)}, \mathbf{\Sigma}_i^{(1)}), \tag{6.36}$$

  where $\mu_i^{(1)} = \mu_i + \mathbf{K}_i^{(1)}(\mathbf{z}_1 - \mathbf{u}_i^{(1)})$, $\mathbf{\Sigma}_i^{(1)} = (\mathbf{I} - \mathbf{K}_i^{(1)}\mathbf{H})\mathbf{\Sigma}_i$, $\mathbf{P}_i^{(1)} = \mathbf{H}\mathbf{\Sigma}_i\mathbf{H}^T + \mathbf{R}$, $\mathbf{u}_i^{(1)} = \mathbf{H}\mu_i$ and

$$\beta_i^{(1)} = \frac{\alpha_i \mathcal{N}(\mathbf{z}_1; \mathbf{u}_i^{(1)}, \mathbf{P}_i^{(1)})}{\sum_{i=1}^{N} \alpha_i \mathcal{N}(\mathbf{z}_1; \mathbf{u}_i^{(1)}, \mathbf{P}_i^{(1)})}.$$

  Estimate of $\mathbf{x}_1$ yields

$$\hat{\mathbf{x}}_1 = \sum_{i=1}^{N} \beta_i^{(1)} \hat{\mu}_i^{(1)}. \tag{6.37}$$

- For $k = 2$: Given observation $\mathbf{z}_2$,

$$p(\mathbf{y}_2) \sim \sum_{i=1}^{N} \gamma_i^{(2)} \mathcal{N}(\mathbf{m}_i^{(2)}, \mathbf{Q}_i^{(2)}), \tag{6.38}$$

  where $\gamma_i^{(2)} = \beta_i^{(1)}$, $\mathbf{m}_i^{(2)} = \mathbf{M}\mu_i^{(1)}$ and $\mathbf{Q}_i^{(2)} = \mathbf{M}\mathbf{\Sigma}_i^{(1)}\mathbf{M}^T$, and

$$p(\hat{\mathbf{x}}_2) \sim \sum_{j=1}^{N} \sum_{i=1}^{N} \hat{\beta}_{i,j}^{(2)} \mathcal{N}(\hat{\mu}_{i,j}^{(2)}, \hat{\mathbf{\Sigma}}_{i,j}^{(2)}), \tag{6.39}$$

where $\mathbf{u}_{i,j}^{(2)} = \mathbf{H}\mu_i + \mathbf{m}_j^{(2)}$, $\mathbf{P}_{i,j}^{(2)} = \mathbf{H}\mathbf{\Sigma}_i\mathbf{H}^T + \mathbf{Q}_j^{(2)} + \mathbf{R}$, $\hat{\mu}_{i,j}^{(2)} = \mu_i + \mathbf{K}_{i,j}^{(2)}(\mathbf{z}_2 - \mathbf{u}_{i,j}^{(2)})$, $\hat{\mathbf{\Sigma}}_{i,j}^{(2)} = (\mathbf{I} - \mathbf{K}_{i,j}^{(2)}\mathbf{H})\mathbf{\Sigma}_i$, $\mathbf{K}_{i,j}^{(2)} = \mathbf{\Sigma}_i\mathbf{H}^T(\mathbf{P}_{i,j}^{(2)})^{-1}$ and

$$\hat{\beta}_{i,j}^{(2)} = \frac{\alpha_i\gamma_j^{(2)}\mathcal{N}(\mathbf{z}_2; \mathbf{u}_{i,j}^{(2)}, \mathbf{P}_{i,j}^{(2)})}{\sum_{j=1}^{N}\sum_{i=1}^{N}\alpha_i\gamma_j^{(2)}\mathcal{N}(\mathbf{z}_2; \mathbf{u}_{i,j}^{(2)}, \mathbf{P}_{i,j}^{(2)})}.$$

After reduction of mixtures in $p(\hat{\mathbf{x}}_2)$,

$$p(\hat{\mathbf{x}}_2) \sim \sum_{i=1}^{W}\beta_i^{(2)}\mathcal{N}(\hat{\mu}_i^{(2)}, \hat{\mathbf{\Sigma}}_i^{(2)}). \tag{6.40}$$

Estimate of $\mathbf{x}_2$ yields

$$\hat{\mathbf{x}}_2 = \sum_{i=1}^{W}\beta_i^{(2)}\hat{\mu}_i^{(2)}. \tag{6.41}$$

Refined distribution of $\mathbf{y}_2$ given observation $\mathbf{z}_2$ is

$$p(\hat{\mathbf{y}}_2) \sim \sum_{j=1}^{N}\sum_{i=1}^{N}\hat{\beta}_{i,j}^{(2)}\mathcal{N}(\hat{\mathbf{m}}_{i,j}^{(2)}, \hat{\mathbf{Q}}_{i,j}^{(2)}), \tag{6.42}$$

where $\hat{\mathbf{m}}_{i,j}^{(2)} = \mathbf{m}_j^{(2)} + \tilde{\mathbf{K}}_{i,j}^{(2)}(\mathbf{z}_2 - \mathbf{u}_{i,j}^{(2)})$, $\hat{\mathbf{Q}}_{i,j}^{(2)} = (\mathbf{I} - \tilde{\mathbf{K}}_{i,j}^{(2)})\mathbf{Q}_j^{(2)}$ and $\tilde{\mathbf{K}}_{i,j}^{(2)} = \mathbf{Q}_j^{(2)}(\mathbf{P}_{i,j}^{(2)})^{-1}$. After reduction of mixtures in $p(\hat{\mathbf{y}}_2)$,

$$p(\hat{\mathbf{y}}_2) \sim \sum_{i=1}^{L}\hat{\gamma}_i^{(2)}\mathcal{N}(\hat{\mathbf{m}}_i^{(2)}, \hat{\mathbf{Q}}_i^{(2)}). \tag{6.43}$$

- For $k = 3$: Given observation $\mathbf{z}_3$,

$$p(\mathbf{y}_3) = \sum_{j=1}^{W}\sum_{i=1}^{L}\beta_j^{(2)}\hat{\gamma}_i^{(2)}\mathcal{N}(\mathbf{y}_3; \mathbf{m}_{i,j}^{(3)}, \mathbf{Q}_{i,j}^{(3)}), \tag{6.44}$$

where $\mathbf{m}_{i,j}^{(3)} = \hat{\mathbf{m}}_i^{(2)} + \mathbf{M}\hat{\mu}_j^{(2)}$ and $\mathbf{Q}_{i,j}^{(3)} = \hat{\mathbf{Q}}_i^{(2)} + \mathbf{M}\hat{\mathbf{\Sigma}}_j^{(2)}\mathbf{M}^T$. After reduction of mixtures in $p(\mathbf{y}_3)$,

$$p(\mathbf{y}_3) = \sum_{i=1}^{G}\gamma_i^{(3)}\mathcal{N}(\mathbf{y}_3; \mathbf{m}_i^{(3)}, \mathbf{Q}_i^{(3)}). \tag{6.45}$$

...

...

...

- For $k = k$: (Model Forecast Step)

$$p(\mathbf{y}_k) = \sum_{j=1}^{W} \sum_{i=1}^{L} \beta_j^{(k-1)} \hat{\gamma}_i^{(k-1)} \mathcal{N}(\mathbf{y}_k; \mathbf{m}_{i,j}^{(k)}, \mathbf{Q}_{i,j}^{(k)}), \tag{6.46}$$

where $\mathbf{m}_{i,j}^{(k)} = \hat{\mathbf{m}}_i^{(k-1)} + \mathbf{M}\hat{\mu}_j^{(k-1)}$ and $\mathbf{Q}_{i,j}^{(k)} = \hat{\mathbf{Q}}_i^{(k-1)} + \mathbf{M}\hat{\mathbf{\Sigma}}_j^{(k-1)}\mathbf{M}^T$. After reduction of mixtures in $p(\mathbf{y}_k)$,

$$p(\mathbf{y}_k) = \sum_{i=1}^{G} \gamma_i^{(k)} \mathcal{N}(\mathbf{y}_k; \mathbf{m}_i^{(k)}, \mathbf{Q}_i^{(k)}). \tag{6.47}$$

Given observation $\mathbf{z}_k$, (Data Assimilation Step)

$$p(\hat{\mathbf{x}}_k) \sim \sum_{j=1}^{G} \sum_{i=1}^{N} \hat{\beta}_{i,j}^{(k)} \mathcal{N}(\hat{\mu}_{i,j}^{(k)}, \hat{\mathbf{\Sigma}}_{i,j}^{(k)}), \tag{6.48}$$

where $\mathbf{u}_{i,j}^{(k)} = \mathbf{H}\mu_i + \mathbf{m}_j^{(k)}$, $\mathbf{P}_{i,j}^{(k)} = \mathbf{H}\mathbf{\Sigma}_i\mathbf{H}^T + \mathbf{Q}_j^{(k)} + \mathbf{R}$, $\hat{\mu}_{i,j}^{(k)} = \mu_i + \mathbf{K}_{i,j}^{(k)}(\mathbf{z}_k - \mathbf{u}_{i,j}^{(k)})$, $\hat{\mathbf{\Sigma}}_{i,j}^{(k)} = (\mathbf{I} - \mathbf{K}_{i,j}^{(k)}\mathbf{H})\mathbf{\Sigma}_i$, $\mathbf{K}_{i,j}^{(k)} = \mathbf{\Sigma}_i\mathbf{H}^T(\mathbf{P}_{i,j}^{(k)})^{-1}$ and

$$\hat{\beta}_{i,j}^{(k)} = \frac{\alpha_i \gamma_j^{(k)} \mathcal{N}(\mathbf{z}_k; \mathbf{u}_{i,j}^{(k)}, \mathbf{P}_{i,j}^{(k)})}{\sum_{j=1}^{G} \sum_{i=1}^{N} \alpha_i \gamma_j^{(k)} \mathcal{N}(\mathbf{z}_k; \mathbf{u}_{i,j}^{(k)}, \mathbf{P}_{i,j}^{(k)})}.$$

After reduction of mixtures in $p(\hat{\mathbf{x}}_k)$,

$$p(\hat{\mathbf{x}}_k) \sim \sum_{i=1}^{W} \beta_i^{(k)} \mathcal{N}(\hat{\mu}_i^{(k)}, \hat{\mathbf{\Sigma}}_i^{(k)}). \tag{6.49}$$

Estimate of $\mathbf{x}_k$ yields

$$\hat{\mathbf{x}}_k = \sum_{i=1}^{W} \beta_i^{(k)} \hat{\mu}_i^{(k)}. \tag{6.50}$$

Refined distribution of $\mathbf{y}_k$ given observation $\mathbf{z}_k$ is

$$p(\hat{\mathbf{y}}_k) \sim \sum_{j=1}^{N} \sum_{i=1}^{N} \hat{\beta}_{i,j}^{(k)} \mathcal{N}(\hat{\mathbf{m}}_{i,j}^{(k)}, \hat{\mathbf{Q}}_{i,j}^{(k)}), \tag{6.51}$$

where $\hat{\mathbf{m}}_{i,j}^{(k)} = \mathbf{m}_j^{(k)} + \tilde{\mathbf{K}}_{i,j}^{(k)}(\mathbf{z}_k - \mathbf{u}_{i,j}^{(k)})$, $\hat{\mathbf{Q}}_{i,j}^{(k)} = (\mathbf{I} - \tilde{\mathbf{K}}_{i,j}^{(k)})\mathbf{Q}_j^{(k)}$ and $\tilde{\mathbf{K}}_{i,j}^{(k)} = \mathbf{Q}_j^{(k)}(\mathbf{P}_{i,j}^{(k)})^{-1}$. After reduction of mixtures in $p(\hat{\mathbf{y}}_k)$,

$$p(\hat{\mathbf{y}}_k) \sim \sum_{i=1}^{L} \hat{\gamma}_i^{(k)} \mathcal{N}(\hat{\mathbf{m}}_i^{(k)}, \hat{\mathbf{Q}}_i^{(k)}). \tag{6.52}$$

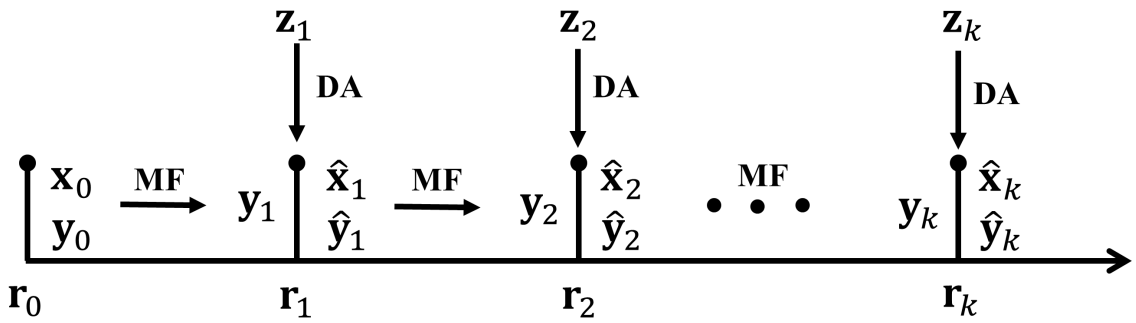


Figure 6.1: Diagrammatic view of the role of observations and models in SGMPE. In the figure, MF refers to Model Forecast and DA refers to Data Assimilation.

Fig. 6.1 shows a diagrammatic view of the role of observations and models in the sequential Gaussian mixture parameter estimator. As it can be seen that the SGMPE approach is quite straightforward. From the beginning of the radar beam path, $\mathbf{y}_k$ is first obtained from estimations of $\hat{\mathbf{x}}_{k-1}$ and $\hat{\mathbf{y}}_{k-1}$ at the previous range bin. This step is known as the Model Forecast step in Kalman filtering. After observation $\mathbf{z}_k$ is acquired, $\mathbf{y}_k$ is refined and $\mathbf{x}_k$ is estimated both by maximizing the conditional probability of $\mathbf{y}_k$ and $\mathbf{x}_k$ given $\mathbf{z}_k$. This step is known as the Data Assimilation step in Kalman filtering.

In conclusion, the sequential GMPE approach is able to model the dependency of weather radar measurements of one bin on properties of previous bins and proceed in a Kalman filter manner such that the estimation at each range bin is the 'best' estimate given the radar measurements of that bin, in terms of minimum-variance and unbiased performance. The only drawback of SGMPE is the number of mixtures in accumulation vector $\mathbf{y}_k$ increases exponentially from bin to bin. Ways to reduce mixtures and keep the number of mixtures as small as possible without losing significant information are introduced and discussed in section 6.2.

6.2 SGMPE Mixture Reduction

As shown in section 6.1, a possible drawback of the recursive processing of Gaussian mixture models is the inevitable increase of mixture components at an exponential rate. How to keep the number of mixtures from growing too large while preserving significant distribution information has been the focus of many studies (e.g., Williams and Maybeck 2003; Runnalls 2007; Huber and Hanebeck 2008; Schieferdecker and Huber 2009). Moreover, the mixture reduction procedure should be computationally efficient, since many recursive GMM applications require real-time processing.

The simplest way of reducing Gaussian components is to eliminate those 'unimportant' ones (Blackman 2004). Since the influence of one component on the whole GMM model is characterized by the weighting of the component, components with low weightings may be eliminated from the model without losing much fidelity. Such mixture reduction methods are also known as 'pruning' or 'forgetting'.

Alternatively, another natural way of reducing Gaussian mixture components is to merge components that are close (Salmond 2009). There are many ways to measure the similarity between components, such as the distance between their means or the overlapping area between components. 'Merging' is considered more attractive than 'forgetting', since 'Merging' preserves information in some sense while pruning would certainly loses those information.

More advanced techniques for mixture reduction are also reported in literature. They may be classified into two categories: *bottom-up* approaches that begin with a single Gaussian mixture and iteratively add additional components until the original GMM is approximated appropriately, such as the PGMR (Progressive Gaussian Mixture Reduction) algorithm presented in Huber and Hanebeck (2008), and *top-down* approaches that start with the original GMM and iteratively decrease the number of mixture components according to characteristics of the overall model or just individual mixtures, such as Williams's algorithm (Williams and Maybeck 2003)

and the GMRC (Gaussian Mixture Reduction via Clustering) algorithm introduced in Runnalls (2007). Crouse et al. (2011) gives a review of Gaussian mixture reduction algorithms and compares two of the best algorithms, the GMRC algorithm from Schieferdecker and Huber (2009) and the COWA (Constraint Optimized Weight Adaptation) algorithms from Chen et al. (2010), where the GMRC algorithm is shown to have better performance in terms of Integral Squared Error (ISE).

It is worth mentioning that more advanced and sophisticated mixture reduction algorithms generally require more computation time. Mixture reduction is always a compromise between accuracy and computation time. The choice of mixture reduction algorithm depends on different applications and requirements.

Details of two widely used Gaussian mixture reduction algorithms are shown as follows:

- Pruning/Forgetting

  Many Gaussian mixture reduction algorithms are greedy in nature, such as the Pruning algorithm. Given a Gaussian mixture consisting of N components, pruning can be easily done by giving zero weight to mixture components with weights that are lower than some threshold values, such as 0.01 or 0.001. Number of mixtures can be limited to a small number by setting a proper threshold, though there is usually no control of the actually number. If the number of mixtures needs to be reduced, say, L, one can simply discard the $N - L$ components having the lowest weights. Besides weights, pruning may be performed according to other cost measures (Crouse et al. 2011). Since usually after one iteration, most of the components in a GMM would have very small weights, pruning is a simple but efficient way to reduce number of mixture. More importantly, pruning does not require heavy computation.

- Merging

Mixture reduction may be achieved by merging two or more mixture components into one component, where the first two moments of the overall mixture are preserved. Assuming the index of the mixtures being merged are $i = 1, ..., M$, the weighting, mean and covariance of the new Gaussian component are given by

$$\alpha_{new} = \sum_{i=1}^{M} \alpha_i \tag{6.53a}$$

$$\mu_{new} = \frac{1}{\alpha_{new}} \sum_{i=1}^{M} \alpha_i \mu_i \tag{6.53b}$$

$$\mathbf{\Sigma}_{new} = \sum_{i=1}^{M} \frac{\alpha_i}{\alpha_{new}} (\mathbf{\Sigma}_i + (\mu_i - \mu_{new})(\mu_i - \mu_{new})^T). \tag{6.53c}$$

The choice of which components to be merged often depends on distance or similarity among components. (Salmond 1989) utilizes the following *ad hoc* distance definition

$$d_{ij}^2 = \frac{\alpha_i \alpha_j}{\alpha_i + \alpha_j} (\mu_i - \mu_j)^T \mathbf{\Sigma}^{-1} (\mu_i - \mu_j). \tag{6.54}$$

Runnalls (2007) defined measure of similarity between components i and j as

$$c_{ij} = \frac{1}{2}[(\alpha_i + \alpha_j) log(|\mathbf{\Sigma}_{ij}|) - \alpha_i log(|\mathbf{\Sigma}_i|) - \alpha_j log(|\mathbf{\Sigma}_j|)] \tag{6.55}$$

based on the Kullback-Leibler (Kullback and Leibler 1951) discrimination measure. In Eq. (6.55), $\mathbf{\Sigma}_{ij}$ corresponds to the new covariance matrix after two components are merged. Merging algorithms, though differs in how they measure distance among components, usually merge two components that has the lowest distance at a time until the desired number of mixtures has been reached.

6.3 Rainfall Rate Estimation at X-band Using SGMPE

Section 5.5 introduced two iterative GMPE approaches, DP-GMPE and CI-GMPE, for path-integrated attenuation correction of rain. It should be pointed out that correcting PIA is not the final goal but an intermediate stage. The recovered reflectivity and differential reflectivity are applied to other meteorological applications such as rainfall rate estimation. Conventional approaches for rainfall rate estimation in C-band or X-band, where attenuation effects can not be neglected, tend to divide the job into two separated stages: attenuation correction and rainfall estimation. Those two stages are independent. Better estimation results may be achieved if rainfall rate estimation algorithms are able to compensate the error and uncertainties from attenuation corrections outputs, instead of expecting the outputs from attenuation correction algorithms to be perfect. If one estimation is made upon another estimation, estimation errors from the previous estimation would be accumulated in the new estimation. An example can be found in section 5.4, where it is shown that the rainfall rate directly estimated from the radar moments is more precise than the rainfall rate retrieved from the estimated DSD parameters.

Differential phase has played an major role in attenuation correction applications and estimating rainfall rate from high attenuation environment due to its immunity to attenuation effects. Either use differential phase as the only input or as a constraint, the algorithms are heavily dependent on phase measurements. Since phase measurements are not always available and are easily contaminated by instrumentation noise, it would be even better if the rainfall rate estimation algorithm for X-band works with phase measurement when it is available but does not require or depend on phase measurement.

The Gaussian Mixture Parameter Estimator (SGMPE) introduced in section 6.1 is developed for radar meteorological applications in higher frequency bands such as C-band, X-band, Ku-band and Ka-band. The SGMPE approach is also designed to take attenuation effects into consideration and make the best use of radar measurements for different applications.

In this section, a SGMPE is built for rainfall rate estimation in X-band as a demonstration. Results of SGMPE approach with different inputs are compared with those from DP-GMPE and CI-GMPE. Gaussian mixture reduction in practical SGMPE applications is also discussed.

6.3.1 GMPE Construction

The X-band simulation dataset used in the PIA correction study (5.5) is also used here. Details of the simulation dataset can be found in Table 5.12. The dataset consists of 15,000 cases that are generated in the single-cell Monte Carlo simulation. Raindrop size distribution is represented by a normalized Gamma DSD whose parameters are uniformly distributed in a predefined range used in many studies (e.g., Vulpiani et al. 2005; Gorgucci et al. 2006). Similar to the PIA correction study, The simulation dataset is divided into 2 portions. 12000 cases are used for training and the remaining 3000 cases are used for testing.

State vector is constructed as $\mathbf{x} = [R, A_h, A_{dp}, Z_H, Z_{DR}, K_{dp}]^T$. Once the prior distribution of $\mathbf{x}$, $p(\mathbf{x})$ has been approximated by a GMM, it is ready to be adapted to different radar systems, such as $\mathbf{z} = [Z_H]^T$ for legacy single polarization radar, $\mathbf{z} = [Z_H, Z_{DR}]^T$ for dual-polarized radar without (or with low quality) differential phase measurements and $\mathbf{z} = [Z_H, Z_{DR}, K_{dp}]^T$ for radars with full dual-polarization capabilities. Fig. 6.2 shows the RMSEs of rainfall estimation from GMPE with different inputs as number of mixture increases. As shown in Fig. 6.2, if only one dual-pol variable is input to GMPE, K_{dp} is much better choice than Z_H. More variables input

to GMPE generally leads to better performance. Performance of GMPE with different inputs reach their best performance points when GMM has 6 or more mixtures. Therefore, a GMM with 6 mixtures is trained and used in both GMPE and SGMPE for this study.

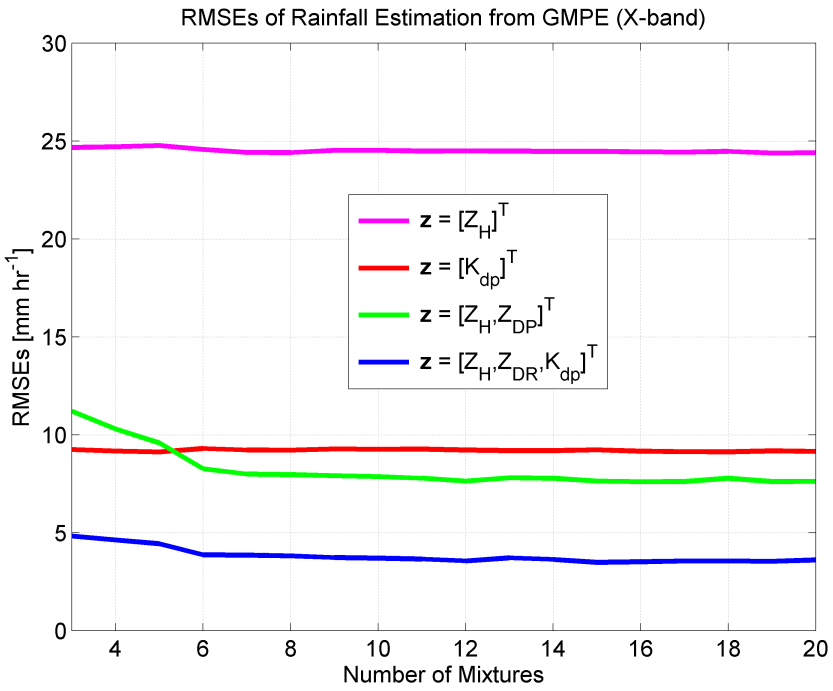


Figure 6.2: RMSEs of rainfall estimation from GMPE with different inputs as number of mixtures increases.

Table 6.1: Performance of GMPE with 6 mixtures for rainfall rate estimation (all in [mm hr^{-1}])

	Bias	SD	RMSE	FSE
GMPE($\mathbf{z} = [K_{dp}]^T$)	-0.1663	9.2998	9.3012	33.39%
GMPE($\mathbf{z} = [Z_H]^T$)	-0.8859	24.5524	24.5684	88.18%
GMPE($\mathbf{z} = [Z_H, Z_{DR})$	-0.5607	8.2415	8.2605	29.65%
GMPE($\mathbf{z} = [Z_H, Z_{DR}, K_{dp}]^T$)	-0.1495	3.8681	3.8710	13.89%

Table 6.1 shows the performance of GMPE with 6 mixtures for rainfall rate estimation at X-band. Since the test dataset is noise-free, the rainfall rate estimation results can be considered as the upper bound for the DP-GMPE approach, CI-GMPE approach and SGMPE approach with same inputs. For example, the best RMSE DP-GMPE and SGMPE with $\mathbf{z} = [K_{dp}]^T$ may have for rainfall rate estimation is 9.3012 [mm hr^{-1}]. Similarly, for CI-GMPE and SGMPE with $\mathbf{z} = [Z_H, Z_{DR}, K_{dp}]^T$, the best RMSE is 3.8710 [mm hr^{-1}].

6.3.2 Performance Evaluation for SGMPEs

To evaluate the performance of DP-GMPE, CI-GMPE and SGMPE for rainfall rate estimation in presence of PIA, a total of 15 rain paths are constructed from the test dataset. Each rain path consists of 200 range bins with the range spacing of 150 [m] and each range bin is a simulated case randomly taken from the test dataset. It can be seem that, although such rain paths may not be realistic, having a rain path with randomly varying DSD parameters is one of the most challenging scenarios for rainfall rate estimation approaches, especially when the PIA effects are strong. Since all the cases are from the same test dataset, the lower bound of performance for each algorithm can be obtained. The expected performance of each algorithm in real-world environment will be somewhere in between.

As shown in Section 6.1, number of mixtures needed in SGMPE will grow exponentially from bin to bin. Therefore, number of mixtures needed and how to reduce mixtures to the desired number has to be considered. There are three numbers of mixtures needed. As shown in Eq. (6.35c), (6.35d) and (6.35e), they are W for $p(\hat{\mathbf{x}}_k)$, G for $p(\mathbf{y}_k)$ and L for $p(\hat{\mathbf{y}}_k)$. W, G and L can be any number and can be modified from bin to bin. To facilitate the actual implementations, W, G and L in this study are set as a same number and fixed over range.

Weather radar systems usually employ a pulse length at the level of one microsecond and a pulse repetition time at the level of one millisecond, which means observations of several hundred range bins can be finished in less than one second. Accordingly, mixture reduction for SGMPE need to be performed several hundred times or more within one second. For potential applications of the SGMPE algorithms in practical radar systems, the choice of Gaussian mixture reduction algorithms has to take into account the time efficiency of the algorithms. In this study, the 'pruning' mixture reduction technique introduced in section 6.2 is used, where the desired number of mixtures with the largest weights are kept while the rest of the mixtures are dropped. For comparison purpose, the 'merging' mixture reduction technique is also implemented where the Salmond's distance definition (Eq. 6.54) is adopted. Note that, 'merging' mixture reduction technique is computationally intense and slow. It may not be applicable to practical radar systems.

If observation for SGMPE is $\mathbf{z}_k = [Z_H^m(r_k), Z_{DR}^m(r_k), \Delta\Phi_{DP}^f(r_0, r_k)]^T$, the observation matrix $\mathbf{H}$ and accumulation matrix $\mathbf{M}$ are given in Eq. (6.7) and Eq. (6.8), respectively. For SGMPE with $\mathbf{z}_k = [Z_H^m(r_k), Z_{DR}^m(r_k)]^T$, the observation matrix $\mathbf{H}$ and accumulation matrix $\mathbf{M}$ are constructed as

$$\mathbf{H} = \begin{bmatrix} 0 & -2\Delta r & 0 & 1 & 0 & 0 \\ 0 & 0 & -2\Delta r & 0 & 1 & 0 \end{bmatrix}$$

and

$$\mathbf{M} = \begin{bmatrix} 0 & -2\Delta r & 0 & 0 & 0 & 0 \\ 0 & 0 & -2\Delta r & 0 & 0 & 0 \end{bmatrix}.$$

Similarly, for SGMPE with $\mathbf{z}_k = [Z_H^m(r_k)]^T$, $\mathbf{H} = [0, -2\Delta r, 0, 1, 0, 0]$ and $\mathbf{M} = [0, -2\Delta r, 0, 0, 0, 0]$. If phase is the only input to SGMPE, $\mathbf{H} = [0, 0, 0, 0, 0, 2\Delta r]$ and $\mathbf{M} = [0, 0, 0, 0, 0, 2\Delta r]$.

To quantify the impacts of mixture reduction, DP-GMPE, CI-GMPE and SGMPE with different inputs are tested using the 15 randomly generated rain paths. To show only the impacts of mixture reduction, this test assumes a noise-free environment just

like the previous GMPE test. It should be pointed out that CI-GMPE and SGMPE are expected to perform worse than GMPE with the same input while DP-GMPE is expected to have the same performance. This is because there are only errors of estimating rainfall rate in previous GMPE test while in this 'clean' rain path test, there are not only errors of estimating rainfall rate but also errors from estimating and correcting PIAs. Since no power measurement is involved in DP-GMPE, there is no PIA errors for DP-GMPE. DP-GMPE and GMPE with K_{dp} should have the same performance. Fig. 6.3 shows the results of this 'clean' rain path test. It is noted that, mixture reduction does not apply to DP-GMPE or CI-GMPE. They are plotted in the same figure with SGMPE who shares the same input as reference.

As shown in Fig. 6.3(a), there is not much difference between the performance of SGMPEs with 'Pruning' and 'Merging' mixture reduction algorithms as the blue line and red line pretty much overlap. So for this 'clean' rain path test, the 'Merging' algorithm who requires intense computation does not show obvious advantage over the simple 'Pruning' algorithm. As number of mixtures increases (after reduction), the RMSEs of SGMPE do not decrease but increase a little, though the difference is small, about 0.01 [mm hr^{-1}]. Compared with performance of GMPE with the same input in Fig. 6.2 (blue line), CI-GMPE has a larger RMSE, about 0.3 [mm hr^{-1}], which is from the errors of DP-GMPE for estimating PIAs (CI-GMPE uses the power measurements corrected by CI-GMPE as input). Performance of SGMPE with the same input is worse for around 0.5 [mm hr^{-1}] which is the combination of errors from mixture reduction and estimating attenuations. So the impacts of mixture reduction leads to less than 0.5 [mm hr^{-1}] RMSE in SGMPE with $\mathbf{z}_k = [Z_H^m(r_k), Z_{DR}^m(r_k), \Delta\Phi_{DP}^f(r_0, r_k)]^T$ as input, which is not significant.

Fig. 6.3(b) shows the comparison between DP-GMPE and SGMPE with K_{dp} as input. DP-GMPE has the same performance as GMPE($\mathbf{z} = [K_{dp}]^T$) (red line in Fig. 6.2). SGMPE with K_{dp} as input performs worse than DP-GMPE by about 0.8

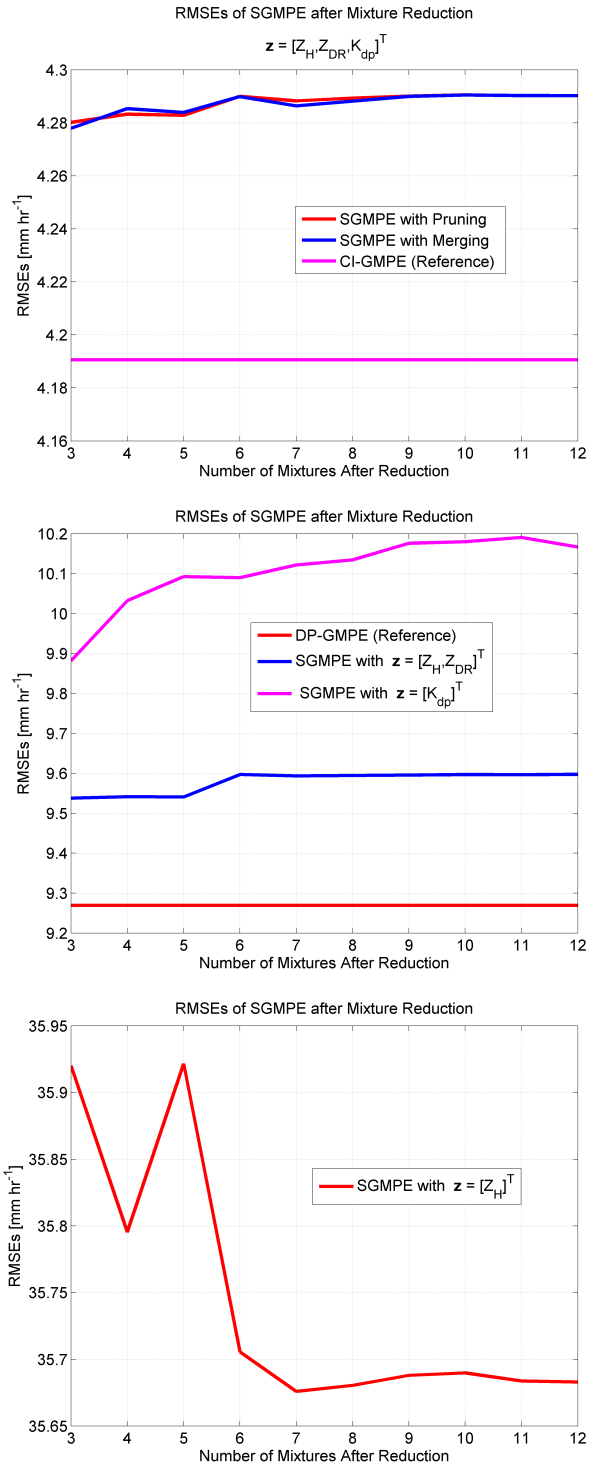


Figure 6.3: RMSEs of SGMPEs after mixture reduction for the 'clean' rain path test. From top to bottom, (a) Comparision between 'Pruning' and 'Merging'; (b) Comparison between DP-GMPE and SGMPE with K_{dp} as input; (c) RMSEs of SGMPE with Z_H as input.

[mm hr^{-1}] due to the impacts of mixture reduction. For SGMPE with $\mathbf{z} = [Z_H, Z_{DR}$, there is a 1.3 [mm hr^{-1}] performance degradation due to the impacts of mixture reduction as well as errors from estimating attenuations. It is worth mentioning that, errors from estimating attenuation in SGMPE with $\mathbf{z} = [Z_H, Z_{DR}$ are expected to be larger than errors in SGMPE with $\mathbf{z}_k = [Z_H^m(r_k), Z_{DR}^m(r_k), \Delta\Phi_{DP}^f(r_0, r_k)]^T$ as input, since with more input variables, more precise estimation of attenuation from SGMPE can be obtained. Similar to SGMPE with $\mathbf{z}_k = [Z_H^m(r_k), Z_{DR}^m(r_k), \Delta\Phi_{DP}^f(r_0, r_k)]^T$, the RMSEs of SGMPE increase as number of mixtures after reduction increases for both SGMPE with $\mathbf{z} = [K_{dp}]$ and $\mathbf{z} = [Z_H, Z_{DR}]$. However, the variation of RMSEs are small for both cases when number of mixtures after reduction increases from 3 to 12.

Huge performance difference (10 [mm hr^{-1}]) between GMPE($\mathbf{z} = [Z_H]^T$) and SGMPE($\mathbf{z} = [Z_H]^T$) can be observed in Fig. 6.3(c) and Fig. 6.2(the magenta line). Such difference are mainly contributed by the large errors of SGMPE($\mathbf{z} = [Z_H]^T$) from estimating attenuations as illustrated in Fig. 5.20. In this case, SGMPE performs a little better when more mixtures are used after reduction.

To further test the performance of DP-GMPE, CI-GMPE and SGMPE with different inputs in noisy environments, zero mean Gaussian noise with standard deviation of 1 [dB] for Z_H, 0.3 [dB] for Z_{DR} and 2° for Φ_{dp} are added to the 15 rain paths. It should be pointed out that the DP-GMPE approach and the CI-GMPE approach are expected to have much worse performance in this 'noisy' rain path test than in previous 'clean' rain path test, since K_{dp} measurements will be severely contaminated by noise considering K_{dp} for rain in X-band are mostly lower than 10°. This is the reason why measurements of K_{dp} are often unreliable. Rainfall rate estimation results from this 'noisy' rain path test can be considered as the lower bound for the performance of DP-GMPE, CI-GMPE and SGMPE with different inputs.

As shown in Fig. 6.4(a), there is also not much difference between the performance of SGMPEs with 'Pruning' and 'Merging' mixture reduction algorithms

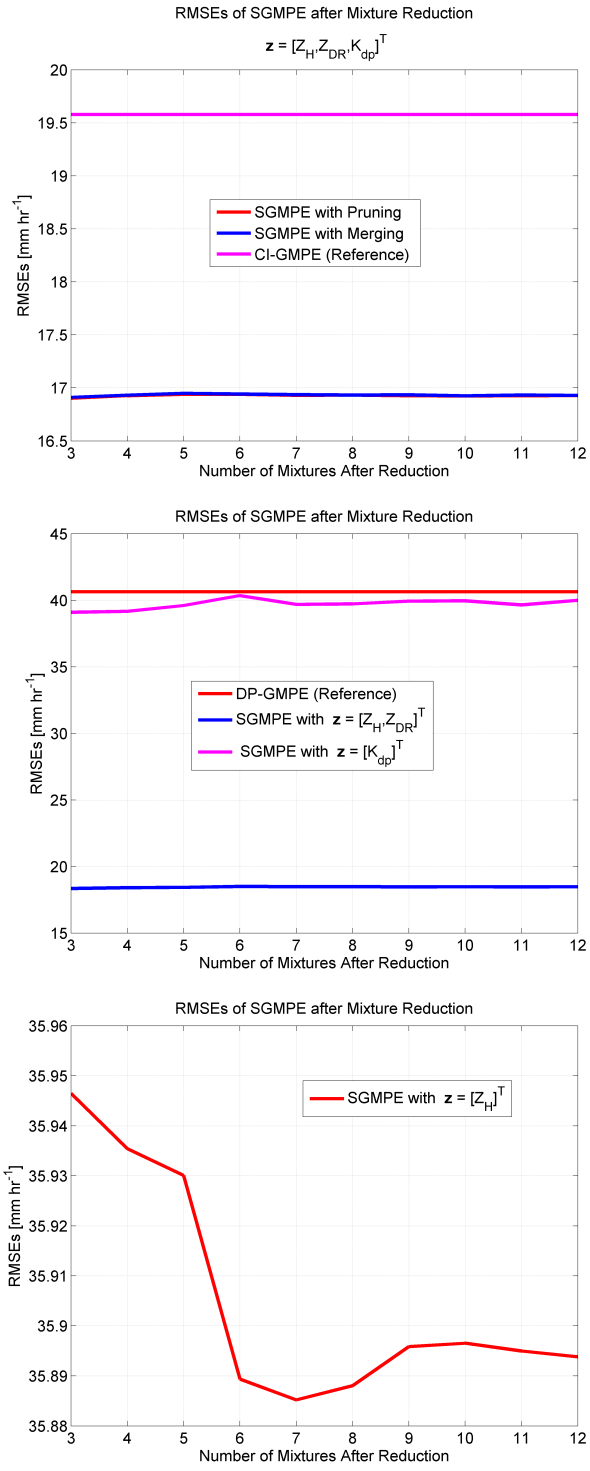


Figure 6.4: RMSEs of SGMPEs after mixture reduction for the 'noisy' rain path test. From top to bottom, (a) Comparision between 'Pruning' and 'Merging'; (b) Comparison between DP-GMPE and SGMPE with K_{dp} as input; (c) RMSEs of SGMPE with Z_H as input.

even in noisy environment. The RMSEs of SGMPE do not have notable changes when the number of mixtures after reduction increases. Compared with the results in Fig. 6.3(a), there is a 13 [mm hr^{-1}] difference for SGMPE with input $\mathbf{z}_k = [Z_H^m(r_k), Z_{DR}^m(r_k), \Delta\Phi_{DP}^f(r_0, r_k)]^T$ due to noise contamination. CI-GMPE is more sensitive to noise than SGMPE since SGMPE utilizes not only phase measurement but also power measurements, which are more noise-robust. Despite CI-GMPE and SGMPE performs similar in 'clean' environment, SGMPE shows better RMSE of 2.5 [mm hr^{-1}] than CI-GMPE in this 'noisy' rain path test.

Fig. 6.4(b) shows the performance comparison between DP-GMPE and SGMPE with K_{dp} as input for this 'noisy' rain path test. It may seem surprising that SGMPE with K_{dp} outperforms DP-GMPE in noisy environment. SGMPE is capable of refining Φ_{dp} estimation everytime when there is an phase measurement available while DP-GMPE does nothing but use the measured phase which is affected by noise. Compared the results with those from the 'clean' rain path test, both DP-GMPE and SGMPE with K_{dp} perform much worse in this 'noisy' rain path test as expected. There is a 30 [mm hr^{-1}] (300%) degradation in terms of RMSE for DP-GMPE and SGMPE with K_{dp} in noisy environment. Also affected by noise, performance of SGMPE with $\mathbf{z} = [Z_H, Z_{DR}]$ degrades by about 10 [mm hr^{-1}]. Similar to the 'clean' rain path test, the variation of RMSEs are small for all three algorithms when number of mixtures after reduction increases from 3 to 12.

It seems that noise does not have much impacts on the performance of SGMPE with $\mathbf{z} = [Z_H]$ as shown in Fig. 6.4(c). Errors from noise are small compared to the errors of SGMPE with $\mathbf{z} = [Z_H]$ when estimating attenuations. SGMPE performs almost the same for different numbers of mixtures after reduction.

Previous two tests show that the 'Pruning' mixture reduction algorithm can be used even when the number of mixture after reduction is as small as three. Using more number of mixtures after reduction does not necessary lead to better performance

for SGMPE. To evaluate performance of DP-GMPE, CI-GMPE and SGMPE with different inputs over range, a total of 50 realizations, in which there are 15 random paths in each realization, are generated from the test dataset. Zero mean Gaussian noise with standard deviation of 1 [dB] for Z_H, 0.3 [dB] for Z_{DR} and 2° for Φ_{dp} are added to all the paths. To be consist with the 6 mixture GMM used, the number of mixtures after reduction is also set at 6. Results of each approach are shown in Fig. 6.5.

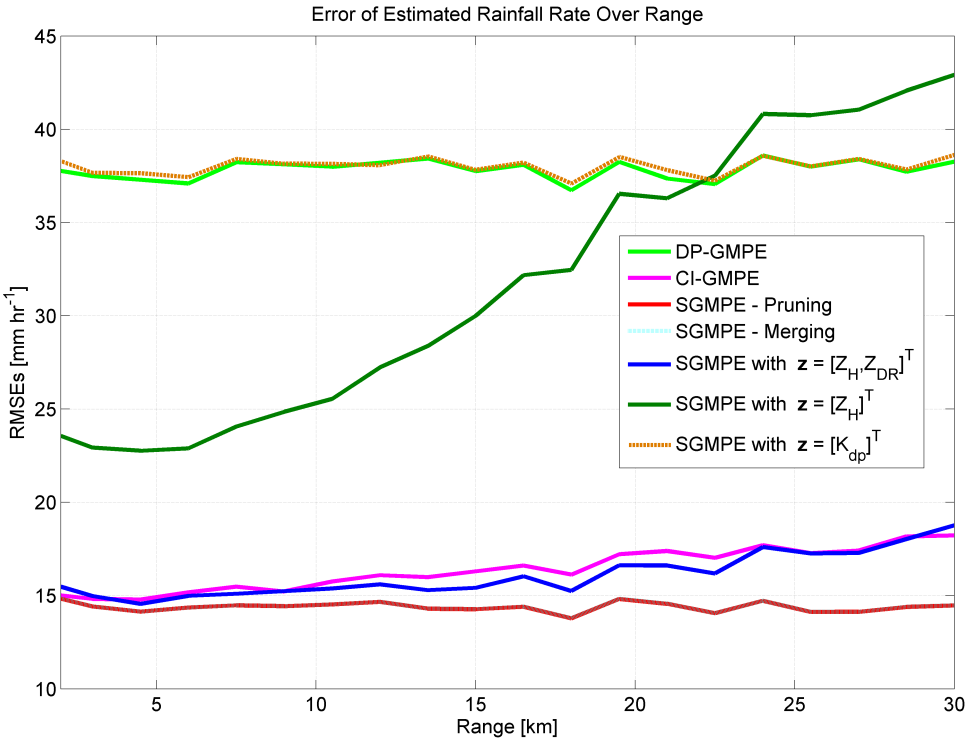


Figure 6.5: Error of estimated rainfall rate over range. Results are obtained by taking the average of 750 random paths. In the figure, 'SGMPE - Pruning' and 'SGMPE - Merging' both refer to SGMPE with $\mathbf{z}_k = [Z_H^m(r_k), Z_{DR}^m(r_k), \Delta\Phi_{DP}^f(r_0, r_k)]^T$ but different mixture reduction algorithm.

As shown in Fig. 6.5, results from 'SGMPE - Pruning' and 'SGMPE - Merging' are overlapped together, which again proves that the computationally expensive 'Merging' algorithm shows no advantage over the simple 'Pruning' algorithm for this application. Performance of DP-GMPE, SGMPE with K_{dp} and SGMPE with $\mathbf{z}_k = [Z_H^m(r_k), Z_{DR}^m(r_k), \Delta\Phi_{DP}^f(r_0, r_k)]^T$ is consistant over rage while the performance of the rest fo the algorithms are more or less degraded. For CI-GMPE and SGMPE with $\mathbf{z} = [Z_H, Z_{DR}]$, there is a 4 [mm hr^{-1}] difference in RMSE between the beginning of the path and the end of the path over a range of 30 km. This is because the accumulated error from estimating attenuation and mixture reduction. However, such degradation is acceptable. Assuming there is a long, continuous rain cell over 150 km, the average RMSEs of CI-GMPE and SGMPE with $\mathbf{z} = [Z_H, Z_{DR}]$ for the whole path would be around 25 [mm hr^{-1}], which is still not bad. Actually, even the 150 km long rain cell exists in nature, X-band radar is not able to see through it since attenuated return signal may be already under the receiver's noise floor after 40 or 50 km. Performance of SGMPE with $\mathbf{z} = [Z_H]$ significantly degrades when range increases, this is due to the large error of $\mathbf{z} = [Z_H]$ for estimating both rainfall rate and attenuation. So applications of SGMPE with $\mathbf{z} = [Z_H]$ should be limited to a shorter range, such as 50 to 100 km, to avoid significant degradation of performance.

6.3.3 Conclusions

Sequential Gaussian mixture parameter estimator is applied to rainfall rate estimation at X-band in this study. Results from numerical simulation show that the 'Pruning' mixture reduction algorithm can be used to limit the number of mixture in SGMPE without losing much accuracy. Number of mixtures after reduction can be as small as 3 and SGMPE still performs well. With the same inputs, SGMPE outperforms DP-GMPE and CI-GMPE in noisy environment. While both DP-GMPE and CI-GMPE are heavily dependent on K_{dp} measurements which are easily contaminated by noise,

SGMPE is capable of performing with or without phase measurement. Moreover, SGMPE provides a general frame work for meteorological applications in frequency bands where attenuation effects cannot be neglected. SGMPE is also applicable to other radar systems, such as dual-frequency radars, besides dual-polarized radars.

As the spatial extension of the GMPE approach, SGMPE carries all the properties from GMPE, for example, estimates from the SGMPE approach are optimized in terms of minimum variance and unbiased performance given radar observations at each radar resolution bin. Even with mixture reduction, close to optimum performance can still be obtained by SGMPE. The structure of the SGMPE is also possible to be extended to radar network applications.

Chapter 7

Conclusions

7.1 Summary

In this dissertation, a Gaussian mixture model (GMM) is introduced to characterize the prior distribution of weather parameters and the corresponding radar observation variables. The convergence capability of the GMM not only provides a general framework to accommodate diverse information but also supports statistically optimized hydrometeor classification and weather parameters estimation through a Bayesian approach. A Bayesian hydrometeor classifier is constructed based on the GMM and tested using simulated PRM from numerical weather prediction (NWP) model. A GMM-based linear Bayesian estimator (GMPE) is developed and applied to applications such as DSD retrieval, rainfall rate estimation and attenuation correction. The GMPE approach is further extended to a sequential Kalman filter structure. The sequential GMPE is applied and evaluated in rainfall rate estimation at X-band.

The overall contributions of this dissertation are summarized as follows:

- A single-cell Monte Carlo simulation is developed based on the idea that microphysics variables such as hydrometeor shape, canting angle, melting ratio and drop size distribution are allowed to have uncertainties (randomness) to avoid assumptions or losing generality. Any microphysics model can be incorporated into the framework. Realistic radar returns of different hydrometeors

at different frequency bands can be generated by the single-cell Monte Carlo simulation.

- To assist modern airborne radar development and evaluate radar performance in extreme scenarios, the single-cell simulation is applied to the entire radar scanning volume supported by numerical weather prediction model outputs. Dual-polarization airborne radar signatures corresponding to a mixed-phase storm case from both plan position indicator (PPI) and range height indicator (RHI) scan schemes at different layers of the atmosphere are generated.

- Dual-pol variables of rain at S-, C- and X-band are obtained using single-cell Monte Carlo simulations to better support and serve the development of polarimetric rain attenuation correction algorithms and rainfall rate estimation algorithms.

- A Gaussian mixture model is adopted to model the prior distribution of microphysics variables and the corresponding radar observation variables.

- A GMM-based hydrometeor classifier is developed based on radar signatures of different hydrometeors simulated from the single-cell Monte Carlo simulation. The classifier is then applied to hydrometeor hazard detection for airborne Sense-and-Avoid radar. Hail hazard detection by the GMM-based hydrometeor classifier is performed on PPI scans of snow-hail mixture as well as rain-hail mixture. Detection results with and without attenuation effects are shown and discussed.

- Based on GMM and Bayesian estimation theory, a linear Bayesian estimator (GMPE) for weather parameter estimation is developed and evaluated through two applications: attenuation estimation for different hydrometeors and rainfall

rate estimation using dual-frequency polarimetric radar measurements. Construction of state variables and impacts of number of mixtures are discussed and analyzed.

- The GMPE is applied to DSD parameter retrieval using S-band polarimetric radar measurements. Retrieval results are compared with those from two polarimetric radar DSD retrieval algorithms, the β method and the C-G method. GMPE shows better performance in every error category.

- A Gaussian Mixture Rainfall-rate Estimator is developed for polarimetric radar-based rainfall rate estimation. The GMRE is trained from a simulation dataset that is designed to favor rainfall rate lower than 40 [mm hr^{-1}]. The GMRE approach is validated by using data collected during the Joint Polarization Experiment from the well-gauged central Oklahoma region and S-band radar data from the KOUN radar. Performance of GMRE is compared to other rainfall rate estimators that were developed and tested on the JPOLE dataset. The proposed GMRE approach outperforms the JPOLE-tuned synthetic R_{SYN} relation in terms of bias and RMSE.

- The GMPE approach is further extended to an iterative form for path-integrated attenuation correction of rain to retrieve both horizontal reflectivity and differential reflectivity using polarimetric radar measurements. Two iterative GMM approaches, the DP-GMPE approach and the CI-GMPE approach, are developed and tested along with other famous PIA correction algorithms using X-band radar measurements from simulated rain profiles generated under different microphysical scenarios. Performance of DP-GMPE and CI-GMPE over range are also analyzed. Both proposed GMPE-related approaches, DP-GMPE and CI-GMPE, are capable in PIA correction application and shows better performance than conventional PIA correction algorithms with the same inputs.

- The GMPE approach is reconstructed to adopt the sequential Kalman filter structure for radar meteorological applications in frequency bands where attenuation effects cannot be ignored. Derivation of the GMPE with sequential filtering structure is presented. Algorithms for Gaussian mixture reduction are introduced and discussed. The SGMPE approach with different inputs is applied to rainfall rate estimation for X-band. Estimation results are compared with those from the DP-GMPE approach and the CI-GMPE approach. Impacts of mixture reduction and performance of SGMPE over range are presented and analyzed. SGMPE is shown to perform better even without phase measurement.

7.2 Major Achievements

The major achievement of this study is the introduction of a Gaussian mixture model to characterize the prior distribution of radar observation variables and the underlying microphysics variables. Ensured by the convergence of GMM to any specific distribution as number of mixtures increase, microphysics variation in space and time can be learnt and embedded in the model. The convergence capability of GMM also provides a general framework to accommodate extra information not only from dual-polarization diversities, but also from other diversities such as multiple frequencies and multiple observation sources, for instance, measurements from different radars or measurements from radar and satellite-based microwave sensors. Statistically optimized hydrometeor classification and weather parameters estimation through Bayesian approach are made possible by the precisely represented prior distribution. GMMs with different numbers of mixtures can be used to model distributions with different complexities. Individual radar applications may employ a 'small' GMM while a 'larger' GMM may be constructed for more comprehensive applications.

Based on Gaussian mixture model, a Bayesian hydrometeor classifier is developed. Compared with fuzzy logic approaches, the GMM-based Bayesian classifier has several advantages: 1) Cross correlations among different dimensions/variables can be properly modeled; 2) the PDF of the occurrence of each hydrometeor class can also be precisely approximated by GMM; 3) the Classification result is statistically optimal.

A linear Bayesian estimator for radar-based weather parameter estimation is also developed based on GMM and Bayesian estimation theory. GMPE also has several advantages over conventional PLR approaches and other Bayesian approaches: GMPE is a 'best' estimator in terms of minimum-variance and unbiased performance; GMPE is a flexible approach where different radar observation variables can be included/excluded from inputs and remains as optimum; GMPE is applicable to different radar-meteorological applications and estimation of different parameters can be done at the same time. Two iterative GMPE, DP-GMPE and CI-GMPE, are constructed for PIA correction and weather parameter estimation in frequency bands where attenuation effects cannot be ignored.

GMPE is further extended to explore spatial relations of weather radar observations with a sequential Kalman Filter structure. The sequential GMPE is configured to take into account the path-integrated attenuation effects. As the spatial extension of the GMPE approach, SGMPE carries all the advantages of GMPE, such as minimum-variance and unbiased estimations for every radar range bin. Even though the mixture reduction procedure may degrade the performance of SGMPE, close to optimum performance can still be obtained by SGMPE. Other advantages of the SGMPE approach includes: 1) SGMPE is capable of performing in high attenuation environment with or without phase measurement while most existing algorithms heavily rely on phase measurements; 2) The structure of the SGMPE also make it possible to be extended to radar network applications.

Results from the GMM-based hydrometoer classifier, the GMPE approach and the sequential GMPE approach are statistically optimized as long as the prior distribution represented by GMM is precise and accurate. Since GMM would converge to any distribution, the three GMM-based approaches provide a general solution for radar-meteorological applications such as hydrometeor classification, DSD retrieval, rainfall rate estimation and attenuation correction at different radar frequencies. It can be used in different types of radar systems, such as single polarization, dual-polarization and dual-frequency radars. As such, attentions and interests may be shifted from developing new algorithms based on phenomenological or empirical relationships to construct better training dataset from simulations aided by physical knowledge of radar signatures or real measurements.

7.3 Future Work

A general framework for radar-meteorological applications has been developed in this study based on Gaussian mixture model. Future work for this study will be focused on:

- Apply and validate the three GMM-based approaches in practical radar systems, such as KOUN, OU-PRIME and RaxPol. Construct more specific and realistic datasets, either from simulation or measurement, with respect to the practical radar system and application for GMM training. Validate the GMM-based approaches using real radar measurements of different weather conditions. Develop GMPEs and SGMPEs for operational use.

- Improve the GMM-based hydrometeor classifier by employing more hydrometeor classes and adopting more sophisticated hydrometeor models. This study only considers rain, snow and hail as well as melting snow and melting hail, five hydrometer species. For rain, according to different intensities, large drops,

light rain, medium rain and heave rain may be considered. For hail and snow, according to their sizes and shapes, hail, graupel/small hail, ice crystals, dry snow and wet snow may be incorporated. Moreover, a hail/rain mixture species may also be included. For each hydrometeor species, physical properties such DSDs, shapes, melting behaviour and falling speeds need to be properly modeled. Temperature information may also be used in addition to radar observations as inputs to the classifier.

- Apply the sequential GMPE approach to other radar systems, such as the spaceborne radar system where dual-frequency (Ka and Ku) is used and the CASA radar network systems.

Bibliography

Ali-Loytty, S., 2008: Efficient Gaussian mixture filter for hybrid positioning. *Position, Location and Navigation Symposium, 2008 IEEE/ION*, 60–66.

Alspach, D. and H. Sorenson, 1972: Nonlinear Bayesian estimation using Gaussian sum approximations. *IEEE Trans. Autom. Control*, **17 (4)**, 439–448.

Anagnostou, M. N., E. N. Anagnostou, and J. Vivekanandan, 2006: Correction for rain path specific and differential attenuation of X-band dual-polarization observations. *IEEE Trans. Geosci. Remote Sens.*, **44 (9)**, 2470–2480.

Andsager, K., K. V. Beard, and N. F. Laird, 1999: Laboratory measurements of axis ratios for large raindrops. *J. Atmos. Sci.*, **56 (15)**, 2673–2683.

Atlas, D., 1990: *Radar in Meteorology*. American. Meterol. Society, Boston.

Aydin, K. and Y. Zhao, 1990: A computational study of polarimetric radar observables in hail. *IEEE Trans. Geosci. Remote Sens.*, **28 (4)**.

Blackman, S., 2004: Multiple hypothesis tracking for multiple target tracking. *IEEE Trans. Aerosp. Electron. Syst.*, **19 (1)**, 5–18.

Brandes, E. A., G. Zhang, and J. Vivekanandan, 2002: Experiments in rainfall estimation with a polarimetric radar in a subtropical environment. *J. Appl. Meteorol.*, **41 (6)**, 674–685.

Brandes, E. A., G. Zhang, and J. Vivekanandan, 2004: Comparison of polarimetric radar drop size distribution retrieval algorithms. *J. Atmos. Oceanic Technol.*, **21 (4)**, 584–598.

Bringi, V., R. Rasmussen, and J. Vivekanandan, 1986: Multiparameter radar measurements in Colorado convective storms. Part I: Graupel melting studies. *J. Atmos. Sci.*, **43 (22)**.

Bringi, V. N. and V. Chandrasekar, 2001: *Polarimetric Doppler Weather Radar Principles and Applications*. Cambridge University Press, Cambridge, UK.

Bringi, V. N., T. D. Keenan, and V. Chandrasekar, 2001: Correcting C-band radar reflectivity and differential reflectivity data for rain attenuation: A self-consistent method with constraints. *IEEE Trans. Geosci. Remote Sens.*, **39 (9)**, 1906–1915.

Bringi, V. N., T. Tang, and V. Chandrasekar, 2004: Evaluation of a new polarimetrically based Z-R relation. *J. Atmos. Oceanic Technol.*, **21 (4)**, 612–623.

Cao, Q., G. Zhang, E. A. Brandes, and T. J. Schuur, 2010: Polarimetric radar rain estimation through retrieval of drop size distribution using a Bayesian approach. *J. Appl. Meteor. Climate*, **49 (5)**, 973–990.

Chen, H. D., K. C. Chang, and C. Smith, 2010: Constraint optimized weight adaptation for Gaussian mixture reduction. *Proceedings of SPIE: Signal Processing, Sensor Fusion, and Target Recognition XIX*, Vol. 7697, 76970N176970N10.

Cheong, B. L., R. D. Palmer, and M. Xue, 2008: A time series weather radar simulator based on high-resolution atmospheric models. *J. Atmos. Oceanic Technol.*, **25 (2)**, 230–243.

Chiu, J. C. and G. W. Petty, 2006: Bayesian retrieval of complete posterior PDFs of oceanic rain rate from microwave observations. *J. Appl. Meteor. Climate*, **45 (8)**, 1073–1095.

Chuang, C. C. and K. V. Beard, 1990: A numerical model for the equilibrium shape of electrified raindrops. *J. Atmos. Sci.*, **47 (11)**, 1374–1389.

Cifelli, R., V. Chandrasekar, S. Lim, P. C. Kennedy, Y. Wang, and S. A. Rutledge, 2011: A new dual-polarization radar rainfall algorithm: Application in Colorado precipitation events. *J. Atmos. Oceanic Technol.*, **28 (3)**, 352–364.

Crouse, D., P. Willett, K. Pattipati, and L. Svensson, 2011: A look at Gaussian mixture reduction algorithms. *Information Fusion (FUSION), 2011 Proceedings of the 14th International Conference on*, 1–8.

Dempster, A. P., N. M. Laird, and D. B. Rubin, 1977: Maximum likelihood from incomplete data via the EM algorithm. *J. Roy. Statistical Society, Series B*, **39 (1)**, 1–38.

Di Michele, S., A. Tassa, A. Mugnai, F. S. Marzano, P. Bauer, and J. P. V. P. Baptista, 2005: Bayesian algorithm for microwave-based precipitation retrieval: Description and application to TMI measurements over ocean. *IEEE Trans. Geosci. Remote Sens.*, **43 (4)**, 778–791.

Doviak, R. J., V. Bringi, A. Ryzhkov, A. Zahrai, and D. Zrnić, 2000: Considerations for polarimetric upgrades to operational WSR-88D radars. *J. Atmos. Oceanic Technol.*, **17 (3)**, 257–278.

Doviak, R. J., J. K. Carter, V. M. Melnikov, and D. S. Zrnić, 2002: *Modifications to the research WSR-88D to obtain polarimetric data*. National Severe Storms Laboratory Rep., 49 pp.

Doviak, R. J. and D. S. Zrnić, 1993: *Doppler Radar and Weather Observations*. Academic Press, San Diego, Calif., 130 pp, 130-134 pp.

Du, J., Y. Hu, and H. Jiang, 2011: Boosted mixture learning of Gaussian mixture hidden Markov models based on maximum likelihood for speech recognition. *IEEE Trans. Speech Audio Process.*, **19 (7)**, 2091 –2100.

Evans, K. F., J. Turk, T. Wong, and G. L. Stephens, 1995: A Bayesian approach to microwave precipitation profile retrieval. *J. Appl. Meteorol.*, **34 (1)**, 260–279.

Fabry, F. and W. Szyrmer, 1999: Modeling of the melting layer. Part II: Electromagnetic. *J. Atmos. Sci.*, **56 (20)**, 3593–3600.

Fiebrich, C. A., D. L. Grimsley, R. A. McPherson, K. A. Kesler, and G. R. Essenberg, 2006: The value of routine site visits in managing and maintaining quality data from the Oklahoma mesonet. *J. Atmos. Oceanic Technol.*, **23 (3)**, 406–416.

Fulton, R. A., J. P. Breidenbach, D.-J. Seo, D. A. Miller, and T. OBannon, 1998: The WSR-88D rainfall algorithm. *Wea. Forecasting*, **13 (2)**, 377–395.

Gan, G., C. Ma, and J. Wu, 2007: *Data Clustering: Theory, Algorithms, and Applications (ASA-SIAM Series on Statistics and Applied Probability)*. SIAM, Society for Industrial and Applied Mathematics.

Giangrande, S. E. and A. V. Ryzhkov, 2008: Estimation of rainfall based on the results of polarimetric echo classification. *J. Appl. Meteor. Climate*, **47 (9)**, 2445–2462.

Gilmore, M. S., J. M. Straka, and E. N. Rasmussen, 2004: Precipitation uncertainty due to variations in precipitation particle parameters within a simple microphysics scheme. *Mon. Weather Rev.*, **132 (11)**, 2610–2627.

Gomez, R. and T. Kawahara, 2010: Robust speech recognition based on dereverberation parameter optimization using acoustic model likelihood. *IEEE Trans. Speech Audio Process.*, **18 (7)**, 1708 –1716.

Gorgucci, E. and L. Baldini, 2007: Attenuation and differential attenuation correction of C-band radar observations using a fully self-consistent methodology. *IEEE Geosci. Remote Sens. Lett*, **4 (2)**, 326–330.

Gorgucci, E., V. Chandrasekar, and L. Baldini, 2006: Correction of X-band radar observation for propagation effects based on the self-consistency principle. *J. Atmos. Oceanic Technol.*, **23 (12)**, 1668–1681.

Gorgucci, E., V. Chandrasekar, V. N. Bringi, and G. Scarchilli, 2002: Estimation of raindrop size distribution parameters from polarimetric radar measurements. *J. Atmos. Sci.*, **59 (15)**, 2373–2384.

Green, A. W., 1975: An approximation for the shape of large raindrops. *J. Appl. Meteorol.*, **14**, 15781583.

Haddad, Z. S., J. P. Meagher, S. L. Durden, E. A. Smith, and E. Im, 2006: Drop size ambiguities in the retrieval of precipitation profiles from dual-frequency radar measurements. *J. Atmos. Sci.*, **63 (1)**, 204–217.

Hasan, T. and J. Hansen, 2011: A study on universal background model training in speaker verification. *IEEE Trans. Speech Audio Process.*, **19 (7)**, 1890 –1899.

Hendry, A. and G. C. McCormick, 1976: Radar observations of the alignment of precipitation particles by electrostatic fields in thunderstorms. *J. Geophys. Res.*, **81 (30)**, 5353–5357.

Hogan, R. J., 2007: A variational scheme for retrieving rainfall rate and hail reflectivity fraction from polarization radar. *J. Appl. Meteor. Climate*, **46 (10)**, 1544–1564.

Hong, S.-Y., J. Dudhia, and S.-H. Chen, 2004: A revised approach to ice microphysical processes for the bulk parameterization of clouds and precipitation. *Mon. Weather Rev.*, **132 (1)**, 103–120.

Huang, G.-J., V. N. Bringi, and M. Thurai, 2008: Orientation angle distributions of drops after an 80-m fall using a 2D video disdrometer. *J. Atmos. Oceanic Technol.*, **25 (9)**, 1717–1723.

Huber, M. and U. Hanebeck, 2008: Progressive Gaussian mixture reduction. *Information Fusion, 2008 11th International Conference on*, 1–8.

Joss, J. and A. Waldvogel, 1969: Raindrop size distribution and sampling size errors. *J. Atmos. Sci.*, **26 (3)**, 566–569.

Jung, Y., G. Zhang, and M. Xue, 2008: Assimilation of simulated polarimetric radar data for a convective storm using the ensemble Kalman filter. Part I: Observation operators for reflectivity and polarimetric variables. *Mon. Weather Rev.*, **136 (6)**, 2228 –2245.

Kaufman, L. and P. J. Rousseeuw, 1990: *Finding Groups in Data: An Introduction to Cluster Analysis (Wiley Series in Probability and Statistics)*. Wiley-Interscience, Canada.

Keenan, T. D., L. D. Carey, D. S. Zrnić, and P. T. May, 2001: Sensitivity of 5-cm wavelength polarimetric radar variables to raindrop axial ratio and drop size distribution. *J. Appl. Meteorol.*, **40 (3)**, 526–545.

Kessler, E., 1969: On the distribution and continuity of water substance in atmospheric circulations. *Meteor. Monogrv.*, **10 (32)**, 84pp.

Knight, C. A. and N. C. Knight, 1970: The falling behavior of hailstones. *J. Atmos. Sci.*, **27 (4)**, 672–681.

Knight, N. C., 1986: Hailstone shape factor and its relation to radar interpretation of hail. *J. Climate Appl. Meteor.*, **25 (12)**, 1956–1958.

Kullback, S. and R. A. Leibler, 1951: On information and sufficiency. *Annals of Mathematical Statistics*, **22**, 49–86.

Le, K., 2009: *The Use Of Phased Array Radars for Obervations of The Weather*. Dissertation, Norman, OK, 182 pp.

Lee, G. W. and I. Zawadzki, 2005: Variability of drop size distributions: Time-scale dependence of the variability and its effects on rain estimation. *J. Appl. Meteorol.*, **44 (2)**, 241–255.

Lewis, J. M., S. Lakshmivarahan, and S. Dhall, 2006: *Dynamic Data Assimilation: A Least Squares Approach (Encyclopedia of Mathematics and its Applications)*. Cambridge University Press, 680 pp.

Li, Z. and Y. Zhang, 2011: Application of Gaussian mixture model (GMM) and estimator to radar-based weather parameter estimations. *IEEE Geosci. Remote Sens. Lett*, **In Press**.

Li, Z., Y. Zhang, G. Zhang, and B. K. A., 2011: A microphysics-based simulator for advanced airborne weather radar development. *IEEE Trans. Geosci. Remote Sens.*, **49 (4)**, 1356–1373.

Liao, L. and R. Meneghini, 2005: On modeling air/spaceborne radar returns in the melting layer. *IEEE Trans. Geosci. Remote Sens.*, **43 (12)**, 2799– 2809.

Lillesand, T. M., 2006: *Remote Sensing and Image Interpretation*. John Wiley & Sons.

Lim, S., V. Chandrasekar, and V. Bringi, 2005: Hydrometeor classification system using dual-polarization radar measurements: Model improvements and in situ verification. *IEEE Trans. Geosci. Remote Sens.*, **43 (4)**, 792 – 801.

Lin, Y.-L., R. D. Farley, and H. D. Orville, 1983: Bulk parameterization of the snow field in a cloud model. *J. Appl. Meteorol.*, **22 (6)**, 10651092.

MacKeown, P. K., 1997: *Stochastic Simulation in Physics*. Springer-Verlag, New York.

Marshall, J. S. and W. Palmer, 1948: The distribution of raindrops with size. *J. Meteor.*, **5**, 165–166.

Marzano, F. S., G. Botta, and M. Montopoli, 2010: Iterative Bayesian retrieval of hydrometeor content from X-band polarimetric weather radar. *IEEE Trans. Geosci. Remote Sens.*, **48 (8)**, 3059–3074.

Marzano, F. S., D. Scaranari, M. Montopoli, and G. Vulpiani, 2008: Supervised classification and estimation of hydrometeors from C-band dual-polarized radars: A Bayesian approach. *IEEE Trans. Geosci. Remote Sens.*, **46 (1)**, 85–98.

Marzano, F. S., D. Scaranari, and G. Vulpiani, 2007: Supervised fuzzy-logic classification of hydrometeors using C-band weather radars. *IEEE Trans. Geosci. Remote Sens.*, **45 (11)**, 3784–3799.

Maxwell Garnett, J. C., 1904: Colours in metal glasses and in metallic films. *Phil. Trans. R. Soc. A*, **203**, 385–420.

May, R. M., M. I. Biggerstaff, and M. Xue, 2007: A Doppler radar emulator with an application to the detectability of tornadic signatures. *J. Atmos. Oceanic Technol.*, **24 (12)**, 1973–996.

McLachlan, G. and K. Basford, 1988: *Mixture Models: Inference and Applications to Clustering*. Marcel Dekker, New York.

McLachlan, G. J. and T. Krishnan, 2008: *The EM Algorithm and Extensions (Wiley Series in Probability and Statistics)*. 2d ed., Wiley-Interscience.

McPherson, R. A., et al., 2007: Statewide monitoring of the mesoscale environment: A technical update on the Oklahoma mesonet. *J. Atmos. Oceanic Technol.*, **24 (3)**, 301–321.

Meneghini, R. and L. Liao, 1996: Comparisons of cross sections for melting hydrometeors as derived from dielectric mixing formulas and a numerical method. *J. Appl. Meteorol.*, **35 (10)**, 16581670.

Meneghini, R. and L. Liao, 2000: Effective dielectric constants of mixed-phase hydrometeors. *J. Atmos. Oceanic Technol.*, **17 (5)**, 628640.

Metropolis, N. and S. Ulam, 1949: The Monte Carlo method. *J. Amer. Statistical Assoc.*, **44 (247)**, 335–341.

Mishchenko, M. I., 2000: Calculation of the amplitude matrix for a nonspherical particle in a fixed orientation. *Appl. Optics*, **39 (6)**, 1026–1031.

Park, S. G., V. N. Bringi, V. Chandrasekar, M. Maki, and K. Iwanami, 2005: Correction of radar reflectivity and differential reflectivity for rain attenuation at X band. Part I: Theoretical and empirical basis. *J. Atmos. Oceanic Technol.*, **22 (11)**, 1621–1632.

Pena, J., J. Lozano, and P. Larranaga, 1999: An empirical comparison of four initialization methods for the k-means algorithm. *Pattern Recogn. Lett.*, **20**, 10271040.

Pruppacher, H. R. and K. V. Beard, 1970: A wind tunnel investigation of the internal circulation and shape of water drops falling at terminal velocity in air. *Quart. J. R. Met. Soc.*, **96**, 247–256.

Rasmussen, R. M. and A. J. Heymsfield, 1987: Melting and shedding of graupel and hail. Part II: Sensitivity study. *J. Atmos. Sci.*, **44 (19)**, 2764–2782.

Ray, P., B. Johnson, K. Johnson, J. Bradberry, J. Stephens, K. Wagner, R. Wilhelmson, and J. Klemp, 1981: The morphology of several tornadic storms on 20 may 1977. *J. Atmos. Sci.*, **38 (8)**, 16431663.

Ray, P. S., 1972: Broadband complex refractive indices of ice and water. *Appl. Optics*, **11 (8)**, 1836–1844.

Richards, J. A. and X. Jia, 1999: *Remote Sensing Digital Image Analysis: An Introduction*. 3d ed., Springer-Verlag New York, Inc., Secaucus, NJ, USA.

Robert, C. P. and G. Casella, 2004: *Monte Carlo Statistical Methods (2nd ed.)*. Springer-Verlag, New York.

Rose, C. R. and V. Chandrasekar, 2006: A GPM dual-frequency retrieval algorithm: DSD profile-optimization method. *J. Atmos. Oceanic Technol.*, **23 (10)**, 1372–1383.

Rosenfeld, D., D. B. Wolff, and D. Atlas, 1993: General probability-matched relations between radar reflectivity and rain rate. *J. Appl. Meteorol.*, **32 (1)**, 50–72.

Rubinstein, R. Y. and D. P. Kroese, 2007: *Simulation and the Monte Carlo Method (2nd ed.)*. Wiley, New York.

Runnalls, A., 2007: Kullback-leibler approach to Gaussian mixture reduction. *IEEE Trans. Aerosp. Electron. Syst.*, **43 (3)**, 989–999.

Russell, S. and P. Norvig, 2009: *Artificial Intelligence: A Modern Approach (3rd Edition)*. Prentice Hall, 1152 pp.

Ryzhkov, A. V., S. E. Giangrande, and T. J. Schuur, 2005a: Rainfall estimation with a polarimetric prototype of WSR-88D. *J. Appl. Meteorol.*, **44 (4)**, 502–515.

Ryzhkov, A. V., T. J. Schuur, D. W. Burgess, P. L. Heinselman, S. E. Giangrande, and D. S. Zrnić, 2005b: The joint polarization experiment: Polarimetric rainfall measurements and hydrometeor classification. *Bull. Amer. Meteor. Soc.*, **86 (6)**, 809–824.

Ryzhkov, A. V., D. S. Zrnić, J. C. Hubbert, V. N. Bringi, J. Vivekanandan, and E. A. Brandes, 2002: Polarimetric radar observations and interpretation of co-cross-polarcorrelation coefficients. *J. Atmos. Oceanic Technol.*, **19 (3)**, 340–354.

Salmond, D., 1989: Mixture reduction algorithms for target tracking. *State Estimation in Aerospace and Tracking Applications, IEE Colloquium on*, 7/1 –7/4.

Salmond, D., 2009: Mixture reduction algorithms for point and extended object tracking in clutter. *IEEE Trans. Aerosp. Electron. Syst.*, **45 (2)**, 667 –686.

Schieferdecker, D. and M. Huber, 2009: Gaussian mixture reduction via clustering. *Information Fusion, 2009. FUSION '09. 12th International Conference on*, 1536 –1543.

Seliga, T. A. and V. N. Bringi, 1976: Potential use of radar differential reflectivity measurements at orthogonal polarizations for measuring precipitation. *J. Appl. Meteorol.*, **15 (1)**, 69–76.

Shafer, M. A., C. A. Fiebrich, D. S. Arndt, S. E. Fredrickson, and T. W. Hughes, 2000: Quality assurance procedures in the Oklahoma mesonetwork. *J. Atmos. Oceanic Technol.*, **17 (4)**, 474–494.

Skolnik, M., 2001: *Introduction to Radar Systems*. McGraw-Hill, Boston, MA.

Straka, J. M., D. S. Zrnić, and A. V. Ryzhkov, 2000: Bulk hydrometeor classification and quantification using polarimetric radar data: Synthesis of relations. *J. Appl. Meteorol.*, **39**, 1341–1372.

Testud, J., P. Amayenc, and M. Marzoug, 1992: Rainfall-rate retrieval from a space-borne radar: Comparison between single-frequency, dual-frequency, and dual-beam techniques. *J. Atmos. Oceanic Technol.*, **9 (5)**, 599–623.

Testud, J., E. Le Bouar, E. Obligis, and M. Ali-Mehenni, 2000: The rain profiling algorithm applied to polarimetric weather radar. *J. Atmos. Oceanic Technol.*, **17 (3)**, 332–356.

Testud, J., S. Oury, R. A. Black, P. Amayenc, and X. Dou, 2001: The concept of normalized distribution to describe raindrop spectra: A tool for cloud physics and cloud remote sensing. *J. Appl. Meteorol.*, **40 (6)**, 1118–1140.

Tong, M. and M. Xue, 2008: Simultaneous estimation of microphysical parameters and atmospheric state with simulated radar data and ensemble square root Kalman filter. Part I: Sensitivity analysis and parameter identifiability. *Mon. Weather Rev.*, **136 (5)**, 1630–1648.

Ulbrich, C. W., 1983: Natural variations in the analytical form of the raindrop size distribution. *J. Climate Appl. Meteor.*, **22 (10)**, 1764–1775.

Vivekanandan, J., S. M. Ellis, R. Oye, D. S. Zrnić, A. V. Ryzhkov, and J. Straka, 1999: Cloud microphysics retrieval using S-band dual-polarization radar measurements. *Bull. Amer. Meteor. Soc.*, **80 (3)**, 381–388.

Vulpiani, G., S. Giangrande, and F. S. Marzano, 2009: Rainfall estimation from polarimetric S-band radar measurements: Validation of a neural network approach. *J. Appl. Meteor. Climate*, **48 (10)**, 2022–2036.

Vulpiani, G., F. Marzano, V. Chandrasekar, and S. Lim, 2005: Constrained iterative technique with embedded neural network for dual-polarization radar correction of rain path attenuation. *IEEE Trans. Geosci. Remote Sens.*, **43 (10)**, 2305 – 2314.

Vulpiani, G., F. S. Marzano, V. Chandrasekar, A. Berne, and R. Uijlenhoet, 2006: Polarimetric weather radar retrieval of raindrop size distribution by means of a regularized artificial neural network. *IEEE Trans. Geosci. Remote Sens.*, **44 (11)**, 3262–3275.

Vulpiani, G., P. Tabary, J. Parent du Chatelet, and F. S. Marzano, 2008: Comparison of advanced radar polarimetric techniques for operational attenuation correction at C band. *J. Atmos. Oceanic Technol.*, **25 (7)**, 1118–1135.

Waldvogel, A., 1974: The N0 jump of raindrop spectra. *J. Atmos. Sci.*, **31 (4)**, 1067–1078.

Wang, Y. and V. Chandrasekar, 2010: Quantitative precipitation estimation in the casa X-band dual-polarization radar network. *J. Atmos. Oceanic Technol.*, **27 (10)**, 1665–1676.

Williams, J. and P. Maybeck, 2003: Cost-function-based Gaussian mixture reduction for target tracking. *Information Fusion, 2003. Proceedings of the Sixth International Conference of*, Vol. 2, 1047–1054.

Xue, M., K. K. Droegemeier, and V. Wong, 2000: The advanced regional prediction system (ARPS): A multi-scale nonhydrostatic atmospheric simulation and prediction model. Part I: Model dynamics and verification. *Meteor. Atmos. Phys.*, **75**, 161–193.

Xue, M., D. Wang, J. Gao, K. Brewster, and K. K. Droegemeier, 2003: The advanced regional prediction system (ARPS), storm-scale numerical weather prediction and data assimilation. *Meteor. Atmos. Phys.*, **82**, 139–170.

Xue, M., et al., 2001: The advanced regional prediction system (ARPS) : A multi-scale nonhydrostatic atmospheric simulation and prediction tool. Part II: Model physics and applications. *Meteor. Atmos. Phys.*, **76**, 143–165.

Yokoyama, T. and H. Tanaka, 1984: Microphysical processes of melting snowflakes detected by two-wavelength radar. Part I. Principle of measurement based on model calculation. *J. Met. Soc. Japan*, **62 (4)**, 650–667.

Zhang, G., J. Vivekanandan, and E. Brandes, 2001: A method for estimating rain rate and drop size distribution from polarimetric radar measurements. *IEEE Trans. Geosci. Remote Sens.*, **39 (4)**, 830 –841.

Zhang, G., M. Xue, Q. Cao, and D. Dawson, 2008: Diagnosing the intercept parameter for exponential raindrop size distribution based on video disdrometer observations: Model development. *J. Appl. Meteor. Climate*, **47 (11)**, 2983–2992.

Zhang, Y., A. Huston, M. Mallo, Z. Li, and G. Zhang, 2010: A scatterometer system for laboratory study of polarimetric electromagnetic signatures of icy hydrometeors. *IEEE Trans. Instrum. Meas.*, **59 (3)**, 671 –681.

Zhang, Y., R. Palmer, G. Zhang, T.-Y. Yu, K. Brewster, M. Yeary, M. Xue, and P. Chilson, 2008: Multi-functional airborne external hazard monitoring radar with antenna diversity. *Society of Photo-Optical Instrumentation Engineers (SPIE) Conference Series*, Society of Photo-Optical Instrumentation Engineers (SPIE) Conference Series, Vol. 7088.

Zrnić, D. S., A. Ryzhkov, J. Straka, Y. Liu, and J. Vivekanandan, 2001: Testing a procedure for automatic classification of hydrometeor types. *J. Atmos. Oceanic Technol.*, **18 (6)**, 892–913.

Appendix A - List Of Symbols

A	Specific Attenuation
A_h	Specific Horizontal Attenuation
A_v	Specific Vertical Attenuation
A_{dp}	Specific Differential Attenuation
cm	Centimeter, 10^{-2} meters
D	Equivalent Diameter
D_0	Median Volume Diameter
D_e	Effective Diameter
ΔD	Diameter Interval
D_{max}	Maximum Diameter
D_{min}	Minimum Diameter
exp()	Exponential Function
ϵ	Dielectric Constant
ϵ_e	Effective Dielectric Constant of a Mixture
ϵ_i	Dielectric Constant of Ice
ϵ_w	Dielectric Constant of Water
η	Reflectivity or Average Radar Cross Section Per Unit Volume
f	Radar Frequency
$\mathbf{f}$	Scattering Amplitude Matrix
f_v	Fractional Volume
f_w	Fractional Volume of Water

f_a	Fractional Volume of Air
f_i	Fractional Volume of Ice
f_d	Doppler Frequency
$f_{a,b}$	Scattering Amplitude at Major (or Minor) Axis of a Drop without Canting
$f_{hh,vv}$	Scattering Amplitude at H or V Polarization
$\Gamma()$	Gamma Function
γ_w	Melting Ratio
$I(t)/Q(t)$	In-phase/Quadrature Signal
K_{dp}	Specific Differential Phase [deg km^{-1}]
K_{DP}	Specific Differential Phase [deg km^{-1}]
K_w	Dielectric Factor of Water
λ	Wavelength
Λ	Slope Parameter
M_n	The n^{th} DSD Moment
mm	Millimeter, 10^{-3} meters
μ	Shape Parameter
N_0	Intercept Parameter
N_w	Normalized Drop Concentration
$N(D)$	Drop Size Distribution
N_t	Total Number of Hydrometeors Within the Single Cell
N_T	Total Number Concentration
ϕ	Canting Angle of Hydrometeors
ϕ_{dp}	Differential Phase
r	Range
r_a	Axis Ratio

R	Rainfall Rate
R_u	Maximum Unambiguous Range
ρ_{hv}	Correlation Coefficient
ρ_a	Density of Air
ρ_h	Density of Hail
ρ_i	Density of Ice
ρ_s	Density of Snow
ρ_w	Density of Water
σ	Radar Cross Section
Z	Reflectivity Factor
Z_h	Reflectivity Factor at Horizontal Polarization [$\mathrm{mm^6 m^{-3}}$]
Z_H	Reflectivity Factor at Horizontal Polarization [dBZ]
Z_v	Reflectivity Factor at Vertical Polarization [$\mathrm{mm^6 m^{-3}}$]
Z_V	Reflectivity Factor at Vertical Polarization [dBZ]
Z_{dr}	Differential Reflectivity
Z_{DR}	Differential Reflectivity [dB]
τ	Pulse Duration
t	Temperature
T_s	Pulse Repetition Time
v_a	Aliasing Velocity
v_r	Radial Velocity
$v(t)$	Terminal Velocity of Raindrops
ΔV	Radar Resolution Volume

V	Size of the Volume/Single Cell
W	Water Content
y_p	Polarizability Factor

Appendix B - List Of Acronyms and Abbreviations

ARPS	The Advanced Regional Prediction System
ARRC	Atmospheric Radar Research Center
ARS	Agricultural Research Service
ACF	Autocorrelation Function
C-G	Constrained Gamma DSD Model
CI-GMPE	Constrained Iterative Gaussian Mixture Parameter Estimator
DFT	Discrete Fourier Transform
DP	Specific attenuation-Differential Phase Parameterization
DP-GMPE	Differential Phase Gaussian Mixture Parameter Estimator
DSD	Drop Size Distribution
EM	Electromagnetic
E-M	Expectation-Maximization
FSE	Fractional Standard Error
FV	Final Value Algorithm
GMM	Gaussian Mixture Model
GMPE	Gaussian Mixture Parameter Estimator
GMRE	Gaussian Mixture Rainfall-rate Estimator
H	Horizontal
JPOLE	Joint Polarization Experiment

KOUN	Polarimetric Prototype of the WSR88D Radar
LDR	Linear Depolarization Ratio
MAP	Maximum A Posteriori
MBF	Membership Function
MES	Oklahoma Mesonet
MG	Maxwell-Garnett Mixing Formula
M-P	Marshall-Palmer DSD Model
ML	Maximum Likelihood
NEXRAD	Next-Generation Radar
NN	Neural Network
NSSL	National Severe Storms Laboratory
NWP	Numerical Weather Prediction Model
OU	University of Oklahoma
OU-PRIME	Polarimetric Radar for Innovations in Meteorology and Engineering
PDF	Probability Density Function
PIA	Path-Integrated Attenuation
PLR	Power Low Relation
PPI	Plane Position Indicator
PRM	Polarimetric Radar Measurement
PRF	Pulse Repetition Frequency
PRT	Pulse Repetition Time
QPE	Quantitative Precipitation Estimation
QPF	Quantitative Precipitation Forecast
RCS	Radar Cross Section
RHI	Range Height Indicator
RMSE	Root Mean Square Deviation of Error

SCWC	Self-Consistent With Constraints Algorithm
SD	Standard Deviation
SGMPE	Sequential Gaussian Mixture Parameter Estimator
SNR	Signal-to-Noise Ratio
S-Pol	S-band Polarimetric Radar
UAV	Unmanned Aero Vehicles
UBM	Universal Background Model
V	Vertical
WSR-88D	Weather Surveillance Radar-1988 Doppler